High-Resolution Tools for Probing Energy Transport, Conversion, and Storage at the Nanoscale

by

Amin Reihani

A dissertation submitted in partial fulfillment
of the requirements for the degree of
Doctor of Philosophy
(Mechanical Engineering)
in The University of Michigan
2022

Doctoral Committee:

Professor Edgar Meyhofer, Co-Chair
Professor Pramod S. Reddy, Co-Chair
Adjunct Professor Galen B. Fisher
Professor Vikram Gavini
Professor Rajeev V. Ram, Massachusetts Institute of Technology

Amin Reihani

areihani@umich.edu

ORCID iD: 0000-0002-7755-4533

© Amin Reihani 2022

Acknowledgments

Throughout my graduate studies at the University of Michigan, including two years of master's and five years of Ph.D. studies, I interact with some of the most brilliant and passionate people I have met. This social experience has truly reshaped my way of thinking about different aspects of life and formed my future personal and professional goals.

First and foremost, I would like to extend my sincerest gratitude and appreciation to my advisors Prof. Pramod Reddy and Prof. Edgar Meyhofer, without whose guidance and continuous support, this dissertation would not have been possible. I first met Pramod when I took his *Radiative Heat Transfer* course in 2015 and found him a great teacher who can explain complex scientific concepts in concise and simple terms, indicating his deep understanding of the topic. In fact, I had such a good experience in his class that I started following his research and was fortunate enough to join his group in Jan 2018. As an advisor, Pramod has taught me a great deal over the last four years on both professional and personal fronts. Throughout our many discussions, I found him a very smart person who has developed expertise across many scientific disciplines by obtaining a clear understanding of fundamentals and committing to continuous learning.

I have enjoyed many hours of chatting and discussion with Edgar on both scientific and social topics. He is a great advisor and a brilliant experimentalist, who taught me the elements of successful research and lab work, and more importantly the importance of patience and systematic progress to answer a scientific question. I greatly appreciate the amount of time and effort that

Edgar puts into various research tasks in the lab and the continuous help he provides to the students. I am grateful for his significant help to get me up to speed, and for the key solutions he offered on numerous occasions during the development of the calorimetric reactor (described in Chapter 2) as my first project in the lab.

I would like to thank my previous advisor Associate Research Scientist John Hoard, whom I had the opportunity to work with for more than three years. It was his support, guidance, and encouragement that allowed me to start my graduate studies at Michigan and work on several interesting research projects. John is an exceptional experimentalist who has taught me the fundamentals of experimental research and the development of efficient measurement setups. I will forever be grateful for his endless support and the great many things he has taught me.

I would like to extend my appreciation to my previous co-advisor Prof. Galen Fisher, who is also a member of my doctoral committee. Prof. Fisher is a brilliant physicist and chemist who can define important questions in the field and cleverly design experiments to address them. He has taught me a great deal on many different topics on both scientific and social fronts. I deeply appreciate his knowledgeable advice, guidance, and support over the last seven years.

I would like to also thank all my dissertation committee members, Prof. Rajeev Ram, Prof. Vikram Gavini, Prof. Galen Fisher, Prof. Edgar Meyhofer, and Prof. Pramod Reddy for their constructive comments and discussions on various projects presented in this thesis. Specifically, I would like to thank Prof. Rajeev Ram for their continuous support and valuable insights throughout the course of our collaborative project (presented in Chapter 6), which I consider a great learning opportunity for myself.

Furthermore, I acknowledge the funding sources and grants that I received during my graduate studies at Michigan, including the financial and technical support from Ford Motor Co. during the first three years of my studies (on two projects that are not reported in this thesis). In addition, I would like to thank the financial and technical support from Google. Specifically, I would like to thank David Fork for his valuable technical inputs during the development and modeling of the calorimetric reactor reported in Chapter 2. Further, I would like to acknowledge other funding sources from DOE and ONR as well as the Rackham Predoctoral Fellowship and two Rackham Research Grants that enabled various parts of my dissertation research.

I am also grateful to all my current and previous colleagues and fellow graduate students in the lab, specifically Ju Won Lim, Rohith Mittapally, Shen Yan, Yuxuan Luan, Mitchell Bieniek, Mohit Nahata, and Brent Patterson for their help and valuable feedback on numerous occasions as well as many conversations we shared. I am also thankful to all my friends in Ann Arbor, who have accompanied and supported me throughout the years, as well as my friends from my hometown who have called me occasionally and with whom I share some of the most valuable memories.

I owe the greatest debt of gratitude to my family for their unconditional love, support, and prayers; my dad, for his caring and sacrifices for education from my young ages and preparing me for my future; my mom, for her optimism and pride in me and for being a source of motivation for all my efforts; my little sister, for always being around and happy and for building her bright future, which I am so proud to be a part of it. Finally, I am truly grateful to my wife, Shadi, for her love, encouragement, and constant support that allowed me to continue chasing my goals, but most of all for her patience and friendship during the stressful and difficult phases of our life over the past few years.

Table of Contents

Acknowledgments ii
List of Tables ix
List of Figures x
Abstract xxi
Chapter 1 High-Resolution Thermometry and Thermal Microscopy for Study of Micro and Nanoscale Materials and Devices 1
1.1. Introduction 1
1.2. High-resolution thermometry 2
1.3. Thermometry at the micro and nanoscale 4
1.3.1. Scanning thermal microscopy 4
1.4. Thermometry and calorimetry at elevated temperatures 6
1.5. Structure of this thesis 6
Chapter 2 A Microwatt-Resolution Calorimeter for Studying the Reaction Thermodynamics of Nanomaterials at High Temperature and Pressure 9
2.1 Introduction 10
2.2 Calorimetric reactor design 12
2.2.1 Calorimeter design 12
2.2.2 Temperature sensing scheme 15
2.2.3 Gas handling unit and mass balance measurement scheme 17
2.3 Thermal model and characterization of the calorimeter 20
2.3.1 Lumped thermal capacity model 20
2.3.2 Temperature stability and calorimeter resolution 23
2.4 Characterization of hydrogenation of Pd nanoparticles 26
2.4.1 Baseline measurement for reaction calorimetry 27
2.4.2 Enthalpy of hydrogenation of Pd nanoparticles 28
2.5. Conclusion 35

2.6. Appendix 37
2.6.1. Temperature control of outer and inner shields 37
2.6.2. Characterization of Pd nanoparticles 39
2.6.3. Enthalpy of hydrogenation of Pd nanoparticles 40
2.6.4. Equilibrium hydrogen concentration on Pd nanoparticles 42
Chapter 3 Nanokelvin-Resolution Thermometry with a Photonic Microscale Sensor at Room Temperature 43
3.1. Introduction 44
3.2. Design of thermometer and readout optics 45
3.3. Temperature sensing and thermoreflectance coefficient 47
3.4. Characterization of thermometry resolution 50
3.5. Analysis of noise Sources and thermometry noise floor 53
3.6. Conclusions 57
3.7. Methods 58
3.7.1. Experimental setup 58
3.7.2. Device fabrication 59
3.8. Appendix 60
3.7.1. Experimental setup 60
3.7.2. Beam profile and optical alignment 61
3.7.3. Temperature ramp and hysteresis 62
3.7.4. Quantification of the effect of optical nonlinearities and temperature changes on the sensed temperature in band-edge thermometry 62
3.7.5. Sensing of modulated temperatures 65
3.7.6. Estimating the theoretical noise floor of band-edge thermometer 68
3.7.7. Optical modeling of the thermometer 71
3.7.8. Estimation of sensor footprint area 73
Chapter 4 Quantitative Mapping of Unmodulated Temperature Fields with Nanometer Resolution 75
4.1. Introduction 76
4.2. Results 78
4.2.1. Thermal analysis for quantification of sample temperature 81
4.2.2. Characterization of temperature sensing resolution and stability of CR-SThM 84
4.2.3. Thermal imaging of steady temperature fields 87

4.3. Conclusion 97
4.4. Methods 97
4.4.1. Experimental setup 97
4.4.2. Temperature readout circuits 98
4.4.3. Scanning thermal probe heating and temperature sensing 98
4.5. Appendix 100
4.5.1. Scanning thermal probe fabrication 100
4.5.2. Mechanical stiffness and thermal conductance of scanning thermal probe 101
4.5.3. Sample temperature stabilization 102
4.5.4. Self-heated Pt line sample temperature rise measurement 103
4.5.5. Lumped-capacitance thermal model of scanning thermal probe 104
4.5.6. Temperature measurement stability and noise 108
4.5.7. Estimation of spatial resolution of scanning thermal microscopy 109
4.5.8. Heat transfer model for estimation of temperature profile 111
4.5.9. Histogram analysis of scanning thermal scans 113
4.5.10. Scanning image distortion correction 114
4.5.11. Temperature profile and characteristic length scales 115
Chapter 5 Quantifying the Temperature of Heated Microdevices Using Scanning Thermal Probes 116
5.1. Introduction 117
5.2. Results 118
5.3. Conclusions 127
5.4. Appendix 129
5.4.1. Scanning thermal probe fabrication 129
5.4.2. Finite element modeling of scanning thermal probe 130
5.4.3. Scheme employed for heating and measuring temperatures of STPs 131
5.4.4. Heating and temperature sensing of the heated microdevice sample 132
5.4.5. Thermal analysis 132
5.5.6. Analysis of thermal contact resistance 135
Chapter 6 Measurement of Heat Exchange on Operating Tunnel Diodes via Quantitative Scanning Thermal Microscopy 136
6.1. Introduction 137
6.1.1. Current-voltage characteristic of tunnel diodes 138

6.1.2. Energy transfer in various operating regimes of tunnel diodes 140
6.2. Measurement setup 143
6.3. Tunnel diode sample 144
6.4. Scanning thermal microscopy results 148
6.4.1. Steady state temperature field measurements under unmodulated bias conditions 149
6.4.2. Time-dependent local temperature measurements under modulated bias conditions 153
6.4.3. Time-dependent temperature field measurements under modulated bias conditions 156
6.6. Conclusions 159
References 161

List of Tables

Table 2.1 Comparison to relevant previously developed calorimetry instruments for study of surface and catalytic reactions 12
Table 2.2: Experimental steps employed for the measurement of the hydrogenation enthalpy of Pd nanoparticles 27
Table 2.3: Summary of the measurements of the reaction calorimetry on hydrogenation of Pd nanoparticles. To estimate the error on enthalpy (ΔH), the maximum error of heat of reaction (q) is normalized by amount of absorbed reactant (mol-H_2) 33

List of Figures

Figure 1.1 A comparison of high-resolution thermometers with an operating range close to room temperature[7,15-24]. Various thermometers are shown as a function of thermometry noise floor and sensor footprint area. 3

Figure 1.2 Various operating modes of scanning thermal probe for mapping of surface temperature 5

Figure 2.1. (a) A detailed cross-sectional view of the calorimeter showing the internal components along with a scale bar. The outer copper shield and the inner aluminum shield are shown. The suspended glass tube extends along the length of the calorimeter. The location of thermistors for temperature measurements are shown as small blue circles. Although not apparent from the drawing, the inlet tube and gas inlet are internally connected. (b) A zoomed-in view of the center of glass tube and sample holder capsule assembly. (c) A schematic view of the calorimeter (not to scale). 13

Figure 2.2. Wheatstone bridge circuit with switching balance resistor for readout of the thermistor resistance R_x. The bridge is driven via an AC voltage with amplitude of 100 mV at 199 Hz, and V_g is recorded using a lock-in technique. The balance resistor R_2 is switched automatically using a look-up table at discrete values of resistance ranging from 1 MΩ to 1 kΩ to keep the bridge in range as the thermistor value R_x changes in the operating temperature range of 25 to 300 °C. R_1 and R_3 have a constant value of 10 kΩ. 16

Figure 2.3. Gas handling unit and flow path of the calorimetric reactor. The valves V_0 to V_5 are miniature solenoid valves. During a hydrogen absorption experiment, the prechamber is loaded with the reactant gas to a desired pressure p_1; then this known amount of gas is introduced to the reaction tube while pressure recording provides a means for resolving the mass of absorbed gas on the sample. 17

Figure 2.4 Measured pre-chamber pressure during gas introduction from the pre-chamber to the capillary for resolving the amount of absorbed gas, $\Delta n_{absorbed}$, and equilibrium H/Pd ratio. The dashed line shows a baseline experiment performed using an inert sample capsule with no material. The blue line shows a subsequent experiment with a Pd nano-powder sample of mass 5.19 mg. The red line in the inset indicates the drop in the pressure trace due to absorption of gas on the solid sample. 19

Figure 2.5 Lumped thermal capacity model. The center part of the capillary tube including the sample capsule and the sample, as well as the two thermistors mounted on this region are lumped as a single thermal capacity of $C_{c\text{-}mid}$. Five thermal resistances are included which connect the center node to capillary left/right, inner shield left/right and outer shield..... 21

Figure 2.6 (a) Modeled thermal conductance values (G_{cl}, G_{cr}, G_{isl}, G_{isr}, and G_{os} are the conductance values corresponding to Figure 2.5, $G_{gas\text{-}l}$ and $G_{gas\text{-}r}$ are the gas conductance of left and right part of capillary, $G_{tot,calculated}$ is the sum of all the above conductances) and the measured total effective thermal conductance of the calorimeter ($G_{experimental}$), (b) Modeled thermal capacitance (C_{cm}) and the thermal time constant (τ) along with the measured thermal time constant of the calorimeter. The modeled capacitance is calculated using two different relations for heat capacity of borosilicate glass obtained from [67,68]. 23

Figure 2.7 Stability of the inner shield temperature controller during introduction of reactants to the capillary tube at setpoint of (a) 122°C, and (b) 222°C. The reactant gas (H2 here) is introduced at t = 1 h, perturbing $T_{c\text{-}left}$ and $T_{c\text{-}right}$ temperatures. The temperatures settle back to millikelvin stability within 15 minutes after introduction. The RMS temperature variation in a 1 Hz bandwidth is shown for two time intervals before and after gas introduction (0-0.9 hours and 1.5-6 hours).24

Figure 2.8 Characterization of calorimeter at two different temperatures ($T_{c\text{-}mid}$) values of: (a), (b) 30 °C, and (c), (d) 230 °C. Each experiment is repeated at two different H_2 pressures. Panels (a) and (c) show the transient response of the calorimeter to step inputs to heat flow ($qmid$) with ~1 Hz sampling frequency. Panels (b) and (d) figure shows the steady temperature rise as a function of heat flow input, where the effective thermal conductance and the heat flow resolution of the calorimeter are obtained..... 25

Figure 2.9 Experimental measurements of the temperature rise and heat release rate associated with absorption of H_2 on Pd samples. Data were obtained following the protocol described in Table 2 at an absolute pressure of 7 bar at various temperatures of 30 °C for (a) and (b), 125 °C for (c) and (d), 230 °C for (e) and (f). Panels (a), (c) and (e) show the recorded ΔT of the baseline experiment with an empty sample holder, as well as the absorption experiment using the Pd sample. The capillary reaction tube is initially under vacuum and, at time t = 1h, hydrogen is introduced to the reaction tube, resulting in an exothermic reaction and a transient heat output signal shown in panels (b), (d) and (f). The heat of reaction (q) was obtained by integrating the heat flow between t = 1 to 1.3 h. Δq_{long} is a measure of the long-term stability, which is the maximum cumulative heat release from t = 5 to 6 h. The insets in (a), (c), and (e) show the long-term response, and the insets in (b), (d), (f) show the short-term response. The mass of the Pd sample was 5.10 mg, 3.89 mg and 3.77 mg for the reaction a 30, 125 and 230 °C, respectively. 30

Figure 2.10 (a) Internal energy of reaction per unit mass of Pd samples. Red dots show previous measurements on bulk Pd adapted with permission from [75]. Copyright 2006 Elsevier. (b) Enthalpy per moles of absorbed H_2 at three reaction temperatures and two pressure levels. Error bars are estimated from the maximum long-term stability..... 35

Figure 2.11 Location of the T_{os} thermistor and a planar film heater on the outer shield. 37

Figure 2.12 Stability of the capillary left ($T_{c\text{-}left}$), capillary right ($T_{c\text{-}right}$), and outer shield (T_{os}) temperatures during introduction of reactants to the capillary tube at setpoint of 30°C. The reactant gas (H_2 here) is introduced at t = 1 h, perturbing $T_{c\text{-}left}$ and $T_{c\text{-}right}$ temperatures. The temperatures settle back to millikelvin stability within 15 minutes after introduction. The outer shield temperature is not affected by the introduction of reactants and remains steady. The RMS temperature variation in a 1 Hz bandwidth is shown in the intervals indicated by blue brackets. 38

Figure 2.13. SEM micrographs of a) unprepared commercial Pd nanoparticle samples, b) dispersed sample by sonication in DI water, c) EDX spectrum of the sample showing peaks of Pd and carbon (C). 39

Figure 2.14 Experimental data of temperature rise and heat release rate associated with adsorption of H_2 on Pd samples obtained following the protocol described in Table 2.2 at an absolute pressure of 3 bar and at various temepratures (30 °C (a, b), 125 °C (c, d), and 230 °C (e, f). Panels (a), (c), and (e) show the ΔT recorded during the empty sample holder baseline experiment, as well as the absorption experiment using the Pd sample. The capillary reaction tube is under vacuum during the first hour of the experiment, at time t = 1 h hydrogen is introduced to the reaction tube resulting in an exothermic reaction and a transient heat output signal shown in panels (b), (d), and (f). The heat of reaction (q), shown by the shaded area in the right hand graphs, is obtained by integrating the heat flow between t = 1 to 1.3 h. The bounds on q show the long term stability from t = 5 to 6 h. The mass of the Pd sample was a, b) 5.28 mg, c, d) 3.89 mg, e, f) 3. 77 mg. 41

Figure 2.15. Equilibrium H/Pd ratio of 15 nm Pd nanoparticles obtained from current instrument plotted on the phase diagram of H-Pd system of 32 nm Pd nanocubes. Solid lines show the results of a statistical mechanics Ising model (adapted with permission from Griessen et al. [69]. Copyright 2013 Springer Nature) and filled circles are experimental results using luminescent based sensing of H-content (adapted with permission from Griessen et al. which are scaled results measured by Bardhan et a. [78]). 42

Figure 3.1 Device structure and experimental setup. (a) 3D schematic of the suspended GaAs device, not to scale (b) Cross sectional schematic of the suspended GaAs asymmetric Fabry–Pérot resonator showing the incident and reflected beams and the Au reflector, (c) Bow tie-shaped copper chip holder with the optical thermometer mounted at the center. The temperature of the chip holder is measured using a thermistor and feedback controlled using Peltier elements and resistive heaters, (d) SEM image of a tilted device, showing the suspended GaAs structure and patterned Pt heater/thermometers with the electronic measurement connections. Insets show false colored images of portions of the PRT and ring heater where connections are made in a four-wire configuration. (e) Measurement setup including the laser, optics, vacuum chamber, and electronics for feedback control. Here, FPG: fiber Bragg grating; LP: linear polarizer; EOM: electro-optic (intensity) modulator; HWP: half-wave plate; PM: polarization-maintaining; PBS: polarizing beamsplitter; RS: rotation stage; P: pinhole, PD: photodiode; TIA: transimpedance amplifier… 46

Figure 3.2 Thermoreflectance coefficient of band-edge thermometer (a) Temperature-dependent reflectivity (AC and DC as defined by Eq. 2.1) of the suspended resonator at the band edge (895 nm) for an incident angle of 30°, measured by systematically ramping the temperature from 20 to 42 °C. In addition, the DC reflectance obtained from scattering matrix model is also shown as red dashed curve. (b) Thermoreflectance coefficient (k) for DC and AC reflectivities showing highly temperature-sensitive peaks. (c) Thermoreflectance coefficient around the maximum sensitivity point obtained from a finer temperature ramp. (d) Variation of the AC reflectivity around the maximum sensitivity point of $k_{AC} \sim 30$ when the device temperature (T_{res}) is varied in steps of 1 mK..... 50

Figure 3.3 Characterization of thermometry resolution. (a) Time series of the measured device temperature using platinum resistance thermometry (blue line) and band-edge thermometry (black line), in a 50 Hz measurement bandwidth for a square wave input of heating power (red dashed line) with a periodicity of 0.32 Hz. From the measured data, a thermal response time of 0.10 s is estimated. (b) Bode plot of the temperature rise shows a thermal roll-off frequency $f_c = 1.69$ Hz. (c and d) Characterization of band-edge and platinum resistance thermometry resolution by modulated heat inputs at (c) $f_{mod} = 1$ Hz, (d) $f_{mod} = 2$ Hz. The measurement bandwidth is 0.1 Hz. The error bars show standard deviation of averaging. The dashed lines show the expected temperature rise based on the thermal conductance of the suspended thermometer. Insets show the corresponding time series measurements from two thermometers in a 50 Hz measurement bandwidth..... 51

Figure 3.4 Estimated and experimentally measured noise floor of the band-edge thermometer. (a) Amplitude spectrum of temperature variations of the suspended region (T_{sens}) with (black line) and without (blue) feedback stabilization along with the estimated noise floor, which is the sum of shot noise, Johnson noise, photothermal absorption and optical nonlinearity effects. Further, the estimated noise from thermodynamic fluctuations is also shown (green line). In both cases, the reservoir temperature (T_{res}) is separately stabilized. Data shown in blue, balck and red lines represents an average of 20 spectra. (b) A comparison with other high-resolution, room-temperature thermometers highlights how band-edge thermometry offers significant potential for combining high low thermometry noise floor and small sensor footprint. To estimate the sensor footprint area, the portion of the sensor which needs to thermalize with the environment to sense its temperature (i.e. the active region) was used (see Appendix Section 3.7.8. Estimation of sensor footprint area for details). 55

Figure 3.5 Beam intensity profiles. (a) Intensity profile of the beam focused on suspended thermometer, (b) reflected beam from the suspended thermometer and (c) intensity distribution of the light transmitted through the suspended thermometer. 61

Figure 3.6 (a) The temperature profile of the resonator (T_{sens}) as measured by the integrated platinum resistance thermometer during a ramp up and down protocol. The temperature change

corresponds to a rate of 2.5 mK/s. (b) Measured resonator reflectance during a temperature ramp up and down experiment from around the absorption peak of 32.8 °C. 62

Figure 3.7 Measurement of the effect of optical nonlinearity on reflectance at the resonator absorption peak (T_{res} = 32.79 °C, point of no temperature sensitivity and large absorption). The incident beam was focused to a spot with a diameter of 125 μm. As the incident intensity is increased the reflectance also increases due to nonlinearities in the optical properties as described in the text..... 65

Figure 3.8 (a) Time-averaged temperature of the suspended region (T_{sens}) as obtained from band-edge thermometry and PRT when the temperature is modulated at f_{mod} = 2 Hz. (b) Zoomed plot of time-averaged temperature obtained by band-edge thermometer. The sampling frequency of the time series is 20 Hz, and 100 curves were averaged to obtain the plotted curve..... 67

Figure 3.9 Feedback control schemes for temperature stabilization of the suspended thermometer. (a) Characterization of thermometer resolution for modulated temperature sensing at f_{mod}. (b) Unmodulated temperature sensing and stabilization. 68

Figure 3.10 Amplitude spectrum of temperature variations of the suspended region (T_{sens}) with (black line) and without (blue) feedback stabilization along with the estimated noise floor, which is the sum of shot noise, Johnson noise, photothermal absorption, and optical nonlinearity effects. Further, the estimated noise from thermodynamic fluctuations is also shown (green line). As can be seen, the thermometry noise floor is limited by photothermal absorption (due to probe beam intensity fluctuations) at low frequencies and shot noise at high frequencies. 70

Figure 4.1 (a) Optical microscopy image of the scanning thermal probe showing a suspended region (red dashed box) which acts as a thermal reservoir and the scanning thermal probe (blue dashed box). (b) Tilted false color SEM micrographs (top left panel) of the scanning thermal probe (STP), along with zoomed in image (top right panel) showing the Pt serpentine and T-beams. Bottom panels show zoomed in images of the probe tip. (c) Schematic of the probe during measurement. A DC current (I_{sample}) is sourced through the Pt line which generates a steady state temperature field on the sample. A wheatstone bridge driven by an AC voltage is used to read the resistance of the first PRT for sensing the reservoir temperature (T_R). (d) Schematic of the scanning thermal microscope in contact with a heated Pt line. The second PRT integrated into the STP is connected to a Wheatstone bridge, driven by a specific current waveform (I_{probe}) which is used for temperature sensing and modulated heating of the STP (see main text and methods). 80

Figure 4.2 (a) Lumped-capacitance thermal network of the STP in contact with the sample. T_R, T_P, and T_S are the thermal reservoir temperature, probe temperature, and sample surface temperature respectively. R_P and C_P are the thermal resistance and thermal capacitance of the probe, and the R_{TS} is the probe tip-sample thermal contact resistance. Further, $\dot{q}_P$ is the heat deposited on the probe by the probe heater and the AFM laser. (b) Schematic demonstration of different contact geometries established during thermal scanning in perpendicular direction to a heated Pt line

sample. (c) Thermal frequency response of the STP to an AC heat input with a peak amplitude of 8.5 μW that is deposited on the STP heater at various STP temperatures (T_{DC}). Inset shows the variation of thermal resistance and lumped capacitance of STP as a function of STP temperature (T_{DC}). The measurements were performed under out-of-contact conditions at a gap-size of ~2 μm from the sample surface. 83

Figure 4.3 (a) SEM micrograph of the Pt line sample employed in this work. The Pt line is 250 nm wide and 50 nm thick. The white arrows show the path of the unmodulated electrical current (I_{sample}) employed to heat the Pt line via Joule heating, and the dashed square marks the region where thermal scanning was performed for the data shown in Figure 7. (b) Measured DC temperature rise of the probe when the probe is placed in contact with the Pt line at location A shown in panel (a) as a function of square of heating current sourced to the Pt line sample. Inset shows stepwise increase of square of heating current sourced to the sample during this experiment. (c) The data points on left vertical axis represent the rise in sample (Pt-line) temperature estimated using Eq. 3.1. To obtain the sample temperature, the value of R_{TS} was extracted using Eq. 3.2 and plotted in this panel on the right vertical axis. The dashed line represents the Pt temperature rise as estimated from independent measurements of temperature rise vs heating current described in Appendix Section 4.5.4. Self-heated Pt line sample temperature rise measurement. (d) Allan deviation plot illustrating the stability of the sensed sample temperature (T_S) with and without compensation for laser power fluctuations. It is clear from this data that accounting for fluctuations in laser power output improves the measurement stability at all time scales. 86

Figure 4.4 Data obtained from thermal scan of a Pt line sample at zero heating current. Data shown in all panels was obtained simultaneously in a single scan. (a) Topography map showing the 250 nm-wide Pt line on a SiO_2 substrate, (b) DC temperature (T_{DC}) measured by the probe's platinum resistance thermometer (PRT), (c) amplitude of AC temperature oscillations (T_{AC}) of the probe measured by probe's PRT. (d) Estimated tip-sample thermal resistance R_{TS} obtained from Eq. 3.2, (e) thermal reservoir temperature (T_R) measured using an integrated PRT on the probe thermal reservoir, (f) extracted surface temperature map (T_S) using Eq. 3.1, with a pixel-to-pixel standard deviation of 174 mK. Refer to Appendix Section 4.5.9. Histogram analysis of scanning thermal scans for the histogram distribution of the pixel values. 90

Figure 4.5 Data obtained from thermal scan of a Pt line sample at a heating current of I_{sample} = 0.5 mA. Data shown in all panels was obtained simultaneously in a single scan. (a) Topography map showing the 250 nm-wide Pt line on SiO_2 substrate, (b) DC temperature (T_{DC}) measured by the probe platinum resistance thermometer (PRT), (c) amplitude of AC temperature oscillations (T_{AC}) of the probe measured by probe's PRT (d) estimated tip-sample thermal resistance R_{TS} obtained from Eq. 3.2, (e) thermal reservoir temperature (T_R) measured using an integrated PRT on the probe thermal reservoir, (f) extracted surface temperature map (T_S) using Eq. 3.1. The pixels in the dashed box have a standard deviation of 221 mK. Refer to Appendix Section 4.5.9. Histogram analysis of scanning thermal scans, for the histogram distribution of the pixel values. 91

Figure 4.6 Averaged profiles obtained during thermal scanning of a Pt line such as the scans shown in Figure 4.4-5. To obtain the averaged profiles the image was averaged in y-direction (i.e. the line scans were averaged). (a) Topography profile showing the 250 nm-wide Pt line. (b) DC and AC temperatures measured by the probe's PRT. (c) Estimated tip-sample thermal resistance R_{TS} obtained from Eq. 3.2. (d) Extracted sample surface temperature profile when a DC electrical current of 0.5 mA was supplied to the Pt line sample. (e) Averaged sample surface temperature profiles for three sample heating currents of 0 mA, 0.5 mA, and 0.707 mA. Shaded error bars represent the standard deviation of the measured data. 93

Figure 4.7 Quantitative mapping of temperature fields from a sample consisting of two overlapping 1 μm-wide and 250 nm-wide Pt lines that are heated by a DC current of 0.707 mA. Data shown in all panels were obtained simultaneously in a single scan. (a) Topography map showing the electrical current path by arrows, (b) DC temperature (T_{DC}) measured by the probe's PRT, (c) amplitude of AC temperature oscillations (T_{AC}) of the probe measured by probe's PRT (d) estimated tip-sample thermal resistance R_{TS} obtained from Eq. 3.2, (e) thermal reservoir temperature (T_R) measured using an integrated PRT on the probe thermal reservoir, (f) extracted surface temperature map T_S. The temperature profiles averaged along two lines indicated in the image are shown in Appendix Section 4.5.11. Temperature profile and characteristic length scales. All images were corrected for distortion arising from piezo scanner saturation (see Appendix Section 4.5.10. Scanning image distortion correction). The pixel values in the dashed box have a standard deviation of 238 mK. 96

Figure 4.8 Process steps for fabrication STPs with integrated platinum resistive heater/thermometer and thermal reservoir temperature sensing capability 101

Figure 4.9 (a) Finite element simulation of STP deflection under an applied load. (b) Temperature rise of the probe as a function of heat input to the tip. The slope of the linear fit shows the probe thermal resistance R_P. 102

Figure 4.10 The measured bulk temperature of the feedback-stabilized sample as a function of time. 103

Figure 4.11 Temperature rise of the heated Pt line (250 nm wide, 50 nm thick, 18 μm long) as a function of square of heating current amplitude. 104

Figure 4.12 (a) Allan deviation plot illustrating the stability of the measured sample temperature (T_S) with and without compensation for laser power fluctuations and reservoir temperature (T_R) drift. (b) Amplitude spectrum of measured sample temperature (T_S) for the three cases mentioned above. It is clear from this data that accounting for drift in laser power output and reservoir temperature increases mid to long-term stability and noise..... 109

Figure 4.13 Surface temperature obtained using a line scan perpendicular to a 200 nm-wide Pt line close to the edge of the Pt line (where a significant thermal gradient is present). The surface current

corresponds to a situation where an electrical DC current of 0.7 mA is supplied. (a) Original line scan data with data point spacing of 0.488 nm, (b) Subsampled data at a rate of 1/3, with data point spacing of 1.46 nm. 111

Figure 4.14 (a) Computational domain for the finite-element heat transfer model. (b) Example of obtained steady-state temperature contour for a volumetric heat source of 6×10^{14} W/m^3 applied on the Pt line. 113

Figure 4.15 (a) Scanned surface temperature (T_S) pixel histogram obtained from: (a) the entire image of Figure 4.4f, which shows a standard deviation of 174 mK, and (b) from the pixels inside the dashed box in Figure 4.5f which shows and standard deviation of 221 mK. 114

Figure 4.16 (a) Raw AFM topography image, (b) distortion-corrected topography image. 115

Figure 4.17 Averaged temperature profiles obtained along the lines plotted in Figure 4.7. Profile 1 corresponds to temperature distribution on SiO_2 substrate, and profile 2 corresponds to the temperature profile on 50 nm thick Pt line. 115

Figure 5.1 Scanning electron micrograph (SEM) of the STP probe with an integrated Pt heater thermometer and T-shaped beams. The inset shows the STP tip. (b) SEM of the suspended microdevice (DUT) with embedded Pt heater/thermometer. (c) Schematic illustrating the geometry of the STP in contact with heated DUT. Note, to obtain a clear view, the tip height is exaggerated. (d) DC- and (e) AC-equivalent thermal resistance network corresponding to the geometry shown in (the temperatures T_R and T_S are set to zero for AC network) (c). T_{DC} and T_{AC} represent the STP tip DC temperature and AC temperature amplitude respectively. T_S, R_C and R_{TS} represent the DUT temperature, thermal resistance corresponding to the beams of the STP and tip-sample thermal contact resistance, respectively. While $C_{probe,}$, qDC and qAC represent the lumped thermal capacitance of the STP, and the DC and AC components of the heat input to the STP, respectively. 119

Figure 5.2 Frequency response of a STP probe that is located away (10 μm) from the sample surface measured at various STP tip DC temperatures established by varying the laser power incident on the STP. All data points obtained at constant heating amplitude of $\dot{q}_{AC}$ = 6.1 μW. (b) Thermal conductance of the probe at the low-frequency limit (0.5 Hz) as a function of probe temperature. (c) Thermal cut-off frequency of the STP probe based on the -3dB point as a function of probe temperature. 121

Figure 5.3 Time series of DC and AC temperatures of STP tip (T_{tip}) during two successive contact (pink shaded regions) and retraction cycles (unshaded) on the silicon mesa of the heated microdevice. The surface temperatures are chosen to be T_S = 25.1 °C for the experiment shown in (a) and T_S = 330.6 °C for the experiment show in (b). 124

Figure 5.4 Values of surface temperature (T_S) and tip-sample thermal contact resistance (R_{TS}) estimated from the data shown in Figure 5.3. For the data shown in (a), the surface temperature of the microdevice (T_S) was set to be 25.1 °C, whereas for the data shown in (c), it was chosen to be 330.6 °C. (b) Histogram constructed from the T_S data shown in (a). (d) Same as (b), but for data shown in (c). Gaussian fits to the data in (c) and (d) shown in red. 126

Figure 5.5 Measured temperature (T_S) of heated microdevice (DUT) using the STP (blue) and a Pt resistance thermometer (red) integrated into the heated microdevice as a function of power dissipated in the microdevice (Q_{DUT}). Note, T_S is not a linear function of Q_{DUT} because the thermal conductance of the heated microdevice decreases from 238 $\mu W \cdot K^{-1}$ to 178 $\mu W \cdot K^{-1}$ as the temperature is increased from 25°C to 372 °C. The error bars correspond to ±1 standard deviation as estimated from the Gaussian fits to the histograms shown in Figure 5.4. 127

Figure 5.6 Process steps for fabrication STPs with integrated platinum resistive heater/thermometer. 130
Figure 5.7 Finite element simulation of STP deflection under an applied load. **(b)** Temperature rise of the probe as a function of heat input to the tip, the slope of the linear fit shows the probe thermal resistance ($R_{probe} = 1/G_{probe}$). 131

Figure 6.1 Static current-voltage characteristics of a typical tunnel diode (solid line). The total current comprises three components: tunneling current, excess current, and diffusion current as shown by dashed lines[155]. 139

Figure 6.2 Simplified energy-band diagram of a tunnel diode for: (a) reverse bias with monotonically increasing tunneling current, (b) zero bias or thermal equilibrium, (c) forward bias at $V = V_P$ to obtain the peak tunneling current I_P, (d) forward bias approaching valley current in the negative differential resistance region, (e) forward bias with diffusion current. 140

Figure 6.3 The electrical and thermal transport processes in a tunnel diode at various operating regimes, neglecting the effects of Joule heating and excess current. Left panels show the operating point of the tunnel diode on the I-V characteristic. Right panels show the energy-band diagram. 142

Figure 6.4 Schematic of the measurement setup for cross-sectional scanning thermal microscopy of tunnel diodes. (a) A Beetle type scanning probe microscopy (SPM) stage containing a custom-made aluminum sample holder with tip/tilt/z alignment. Inset shows a cleaved diode sample mounted on a ceramic chip carrier which is mounted on the aluminum sample holder. The scanning thermal probe is shown, which scans on the cross section of the device. (b) Cross section of the SPM stage. The blue ball indicates a glass-encapsulated thermistor used for measurement and stabilization of sample holder temperature (T_{bulk}). A filament heater is used to heat the Aluminum sample holder radiatively from backside. 144

Figure 6.5 SEM micrographs of the cleaved diode surface showing multiple device layers and the doping levels. 145

Figure 6.6 Current-voltage characteristics of the tunnel diode sample used in this study..... 145

Figure 6.7 Cross sectional STEM images of a tunnel diode sample. (a) image taken at the interface of n-InP (top material) and n^+-InGaAs (bottom material). (b) Averaged intensity profile which shows the intensity contrast across the InP/InGaAs interface. (c) Large area STEM image at the expected location of the p-n junction, which shows a uniform crystal structure with no defects or discontinuity across the junction. 146

Figure 6.8 (a) DPC-STEM image of the cross section of a tunnel diode. The top right corner shows the arrangement of segmented DPC detector. The image shows the differential (A-C) signal of the segmented detector. (b) Zoomed in DPC-STEM image (A-C) of the p-n junction. (c) Averaged intensity of the image in panel b along the profile direction shown by red arrow. 147

Figure 6.9 (a) Topography scan at the edge of the cleaved diode, (b) Averaged topography profile along the y-axis of panel a showing different regions of the topography. The inset shows the surface topography on the cleaved cross section of the device having a standard deviation of 1.75 nm. 149

Figure 6.10 Data obtained from thermal scan using the CR-SThM method at the cross section of a tunnel diode at zero bias. Data shown in all panels were obtained simultaneously in a single scan. (a) Topography scan showing different regions of the device, (b) DC temperature (T_{DC}) measured by the probe, (c) Amplitude of AC temperature oscillations (T_{AC}) of the probe measured by probe. (d) Estimated tip-sample thermal resistance R_{TS} obtained using Eq. 3.2, (e) extracted surface temperature map (T_S) using Eq. 3.1. The pixel-to-pixel standard deviation of T_S on the active region plus the substrate is 65 mK. 151

Figure 6.11 Averaged profiles obtained during thermal scanning of a tunnel diode at zero bias. To obtain the averaged profiles the image was averaged in *y*-direction (i.e. the line scans were averaged). The shaded region indicates ±1 standard deviations of the averaged profiles. (a) Topography profile, (b) DC and AC temperatures measured by the probe, (c) Estimated tip-sample thermal resistance R_{TS} obtained from Eq. 2. (d) Extracted sample surface temperature. 152

Figure 6.12 Averaging scheme used in time-domain measurement of sample surface temperature (T_S) when a three-level pulse (-25 mV/ 0 mV/ +25 mV) was applied to the diode. The dashed lines indicate the applied bias waveform. The scanning thermal probe was stationary and parked close to the p-n junction on the cross section of the diode. The red lines indicate the averaged time-series, and the shaded regions indicate the 95% confidence interval of the averaged signal. (a) 200 pulse periods averaged, (b) 500 pulse periods averaged, (c) 1000 pulse periods averaged, (d) 2000 pulse periods averaged, (e) 4000 pulse periods averaged, (f) 8000 pulse periods averaged. 154

Figure 6.13 Time-domain response of the diode temperature to an applied 3-level bias pulse (-25 mV/ 0 mV/ +25 mV) shown by the dashed blue line. For this measurement, the scanning thermal probe was stationary and parked close to the p-n junction on the cross section of the diode. Red curve the shows average of 9900 measurements and the shaded region shows the 95% confidence interval. Four steps of the temperature change during and after the -25 mV bias pulse are labeled. 156

Figure 6.14 Time-domain response of the diode surface temperature to an applied 2-level bias pulse at 0 mV / -25 mV. To calculate the temperature change when a bias pulse is applied, we defined two regions of the time series, shown by blue (for zero bias), and green (for nonzero bias). 157

Figure 6.15 Thermal line scan under modulated bias pulse of 0 mV / -50 mV with a period of 2 s and duty cycle of 50%. (a) Topography scan obtained during the coarse thermal scan (circle markers), and a fine topography scan obtained exactly before the thermal scan (dashed line). (b) Mean surface temperature change ΔT_s obtained by averaging 5000 bias pulses as a function of location and lag time. Error bars represent 95% confidence interval of the mean. 158

Figure 6.16 Measured average temperature change (ΔT_S) under modulated bias condition, with a lag time of $t_{lag} = 0.1$s, for the entire active region of the device. Error bars represent 95% confidence interval of the mean. Blue curve shows quadratic fit to the data, and the green shaded region indicates cooling. 159

Abstract

Probing energy dissipation and transport at the micro- and nanoscale has become increasingly important across various disciplines including solid-state electronics and optoelectronics, thermoelectrics, plasmonics, catalysis, hydrogen storage, and electrochemical energy storage. This thesis describes the development of high-resolution calorimetry, thermometry, and thermal microscopy tools, and next how these techniques can be utilized for investigating nanoscale systems with applications in energy conversion, energy storage, and thermal management of electronics.

First, I present a high-temperature and high-pressure calorimetric micro-reactor with microwatt heat flow resolution for studying heterogeneous reactions and phase transformations of nanomaterials. This instrument enables measurements of enthalpy of reaction and reactant consumption with milligram scale (<10 mg) nanomaterial samples. Next, I describe how we utilized this instrument to study the thermodynamics of hydrogen absorption on Pd nanoparticles, a model metal hydride system, which is beneficial for the design of high-efficiency hydrogen and energy storage systems that rely on solute-induced phase transformations.

Second, I describe an optical thermometry technique to obtain nanokelvin resolution—at room temperature—using a microfabricated sensor. The thermometer consists of an asymmetric Fabry-Pèrot resonator made from GaAs, which is excited by a narrow-linewidth probe laser at the band-edge of the material. Using this system, I demonstrate a resolution of 60 nK/√Hz, which is

attributed to the sharp resonance and strong temperature dependence of bandgap in GaAs. This thermometer outperforms previously developed temperature sensors in sensor size and/or resolution by at least an order of magnitude.

Third, I describe a Scanning Thermal Microscopy (SThM) technique, using custom-fabricated probes with integrated platinum heater and thermometer, for quantitative mapping of steady and time-varying temperature fields with nanometric resolution. I demonstrate—for the first time—the ability to directly measure the tip-sample thermal contact resistance simultaneously during thermal scanning, which enables accurate deconvolution of the effects of sample topography and material variations from the temperature field, achieving a quantitative temperature field that is almost free of artifacts with a spatial resolution of ~7 nm.

Fourth, I describe a high-temperature variant of the aforementioned SThM technique, which was used for quantification of the temperature of heated microdevices at elevated temperatures, where other micro-thermometers often fail due to thermal stress. This technique was validated by performing independent temperature measurements on a heated microdevice. Using this technique, I characterized the temperature of micro-emitters up to 1270 K, which were later employed in high-energy density and efficiency near-field thermo-photovoltaic energy conversion.

Fifth, I describe the results of our collaborative study of the heat transfer processes and internal cooling in semiconductor p-n junctions, which are essential elements of devices such as light-emitting diodes (LEDs), laser diodes, transistors, and solar cells. Theoretical studies have predicted internal cooling in both conventional p-n junctions as well as tunnel junctions. This internal cooling can improve the thermal management of various devices and improve the energy conversion efficiency of LEDs. In this study, we conducted quantitative SThM measurements to probe the time-dependent temperature field in the cross section of a tunnel diode. These results

indicate cooling in the reverse bias tunneling current regime at small bias values, and heating in larger reverse bias and forward bias conditions. These observations are consistent with previous theoretical studies and can be explained based on the energy change of carriers as they transition from the bulk transport states to the tunneling state.

Chapter 1 High-Resolution Thermometry and Thermal Microscopy for Study of Micro and Nanoscale Materials and Devices

1.1. Introduction

Temperature is one of the key quantities in physical systems and a central concept in thermodynamics and statistical mechanics. Temperature can be qualitatively defined as a measure of the hotness or coldness of a medium. For a quantitative definition of temperature, we need to recourse to thermodynamics and the definition of thermal equilibrium. In thermodynamics, the temperature is defined by the property that: two systems that can exchange energy and are in thermal equilibrium have equal temperatures[1,2]. Quantitatively, temperature can be defined using the second law of thermodynamics as the rate of change of internal energy with entropy ($T = \partial U/\partial S$)[3]. Another definition based on the kinetic theory of gases is that temperature is proportional to the mean molecular kinetic energy so that the mean energy is equal to $\frac{3}{2} k_B T$, where k_B is the Boltzmann constant[4].

Temperature is measured using thermometers that convert temperature-dependent physical phenomena into a temperature-dependent signal which is then converted into a temperature value using a calibration. Thermometers can be classified into invasive (e.g. thermocouples), semi-invasive (thermochromic paint), and non-invasive (e.g. pyrometers). Further, thermometers can be

classified based on their operating temperature range, temperature sensitivity (or temperature sensing resolution), sensor size (or spatial resolution), and sensor response time.

Thermometry and temperature control are ubiquitous across various disciplines including engineering, physics, chemistry, and biology. High-resolution thermometry is critical for instrumentation and sensitive measurements[5]. In addition, thermometers are an important component of calorimeters which quantify heat flows generated by various phenomena including chemical reactions[6], metabolism in biological systems[7], and dissipation in electronics[8] and quantum systems[9]. Further, thermometers are used in bolometry which enables broadband detection of electromagnetic radiation[10] and energetic particles[11], as well as mm-wave/THz/Infrared (IR) sensing and imaging applications[12]. In what follows we will discuss thermometers with high temperature sensing resolution, as well as thermometry techniques with high spatial resolution for sensing and thermal imaging at the micro and nanoscale.

1.2. High-resolution thermometry

High-resolution thermometry refers to temperature sensors that can resolve small temperature changes. Here we consider thermometers with better than 100 μK resolution and temperature control systems with better than 100 μK stability at room temperature. The thermometers that can achieve such resolution can be broadly classified into electronic and optical devices. Electronic sensors include thermocouples that work based on the Seebeck effect, resistance-based sensors, and microelectromechanical systems (MEMS)-based sensors. By optical thermometers, we mean sensors that rely on extracting temperature-dependent signals from light beams that are emitted, reflected, or transmitted from a medium. Examples of optical thermometers include Raman scattering thermometry[13], luminescent thermometry (e.g. nitrogen-vacancy (NV) centers in

diamond)[14], and optical resonator-based thermometers which rely on either thermal expansion or change of optical properties such as refractive index as a function of temperature[15,16].

In Figure 1.1 we list several high-resolution thermometry techniques that have been demonstrated in the past with an operating temperature close to room temperature and present their reported thermometry noise floor (units of $\mu K.Hz^{-1}$) and sensor footprint area. To estimate the sensor footprint area, the portion of the sensor which needs to thermalize with the environment to sense its temperature (i.e. the active region) was used. As shown by a red shaded area there are no reported room-temperature thermometers with micron-scale (area <1 mm^2) foot print and sub-microkelvin noise floor (<1 $\mu K.Hz^{-1}$). Such sensors, if successfully developed, could enable future devices and experimental platforms where a miniaturized sensor combined with high resolution is required. Examples of such devices include bolometer arrays for imaging in the THz/IR range, sensors for single-cell bio-calorimeters, and for studies of thermal transport at the nanoscale.

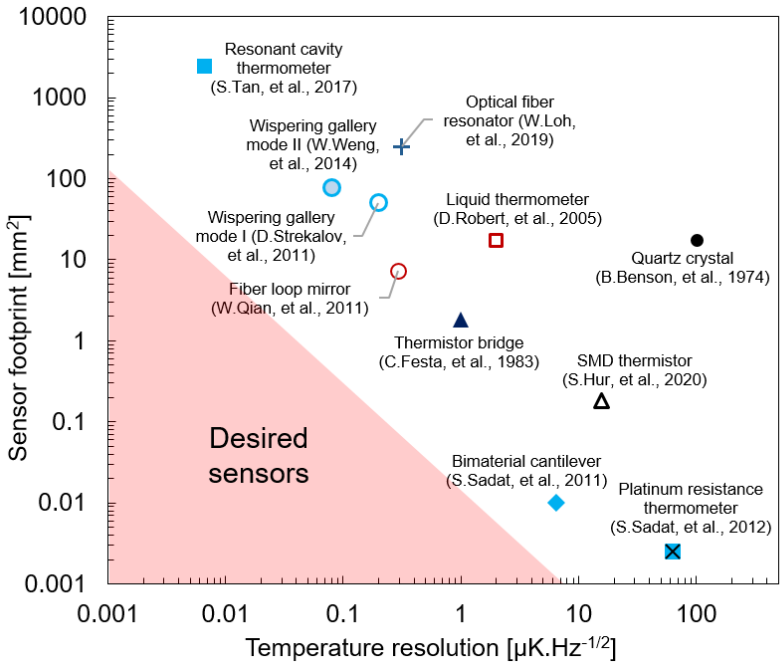


Figure 1.1 A comparison of high-resolution thermometers with an operating range close to room temperature[7,15-24]. Various thermometers are shown as a function of thermometry noise floor and sensor footprint area.

1.3. Thermometry at the micro and nanoscale

In recent years, continuous advancements in nanomaterials and nanotechnology have increased the demand for measurement of physical quantities and material properties at the nanoscale across many disciplines including biomedical research, material synthesis and fabrication, electronics, and emerging quantum systems. For example, miniaturization of electronics and increase in their switching speed has increased the associated energy dissipation at the nanoscale which requires accurate knowledge of localized heating and temperature field in order to improve the design and manufacturing of devices[25]. As another example, accurate knowledge of temperature fields associated with living cells can provide valuable information on the metabolic activity for monitoring the state of health of the cell[26,27]. For example, cancer cells demonstrate an increased metabolic activity compared to normal tissue leading to a higher cell temperature, which can be used as a diagnosis tool[28]. Such information can be obtained using thermometers with sub-micrometer spatial resolution, which is typically defined as the minimum distance that the sensor needs to move to detect a temperature change greater than the thermometry resolution[29]. While many techniques are available for thermometry with sub-micrometer resolution, such as thermoreflectance[30], Raman scattering[13], and luminescence thermometry[14], in this dissertation I will focus on Scanning Thermal Microscopy (SThM) techniques, which enable surface temperature mapping with a spatial resolution of <10 nm[31].

1.3.1. Scanning thermal microscopy

Scanning Thermal Microscopy (SThM) is a measurement technique based on Scanning Probe Microscopy (SPM)[32] which enables a variety of capabilities such as mapping of surface temperature[33,34], measurement of substrate thermal properties (e.g. thermal conductivity[35,36], phase transformation temperature[37]) and nanofabrication via surface lithography[38] using high-

temperature probes with nanometer spatial resolution and fast response time (order of milliseconds)[31]. Here we focus primarily on the nanoscale temperature mapping capability of SThM.

Figure 1.2 schematically shows the operating modes of SThM. The scanning thermal probe consists of a body (thermal reservoir), a cantilever, and a sharp tip with an integrated thermometer. It can be operated in contact mode where the heat transfer between the sample and the probe is dominated by conduction, or non-contact mode where the probe is maintained tens to hundreds of nanometer above the surface where heat conduction through the air (when operated in ambient condition) or near-field heat transfer (when operated under high vacuum condition) dominate the sample-probe heat transfer. In addition, the SThM probe can be operated either in an *active mode* where the probe is actively heated either using joule heating or via an optical beam, and the tip of the probe acts as a nanoscale local heater on the sample, or in a *passive mode* where the probe acts as a local thermometer with minimal heat dissipation[31].

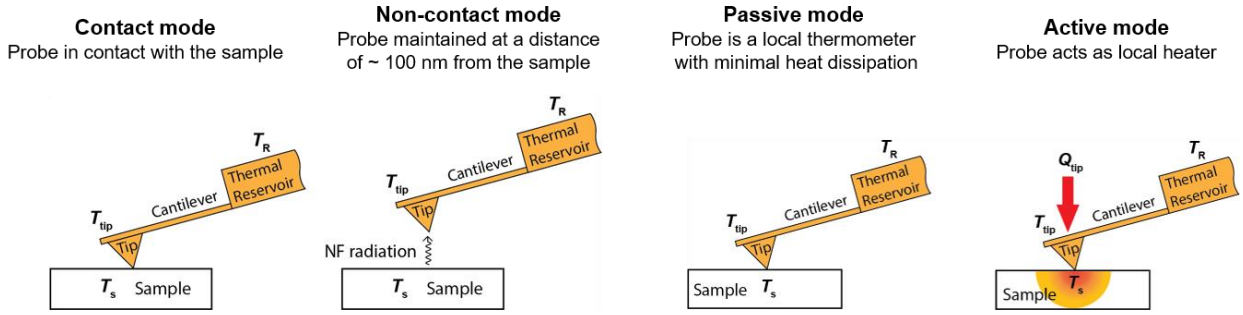


Figure 1.2 Various operating modes of scanning thermal probe for mapping of surface temperature

The key challenges associated with temperature mapping using SThM are modeling or calibration of the tip-sample heat transfer rate which is necessary for quantitative temperature mapping, and vulnerability to topological artifacts and abrasion of the tip which can cause large measurement variability. Due to these challenges commercial SThM systems are not widely available[31].

1.4. Thermometry and calorimetry at elevated temperatures

In the previous sections, we discussed thermometry techniques with high temperature sensing resolution and high spatial resolution with an operating range close to room temperature. However, a variety of applications and experimental studies require thermometry at elevated temperatures and small scales. Examples include high-temperature calorimetry for the study of thermodynamics of chemical reactions and phase transformation of nanomaterials for heterogeneous catalysis[39,40], energy storage[41,42], and hydrogen storage[43-45] applications. Other examples include high-temperature thermometry of microscale devices, which is critical for successfully employing them in probing nanoscale transport via conduction[46,47] and radiation[48], as well as novel thermal energy conversion applications such as near-field thermophotovoltatics[49,50]. Such temperature measurements become challenging for small devices at high temperatures due to the difficulties in integrating reliable thermometers. The techniques for high-temperature thermometry at the micro/nanoscale include phase change of nanoparticles[51], Raman spectroscopy[52], integration of fine thermocouples[49] that may lead to the destruction of the microdevice and other optical approaches[53].

1.5. Structure of this thesis

In my doctoral work, I first focused on the development of high-resolution calorimetry, thermometry, and thermal microscopy tools, and next utilized these techniques for investigating a number of nanoscale systems with applications in energy conversion and storage and thermal management of electronics. The results are presented in five chapters as briefly described below.

In **chapter 2**, I present the development of a high-temperature and high-pressure calorimetric micro-reactor with microwatt heat flow resolution for studying heterogeneous reactions and phase transformations of nanomaterials. The challenges associated with resolving enthalpy of reaction and reactant consumption with milligram scale of nanomaterial samples at such operating conditions, including instrument stability and long-term drift are specifically discussed. Next, we utilized this instrument to study the thermodynamics of hydrogen absorption on Pd nanoparticles. The study of the Pd-H system is beneficial for the design of high-efficiency hydrogen storage systems, batteries, and thermochemical energy storage systems, all of which rely on solute-induced phase transformations.

In **chapter 3**, we demonstrate a novel thermometry technique to obtain nanokelvin resolution at room temperature using a micro-sensor with an all-optical readout. The temperature sensing mechanism and device design and fabrication are first discussed. Afterward, the optical measurement setup and characterization of the thermometry resolution for sensing modulated/unmodulated temperature as well as closed-loop temperature stabilization are presented. The experimental results are explained via a detailed scattering matrix model of the sensor. Finally, the contributions of different noise sources, as well as the theoretical limit to the thermometry resolution are calculated.

In **chapter 4**, we present a Scanning Thermal Microscopy (SThM) technique using custom fabricated probes for quantitative mapping of temperature fields with nanometric resolution on samples with topography and material variations. We present a novel measurement scheme that enables reliable de-convolution of the effect of variation in probe tip-sample thermal contact resistance from the measured temperature field. This scheme was demonstrated by scanning temperature fields in the vicinity of a self-heated 200 nm wide Pt line and was able to suppress the

temperature artifacts at the boundaries of the Pt line, as well as the artifacts associated with probe tip abrasion. Further, the measured temperature profile was validated against a continuum heat transfer model of the heated line sample. In addition, a variant of this technique was used in **chapter 5**, for quantification of temperature of headed microdevices at elevated temperatures, where other micro-thermometers often fail due to thermal stress. This technique was validated by performing independent temperature measurements on a heated microdevice. Further, this technique was utilized to characterize the temperature of micro-emitters up to 1270 K, which were later employed in high-energy density and efficiency near-field thermo-photovoltaic energy conversion.

In **chapter 6**, I present results of our collaborative study on the heat transfer processes involved in semiconductor p-n junctions, which are essential elements of devices such as light-emitting diodes (LEDs), laser diodes, transistors, and solar cells. Theoretical studies have predicted internal cooling in both conventional p-n junctions as well as tunneling junctions which operate based on interband tunneling of charge carriers. This internal cooling can improve the thermal management of various devices and improve the energy conversion efficiency of LEDs. We conducted quantitative SThM measurements to probe the time-dependent temperature field *operando* on the cross section of a tunnel diode sample. The experimental results demonstrate cooling at the cross-section of the diode in the reverse bias tunneling current regime at small bias values, and heating in larger reverse bias and forward bias conditions, consistent with previous theoretical studies. The observed phenomenon is important for the design of a number of optoelectronic and electronic devices.

Chapter 2 A Microwatt-Resolution Calorimeter for Studying the Reaction Thermodynamics of Nanomaterials at High Temperature and Pressure

Reproduced with permission from the *American Chemical Society*. See Ref. 6

Amin Reihani, Ju Won Lim, David Fork, Edgar Meyhofer, Pramod Reddy

Calorimetry of reactions involving nanomaterials is of great current interest but requires high-resolution heat flow measurements and long-term thermal stability. Such studies are especially challenging at elevated reaction pressures and temperatures. Here, we present an instrument for measuring the enthalpy of reactions between gas phase reactants and milligram scale nanomaterial samples. This instrument can resolve the net change in the amount of gas phase reactants due to surface reactions in an operating range from room temperature to 300 °C and reaction pressures of 10 mbar to 30 bar. The calorimetric resolution is shown to be <3 μW/√Hz, with a long-term stability <4 μW/hour. The performance of the instrument is demonstrated via a set of experiments involving H_2 absorption on Pd nanoparticles at various pressures and temperatures. For this specific reaction, we obtained a mass balance resolution of 0.1 μmol/√Hz. Results from these experiments are in good agreement with past studies establishing the feasibility of performing high resolution calorimetry on milligram scale nanomaterials, which can be employed in future studies probing catalysis, phase transformations, and thermochemical energy-storage.

2.1 Introduction

Knowledge of the thermodynamics of surface reactions and phase transformations in nanomaterials is of crucial importance to heterogeneous catalysis, sustainable production of fuels and chemicals, as well as for hydrogen storage and fuel cell applications[54]. In particular, nanomaterials, such as noble metal nanoparticles, are excellent candidates for these applications as they provide a high surface to volume ratio and low resistance to reactant mass diffusion[55]. Further, in the context of hydrogen storage for renewable energy and transportation applications, metal hydride nanoparticles are considered to be a promising platform as they enable storage of large amounts of hydrogen (volumetric hydrogen storage density) in the interstitial sites of crystal lattices and feature rapid kinetics at room temperature[54].

Calorimetric reactors enable direct measurement of reaction thermodynamics and kinetics, and past work[40,43,56-58] has developed sensitive calorimeters to study surface reactions and catalysis. In Table 1 we summarize data from five representative studies, listing their operating range and main figures of merit. The instruments employ various temperature sensors, such as RTDs[56], thermocouples[43,57], and pyroelectric heat detectors[40]. In addition, they use several techniques for quantifying the mass of gas phase reactants, such as pressure-concentration measurements[56,57], molecular beams with known fluxes of reactants[40], and gravimetric measurements using a microbalance[58]. Additionally, the specifications of two relevant, commercially available instruments are listed in Table 1. An important criterion for calorimetric measurements of chemical reactions is the amount of sample required for measurements. The amount and type of catalyst samples differ across previous studies: some use powdered samples, typically on the gram-scale[43,56,57], while others use either thin-film single crystals or dispersed samples[40,58]. While the former group can achieve high temperature and pressure reaction conditions, the latter group is

limited to low pressures and operation close to room temperature, largely due to use of microfabricated devices, sensors incompatible with high pressure or temperature or the need for operation under vacuum environment. In addition, the high temperature and pressure operation of the calorimeters utilizing powdered samples is impeded by poor long-term temperature stability and low heat flow resolution due to high effective thermal conductance of the calorimeter. Moreover, given that lab synthesis of novel catalysts and nanoparticles on the gram scale is often challenging, it is highly beneficial to develop calorimeter tools capable of accurate heat of reaction measurements with milligram scale samples, at high-temperature and pressure conditions. Here, we present an instrument that addresses this need by enabling high heat flow resolution (<3 $\mu W/\sqrt{Hz}$) as well as long-term stability (<4 μW/hour) at temperature from 23 to 300 °C and reaction pressures of 10 mbar to 30 bar to resolve reaction energetics with high signal to noise ratio over a duration of several hours. This instrument has been tested over a duration of several days at up to 280 °C, and for durations of several hours at 300 °C.

Table 2.1 Comparison to relevant previously developed calorimetry instruments for study of surface and catalytic reactions

Study	Typical sample size	p range	T range	Thermal time constant	T resolution	Power resolution	Long-term stability	Mass balance ability	Mass balance resolution
Ref. #	-	Bar	°C	s	K/√Hz	W/√Hz	W/h	-	mol
Ref. [56]	~ 4 g	0.1 -200	100-600	90	10^{-3}	10^{-3}	<0.5	Yes	NA
Ref. [57]	~ 1 g	1- 33	RT-1300	~1800	<0.1	0.44	<0.75	Yes	0.02 mol
Ref. [43]	0.4 g	1-1.3	RT	~ 60 s	NA	NA	0.007 K/hour	Yes	NA
Ref. [40]	1µm films	10^{-6} – 10^{-3}	-173 - +27	0.15	NA	~10^{-7} W	1 mK/h	Yes	8×10^{-12} mol/cm^2 of sample
Ref. [58]	10 µg	Vacuum-1	RT-45	NA	10^{-4}	10^{-6}	10^{-6}	Yes	0.01 mol
TA Instruments Nano ITC	Volume 1.0 ml	NA	2-80	13	NA	10^{-7} W	<2×10^{-8}	No	NA
Setaram C80	Volume 12.5 ml	up to 1000 bar	Ambient to 300	~320 s *	0.1	10^{-6} W	NA	Yes	NA
Current instrument	1-5 mg	10 mbar-30 bar	22-300	<75s @25°C <30s @300°C	<10^{-3}	< 3×10^{-6}	<4×10^{-6}	Yes	0.1 µmol/√Hz

***** Calculated from heat release data in Ref [44].

2.2 Calorimetric reactor design

2.2.1 Calorimeter design

The design of the calorimeter developed in this work is illustrated schematically in Figure 2.1. It consists of two thermal shields to minimize temperature fluctuations that were machined from copper and aluminum. A borosilicate glass capillary (Inner diameter (ID) = 2 mm, Outer diameter (OD) = 3 mm) is encapsulated by the shields. The capillary has an inward notch at the center of the capillary to hold a borosilicate sample holder (capsule) (see Figure 2.1b) where the reaction

occurs. The volume enclosed by the outer shield is under a high vacuum (<7 µtorr) and its temperature is stabilized, via a feedback control loop, above room temperature (typically set to a temperature in the range of 23 to 36 °C) using two planar film heaters (see Appendix Figure 2.11). The outer shield is placed on four ceramic balls (see Figure 2.1a) to thermally isolate it from the environment and gas handling unit.

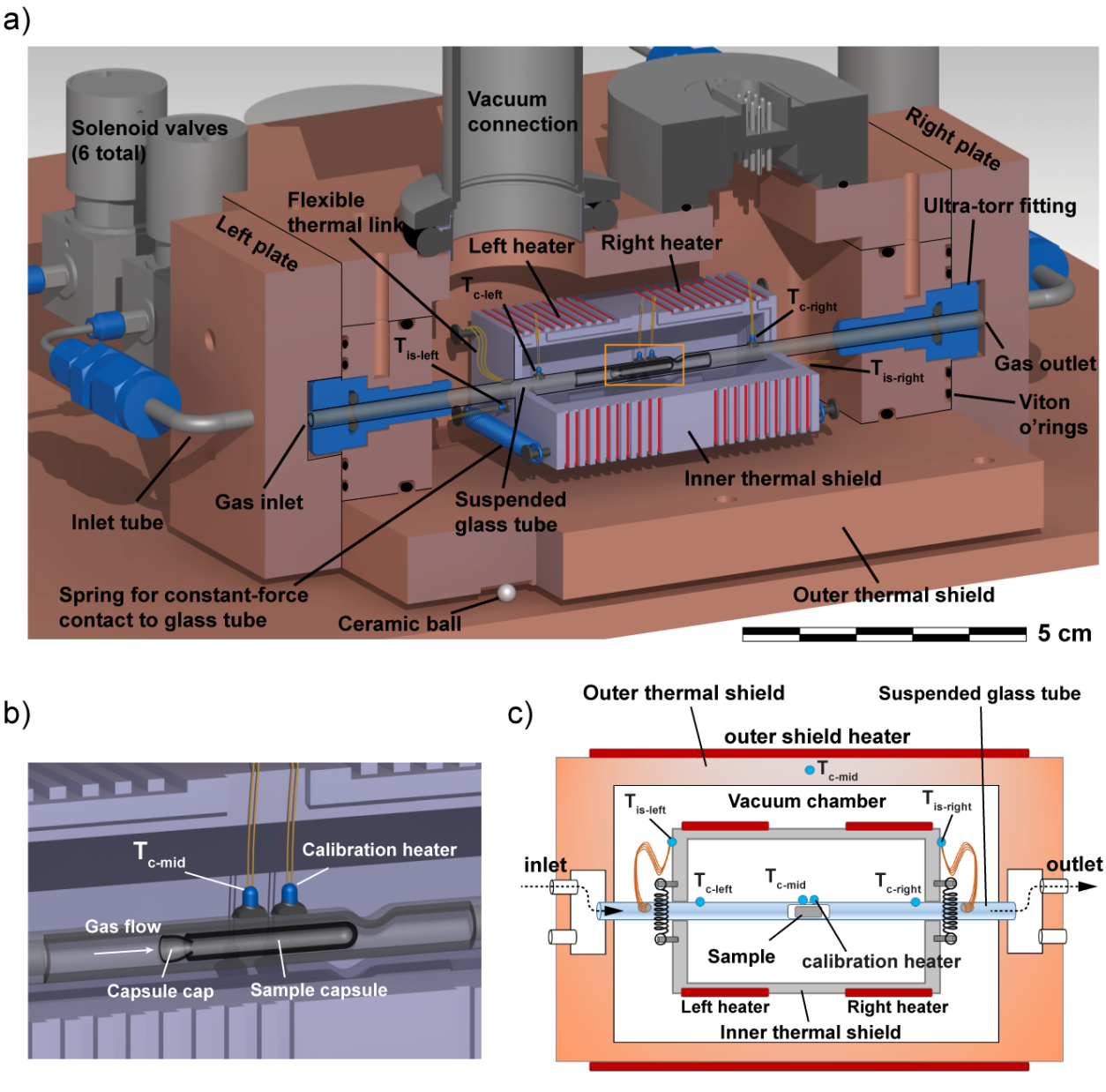


Figure 2.1. (a) A detailed cross-sectional view of the calorimeter showing the internal components along with a scale bar. The outer copper shield and the inner aluminum shield are shown. The suspended glass tube extends along the

length of the calorimeter. The location of thermistors for temperature measurements are shown as small blue circles. Although not apparent from the drawing, the inlet tube and gas inlet are internally connected. (b) A zoomed-in view of the center of glass tube and sample holder capsule assembly. (c) A schematic view of the calorimeter (not to scale).

The inner shield (shown in Figure 2.1a, c) covers the central part of the capillary tube, which is heated to the target reaction temperature (25 - 300 °C) using two resistive heaters made of NiChrome wire (AWG 38) (shown by red lines in Figure 2.1a), which cover the circumference of the shield and uniformly heat the inner shield. A thin (50-100 μm) layer of a ceramic adhesive (Ted Pella, 16026) is applied underneath the NiChrome wire to provide electrical insulation from the aluminum inner shield. The inner shield is split in the middle and held together via two springs to compensate for the mismatch of radial thermal expansion between aluminum and the borosilicate tube at high temperatures.

The line contact between the inner shield halves and the tube surface results in a weak thermal link (i.e. low thermal conductance); therefore, fluctuations in the thermal conductance of this weak link have a relatively small impact on the temperature of the capillary tube. Nevertheless, a stable strong thermal link between the inner shield and capillary tube is required to enable efficient heating of the central part of the capillary tube. This strong thermal link is achieved via flexible copper wires (fifteen AWG38 wires with a length of 20 mm were used on each side of the inner shield), which on one end are connected mechanically to the inner shield and on the other end soldered ultrasonically directly on the capillary tube as shown in Figure 2.1a. This method of thermal connection via flexible wires is robust and insensitive to thermal expansion, therefore, it provides high long-term thermal stability over a large number of operating cycles. During the development of this apparatus, we found that other thermal contacts, such as high-temperature ceramic epoxy (Ted Pella, 16026) and leaf springs inserted in the clearance between the inner shield and capillary tube, were not suitable. Their thermal conductance drifted excessively over

time due to the mismatch in thermal expansion between the aluminum inner shield and glass capillary tube.

The calorimeter temperature is monitored at six points using glass-encapsulated thermistors that are read out with Wheatstone bridges as described below. The temperature of the outer shield (T_{os}) is measured by a thermistor located 6 mm inside the bulk of the outer shield (see Appendix Figure 2.11). The temperatures at the left (T_{is_left}) and the right (T_{is_right}) side of the inner shield are measured close to the contact points of the copper wires with the capillary tube (see Figure 2.1a, and c). The temperature of the capillary tube is monitored at three different locations; left, right, and center of the capillary tube and are labeled $T_{c\text{-}left}$, $T_{c\text{-}right}$, and $T_{c\text{-}mid}$, respectively. The glass-encapsulated thermistors were connected to the capillary tube using ultrasonic glass soldering to minimize long-term changes in contact thermal conductance. At the center of the tube, an additional thermistor was installed to act as a dedicated heater (by Joule heating) and employed for calibration of the calorimeter as described below. The heat conduction via thermistor leads is minimized by using thin electrical connection wires (AWG 42 to AWG 50) that are >30 mm in length.

2.2.2 Temperature sensing scheme

Temperature sensing is performed using 1 MOhm glass-encapsulated thermistors (US Sensor GP105V8J), which are read out as reported previously[59]. In this scheme, the thermistor's resistance is measured via a full Wheatstone bridge (see Figure 2.2) driven by an AC voltage of 100 mV peak amplitude at 199 Hz sourced by an Agilent 33120 function generator. The output voltage of the bridge (V_g) is first amplified (40 dB) by an instrumentation amplifier (Analog Devices AD524ADZ), then low pass filtered at a cut off frequency of 220 Hz using a 4th order Butterworth filter (Krohn-Hite 3384) and amplified by 10 dB, and is recorded using an analog input DAQ

channel (NI PCI-6014) at 19.9 kHz sampling rate. The signal amplitude and phase with respect to the excitation are synchronously measured, at the excitation frequency, using a LabView lock-in program. In addition, the effect of thermal drift is minimized by using electronic components featuring very low temperature coefficients of resistance, such as Vishay's ultra high precision Z-foil resistors (Y145310K0000V9L).

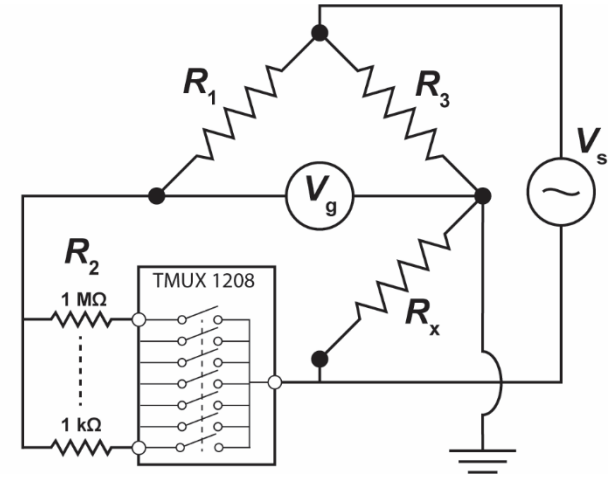


Figure 2.2. Wheatstone bridge circuit with switching balance resistor for readout of the thermistor resistance R_x. The bridge is driven via an AC voltage with amplitude of 100 mV at 199 Hz, and V_g is recorded using a lock-in technique. The balance resistor R_2 is switched automatically using a look-up table at discrete values of resistance ranging from 1 MΩ to 1 kΩ to keep the bridge in range as the thermistor value R_x changes in the operating temperature range of 25 to 300 °C. R_1 and R_3 have a constant value of 10 kΩ.

Since the measurement range for the capillary and inner shield thermistors spans from 25 to 300°C, their electrical resistance changes accordingly from 1 MΩ to 0.5 kΩ (at 300 °C). This large variation of resistance significantly reduces the Wheatstone bridge sensitivity. Therefore, to achieve the desired sub-millikelvin sensitivity in the entire operating range, the balance resistor (R_2) of the Wheatstone bridge (Figure 2.2) is actively varied using a resistor bank and a multiplexer (TMUX 1208) with eight resistors with values ranging from 1 MOhm to 1 kOhm so as to balance the Wheatstone bridge at all desired temperatures of operations. The upper resistors in the bridge, R_1 and R_3, have a constant value of 10 kOhm.

2.2.3 Gas handling unit and mass balance measurement scheme

The gas handling unit and the flow path for the gases into the calorimeter are shown in Figure 2.3. The gas handling unit consists of a prechamber, a capillary tube, and six miniature fast switching solenoid valves (Parker Hannifin, Series 99). In order to quantify the mass of the introduced gas, a pressure measurement scheme is used as described below.

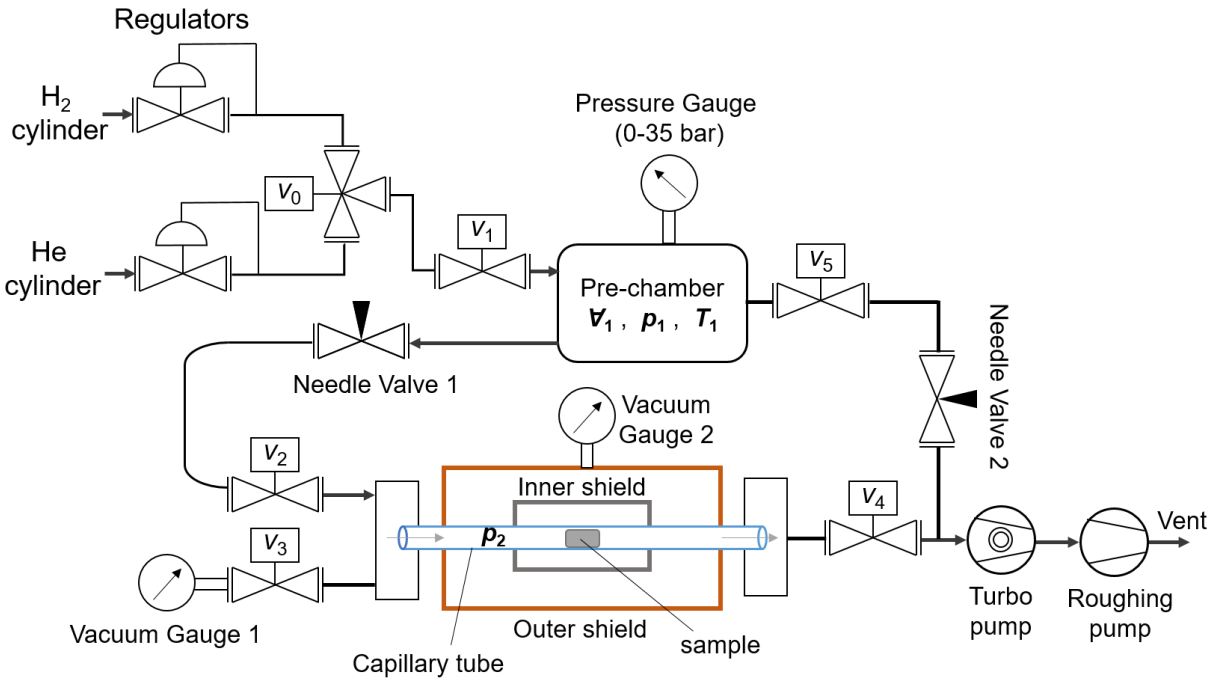


Figure 2.3. Gas handling unit and flow path of the calorimetric reactor. The valves V_0 to V_5 are miniature solenoid valves. During a hydrogen absorption experiment, the prechamber is loaded with the reactant gas to a desired pressure p_1; then this known amount of gas is introduced to the reaction tube while pressure recording provides a means for resolving the mass of absorbed gas on the sample.

Initially, the pre-chamber and capillary tube are pumped down to a low vacuum level (<10 mtorr) via a turbomolecular pump by opening valves 4 and 2 and keeping all other valves closed. The vacuum level can be measured using vacuum gauge 1 (MKS 925 Micro Pirani) when valve 3 is open. Prior to gas introduction, valve 3 is closed to isolate the large parasitic volume of this vacuum gauge from the rest of the calorimeter, and prevent damage to the gauge at high pressures. Then all other valves are closed for a short duration of few seconds to prevent unwanted gas

introduction to the vacuum system when valve 1 is opened. When valve 1 is opened, a known volume (3.80 ml) of reactant gas, at the pressure set by the gas cylinder regulator, is first introduced into the pre-chamber. Then the gas pressure in the pre-chamber is measured using a high accuracy pressure transducer (Omega PXM409-035BA10V) with a range of 35 bar and is adjusted to the required set point by bleeding off excess pressure using valve 5. After the pressure and temperature are stabilized in the pre-chamber, the gas is expanded into the capillary by opening valve 2, during which the pressure p_1 (of the pre-chamber) is continuously recorded at a 20 Hz sampling rate. The needle metering valve (Swagelok SS-SS1), shown as the needle valve 1 in Figure 2.3, is incorporated to adjust the rate of gas introduction to the chamber, and is kept at a constant position during a set of experiments.

By knowing the exact gas volume, pressure, temperature, and composition before and after expansion, it is possible to calculate the amount of gas absorption ($\Delta n_{\text{absorbed}}$ [μmol]) based on the mass balance of a closed system using Eq. 1.1, where $\forall_1$ is the volume of pre-chamber, and $\forall_2$ is the sum of volumes of capillary tube, connection tubes, and parasitic volume of valves. In other words, $\forall_1$, is the volume of gas prior to expansion, and $\forall_1 + \forall_2$ is the volume of gas after expansion. Similarly, $\bar{\rho}_1$ and $\bar{\rho}_2$, the volume-averaged molar densities of gas before and after expansion, were obtained from the measured temperature and pressure of the gas and by linearly interpolation the density data obtained from NIST thermophysical properties[60]. Calculation of $\bar{\rho}_2$ involves consideration of local densities due to difference of temperature at various locations in the reaction tube calculated as $\bar{\rho}_2 = \sum_i \rho_i V_i / \sum_i V_i$. We estimated the local gas temperature along the length of the capillary tube by linearly interpolating between the measured temperatures at the three sensors and calculated the gas absorption from:

$$\Delta n_{absorbed} = n_1 - n_2 = \forall_1 \bar{\rho}_1 - (\forall_1 + \forall_2)\bar{\rho}_2 \quad (1.1)$$

The pre-chamber volume ($\forall_1$) was determined separately to be 3.80 ml by measuring the amount of water required to fill the pre-chamber. For accurate quantification of $\forall_2$ we used a baseline measurement using an empty sample capsule, where $\forall_2$ is calculated by setting $\Delta n_{\text{absorbed}} = 0$ in Eq. 1.1, and was found to be 2.79 ± 0.03 ml. The pressure sensing resolution is estimated to be 40 Pa/√Hz (approximated from a pressure measurement of a pressurized closed chamber under equilibrium) leading to a mass balance resolution better than 0.1 µmol in the entire operating range of the instrument. Figure 2.4 shows the pressure measurements during H_2 absorption in a baseline experiment for quantification of $\Delta n_{\text{absorbed}}$. The three steps where the chamber is evacuated, gas is loaded into the pre-chamber, and reactant is introduced into capillary tube (labelled *Vacuum*, *Pre-chamber loading* and *Reactant introduction*, respectively) are shown in this figure. We also shown in the inset (red vertical line) the drop in the equilibrium H_2 pressure with respect to the baseline after introduction of H_2. This drop in pressure is due to absorption of H_2 on the sample and can be used to quantify $\Delta n_{\text{absorbed}}$.

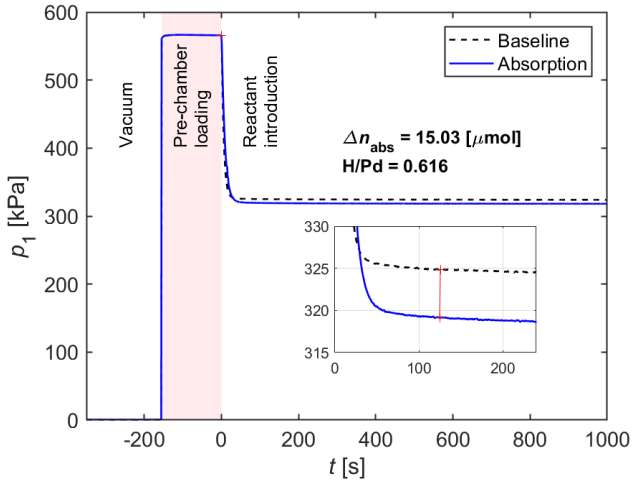


Figure 2.4 Measured pre-chamber pressure during gas introduction from the pre-chamber to the capillary for resolving the amount of absorbed gas, $\Delta n_{\text{absorbed}}$, and equilibrium H/Pd ratio. The dashed line shows a baseline experiment performed using an inert sample capsule with no material. The blue line shows a subsequent experiment with a Pd

nano-powder sample of mass 5.19 mg. The red line in the inset indicates the drop in the pressure trace due to absorption of gas on the solid sample.

2.3 Thermal model and characterization of the calorimeter

A lumped thermal capacity heat transfer model[61] was developed to understand and predict the thermal response of the calorimeter. The physical parameters of the model, including thermal resistances and capacitances, were identified via calibration runs.

2.3.1 Lumped thermal capacity model

In order to accurately interpret the results of experiments and convert the recorded values, such as temperature, pressure, and heating power to quantities of interest (heat output in reactions), a lumped thermal capacity model of the system was developed. The equivalent thermal circuit of the lumped thermal capacity model is shown in Figure 2.5, where the central part of the capillary tube that includes the sample capsule as well as the two central thermistors (shown in Figure 2.1c) is abstracted as a node with lumped heat capacity $C_{c\text{-}mid}$. Whereas R_{cl} and R_{cr} represent the thermal resistances from the aforementioned center node of the capillary to the left and right nodes and capture the effects of heat conduction through the borosilicate tube as well as the gas inside the tube. R_{os} is the thermal resistance through $T_{c\text{-}mid}$ thermistor and calibration heater lead wires to the outer shield. In addition, R_{isl} and R_{isr} are the thermal resistances between the $T_{c\text{-}mid}$ node and the left and right nodes of the inner shield, respectively. Since the space inside the outer and inner shields is kept at a high vacuum (<7 μTorr), R_{isl} and R_{isr} capture the effects of heat transfer via thermal radiation and become especially important at high temperatures. Finally, $\dot{q}_{mid}$ is the sum of all heat flows to the center node, which includes the heat of reaction, heat transfer via the reactant gas, and heating by the calibration thermistor. Note, the heating by the measurement thermistor is negligible and was ignored. The transient behavior of this model can be described by

a first order ordinary differential equation, where the heat release rate at the center node ($\dot{q}_{mid}$) can be calculated using Eq. 1.2. Here, the first term indicates the heat flow due to conduction from multiple parallel paths with thermal resistances R_i (as shown in Figure 2.5), and the second term indicates the transient heat flow due to variation in stored thermal energy in the central node.

$$\dot{q}_{\text{mid}} = \sum_i (T_{\text{c-mid}} - T_i)/R_i + C_{\text{c-mid}} \frac{dT_{\text{c-mid}}}{dt} \tag{1.2}$$

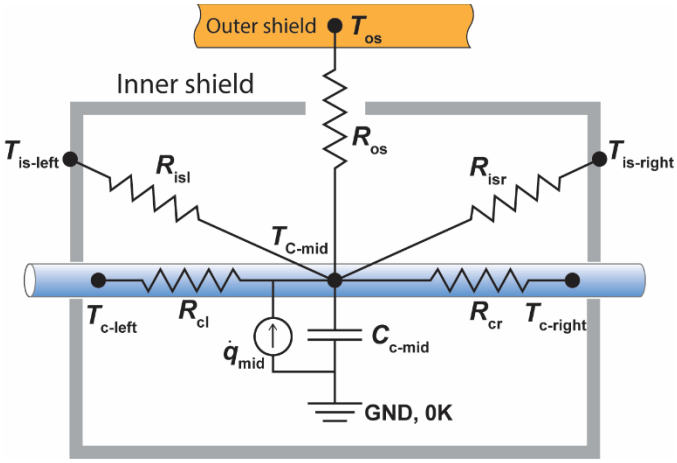


Figure 2.5 Lumped thermal capacity model. The center part of the capillary tube including the sample capsule and the sample, as well as the two thermistors mounted on this region are lumped as a single thermal capacity of $C_{\text{c-mid}}$. Five thermal resistances are included which connect the center node to capillary left/right, inner shield left/right and outer shield.

1.3.1.1 Identification of Thermal Parameters and Calibration Runs

The values of thermal resistances (R) and thermal capacitance (C) associated with the central node of the calorimeter are estimated by considering the material properties using simple heat conductance and capacitance relations shown in Eqs. 1.3 and 1.4:

$$R = \frac{1}{G} = \frac{L}{A_{cross}\, k} \tag{1.3}$$

$$C = \sum_i m_i\, c_i \tag{1.4}$$

Here, G is the thermal conductance and L, A_{cross}, and k are the length, cross sectional area, and the thermal conductivity of a heat conduction path, respectively, and m_i and c_i are the mass and specific heat capacity (per mass) of the i^{th} component of the lumped material in a thermal node. Temperature-dependent thermal conductivity data for borosilicate glass[62] and copper[63] were used to model the capillary's thermal conductance (G_{cl} and G_{cr}) and the thermal conductance of copper wires connecting the central thermistors to the outer shield, respectively. The thermal conductance of gas in the glass tube, was estimated using the pressure and temperature-dependent thermal conductivity of hydrogen[64]. The thermal conductance from the center node to inner shield (G_{isl} and G_{isr}) via radiation is estimated from:

$$G_{\mathrm{radiation}} = 4\varepsilon\sigma A_1 F_{1\to 2} T_{c-mid}^3, \tag{1.5}$$

where A_1, ε, and $T_{\mathrm{c\text{-}mid}}$ are the surface area, emissivity and temperature of the center node, respectively, and σ is the Stefan-Boltzmann constant. In these calculations a surface-averaged emissivity of 0.92 is assumed for borosilicate glass[65], and 0.1 for the solder[66] covering the glass surface along with a view factor ($F_{1\to 2}$) of unity, since the inner shield completely encloses the central part of capillary. The heat capacity of the central node was estimated from data for the heat capacity of borosilicate glass[67,68]. The calculated parameters are shown as a function of the inner shield temperature in Figure 2.6. To confirm the validity of these estimates, we ran a set of calibration experiments and compared the measured total thermal conductance and thermal time constant with those predicted by our thermal model (Figure 2.5). The details of the calibration runs are described in the next section. Finally, the aforementioned thermal parameters as well as the time series measurements of various temperatures T_{i} are used in Eq. 1.2 to calculate the heat release rate from the central node ($\dot{q}_{\mathrm{mid}}$).

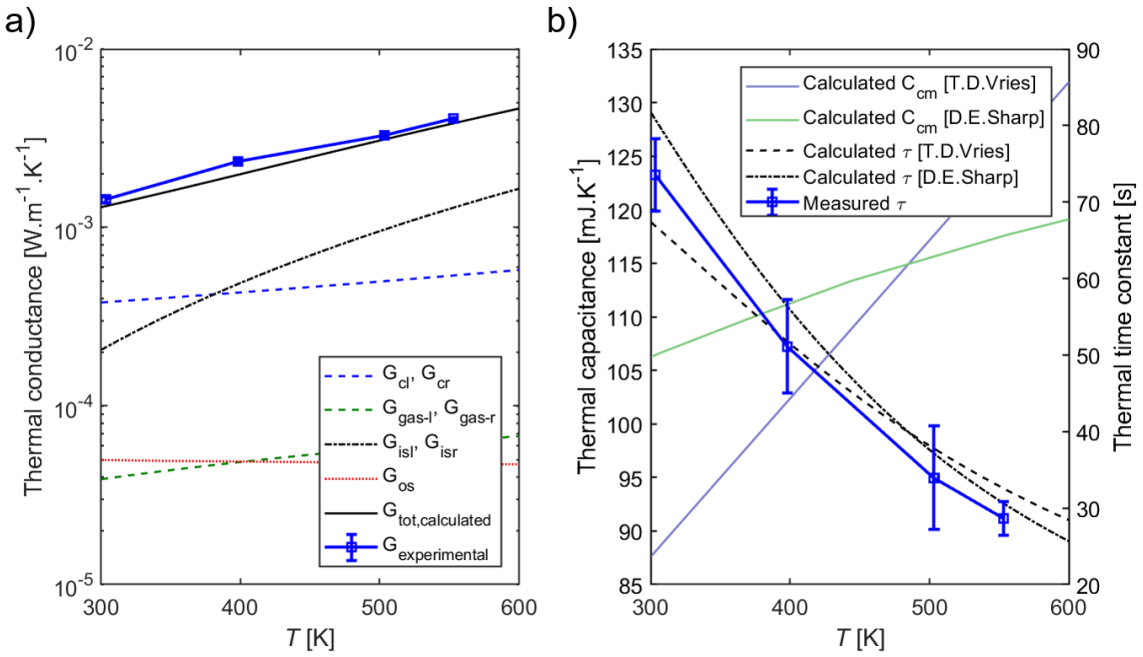


Figure 2.6 (a) Modeled thermal conductance values (G_{cl}, G_{cr}, G_{isl}, G_{isr}, and G_{os} are the conductance values corresponding to Figure 2.5, G_{gas-l} and G_{gas-r} are the gas conductance of left and right part of capillary, $G_{tot,calculated}$ is the sum of all the above conductances) and the measured total effective thermal conductance of the calorimeter ($G_{experimental}$), (b) Modeled thermal capacitance (C_{cm}) and the thermal time constant (τ) along with the measured thermal time constant of the calorimeter. The modeled capacitance is calculated using two different relations for heat capacity of borosilicate glass obtained from [67,68].

2.3.2 Temperature stability and calorimeter resolution

The outer shield temperature was feedback-controlled using a PID controller with a bandwidth of 1 Hz which was sufficient to maintain, depending on operating conditions, a target temperature of 23-36°C with <5 mK RMS temperature variation during the entire experiment. The inner shield temperature is controlled via two feedback loops for the left and right part of the inner shield running at 10 Hz (see details of controller tuning and temperature stability in Appendix Section 2.6.1. Temperature control of outer and inner shields). The measured temperature stability of the capillary located inside the inner shield is shown in Figure 2.7, where, during the first hour of the experiment, the capillary tube is under vacuum and has a temperature stability of better than 1 mK. At time t = 1 hr, the reactant gas (H_2) is introduced into the capillary tube leading to perturbation

of $T_{c\text{-left}}$ and $T_{c\text{-right}}$, which settle back to millikelvin stability within 15 minutes of reactant introduction.

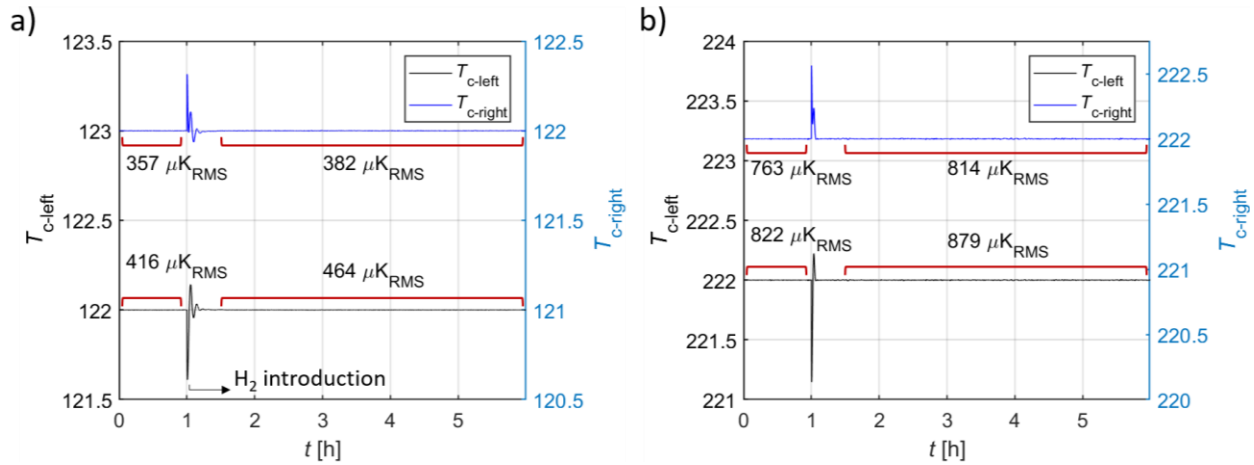


Figure 2.7 Stability of the inner shield temperature controller during introduction of reactants to the capillary tube at setpoint of (a) 122°C, and (b) 222°C. The reactant gas (H2 here) is introduced at t = 1 h, perturbing $T_{c\text{-left}}$ and $T_{c\text{-right}}$ temperatures. The temperatures settle back to millikelvin stability within 15 minutes after introduction. The RMS temperature variation in a 1 Hz bandwidth is shown for two time intervals before and after gas introduction (0-0.9 hours and 1.5-6 hours).

To characterize the calorimeter resolution, as well as the effective calorimeter conductance, the temperatures of the outer and inner shields are feedback-controlled at constant values and pulses of heat of increasing amplitude are deposited at the center node ($T_{c\text{-mid}}$) of the calorimeter using the calibration thermistor as a Joule heater. This test was repeated at different temperatures with the capillary tube being either under vacuum or filled with H_2 at different pressure levels. Figure 2.8 shows the results of calorimeter characterization experiments at $T_{c\text{-mid}}$ values of 30 °C and 230 °C. The transient response of the calorimeter to heat flow pulses (shown in Figure 2.8a and c) is used to extract the thermal time constant (i.e. the rise time to a temperature equal to $(1 - e^{-1}) \times \Delta T_{steady}$)[61]. In addition, the total conductance of the center node ($T_{c\text{-}mid}$) to the surrounding nodes is obtained by a linear fit to the temperature rise as a function of power input (see Figure 2.8b and d). For instance, in Figure 2.8b, total thermal conductances of 1.485 mW/K and 1.523 mW/K are obtained under vacuum conditions and when filled with H_2 under 7.0 bar of pressure,

respectively, at 30°C. The slight increase in thermal conductance in the latter case is due to the contribution arising from H_2. In addition, a heat flow resolution of 0.51 and 2.41 μW/√Hz is observed at 30 and 230 °C respectively. The decrease in calorimetric resolution at higher temperatures is due to (i) a decrease in inner shield temperature stability, and (ii) a decrease in thermistor resistance leading to a lower signal to noise ratio as discussed in more detail below.

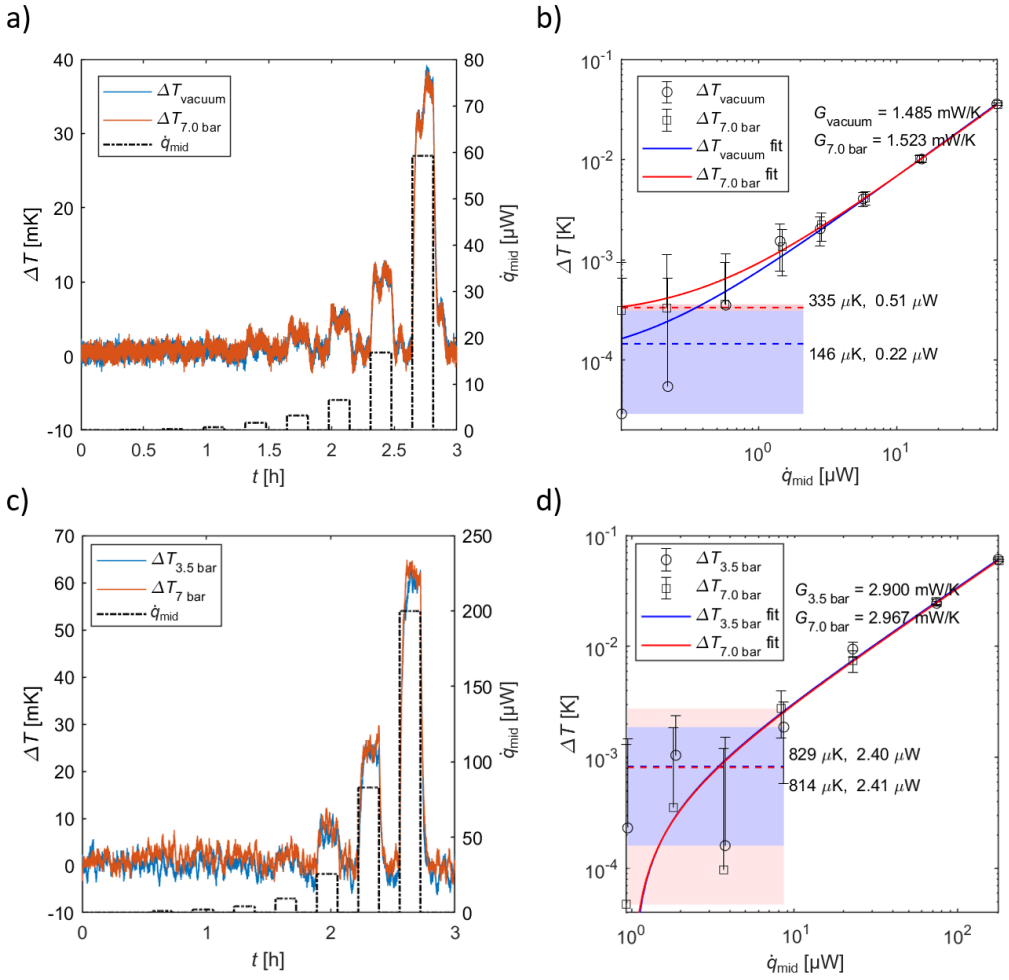


Figure 2.8 Characterization of calorimeter at two different temperatures ($T_{c\text{-}mid}$) values of: (a), (b) 30 °C, and (c), (d) 230 °C. Each experiment is repeated at two different H_2 pressures. Panels (a) and (c) show the transient response of the calorimeter to step inputs to heat flow ($\dot{q}_{mid}$) with ~1 Hz sampling frequency. Panels (b) and (d) figure shows the steady temperature rise as a function of heat flow input, where the effective thermal conductance and the heat flow resolution of the calorimeter are obtained.

2.4 Characterization of hydrogenation of Pd nanoparticles

In order to demonstrate the utility of our calorimeter, we probed hydrogenation of palladium (Pd) nanoparticles. In this reaction, hydrogen gas is absorbed on Pd particles, and it is expected[69] that depending on the concentration of H in Pd lattice either a low concentration α-phase, a high concentration β-phase, or a supercritical palladium hydride (PdH_x) is formed. The sample in our experiments was composed of commercially available Pd nanoparticles with a mean diameter of 15 nm (US Research Nanomaterials Inc., Pd 99.95 %, see Appendix Section 2.6.2. Characterization of Pd nanoparticles for sample characterization). Experiments at two pressure levels, 3 and 7 bar-absolute, and three temperature levels of 30, 125, and 230 °C, were conducted.

The experiments were performed on seven different samples of identical Pd nanoparticles. As some of the samples were tested multiple times, it is important to consider the issue of hysteresis in hydrogen absorption/desorption. To minimize the effect of hysteresis, prior to each absorption experiment, the sample was pretreated under vacuum (< 10 mTorr) and at high temperature (>150 °C) for a duration of at least two hours. Based on past work [69,70] on hydrogenation of Pd nanoparticles, at such low pressures and high temperatures it is expected that absorbed hydrogen is mostly desorbed and the absorption and desorption curves overlap. In addition, based on past work [44,71], the aforementioned preheating step is required for removing a substantial portion of absorbed O_2 and water from the samples. For full O_2 removal from the Pd nanoparticles the samples need to be reduced under hydrogen environment; however, we have avoided this reduction step during the sample pretreatment in order to be able to conduct a measurement on the enthalpy of reaction during the first exposure of the sample to H_2, as well as subsequent exposures to H_2

during the repeats of the measurement. The detailed experimental conditions for these measurements are summarized in Table 2.

Table 2.2: Experimental steps employed for the measurement of the hydrogenation enthalpy of Pd nanoparticles

	Experimental Step	**Duration**
1	Temperature ramp from 30 °C to 150 °C	65 min
2	Pretreatment under vacuum	120 min
3	Ramp to target temperature	-
4	Stabilize inner & outer shield temperatures	120 - 240 min
5	Pre-chamber gas introduction	30 s
6	Stabilize pre-chamber pressure	2 min
7	Gas introduction to capillary tube	~ 20 s
8	Measurement of thermal response	300 min
9	Calibration run: heat flow step input sequence to capillary center	160 min
10	Vacuum	60 min

2.4.1 Baseline measurement for reaction calorimetry

During the introduction of gas-phase reactants into the calorimeter, a number of effects need to be considered to prevent artifacts in the measurement of the heat of reaction. These effects include:

a) Cooling of reaction tube due to introduction of reactant gases at a lower temperature, as well as the Joule-Thomson effect due to expansion of the gas from the pre-chamber to the reactor capillary.

b) The aforementioned cooling of the reaction tube imposes an additional transient thermal load on the heaters, which can disturb the closed-loop temperature controller of the inner shield and temporarily perturb the temperature of different parts of the inner shield as shown in Figure 2.7.

c) Introduction of gas into the capillary tube results in a change of its conductance which in turn leads to variations of the thermal resistance network and changes the steady-state temperature of the capillary center ($T_{\text{c-mid}}$), despite all other inner/outer shield temperatures maintained at constant values.

In order to eliminate the effects of the aforementioned artifacts, a baseline experiment was performed prior to each reaction experiment with operating conditions identical to the actual reaction experiment, i.e., identical sequence and timing of valve operation, gas introduction, and temperature set points. The baseline experiment can in principle be done using one of the following two approaches:

1. Using an empty sample capsule or using a non-reacting and non-absorbing sample.
2. Using an inert gas with similar thermal properties as the main reactant.

Below, we describe the results obtained using the first approach.

2.4.2 Enthalpy of hydrogenation of Pd nanoparticles

To evaluate the performance of the calorimeter, we performed a series of experiments and characterized the hydrogenation of small samples of Pd nanoparticles (mass ranging from 3.77 to 5.28 mg). Some examples of the absorption measurements at a hydrogen pressure of 7 bar are shown in Figure 2.9 (results at 3 bar are shown in Appendix Figure 2.14). As stated above, for all experiments, we first conducted a baseline measurement using an empty sample holder. In all these figures a time span of 6 hours is shown, where initially the reaction capillary tube is under vacuum in the temperature stabilization step (step 4 in table 2). Then the chamber is pressurized (steps 5

and 6 in table 2) and the reactant (H_2) at specified pressure is introduced into the reaction tube at t = 1 h (step 7 in table 2). Although the heat output associated with the hydrogenation reaction returns to undetectably low levels 10 to 20 minutes after the start of the reaction, the experiments were continued for 5 hours in order to establish the long-term thermal stability of the calorimeter. Panels (a), (c), and (e) in Figure 2.9 show the temperature rise (ΔT) of the capillary center obtained by subtracting from the measured mid-point temperature ($T_{\text{c-mid}}$) the expected temperature of the midpoint ($T_{\text{c-mid, expected}}$) in the absence of heat generation in the capillary tube. The resistance network shown in Figure 2.5 can be employed to obtain the expression shown in Eq. 1.6 for evaluating $T_{\text{c-mid, expected}}$.

$\Delta T = T_{\text{c-mid}} - T_{\text{c-mid,expected}}$, where

$$T_{\text{c-mid,expected}} = R_{\text{tot}} \sum_i {T_i}/{R_i} \text{ , and } \quad R_{\text{tot}} = \left(\sum_i R_i^{-1} \right)^{-1} \tag{1.6}$$

It can be seen that ΔT is steady for the entire 1 h (offset to zero in the plot) prior to the addition of hydrogen. Following the addition of hydrogen, the reaction is rapidly initiated and a transient reaction lasting for ~0.3 hours is observed. Following this initial hydrogen absorption reaction, the calorimetric heat signatures settle to a new steady-state value. This offset relative to the pre-hydrogen incubation level (~25 mK at 30 °C, up to ~ 200 mK at 230 °C) is due to a change in thermal conductance of the capillary tube, which effectively changes the steady-state value of $T_{\text{c-mid}}$ at thermal equilibrium and is discussed in the previous section. This offset is well captured by the baseline experiment, eliminating a possible misinterpretation of “continuous” heat generation. Other transient artifacts which could occur in the first few minutes after reactant introduction, due to heat transfer to the reactant gas and temperature controller disturbance (as described in the previous section), are also eliminated by the baseline experiment.

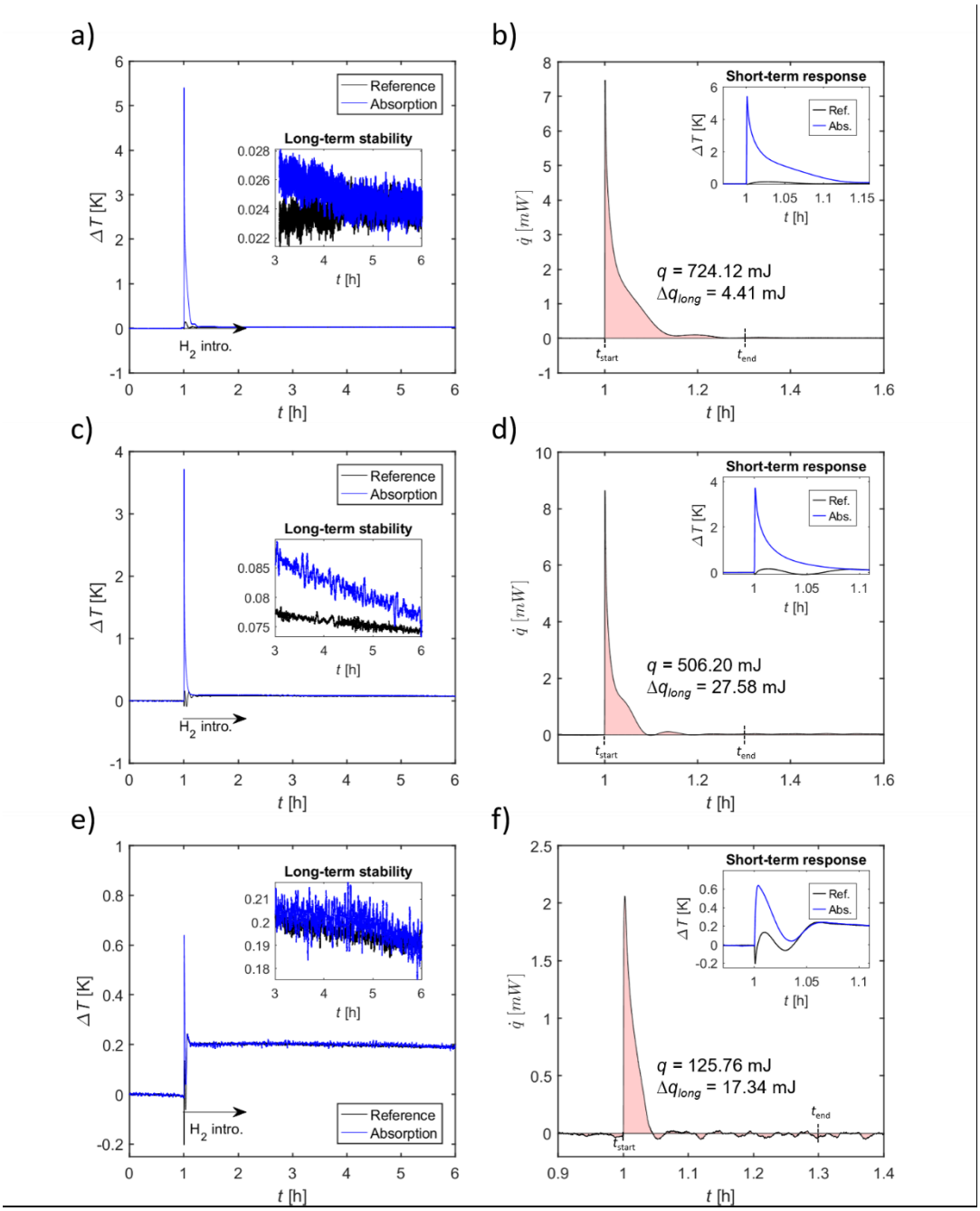


Figure 2.9 Experimental measurements of the temperature rise and heat release rate associated with absorption of H_2 on Pd samples. Data were obtained following the protocol described in Table 2 at an absolute pressure of 7 bar at various temperatures of 30 °C for (a) and (b), 125 °C for (c) and (d), 230 °C for (e) and (f). Panels (a), (c) and (e) show the recorded ΔT of the baseline experiment with an empty sample holder, as well as the absorption experiment using the Pd sample. The capillary reaction tube is initially under vacuum and, at time t = 1h, hydrogen is introduced to the reaction tube, resulting in an exothermic reaction and a transient heat output signal shown in panels (b), (d) and (f). The heat of reaction (q) was obtained by integrating the heat flow between t = 1 to 1.3 h. Δq_{long} is a measure of the long-term stability, which is the maximum cumulative heat release from t = 5 to 6 h. The insets in (a), (c), and (e) show the long-term response, and the insets in (b), (d), (f) show the short-term response. The mass of the Pd sample was 5.10 mg, 3.89 mg and 3.77 mg for the reaction a 30, 125 and 230 °C, respectively.

In order to obtain the heat generation rate at the capillary center due to chemical reactions, we subtract the net heat release rate (estimated using Eq. 1.2) of the baseline from the absorption experiment ($\dot{q}_{rxn} = \dot{q}_{absorption} - \dot{q}_{baseline}$), and is shown in panels (b), (d), and (f) of Figure 2.9. Inspection of the heat release plots reveals up to three features, depending on the reaction temperature. (i) All heat release plots show a sharp positive peak flowing the introduction of hydrogen (t = 1h) with a full width (duration) at half maximum of less than 1 min at all temperatures, which is limited by the calorimeter's response time. This sharp peak is attributable to the initial step of hydrogenation, which is the dissociative chemisorption of H_2 molecules on the surface of Pd and is highly exothermic. Because of the low activation energy[44] of hydrogeneation, the initial heat generation does not show a large temperature dependence, and occurs faster than the thermal response of the calorimeter at all reaction temperatures. ii) Following the initial saturation of chemisorbed hydrogen on the surface, the net heat release curves show a small shoulder (i.e. a significantly smaller secondary peak), which we attribute to two possible processes: Hydrogen uptake by a subsurface layer of Pd [72], and subsequent diffusion to bulk Pd for forming α-phase hydride [44]. Both these steps are moderately exothermic and based on previous reports have activation energies of (~ -29 and -25 kJ/mol-H_2) [72,73] due to which they exhibit temperature-dependent rates. The duration of this step is about 6 minutes at 30 °C, decreasing to 2 minutes at 230 °C. (iii) An additional broad feature after 1.15 to 1.2 hours is seen in the recordings at 30 and 125 °C, which requires further studies to elucidate its origin, but can possibly be related to further bulk diffusion of hydrogen or to the formation of β-phase of Pd-hydride, which is expected to occur on comparable timescales based on past work on α→β phase transformation kinetics [74].

It should be noted that, upon successfully incorporating the effect of the offset in ΔT via the baseline experiment, the heat release rate is seen to be close to zero ~0.3 hours after H_2

introduction in all experiments. Therefore, we use the integral of heat release rate from t_{start} = 1 h (start of reaction) to t_{end} =1.3 h to obtain the heat of reaction (q) listed on the panels (b), (d), and (f) of Figure 2.9. To obtain a bound on the long-term thermal stability of the instrument, we calculated the maximum deviation of cumulative heat release rate from zero in the period from t = 5 h to t = 6 h, which is listed as Δq_{long} in the plots. As can be seen, the long-term uncertainty values are small compared to heat of hydrogenation during a five hour long experiment, indicating that the instrument can readily resolve the heat of reaction over several hours.

The results from these experiments along with some repeats are listed in Table 2.3. The second column shows the sample label for the experiments. The samples are all taken from a single batch of Pd nanoparticles; therefore, on average their properties are expected to be identical. The third and fourth columns list the mean reaction temperature during measurement and equilibrium hydrogen pressure after its introduction into the capillary tube, respectively. The main results are the internal energy (ΔU) and enthalpy (ΔH) of hydrogenation calculated using Eqs. 7 and 8, and the equilibrium atomic ratio of hydrogen to palladium (H/Pd). In Eq. 1.8, the $V\Delta p$ term is the heat of compression, where $V = \forall_1 + \forall_2$ = 6.59 ml is the total volume of the gas after introduction to the capillary, and Δp is the pressure change as a result of reaction. The contribution of $V\Delta p$ is relatively small in our system, e.g. at 30 °C and 7 bar, $V\Delta p$ = 6.59 ml × (- 7.52 kPa) = - 49.58 mJ compared to the heat of reaction of q = 724.12 mJ. The measurements at 30 °C and 3 bar are repeated twice, with and without preheating a fresh sample at 150 °C. The experiment with a fresh sample without preheating shows a much larger enthalpy of hydrogenation, which we believe is due to oxidation of hydrogen by the residual oxygen on the sample. Based on past work [44,71], preheating a fresh sample under vacuum is necessary to desorb residual oxygen and water and obtain metallic Pd prior to hydrogen introduction.

Table 2.3: Summary of the measurements of the reaction calorimetry on hydrogenation of Pd nanoparticles. To estimate the error on enthalpy (ΔH), the maximum error of heat of reaction (q) is normalized by amount of absorbed reactant (mol-H_2)

Test	Sample label	T_{rxn}	p_{rxn}	m_{pd}	q	max q error	H/Pd	ΔH	Max ΔH error	comment
#	-	°C	bar	mg	mJ	mJ	-	kJ/mol-H_2	kJ/mol-H_2	
1	A	30.27	3.12	5.28	707.58	2.74	0.752	-36.07	0.15	1st absorption
2	A	30.23	3.12	5.28	535.49	6.47	0.725	-27.30	0.36	2nd absorption
3	B	30.29	3.11	5.45	2075.62	31.67	0.881	-89.51	1.40	no pre-heating
4	C	30.23	7.06	5.10	724.12	4.41	0.830	-33.93	0.22	1st absorption
5	D	124.94	3.27	4.77	779.79	24.92	0.683	-47.21	1.51	1st absorption
6	E	125.00	3.22	5.61	727.57	37.72	0.725	-44.75	2.32	1st absorption
7	F	125.43	3.57	3.89	610.14	22.63	0.681	-46.54	1.82	1st absorption
8	F	125.36	6.90	3.89	506.20	27.58	0.747	-34.59	2.02	2nd absorption
9	F	125.34	6.88	3.89	504.73	26.52	0.763	-33.69	1.90	3rd absorption
10	F	125.32	3.27	3.89	477.24	20.61	0.662	-36.96	1.70	4th absorption
11	G	230.10	6.85	3.77	125.76	17.34	0.229	-28.48	4.27	2nd absorption
12	G	230.09	6.86	3.77	130.59	12.59	0.231	-29.43	3.08	3rd absorption
13	G	230.11	7.09	3.77	95.19	22.39	0.179	-27.44	7.04	4th absorption
14	G	230.12	3.31	3.77	42.73	30.87	0.068	-33.11	25.73	5th absorption
15	G	230.17	3.27	3.77	54.95	7.05	0.100	-28.55	3.98	6th absorption

In order to check the accuracy of the instrument and analysis procedure, we have repeated the experiment at 125 °C and 3 bar three times on different Pd samples (test # 5-7 listed in Table 3). The results indicate closely clustered enthalpies of hydrogenation for the three repeats with a standard deviation of 2.75%. This relatively small variation observed may be attributed to sample to sample variation of the equilibrium H:Pd ratio [69] and variation in the equilibrium H_2 pressure.

$$\Delta U = q = \frac{1}{\Delta n_{absorbed}} \int_{t_{start}}^{t_{end}} \left(\dot{q}_{absorption} - \dot{q}_{baseline}\right) dt \tag{1.7}$$

$$\Delta H = \frac{1}{\Delta n_{absorbed}} \left(\int_{t_{start}}^{t_{end}} \left(\dot{q}_{absorption} - \dot{q}_{baseline}\right) dt + V \Delta p \right) \tag{1.8}$$

Figure 2.10a shows the internal energy of hydrogenation of Pd nanoparticles, per unit mass of Pd as a function of equilibrium H/Pd ratio. It can be seen that these data show a linear pattern, and are in good agreement with previous measurements on bulk Pd[75]. Figure 2.10b shows the enthalpy of hydrogenation per mole of adsorbed H_2, which spans a range from -28.45 to -36.96 kJ/mol-H_2. This value is also in agreement with previous studies that mostly rely upon indirect measurement of the enthalpy of hydrogenation using an isotherm method and Van't Hoff's relation, clustered within -28 to -40 kJ/mol-H_2 depending on Pd particle size and measurement technique [69,70,76,77]. The results are also in agreement with past calorimetric measurements, which report a wide range for the enthalpy of hydrogenation of Pd (-32 to ~ -60 kJ/mol-H_2) [43-45]. In Figure 2.10b, the enthalpy of hydrogenation shows no significant trend as a function of temperature; however, a decrease in the absolute value of enthalpy of hydrogenation with the reaction pressure is observed. This effect can be explained based on the variation of equilibrium H/Pd ratio as a function of reaction pressure, where some previous studies have reported that the enthalpy of hydrogenation is higher at lower H/Pd ratios as a result of highly exothermic dissociative chemisorption of H_2 molecules on the Pd surface[44,75].

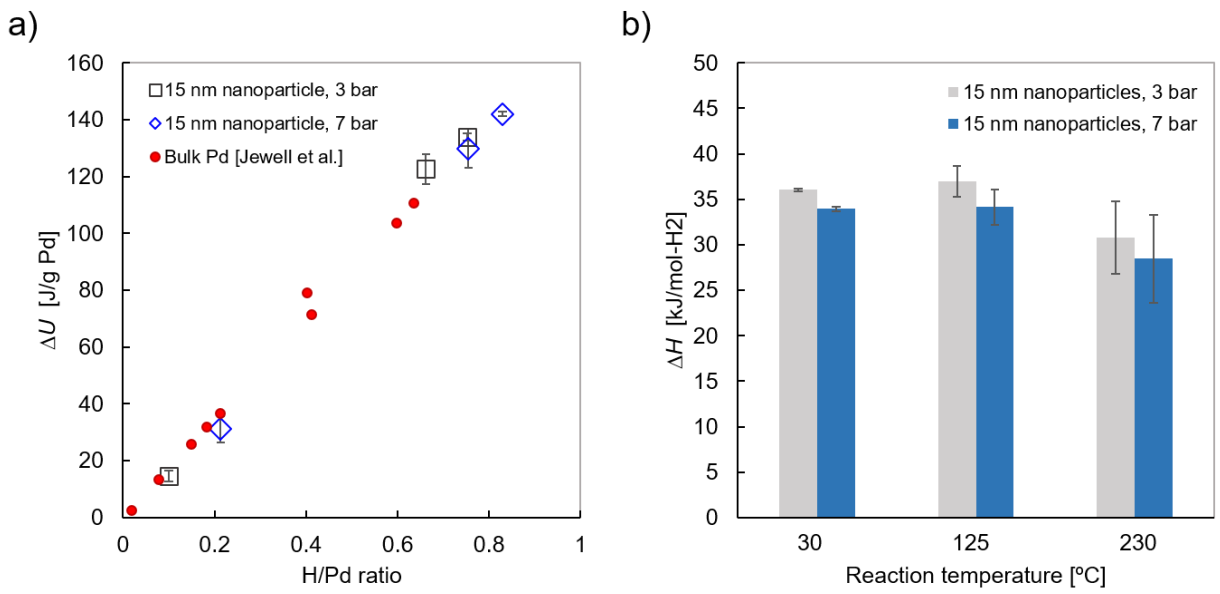


Figure 2.10 (a) Internal energy of reaction per unit mass of Pd samples. Red dots show previous measurements on bulk Pd adapted with permission from [75]. Copyright 2006 Elsevier. (b) Enthalpy per moles of absorbed H_2 at three reaction temperatures and two pressure levels. Error bars are estimated from the maximum long-term stability.

In terms of the equilibrium phase of the Pd hydride, it can be seen that all the measurements at 230 °C (503 K) demonstrate a low equilibrium hydrogen concentration of H/Pd <0.23 after the reaction. Based on previous calculations and measurements on Pd nanoparticles, this low concentration indicates either an α-phase or a supercritical palladium hydride phase [69,78]. On the other hand, measurements at 30 and 125 °C show a higher hydrogen concentration of H/Pd > 0.66 which indicates a β-phase of palladium hydride (see the phase diagram of PdH_x nanoparticles in Appendix Figure 2.15).

2.5. Conclusion

We present a calorimetric reactor for measuring the heat of chemical reactions between a gas phase reactant and milligram-scale solid phase samples. The instrument can also be used to quantify the amount of absorbed reactants on the sample using a pressure-concentration measurement technique with a resolution of 0.1 μmol/√Hz. The instrument is particularly useful for studying

nanomaterial samples, given that typical laboratory synthesis of nanomaterials yields milligram-scale samples. The operating range of this instrument is from room temperature to 300 °C, and 10 mbar to 30 bar. In order to accurately interpret the results of the calorimetry, a one-state lumped-thermal capacity heat transfer model was developed with pressure and temperature-dependent thermal conductance and temperature-dependent heat capacitance. The instrument parameters such as total thermal conductance and thermal capacitance are calibrated using an electrical heater installed at the sample location. The heat flow resolution was demonstrated to be better than 3 $\mu W/\sqrt{Hz}$ in the entire operating range, which was validated via a set of H_2 absorption experiments on Pd nanoparticles with a sample mass in the 3-5 mg range and performed at two pressure levels (3, 7 bar), and three temperatures (30, 125, and 230 °C). The results agree with previously reported values of the enthalpy of hydrogenation of Pd and the equilibrium H/Pd ratio. The advances presented here enable high-resolution calorimetry for measurement of thermodynamics and kinetics of chemical processes on nanomaterials, including catalytic reactions, phase transformations and thermochemical energy storage using metal hydrides.

2.6. Appendix

2.6.1. Temperature control of outer and inner shields

To achieve high calorimetric resolution the temperature of the thermal shields must be maintained at a steady value. To achieve this, the outer shield temperature was measured using a glass-encapsulated thermistor located 6 mm inside the bulk of the side wall of the outer shield as shown in Figure 2.11, and heated using two planar film heaters (Omega Polyimide Film insulated heaters, 1" by 5", power = 2.5 W/in^2). This temperature was feedback-controlled using a PID controller (1 Hz bandwidth) with gains tuned using the Ziegler-Nichols method[79]. This controller was sufficient to maintain the temperature at a target of 23-36 °C (depending on operating conditions) with better than 5 mK_{RMS} stability. As an example, the stability of T_{os} during an H_2 absorption experiment is shown in Figure 2.12 at a setpoint of 23.2 °C.

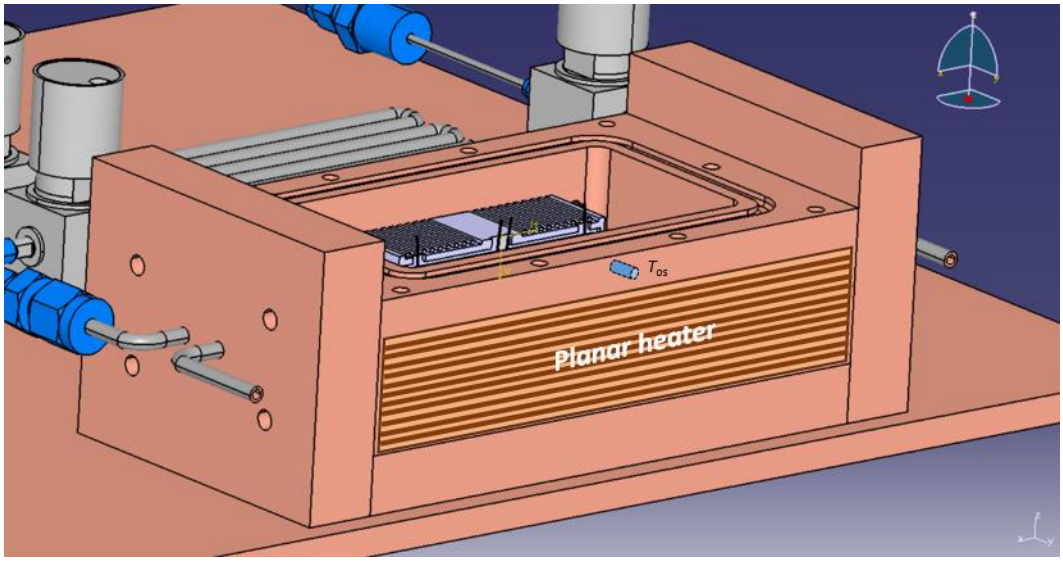


Figure 2.11 Location of the T_{os} thermistor and a planar film heater on the outer shield.

The control of the inner shield temperature is more challenging specifically at higher temperature setpoints due to increased thermal coupling of the inner and outer shield, which increases the disturbance on the inner shield. In addition, the thermal time constant of the inner shield is ~600 s which is significantly smaller than that of the outer shield. The combination of these effects required a relatively high controller bandwidth of 10 Hz to reduce the temperature error band to the desired sub-mK level[80]. In addition, the significant variation in thermal conductance and thermal time constant of the inner shield as a function of temperature makes the thermal system a non-linear plant, which was controlled using a gain-scheduled PID controller where the gains vary as a function of reaction temperature[81]. The stability of the capillary left and right ($T_{\text{c-left}}$ and $T_{\text{c-right}}$) temperatures during an H_2 absorption experiment are shown in Figure 2.12.

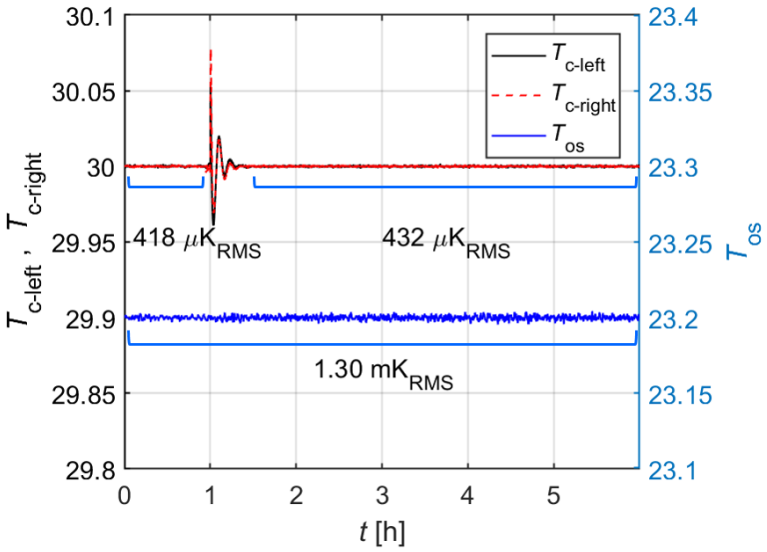


Figure 2.12 Stability of the capillary left ($T_{\text{c-left}}$), capillary right ($T_{\text{c-right}}$), and outer shield (T_{os}) temperatures during introduction of reactants to the capillary tube at setpoint of 30°C. The reactant gas (H_2 here) is introduced at t = 1 h, perturbing $T_{\text{c-left}}$ and $T_{\text{c-right}}$ temperatures. The temperatures settle back to millikelvin stability within 15 minutes after introduction. The outer shield temperature is not affected by the introduction of reactants and remains steady. The RMS temperature variation in a 1 Hz bandwidth is shown in the intervals indicated by blue brackets.

2.6.2. Characterization of Pd nanoparticles

The Pd nanoparticle samples used in this study are commercially available from US Research Nanomaterial Inc., with mean diameter of 15 nm. Figure 2.13a shows a scanning electron microscope (SEM) image of the sample as purchased, showing larger mean diameter of ~57 nm. After dispersion of the sample by five minutes of sonication in DI water, the image in Figure 2.13b is obtained which matches the specification mean diameter of ~15 nm. Figure 2.13c shows the energy-dispersive X-ray spectroscopy (EDX) spectrum of the sample, indicating the Pd and carbon (C) peaks. The elemental analysis shows 99.47 Wt% of Pd and 0.53 Wt% of C, the small carbon content may be due to sample contamination by carrying it in atmospheric condition.

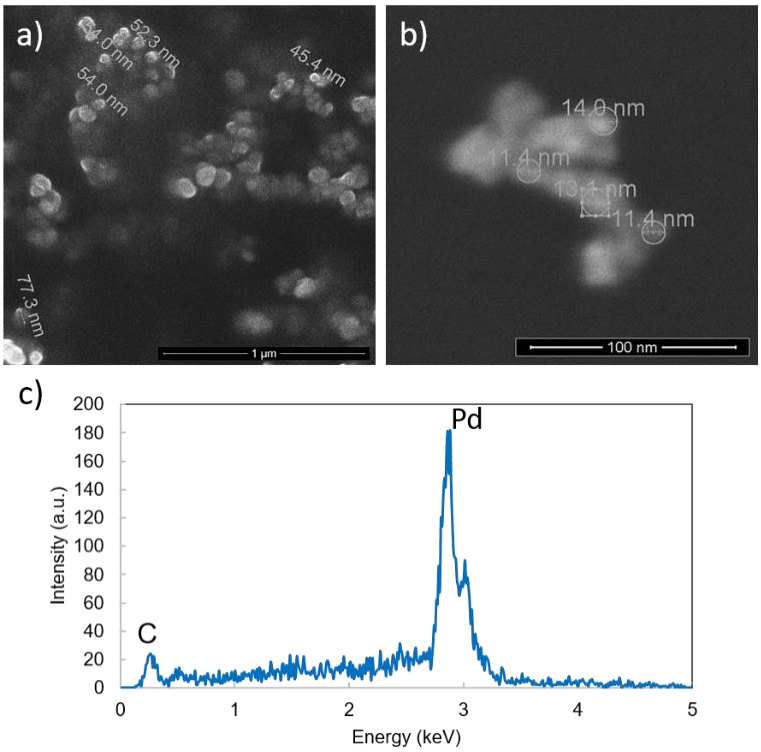


Figure 2.13. SEM micrographs of a) unprepared commercial Pd nanoparticle samples, b) dispersed sample by sonication in DI water, c) EDX spectrum of the sample showing peaks of Pd and carbon (C).

2.6.3. Enthalpy of hydrogenation of Pd nanoparticles

Figure 2.14 shows some examples of the measurement of heat of hydrogenation of Pd nanoparticles at a hydrogen pressure of 3 bar. The heat release curves are of similar shape to the experiments at 7 bar (shown in Figure 2.9). However, they produce a smaller heat output as a result of less hydrogen absorption. The temperature offset after reactant introduction is also slightly different compared to the case of 7 bar which is due to the pressure dependent conductance of the capillary tube, this effect is well captured and eliminated by measurement of baseline at the same reaction pressure of 3 bar. Therefore, at all reaction pressures tested here, the heat release goes to a value close to zero ~0.3 hours after reactant introduction.

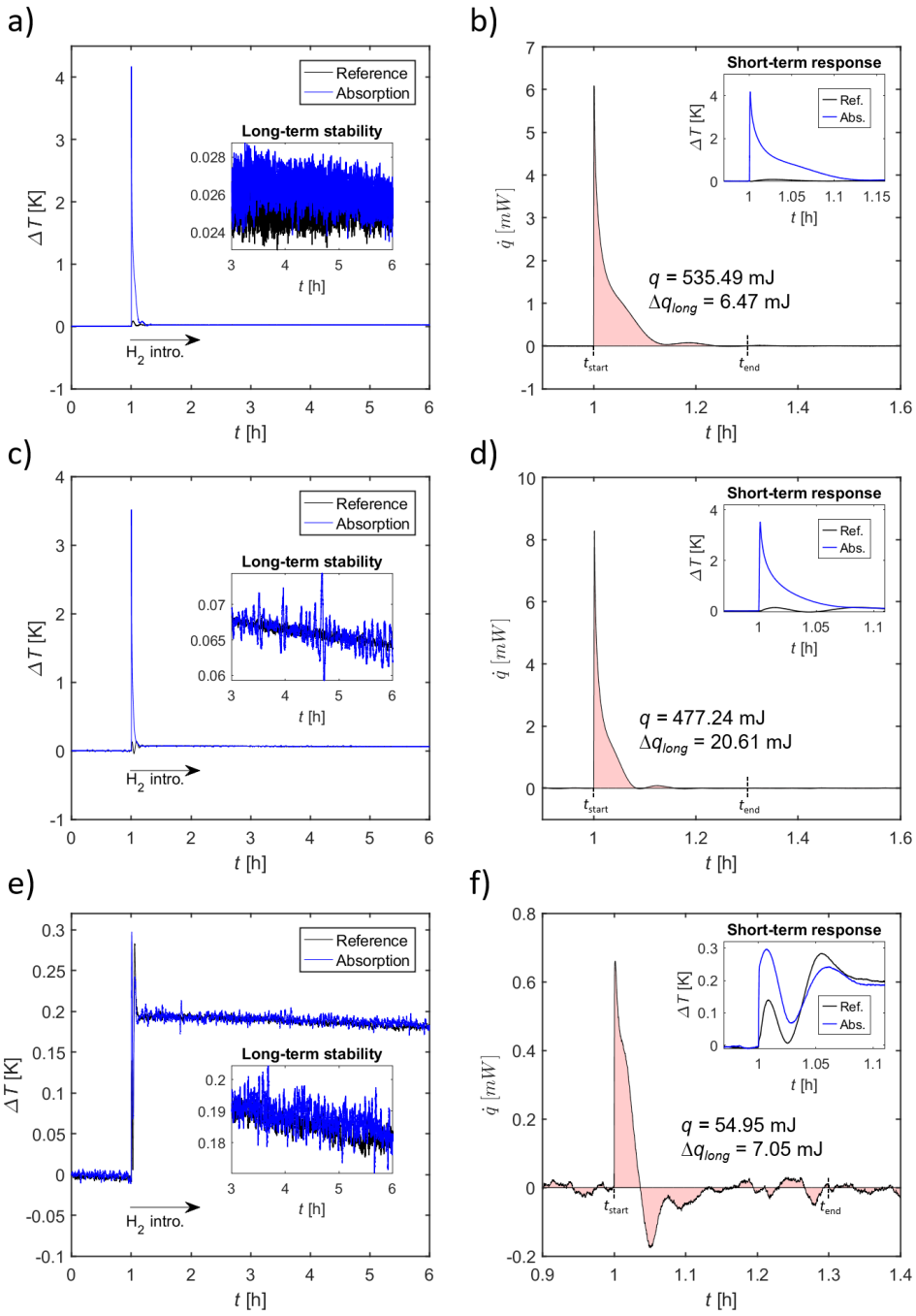


Figure 2.14 Experimental data of temperature rise and heat release rate associated with adsorption of H_2 on Pd samples obtained following the protocol described in Table 2.2 at an absolute pressure of 3 bar and at various temepratures (30 °C (a, b), 125 °C (c, d), and 230 °C (e, f). Panels (a), (c), and (e) show the ΔT recorded during the empty sample holder baseline experiment, as well as the absorption experiment using the Pd sample. The capillary reaction tube is under vacuum during the first hour of the experiment, at time t = 1 h hydrogen is introduced to the reaction tube resulting in an exothermic reaction and a transient heat output signal shown in panels (b), (d), and (f). The heat of reaction (q), shown by the shaded area in the right hand graphs, is obtained by integrating the heat flow between t = 1 to 1.3 h. The bounds on q show the long term stability from t = 5 to 6 h. The mass of the Pd sample was a, b) 5.28 mg, c, d) 3.89 mg, e, f) 3. 77 mg.

2.6.4. Equilibrium hydrogen concentration on Pd nanoparticles

To compare the results with the literature, the equilibrium H/Pd ratio is plotted on the phase diagram of H-Pd system for 32 nm Pd nanocubes in Figure 2.15. The solid lines indicate the results of a statistical mechanics Ising model (adapted from Griessen et al. [69]) and filled circles are experimental results using luminescent based sensing of H-content measured by Bardhan et al. [78]. However, since the photo-luminescent based approach does not provide an absolute value of H-content and only provides relative values, it is scaled by Griessen et al. [69] to fit their model. We have used the scaled values in this plot as well. It can be seen that all the measurements at 230 ºC (503 K) are either in the low concentration α- phase or in the supercritical phase. On the other hand, measurements at 30 and 125 ºC are in the β- phase.

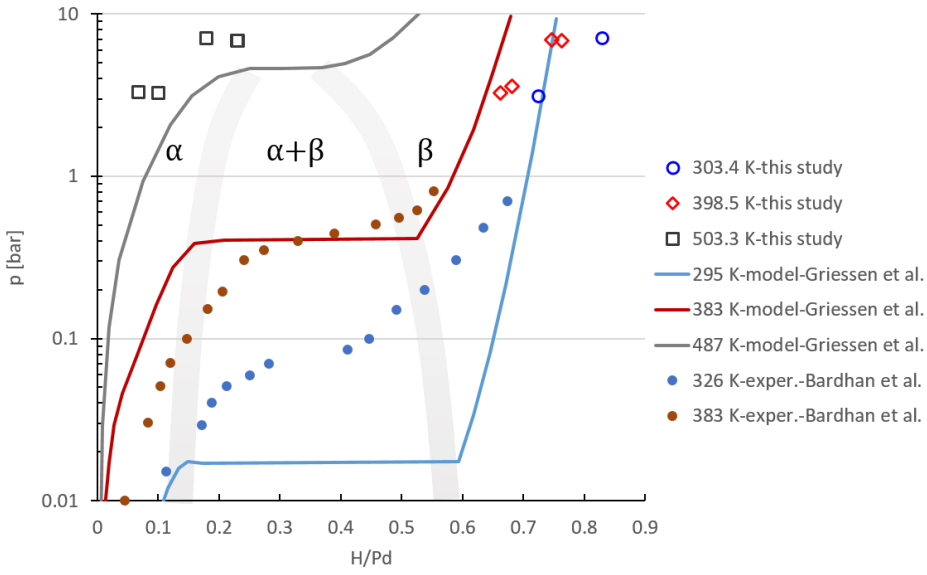


Figure 2.15. Equilibrium H/Pd ratio of 15 nm Pd nanoparticles obtained from current instrument plotted on the phase diagram of H-Pd system of 32 nm Pd nanocubes. Solid lines show the results of a statistical mechanics Ising model (adapted with permission from Griessen et al. [69]. Copyright 2013 Springer Nature) and filled circles are experimental results using luminescent based sensing of H-content (adapted with permission from Griessen et al. which are scaled results measured by Bardhan et a. [78]).

Chapter 3 Nanokelvin-Resolution Thermometry with a Photonic Microscale Sensor at Room Temperature

Reproduced with permission from *Nature Photonics*.

Amin Reihani, Edgar Meyhofer, Pramod Reddy

Ultra-high resolution thermometry—at room temperature and using microscale devices—is critical for future advances in bio-calorimetry[7,82], sensitive bolometry for sensing and imaging[12,83], as well as for probing dissipation in a range of electronic[34], optoelectronic[8] and quantum devices[9]. In spite of recent advances in nanokelvin resolution thermometry[15-18], achieving high-resolution measurements from microscale devices remains an outstanding challenge. Here, we present a novel, room-temperature, band-edge micro-thermometer that relies on the strong temperature dependent optical properties of GaAs at its absorption edge[84-86]. Specifically, by using a suspended asymmetric Fabry-Pèrot resonator and a narrow-linewidth probe laser we demonstrate a thermoreflectance coefficient >30 K^{-1} enabling a thermometry noise floor of ~60 nK/√Hz. This is two orders of magnitude better than that of the highest resolution micro-thermometers of similar size[23]. Further, this sensor is two orders of magnitude smaller than previous optical whispering gallery mode resonators of comparable temperature resolution[16]. The advances presented here are

expected to enable a broad range of studies and applications in calorimetry and bolometry where miniaturized high-resolution thermometers are required.

3.1. Introduction

High-resolution thermometry is critical for probing chemical reactions[6,87], dissipation in electronic and quantum systems[8,9,34], nanoscale energy transport[88,89], mm-wave/THz detection for sensing, imaging, and communication[12,83], and metabolism in biological systems[7,82]. Integrating high-resolution thermometers directly into microscale devices and operating them at room temperature is essential for studies and applications where the time-resolved measurement of localized temperature changes represents the physical basis of the instrument, as, for example, in single-cell bio-calorimeters[7,82], surface reaction measurements on nanomaterials[6], or bolometer arrays for THz imaging applications[12]. Towards this goal, researchers have developed various methods, including microfabricated platinum resistance thermometers (PRT)[24] that achieve 20-100 μK resolution in a footprint of ~30×30 μm^2. In addition, several optical thermometry techniques which have the advantage of remote readout have been developed, such as fluorescence thermometry using nitrogen vacancy centers in diamond for high spatial resolution (<30 nm[27]) thermometry, albeit with a more limited thermometry noise floor[90] of ~5 mK/√Hz. Further, whispering-gallery mode optical resonators[16] have been employed for achieving very low thermometry noise floor (~80 nK/√Hz) at room temperature. However, the dimensions of these resonators are in the range of 5 - 10 millimeters[16,18] and coupling light into them requires accurate positioning of a waveguide or prism in the vicinity of the resonator making their use in microscale applications challenging. Recent theoretical work[91] has also proposed very interesting nanokelvin-resolution thermometry via quantum interference effects; however, this proposed technique is yet to be experimentally realized.

In order to achieve nanokelvin-resolution thermometry with microscale devices, we leveraged the strong temperature dependence of the optical properties of direct bandgap semiconductors[84] for wavelengths corresponding to the band edge (Urbach edge). Briefly, we microfabricated a GaAs-based Fabry–Pérot resonator whose reflectance, at a chosen wavelength of 895 nm corresponding to the band edge of GaAs, is highly sensitive to temperature[85,86] due to the temperature dependence of its band gap (e.g. $\partial Eg/\partial T \sim -4.5\times10^{-4}$ eV/K for GaAs at room temperature[84]). Using this device, we demonstrate a highly temperature-sensitive reflection signal at Fabry–Pérot resonances as well as nanokelvin resolution thermometry.

3.2. Design of thermometer and readout optics

Schematics of the microfabricated thermometer are shown Figure 3.1a and b. The thermometer consists of a suspended circular region (diameter 560 μm) of undoped GaAs with a thickness (d) of 130 μm along with a 300 nm-thick gold back reflector that form an asymmetric Fabry-Pérot resonator (see methods for fabrication details). As shown in Figure 3.1b, the reflectivity of the resonator is measured using a laser beam (wavelength 895 nm) at an incident angle θ. Further, we integrated a resistive circular heater and a PRT in the suspended region, which enable both inputting known amounts of heat and separately measuring the device's temperature for benchmarking the performance of the band-edge thermometer to that of a PRT. The Pt heater and thermometers are electrically isolated from the GaAs structure by a 30 nm-thick layer of Al_2O_3. The microfabricated GaAs thermometer is attached to a copper block as shown in Figure 3.1c, which acts as a thermal reservoir and whose temperature (T_{res}) is measured independently using a thermistor and stabilized to ~100 μK.

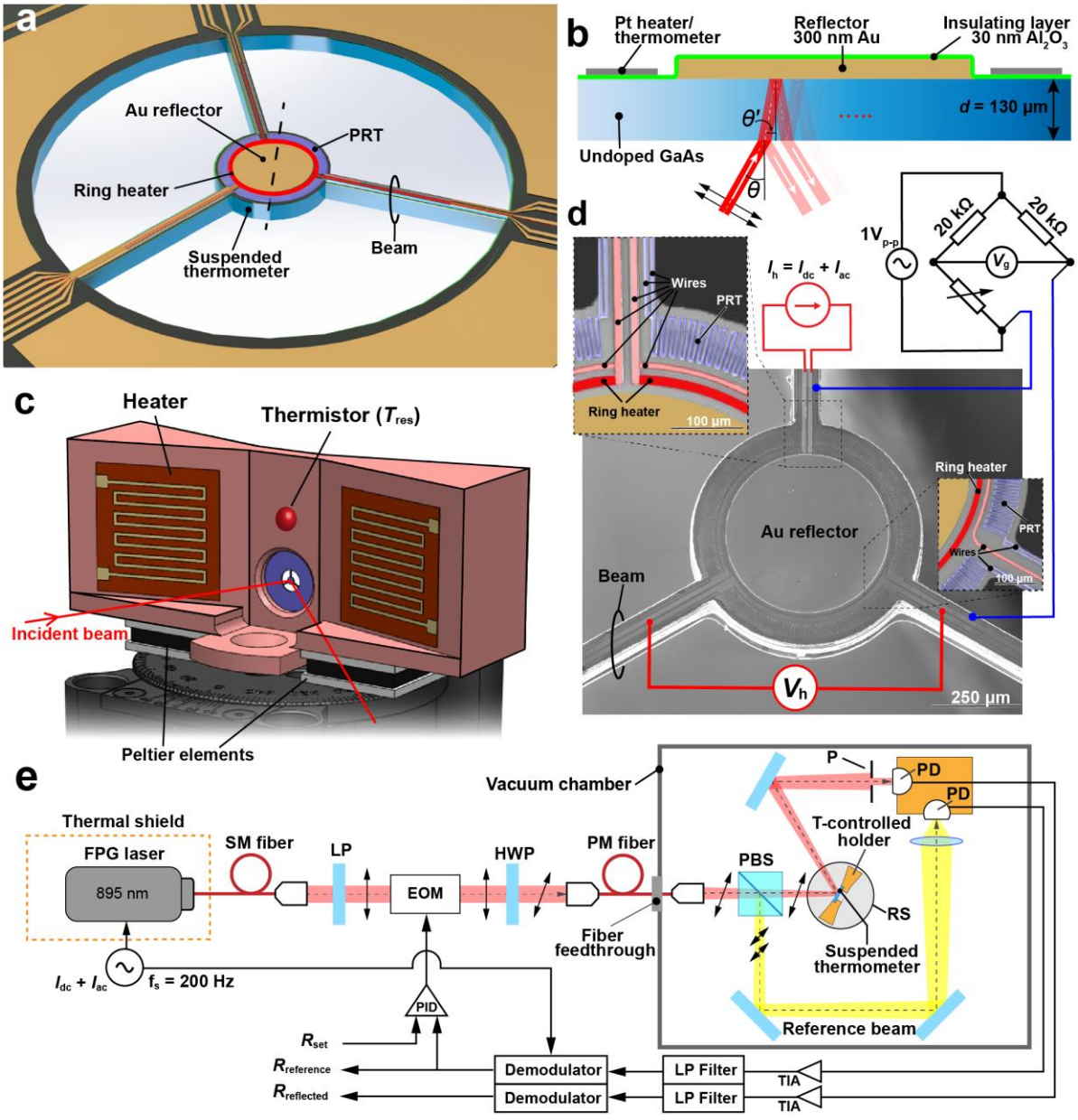


Figure 3.1 Device structure and experimental setup. (a) 3D schematic of the suspended GaAs device, not to scale (b) Cross sectional schematic of the suspended GaAs asymmetric Fabry–Pérot resonator showing the incident and reflected beams and the Au reflector, (c) Bow tie-shaped copper chip holder with the optical thermometer mounted at the center. The temperature of the chip holder is measured using a thermistor and feedback controlled using Peltier elements and resistive heaters, (d) SEM image of a tilted device, showing the suspended GaAs structure and patterned Pt heater/thermometers with the electronic measurement connections. Insets show false colored images of portions of the PRT and ring heater where connections are made in a four-wire configuration. (e) Measurement setup including the laser, optics, vacuum chamber, and electronics for feedback control. Here, FPG: fiber Bragg grating; LP: linear polarizer; EOM: electro-optic (intensity) modulator; HWP: half-wave plate; PM: polarization-maintaining; PBS: polarizing beamsplitter; RS: rotation stage; P: pinhole, PD: photodiode; TIA: transimpedance amplifier.

The optical measurement setup is schematically described in Figure 3.1e. A linearly polarized, 895 nm, wavelength-stabilized laser beam (see Methods for details of the laser) with a narrow line-width (<500 kHz) is split into two components using a polarizing beam splitter. One of the beams (reference beam) which is s-polarized, is incident on a thermally-stabilized photodiode (reference photodiode) to monitor its intensity and apply feedback to stabilize the incident beam's intensity using an electro-optic amplitude modulator (EOM). The second beam is collimated (p-polarized with a convergence angle of 3.4 mrad and a beam diameter of 125 μm) and is incident on the suspended GaAs device at an angle of 30° (see Appendix Section 3.7.2. Beam profile and optical alignment for alignment procedure and beam profile) to quantify the reflectance via a second photodiode that is nominally identical to the reference photodiode. We note that all sensitive components of our setup are enclosed in a low-vacuum (<5 mTorr) chamber (see Figure 3.1e) to improve thermal isolation of the device and eliminate noise arising from fluctuations in air density.

3.3. Temperature sensing and thermoreflectance coefficient

In our experiments, we employed a sinusoidally-modulated laser beam, at frequency f_s = 200 Hz with average power of 6.2 μW and amplitude of 4.8 μW (i.e. instantaneous power varied from 1.4 μW to 11.0 μW), that is incident on the suspended resonator to generate both a modulated (AC) and unmodulated (DC) reflected optical signal. The modulated part of the reflected signal (as well as the reference signal) enabled the use of a lock-in photodetection technique to accurately measure the reflected and reference beam intensities by reducing contributions from background thermal radiation and 1/f noise of the current amplifier. Further, f_s was chosen to be significantly higher than the thermal roll-off frequency (described below) of the

thermometer (1.69 Hz) to minimize temperature perturbations of the resonator caused by modulation of the deposited optical power. We first characterized the temperature dependence of DC reflectance (R_{DC}) and the AC reflectance (R_{AC}), which are defined as:

$$R_{DC} = \frac{\bar{\phi}_{reflected}}{\bar{\phi}_{incident}}, \quad R_{AC} = \frac{\Delta\phi_{reflected}(f=f_s)}{\Delta\phi_{incident}(f=f_s)} \quad , \tag{2.1}$$

where $\bar{\phi}_{incident}$ and $\bar{\phi}_{reflected}$ are the incident and reflected unmodulated intensities, respectively, whereas $\Delta\phi_{reflected}(f=f_s)$ and $\Delta\phi_{incident}(f=f_s)$ are the amplitudes of the reflected and incident modulated light at f_s, respectively. The dependence of R_{DC} and R_{AC} on temperature was quantified by increasing the temperature of the copper chip holder (T_{res}) from 20 – 42 °C using Peltier elements and heaters installed on the copper chip holder (see Figure 3.1c) and is shown in Figure 3.2a. The measured data show periodic resonant absorption peaks that arise from the temperature-dependence of the refractive index (n) of GaAs. Specifically, the temperature differential between the peaks is given by $\Delta T = \frac{\lambda}{2d\cos\theta'}\left(\frac{\partial n}{\partial T}\right)^{-1}$, where θ' is the ray angle inside the resonator medium and d is the resonator thickness (see Figure 3.1b). We note that no hysteresis was observed in the measured reflectance during successive temperature ramp-up/ramp-down experiments (see Appendix Section 3.7.3. Temperature ramp and hysteresis) meeting a key criteria for use of the device (or resonator) as a temperature sensor.

Next, we quantify the temperature sensitivity of reflectance (see Figure 3.2b) via the thermoreflectance coefficient, $k \equiv R^{-1}\,\partial R/\partial T$, which is defined analogous to the temperature coefficient of resistance (TCR) for resistive thermometers[24]. The thermoreflectance coefficient shows local minima and maxima around each of the absorption peaks and a global maximum, corresponding to the most pronounced resonance and the most sensitive point for performing thermometry. In order to more clearly quantify the temperature dependence of k around the optimal

point, we performed a finer temperature ramp that resulted in data shown in Figure 3.2c which reveal maximum absolute values of 13.3 and 31.3 for k_{DC} and k_{AC}, respectively. The value of k_{AC} is larger since the background photodiode signal arising from dark current and thermal radiation is significantly attenuated in the AC measurement. We note that these thermoreflectance coefficients are several orders of magnitude larger than the TCR values of typical thermometers, including sensitive glass encapsulated thermistors (TCR~0.05 K^{-1}) and platinum resistive thermometers (TCR~0.002 K^{-1})[6,24] as well as past thermoreflectance techniques[92,93]. As a first illustration of the use of our device as a thermometer we show in Figure 3.2d, a time domain measurement (in a 50 Hz bandwidth) where the temperature of the reservoir is set close to the maximum sensitivity point and is then changed in step sizes of 1 mK. As can be seen, R_{AC} clearly follows the reservoir's temperature signal. In this context, we note that the temperature range over which the band-edge thermometer has k_{AC} values > 0.9 $k_{ac,max}$ is ~30 mK. Importantly, as estimated from our modelling described below, the location of this maximum temperature-sensitivity can be matched to a desired temperature range by adjusting the laser wavelength and the resonance peaks can be displaced by ~7.5 K/nm. This number was estimated by using our model where the laser wavelength was systematically varied and the temperature corresponding to the most prominent resonance peak was determined.

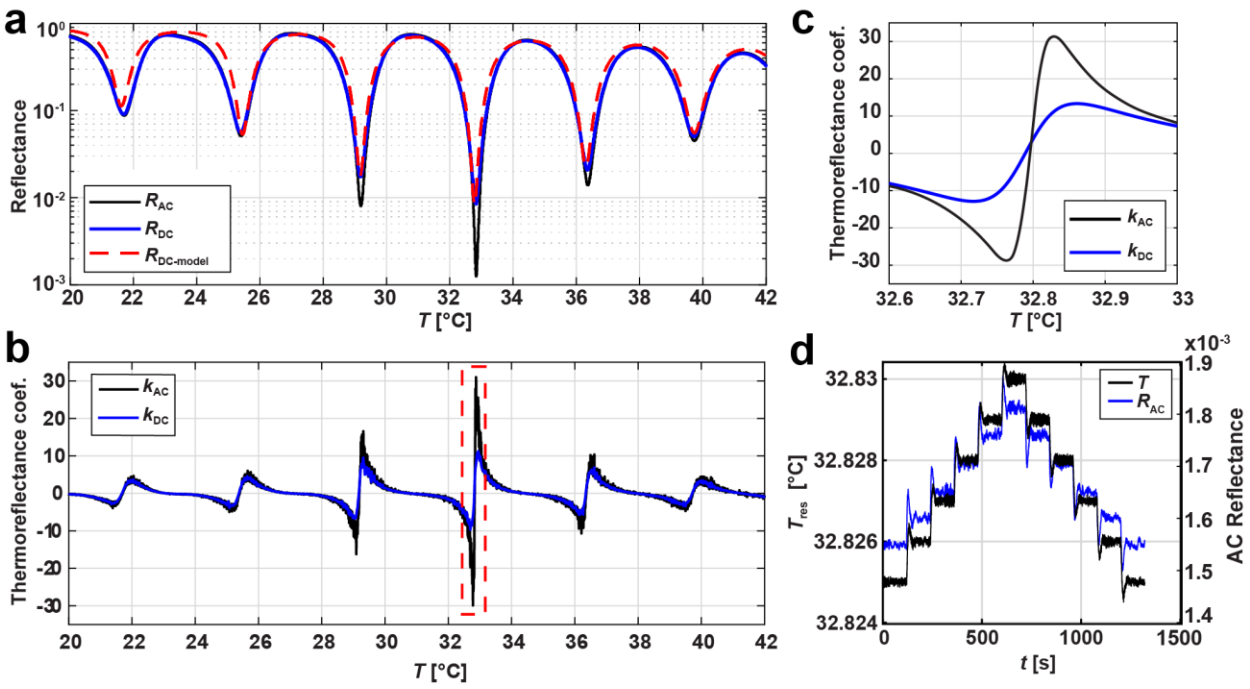


Figure 3.2 Thermoreflectance coefficient of band-edge thermometer (a) Temperature-dependent reflectivity (AC and DC as defined by Eq. 2.1) of the suspended resonator at the band edge (895 nm) for an incident angle of 30°, measured by systematically ramping the temperature from 20 to 42 °C. In addition, the DC reflectance obtained from scattering matrix model is also shown as red dashed curve. (b) Thermoreflectance coefficient (k) for DC and AC reflectivities showing highly temperature-sensitive peaks. (c) Thermoreflectance coefficient around the maximum sensitivity point obtained from a finer temperature ramp. (d) Variation of the AC reflectivity around the maximum sensitivity point of $k_{AC} \sim 30$ when the device temperature (T_{res}) is varied in steps of 1 mK.

3.4. Characterization of thermometry resolution

In order to demonstrate the temperature resolution of the band-edge thermometer we first characterized the thermal time constant (τ) and frequency response of the suspended region. We accomplish this by inputting a square-wave heat input (magnitude 15.4 μW) and measuring the temperature response by using the band-edge thermometer and the integrated PRT (Figure 3.3a). The measured data show a temperature rise of 3.37 mK and a time constant of ~0.10 s. From this measurement we obtained the thermal conductance G_{th} = 15.5 μW/3.37 mK = 4.57 mW/K. Next, the frequency response of the suspended region to sinusoidal heat inputs of amplitude 125 μW was obtained (Figure 3.3b). From these data the roll-off frequency (f_c) is seen to be ~1.69 Hz,

corresponding to a thermal time constant of $\tau = 1/2\pi f_c = 0.094$ s which is in good agreement with the time domain measurement.

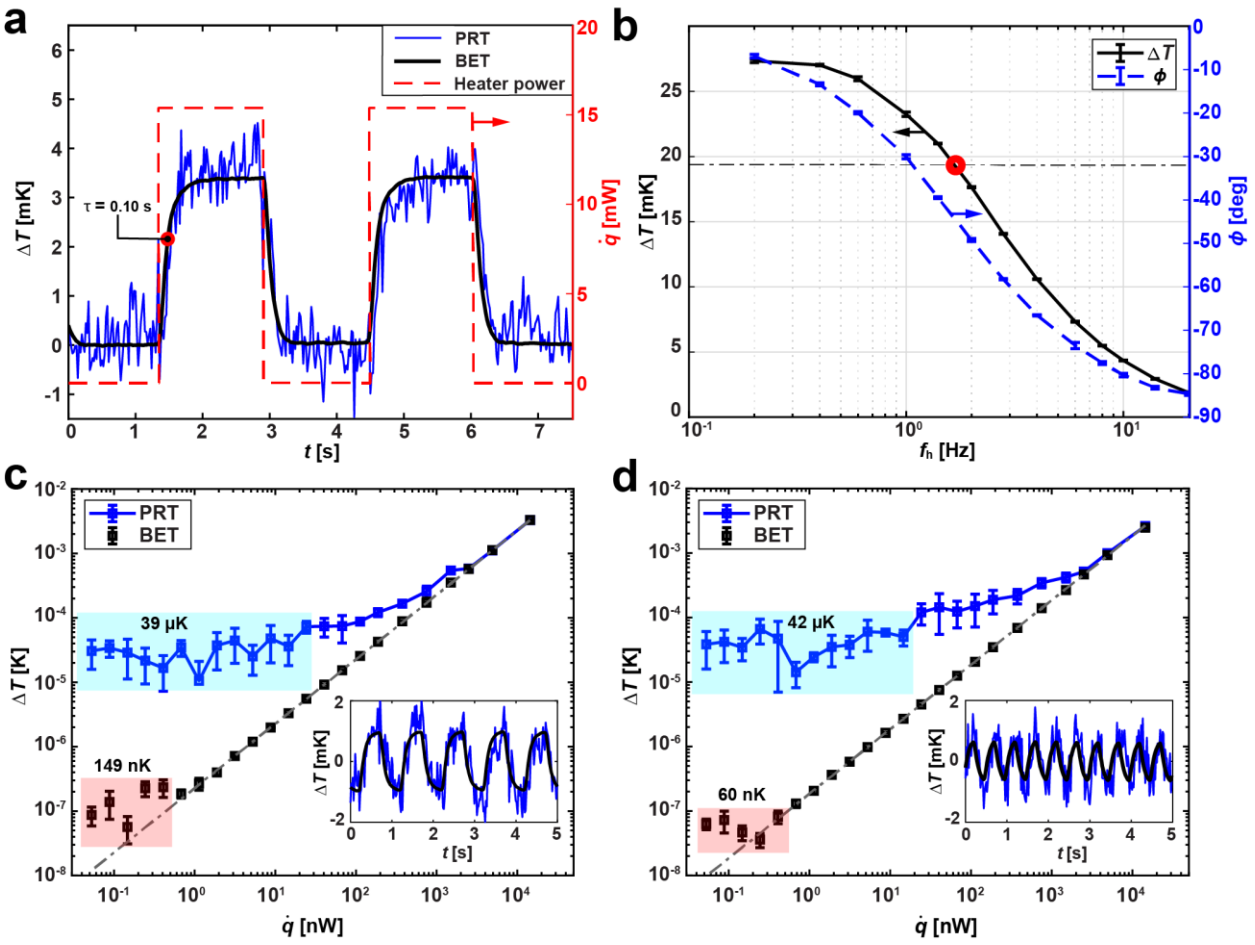


Figure 3.3 Characterization of thermometry resolution. (a) Time series of the measured device temperature using platinum resistance thermometry (blue line) and band-edge thermometry (black line), in a 50 Hz measurement bandwidth for a square wave input of heating power (red dashed line) with a periodicity of 0.32 Hz. From the measured data, a thermal response time of 0.10 s is estimated. (b) Bode plot of the temperature rise shows a thermal roll-off frequency f_c = 1.69 Hz. (c and d) Characterization of band-edge and platinum resistance thermometry resolution by modulated heat inputs at (c) f_{mod} = 1 Hz, (d) f_{mod} = 2 Hz. The measurement bandwidth is 0.1 Hz. The error bars show standard deviation of averaging. The dashed lines show the expected temperature rise based on the thermal conductance of the suspended thermometer. Insets show the corresponding time series measurements from two thermometers in a 50 Hz measurement bandwidth.

Next, we quantified the temperature sensing resolution of our band-edge thermometer by inputting known amounts of heat to the suspended region via the Pt ring heater while measuring the corresponding temperature signal (ΔT_{sens}) using the band-edge thermometer and the PRT. To

maximize the sensitivity of the band-edge thermometer we first set the sensor temperature (T_{sens}) close to 32.83 °C (see Appendix Section 2.7.5.1. Controllers for attenuating temperature drifts for modulated temperature sensing) and subsequently applied modulated square wave heat pulses at a frequency f_{mod} (1 Hz or 2 Hz) to the suspended region via the integrated Pt heater (see Appendix Section 3.7.5. Sensing of modulated temperatures). The resulting temperature fluctuations were first recorded in time domain (bandwidth of 50 Hz) by measuring the time dependent AC reflectance (defined in Eq. 2.1) of the device and the electrical resistance of the PRT using lock-in amplifiers and converting the measured data to temperature changes (see insets of Figure 3.3c, d). It is clear from these data that the resolution of the band-edge thermometer is much higher than that of the PRT. Subsequently we extracted the component of temperature variations corresponding to the heating frequency f_{mod} in a bandwidth of 0.1 Hz for both sensors (see Appendix Section 3.7.5. Sensing of modulated temperatures for details). The measured temperature peak amplitudes from the band-edge thermometer and the PRT as a function of the modulated peak input power are shown in Figure 3.3c and d for f_{mod} = 1 Hz and 2 Hz, respectively. It can be seen that the band-edge thermometer can resolve much smaller temperature changes than the PRT. Specifically, the resolution of the PRT, obtained by averaging the data points in the blue shaded regions in Figure 3.3c and d is 39 and 42 μK, respectively, for the 1 Hz and 2 Hz temperature modulation. This noise floor is consistent with reported values from past studies using PRT with a 10 kOhm resistance[24]. In strong contrast to the PRT, the band-edge thermometer is capable of detecting significantly smaller temperature changes and demonstrates a much lower temperature noise floor of 149 and 60 nK for 1 Hz and 2 Hz temperature modulation, respectively. We attribute the improvement in sensed temperature noise floor at 2 Hz temperature modulation (compared to 1 Hz) to reduced background thermal fluctuations at this frequency.

In order to quantitatively model the performance of our band-edge thermometer we employed a numerically stable scattering matrix approach[94] that enables us to exactly calculate the reflectance of devices employed in our experiments. In performing these calculations the dielectric properties of Au reflector were obtained from ref. [95]. Due to the large variability in the previously reported values of dielectric constant of GaAs near the band edge (depending on material quality and measurement method), we took the following approach for our modeling. First, the temperature dependence of the GaAs bandgap was obtained from:

$$E_g(T) = E_B - a_B \left[1 + \frac{2}{e^{\Theta/T}-1}\right], \tag{2.2}$$

where E_B = 1.571 eV, a_B = 0.057 eV, and Θ = 240 K (Ref. [96]). Subsequently, we calculated the temperature-dependence of the refractive index (n) and absorption coefficient (α) of GaAs at a wavelength of 895 nm by using a least squares fit to the experimental reflectance data in Figure 3.2a. The obtained values of n and α from this approach are in reasonable agreement with previously measured values[85,97] (see Appendix Section 3.7.7. Optical modeling of the thermometer for details), and the results of our scattering matrix calculations (shown as the dashed red curve in Figure 3.2a) are in very good agreement with the experimental data, indicating that the model can accurately explain the experimental observations.

3.5. Analysis of noise Sources and thermometry noise floor

To determine the noise limit of our band-edge thermometer, we characterized the temperature fluctuations of this sensor with and without thermal stabilization of the Fabry-Pèrot resonator. As outlined above, we first increased the reservoir temperature to 32.85 °C which is necessary to ensure high sensitivity of our band-edge sensor. Because of the limited resolution of

the reservoir's thermistor, fluctuations of T_{res} can only be maintained to within ~100 μK. Without any temperature-stabilization of the suspended sensor, T_{sens} was monitored using the DC reflectance and its spectral noise density is plotted as the blue curve (labeled T_{sens} not stabilized) in Figure 3.4a. As can be seen, temperature fluctuations increase substantially at frequencies below 2 Hz and reach values around 10 μK/√Hz at 0.01 Hz. This is principally due to low-frequency temperature fluctuations of the reservoir. In contrast, at higher frequencies, reservoir temperature fluctuations are small due to the large thermal inertia of the reservoir. Next, to experimentally characterize the intrinsic spectral noise floor of our band-edge sensor we followed a commonly used approach (see for example ref.[16]) and employed feedback, using the DC reflectance signal, to attenuate the ambient temperature fluctuations in the sensor (see Appendix Section 2.7.6.1. Temperature stabilization for determination of thermometry noise floor). The resulting spectral noise (black curve in Figure 3.4a, labeled $T_{sens,}$ stabilized) was obtained by averaging 20 spectra and represent the smoothed spectral estimate of the noise floor for our band-edge sensor. As expected, feedback dramatically reduces the influence of (external) disturbances, particularly at frequencies below 1 Hz, except around 1.5 Hz, which is likely due to the waterbed effect in the feedback loop[98]. Therefore, these measurements reveal that the thermometry noise floor averaged in the range of 1-25 Hz is 58 nK/√Hz. Further, the noise floor drops to significantly lower values (< 30 nK/√Hz) at the lowest measured frequencies where feedback stabilization is particularly effective. As a point of comparison, in Figure 3.4a we also show the fundamental thermodynamic fluctuation due to shuttling of phonons from the thermal reservoir to the suspended region (see Appendix Section 3.7.6. Estimating the theoretical noise floor of band-edge thermometer), which has a low-frequency limit of ~34 nK/√Hz. Interestingly, by applying temperature-feedback these

thermodynamic fluctuations can be sensed and attenuated in the low frequency region (Figure 3.4a).

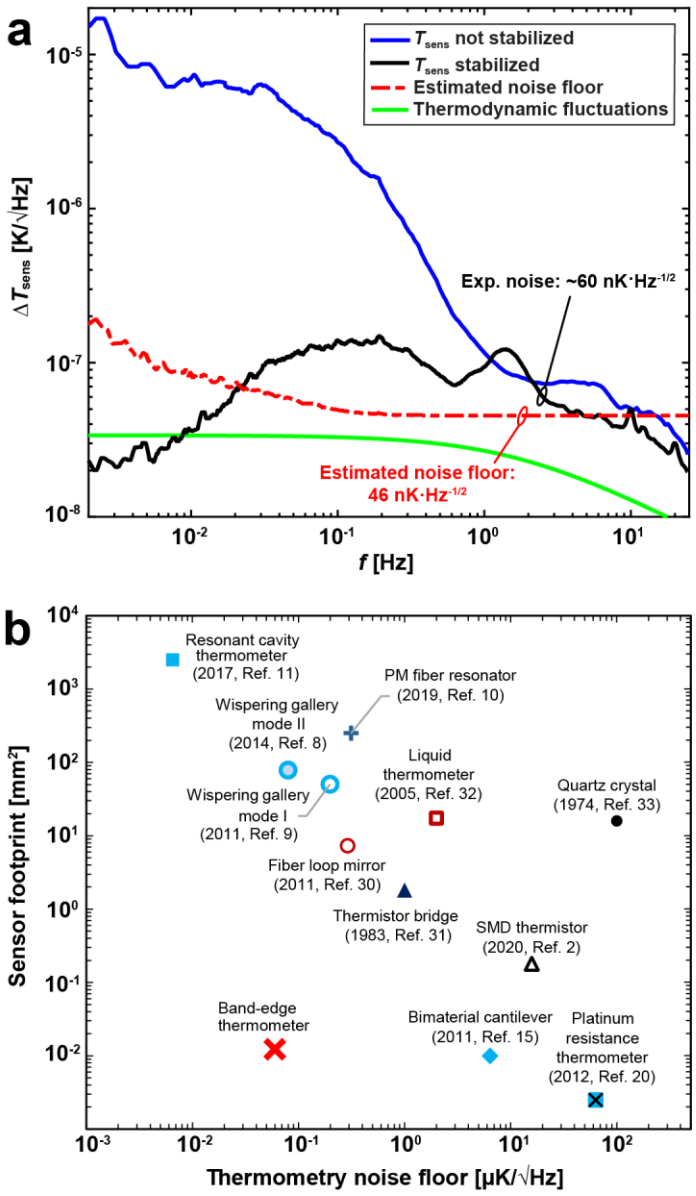


Figure 3.4 Estimated and experimentally measured noise floor of the band-edge thermometer. (a) Amplitude spectrum of temperature variations of the suspended region (T_{sens}) with (black line) and without (blue) feedback stabilization along with the estimated noise floor, which is the sum of shot noise, Johnson noise, photothermal absorption and optical nonlinearity effects. Further, the estimated noise from thermodynamic fluctuations is also shown (green line). In both cases, the reservoir temperature (T_{res}) is separately stabilized. Data shown in blue, balck and red lines represents an average of 20 spectra. (b) A comparison with other high-resolution, room-temperature thermometers highlights how band-edge thermometry offers significant potential for combining high low thermometry noise floor and small sensor footprint. To estimate the sensor footprint area, the portion of the sensor which needs to thermalize with the environment to sense its temperature (i.e. the active region) was used (see Appendix Section 3.7.8. Estimation of sensor footprint area for details).

In order to understand the ultimate limit to the noise floor of our band-edge thermometer, we estimate the noise floor by summing the contribution from the major noise sources: photocurrent shot noise, Johnson noise of the transimpedance amplifier and probe beam intensity noise (see Appendix Sections 3.7.4. Quantification of the effect of optical nonlinearities and temperature changes on the sensed temperature in band-edge thermometry and 3.7.6. Estimating the theoretical noise floor of band-edge thermometer). The estimated noise floor is plotted (red line, Figure 3.4a) and translates into a thermometry noise floor of 46 nK/√Hz at $f > 0.2$ Hz. Further, as shown in Appendix Figure 3.10, at frequencies <0.02 Hz the thermometry noise floor is limited photothermal absorption, while at higher frequencies it is limited by shot noise. These observations suggest that the performance of our thermometer can be improved at all frequencies by using laser sources with improved amplitude stability and higher intensities.

Finally, to compare the performance of the band-edge thermometer with other high-resolution room-temperature thermometers, we compared the sensor footprint area vs thermometry noise floor for relevant technologies[7,15,16,18-24] (Figure 3.4b). To estimate the sensor footprint area, the portion of the sensor which needs to thermalize with the environment to sense its temperature (i.e. the active region) was used (see Appendix Section 3.7.8. Estimation of sensor footprint area details). For the band-edge thermometer the beam diameter of the probe laser, which corresponds to the area of the device that needs to thermalize with the environment sets appropriate length scale for the lateral dimensions of the sensor. It can be seen that, compared to a sensor of comparable thermometry noise floor (e.g. dichroic dual-mode whispering-gallery mode resonator[16] with a noise floor of 80 nK/√Hz), our sensor is significantly smaller, as the diameter of the reported whispering gallery mode resonator is 10 mm. Further, compared to another optical sensor of comparable footprint (bimaterial cantilever thermometer[23]) our thermometer offers significantly lower thermometry

noise floor. Therefore, our band-edge thermometer is well suited for development of future devices and experimental platforms where a small sensor footprint combined with sub-microkelvin resolution is required. Examples of such devices include bolometer arrays for imaging in the THz range, thermal imaging, sensors for single cell bio-calorimeters, and studies of thermal transport at the nanoscale. In applications where it is necessary to operate the band-edge thermometer under ambient conditions, fluctuations in air density can introduce noise in the measured reflectance. This noise can be attenuated by incorporating a design where the spatial separation between the measurement and reference beam paths is minimized so that both beams experience similar local air density. However, to achieve the highest accuracy, the band-edge thermometer needs to be operated under low-vacuum conditions as demonstrated here.

3.6. Conclusions

In summary, we present a band-edge micro-thermometer with a resolution <100 nK that is capable of sensing modulated and unmodulated temperatures. Specifically, we demonstrated resolving a modulated temperature change of 66.2 nK at a bandwidth of 0.1 Hz, and an unmodulated thermometry noise floor of ~60 nK/√Hz. We identified that in the current implementation the resolution is limited by laser amplitude noise at low frequencies and photocurrent shot noise at high frequencies. Our analysis of noise sources indicates that the performance of the thermometer can be improved by using more stable commercially available laser sources to achieve a thermometry noise floor approaching 10 nK/√Hz. Our computational analysis, performed using a scattering matrix approach, quantitatively explained our experimental observations performed on a 130 μm-thick GaAs resonator. Further, we note that the lateral dimensions of the device employed in this study are limited by the incident beam diameter (~125 μm in this study), which can potentially be further reduced. The advances presented here enable,

for the first time, nanokelvin thermometry at room temperature with micron-scale devices, which will enable a broad number of studies and applications in micro-calorimetry and bolometry where high temperature resolution combined with small sensor footprint is required.

3.7. Methods

3.7.1. Experimental setup

The microfabricated GaAs thermometer was attached to a copper block (thermal reservoir) as shown in Figure 3.1c. The copper block was designed to allow incidence angles as large as 65° for the laser beam necessary for probing the thermometer's temperatures. The copper block acts as a thermal reservoir whose temperature (T_{res}) is measured using a 10 kOhm, glass-encapsulated thermistor (U.S. Sensor GP103J4F) and stabilized via a feedback loop to achieve ~100 μK stability about the set point and controlled using a pair of heater and Peltier elements to a range of 10 to 50 °C. To measure the resistance of the thermistor (T_{res}) and the integrated 9 kOhm platinum resistance thermometer[20] on the suspended region (Figure 3.1a), two Wheatstone bridges were used which included 20 kOhm resistors on top legs of the bridge (see Figure 3.1d). In order to minimize the effect of thermal drift in these circuits Vishay's ultra-high-precision foil resistors (Y145310K0000V9L) were used.

All the experiments were conducted in an ultra-low noise chamber whose temperature was controlled to better than 100 mK for the duration of the measurements. All the measurement electronics, instruments, and lock-in amplifiers (Stanford Research Systems SR810-DSP and Zurich Instruments HF2LI), were located in this chamber during measurement. The laser employed in this work (QPhotonics QFBGLD-895 nm) had a nominal power output of 2 mW and a linewidth <500 kHz. This laser is wavelength stabilized using a fiber Bragg grating and coupled to a polarization maintaining fiber. The laser driver was an Arroyo 6301, which allowed precise

control of the laser source temperature. The laser was enclosed by an aluminum thermal shield, which enabled laser temperature control with a stability better than 1 mK.

3.7.2. Device fabrication

The device fabrication started with a 130 μm-thick, epitaxy-ready, undoped GaAs wafer (Wafer Technology Co.). The wafer was mounted on a Si carrier wafer to provide mechanical support. Next, a 300 nm-thick Au reflector was deposited using e-beam evaporation and patterned using standard lithography and lift-off approaches. Next, a 30 nm-thick Al_2O_3 layer was deposited using thermal atomic layer deposition (ALD) everywhere on top of the wafer. Further, the heater and thermometers were formed by deposition and patterning of a 5 nm-thick Ti adhesion layer followed by a 50 nm-thick Pt layer. Next, the GaAs structure was released by lithographically patterning the desired device shape using a 15 μm-thick photoresist layer and subsequent high-density plasma etching. Finally, the processed GaAs wafer was released from the carrier wafer.

3.8. Appendix

3.7.1. Experimental setup

All the experiments were conducted in a vacuum chamber (pressure <5 mTorr) that was in turn located in an ultra-low vibration chamber which was temperature controlled to better than 100 mK over a day. All measurement electronics, lock-in amplifiers and all other instruments were placed in this chamber to minimize thermal drift.

The laser employed for the band-edge thermometry was a QPhotonics QFBGLD-895 nm with a maximum power output of 2 mW and linewidth <500 kHz. This laser is wavelength stabilized using a fiber Bragg grating. The laser driver was an Arroyo 6301, which allowed precise control of the laser die temperature. The laser and connector were enclosed by an aluminum thermal shield achieving <1 mK temperature stability. The output of the laser was coupled into a single-mode fiber. The fiber's output was collimated into free space using a Thorlabs PAF-X-11-PC-B collimator, passed through a linear polarizer (Thorlabs LPVIS050) to ensure the correct polarization required for the modulator, and fed into an electro-optic amplitude modulator (Thorlabs NEL03) for amplitude stabilization. The output of the modulator was passed through a half-wave plate (Thorlabs WPH10M-915), to rotate the polarization if needed, and coupled back to a polarization maintaining fiber (OZ Optics, NEW HPUC-23A-895-P-6.2AS-11), which was then fed into the vacuum chamber using a fiber vacuum feedthrough (OZ Optics, NEW VAC-01-V-SMJ-3A3A-780-5/125-1-1,0.4). Inside the vacuum chamber, the fiber was connected to a collimator (Schäfter and Kirchhoff 60FC-4-A2.7-02) which couples the light into free space for measurement of the resonator reflectance as shown in Figure 3.1e. The bow-tie shaped copper chip holder was mounted on a rotational stage (Thorlabs MSRP01/M) allowing to adjust the incident angle. The reflected beam was passed through a 200 μm diameter precision pinhole (Thorlabs

P200D) to remove reflected beams with greater than 0.5 mrad divergence angle. This resulted in an improved sensitivity of the thermometer. Finally, two identical Si photodiodes (Thorlabs FD11A) were used for measurement of the reflected and reference beams.

3.7.2. Beam profile and optical alignment

The laser beam alignment was done under atmospheric conditions using a beam profiler (Newport LBP2-HR-VIS2). First, the collimator inside the vacuum chamber (Schäfter and Kirchhoff 60FC-4-A2.7-02) was separately focused to position the beam waist on the surface of the suspended thermometer. Figure 3.5a shows the beam profile measured ~40 mm from the collimator outlet (which is the distance of the collimator outlet to the thermometer) showing a beam diameter of 125 µm. Next, the location of the beam on the thermometer was adjusted to avoid the patterned Pt layer. This alignment was confirmed by ensuring that the reflected beam was a circular Gaussian beam as shown in Figure 3.5b. Finally, the beam profiler was placed behind the device to detect any transmitted photons. As can be seen in Figure 3.5c, a very small transmitted flux was detected confirming that the beam is well blocked by the Au reflector on the thermometer.

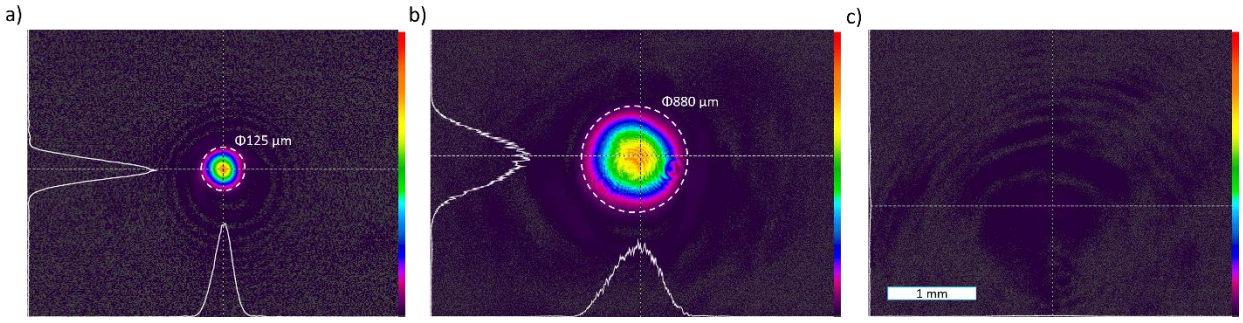


Figure 3.5 Beam intensity profiles. (a) Intensity profile of the beam focused on suspended thermometer, (b) reflected beam from the suspended thermometer and (c) intensity distribution of the light transmitted through the suspended thermometer.

3.7.3. Temperature ramp and hysteresis

In order to quantify the repeatability of our band-edge thermometer, the temperature was ramped up and down many times over an extended duration. As an example, Figure 3.6a shows an applied temperature ramp up and down (± 0.35 C) around the absorption peak at 32.8 °C at a rate of 2.5 mK/s. The measured DC and AC reflectances are plotted as a function of the resonator temperature (measured by the integrated platinum resistance thermometer (PRT) on the resonator) in Figure 3.6b. As can be seen, no significant hysteresis is observed in the reflectance signals, indicating repeatability of the temperature sensing scheme.

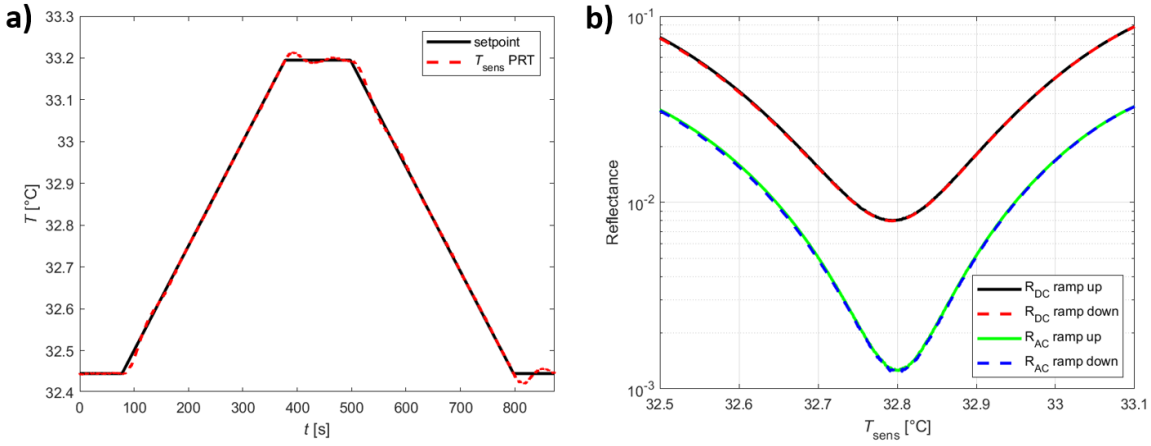


Figure 3.6 (a) The temperature profile of the resonator (T_{sens}) as measured by the integrated platinum resistance thermometer during a ramp up and down protocol. The temperature change corresponds to a rate of 2.5 mK/s. (b) Measured resonator reflectance during a temperature ramp up and down experiment from around the absorption peak of 32.8 °C.

3.7.4. Quantification of the effect of optical nonlinearities and temperature changes on the sensed temperature in band-edge thermometry

In order to quantify the effect of laser amplitude fluctuations on the sensed temperature, two separate effects are considered, (a) optical non-linearity in GaAs and (b) thermal effects, which are discussed below. The optical non-linearity effects in bulk GaAs cause variations in the refractive index and absorption coefficient as the incident flux density changes[99]. In general,

ignoring higher order terms, the refractive index can be written[100] as shown in Eq. (2.3), where $I = \phi/A_{\text{beam}}$ is the radiant flux density, and γ is the third order refractive index coefficient. Similarly, the absorption coefficient can be written as shown in Eq. (2.4), where $\beta^{2\omega}$ is the two-photon absorption coefficient. In Eq. (2.3) and (2.4), T_0 is the resonator temperature at zero intensity (I = 0). Assuming that all the absorbed optical power is converted to heat (neglecting the radiative recombination and luminescence effects which reduce the heating rate), the upper bound in the change of suspended resonator temperature as a result of absorbed irradiance can be written as $\Delta T_{perturb.} = \frac{I\, A_{beam}(1-R)}{G}$, where A_{beam} is the cross section of the incident beam, R is the reflectance and G is the thermal conductance of suspended thermometer. Using the aforementioned parameters, the following relations can be obtained:

$$\begin{aligned} n(\lambda, T_0, I) &= n_0\big(\lambda, T_0 + \Delta T_{perturb}\big) + \gamma(\lambda) I \\ &\approx n_0(\lambda, T_0) + I\left(A_{beam}\frac{\partial n}{\partial T}\frac{(1-R)}{G} + \gamma(\lambda)\right) \end{aligned} \tag{2.3}$$

$$\begin{aligned} \alpha(\lambda, T_0, I) &= \alpha_0\big(\lambda, T_0 + \Delta T_{perturb.}\big) + \beta^{2\omega}(\lambda) I \\ &\approx \alpha_0(\lambda, T_0) + I\left(A_{beam}\frac{\partial \alpha}{\partial T}\frac{(1-R)}{G} + \beta(\lambda)\right) \end{aligned} \tag{2.4}$$

Let us assume that the incident laser beam has the flux density of $I(t) = \bar{I} + I_n(t)$, where $\bar{I}$ is a steady mean value and $I_n(t)$ is the flux density noise. Using the above equations, the collective effect of nonlinear absorption/refraction and temperature variation due to intensity fluctuation on resonator reflectance (R_{FP}, where FP: Fabry–Pérot) can be modeled to first-order by:

$$R(T_0, I) = R_{FP}\big(n(\lambda, T_0, I), \alpha(\lambda, T_0, I)\big) =$$
$$\approx R_{FP}\big(n(\lambda, T_0, \bar{I}), \alpha(\lambda, T_0, \bar{I})\big) + \left(A_{beam}\frac{\partial R}{\partial T}\frac{(1-R)}{G} + \frac{\partial R}{\partial I}\right) I_n \quad (2.5)$$

Here $R_{FP}(n,\ \alpha)$ is the reflectance, while the refractive index and absorption coefficient at a given incident beam wavelength, polarization and angle, are *n* and *α*, respectively.

In order to experimentally determine the effect of nonlinear absorption and dispersion on reflectance (defined by $\partial R/\partial I$ in Eq. 2.5) we first chose an experimental condition to remove the thermal effect on reflectance (defined by the term $A_{beam}(\partial R/\partial T)(1\text{-}R)/G$ in Eq. 2.5). To this end, the temperature of the chip holder was maintained at a constant value of T_{res} = 32.79 °C, i.e. a temperature that corresponds to the DC thermoreflectance coefficient of zero (i.e. $\frac{1}{R}\frac{\partial R}{\partial T} = 0$) leading to minimized thermal effect on reflectivity. At this temperature, the incident beam intensity was square wave-modulated at 0.5 Hz between the two levels of 10.6 and 31.9 μW using an electro-optic modulator at constant wavelength and the incident beam was focused to a spot size with diameter of 125 μm. The measured beam intensity from the reference photodiode, and the resultant reflectance coefficient are shown in Figure 3.7. As can be seen, upon a step increase in intensity, the reflectance also increases. The average nonlinearity coefficient was estimated from the results of Figure 3.7 to be $\partial R/\partial I \approx \Delta R/\Delta I = 1.75\times10^{-4}$ $(\text{mW/mm}^2)^{-1}$. This estimated value was used for calculation of laser amplitude fluctuation noise on the measured temperature in Figure 3.4a.

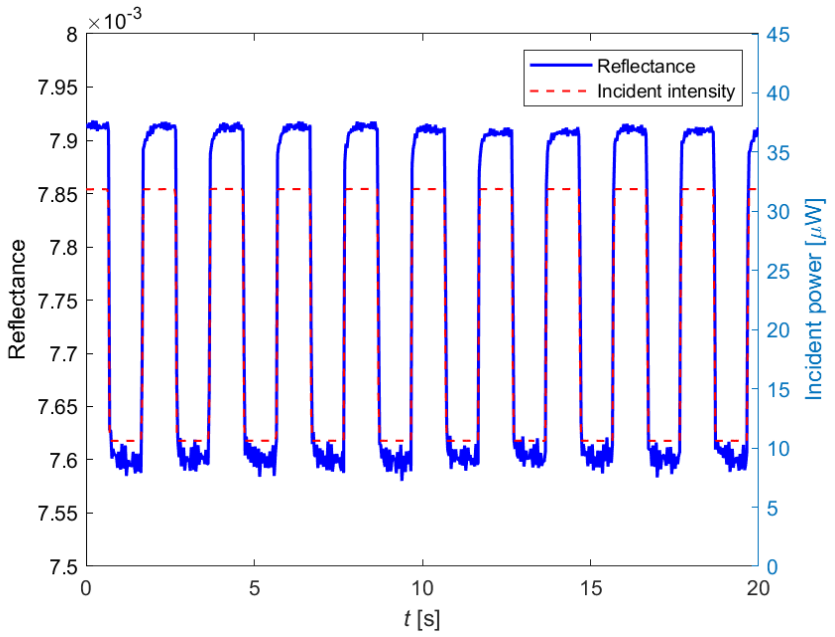


Figure 3.7 Measurement of the effect of optical nonlinearity on reflectance at the resonator absorption peak (T_{res} = 32.79 °C, point of no temperature sensitivity and large absorption). The incident beam was focused to a spot with a diameter of 125 µm. As the incident intensity is increased the reflectance also increases due to nonlinearities in the optical properties as described in the text.

3.7.5. Sensing of modulated temperatures

In order to quantify the temperature sensing resolution of our band-edge thermometer we heated the suspended region by inputting known amounts of heat via Joule heating while measuring the temperature rise via our band-edge thermometer and the integrated PRT. To input known amounts of heat, we applied a square wave-modulated current with an offset ($I = I_{AC}$ (f_{mod}) + I_O) to the integrated Pt ring heater (resistance R_h = 1 kΩ, see Figure 3.1a). Here, I_{AC} is the amplitude of the square wave and f_{mod} (1.0 Hz or 2.0 Hz) is the frequency of the square wave and chosen to be comparable to the thermal cut off frequency, while I_O is a nominally constant offset current superimposed on the square current. The applied current can be represented as a Fourier series (sgn represents the sign function) by:

$$I(t) = I_0(t) + I_{AC} sgn(sin(2\pi f_{mod} t)) = I_0(t) + I_{AC}\left(\frac{4}{\pi}\sum_{n=1,3,5,\ldots}^{\infty}\frac{1}{n}\sin(2\pi n f_{mod} t)\right) \quad (2.6)$$

This applied current results in Joule heating described by:

$$p(t) = R_h\left[I_O^2(t) + I_{AC}^2\right] + 2R_h I_{DC} I_{AC}\left(\frac{4}{\pi}\sum_{n=1,3,5,\ldots}^{\infty}\frac{1}{n}\sin\left(2\pi n f_{mod} t\right)\right) = p_O + p_{AC}\,\mathrm{sgn}\left(\sin\left(2\pi f_{mod} t\right)\right) \quad (2.7)$$

The first term is Eq. (2.7) is weakly dependent on time and is labeled $p_{O,}$ which is used via a feedback loop (explained in section S5.1) to ensure that the DC temperature of the suspended region is stabilized close to 32.83 °C that corresponds to the largest sensitivity of the band-edge thermometer (as identified in Figure 3.2c). The second term, p_{AC} sgn(sin(2π f_{mod} t)), represents a square wave of deposited power with frequency f_{mod} with peak amplitude $p_{AC} = 2R_h I_{DC} I_{AC}$ that generates small modulations in the temperature (at f_{mod}).

Next, we modulated the intensity of the probe laser beam at f_s = 200 Hz and measured the AC reflectance (R_{AC}) at f_s using a lock-in amplifier in a bandwidth of either 20 or 50 Hz. The output of the lock-in-amplifier was related to the resonator temperature ($\Delta T_{sens}(t)$) via $\Delta T_{sens}(t) = \Delta R_{AC}(t)/(R_{AC}\, k_{AC})$ where k_{AC} is the AC thermoreflectance coefficient. Further, the PRT was also employed to concurrently measure the resonator temperature using a Wheatstone bridge by supplying an AC voltage at 400 Hz with a peak-to-peak amplitude of 1 V, measuring the output of the Wheatstone bridge using a lock-in amplifier (20 Hz bandwidth) and converting the resistance of PRT to temperature as a function of time. Next, we post-processed the measured time series data obtained from the band-edge thermometer and the PRT by applying a fast Fourier transform on the recorded temperature signals in a bandwidth of 0.1 Hz, and extracting the component of temperature variations corresponding to the frequency f_{mod} (i.e. the frequency at which the Joule heating was modulated).

To illustrate our approach, we show in Figure 3.8 the time-averaged T_{sens} obtained by first locking in to the AC probe beam, which was modulated at f_s = 200 Hz, to determine the R_{AC} and

then calculating $\Delta T_{sens}(t) = \Delta R_{AC}(t)/(R_{AC}\ k_{AC})$. In Figure 3.8 the sampling frequency of T_{sens} is 20 Hz, obtained from both the band-edge and PRT sensors, when the temperature is modulated at f_{mod} = 2 Hz. To obtain this plot, 100 time-series were averaged, corresponding to an equivalent bandwidth of 20 Hz/100 = 0.2 Hz. As can be seen, the band-edge thermometer clearly shows peak-to-peak temperature modulation of ~7 μK, whereas the PRT signal is very noisy.

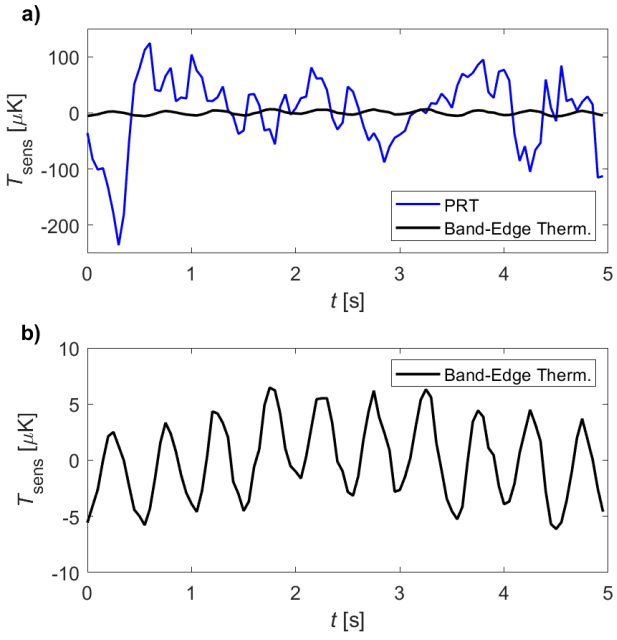


Figure 3.8 (a) Time-averaged temperature of the suspended region (T_{sens}) as obtained from band-edge thermometry and PRT when the temperature is modulated at f_{mod} = 2 Hz. (b) Zoomed plot of time-averaged temperature obtained by band-edge thermometer. The sampling frequency of the time series is 20 Hz, and 100 curves were averaged to obtain the plotted curve.

2.7.5.1. Controllers for attenuating temperature drifts for modulated temperature sensing

The control scheme employed in our measurements is shown in Figure 3.9a. Here, T_{sens} is the temperature measured using the optical scheme. The two control loops are used to suppress slow and fast components of temperature fluctuations by controlling the temperature of the copper chip holder (Figure 3.1c) and the DC temperature of the suspended region, respectively. First, a slow control loop is used to suppress the slow drift (<0.01 Hz) component of T_{sens} by adjusting the power

(p_{res}) being input into the copper chip holder shown in Figure 3.1c. Second, a separate controller is used to suppress the intermediate frequency fluctuations of T_{sens} below the thermal modulation frequency (0.01 Hz to 0.5 f_{mod}) by adjusting the power dissipated (p_{sus}) in the Pt ring heater integrated into the suspended region of the device. The upper bound on the frequency range of this controller (0.5 f_{mod}) is selected to avoid damping the modulated temperature via feedback.

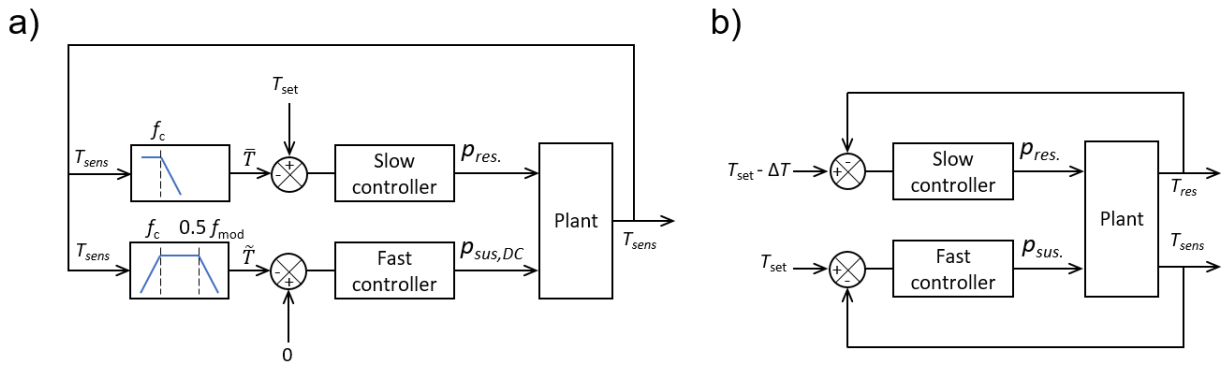


Figure 3.9 Feedback control schemes for temperature stabilization of the suspended thermometer. (a) Characterization of thermometer resolution for modulated temperature sensing at f_{mod}. (b) Unmodulated temperature sensing and stabilization.

3.7.6. Estimating the theoretical noise floor of band-edge thermometer

In order to understand the ultimate limit to the thermometry noise floor of our current design of the band-edge thermometer, we analyze the relevant noise sources. Specifically, we quantify the contributions of photocurrent shot noise $i_{sn} = (2qI\Delta f)^{1/2}$, where I is the photodiode current[101], the Johnson noise associated with the feedback resistor (R_f) of the transimpedance amplifier[101] $i_{Jn} = (4k_B T\Delta f/R_f)^{1/2}$, and the probe beam intensity noise. In estimating the temperature noise associated with probe beam intensity fluctuations, we include both the contributions from photothermal absorption effect (i.e. the variation in resonator temperature due to fluctuations in deposited laser power) and optical nonlinearity effects (i.e. change in the reflectivity due to variation in beam intensity, see section S4). The intensity noise of the probe beam was measured

using the reference photodiode and employed to estimate the photothermal absorption and nonlinearity noises mentioned above. As shown in Figure 3.10 (which is a more detailed version of Figure 3.4a), the thermometry noise floor of the thermometer is limited by photothermal absorption at low frequencies ($f < 0.02$ Hz), and by photocurrent shot noise at higher frequencies. The estimated noise limit, i.e. the sum of the all the aforementioned noise sources, is plotted in red in Figure 3.4a, which shows a noise floor of 46 nK/√Hz at $f > 0.2$ Hz. As a point of comparison, we also show the fundamental thermodynamic fluctuation in temperature (dashed green curve in Figure 3.4a) due to shuttling of phonons from the thermal reservoir to the suspended region, which has a root mean square (RMS) value of $(4k_B T^2/G_{th})^{1/2}$ and a frequency-dependent temperature fluctuation amplitude of $[4k_B T^2/(G_{th}+2G_{th}\pi f\tau_{th})]^{1/2}$ [102].

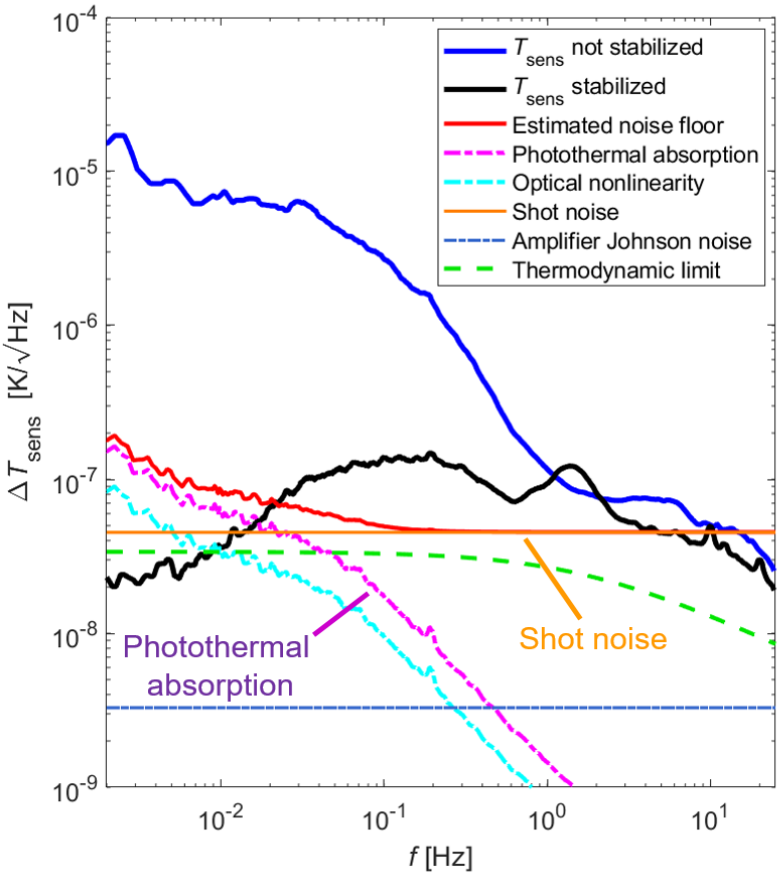


Figure 3.10 Amplitude spectrum of temperature variations of the suspended region (T_{sens}) with (black line) and without (blue) feedback stabilization along with the estimated noise floor, which is the sum of shot noise, Johnson noise, photothermal absorption, and optical nonlinearity effects. Further, the estimated noise from thermodynamic fluctuations is also shown (green line). As can be seen, the thermometry noise floor is limited by photothermal absorption (due to probe beam intensity fluctuations) at low frequencies and shot noise at high frequencies.

2.7.6.1. Temperature stabilization for determination of thermometry noise floor

The temperature stabilization scheme employed by us is shown in Figure 3.9b and works as follows. First, the temperature of the copper bow-tie chip holder (T_{res}) is stabilized using a PID controller with a bandwidth of 50 Hz at a setpoint ΔT = 2 mK lower than the desired setpoint (T_{set}) of the suspended reflector (T_{sens}) to provide sufficient dynamic range for T_{sens} heater during long experiments. Second, the temperature of the suspended thermometer (T_{sens}) is measured using the

DC reflectance signal of the band-edge thermometer and fed to a separate controller at a bandwidth of 50 Hz to stabilize the T_{sens}. This scheme was used for temperature stabilization in Figure 3.4.

3.7.7. Optical modeling of the thermometer

We employed a numerically stable scattering matrix approach[94] that enables us to exactly solve Maxwell's equations to obtain the reflectivity from multilayer structures. We modeled the reflectance of a structure consisting of 130 μm undoped GaAs coated with 300 nm Au on the back side, corresponding exactly to the geometry of the thermometer used in this study, when a p-polarized beam at 895 nm is incident at 30° on the structure. The scattering matrix model requires input of the dielectric properties of each layer as a function of temperature. For the Au reflector layer, the dielectric constant (ε_r = -32.294 + 1.9516i) was obtained from Ref. [95] and we assumed no temperature dependence. The temperature-dependent dielectric properties of GaAs at the Urbach edge (895 nm) were obtained as explained below. First, we obtain the temperature-dependent band gap (E_g) using Eq. 2.8 with empirical parameters; E_B = 1.571 eV, a_B = 0.057 eV, and Θ = 240 K [96]. This temperature dependent E_g was later used in Eq. 2.9, which is valid in the Urbach region [85], to estimate the absorption coefficient (α). In Eq. 2.9, $h\nu$ is the incident photon energy, E_0 is the width of the absorption edge, and α_g is the absorption coefficient exactly at bandgap, which is 8000 cm^{-1} for GaAs[85] and is fixed in our model. The refractive index was modeled as a parabolic polynomial as a function of the difference of photon energy and band gap as shown in Eq. 2.10, where n_0 is the extrapolated refractive index at bandgap based on the fit and is fixed at 3.665 which is in good agreement with Ref. [97]. Please note that, the refractive index functional form considered here is only valid in a small range of bandgap energy variation (~10 meV) in the 20-42 °C temperature range that was used in this study, for larger energy variations other functional forms such as the Sellmeier equation should be used [103].

$$E_g(T) = E_B - a_B\left[1 + \frac{2}{e^{\Theta/T} - 1}\right] \tag{2.8}$$

$$\alpha(h\upsilon) = \alpha_g \exp\left(\frac{h\upsilon - E_g}{E_0}\right) \tag{2.9}$$

$$n(h\upsilon) = n_0 + n_1\left(h\upsilon - E_g\right) + n_2\left(h\upsilon - E_g\right)^2 \tag{2.10}$$

The free parameters of this model are; E_0, n_1, n_2, and ΔT_{offset}, where ΔT_{offset} is the temperature offset of the sensor compared to absolute value of temperature used in the model. These parameters were obtained by fitting the DC reflectance to the experimental results (of Figure 3.2a) using nonlinear constraint optimization (FMINCON)[104] in MATLAB. The parameters of the model were constrained to vary within a reasonable range of previous measurements in Ref. [85] and [105], and the temperature offset was allowed to vary in the range of -2 to 2 °C. Finally, since the DC reflectance was modeled, a constant background reflectance equal to the background obtained from experimental results was added to the modelled reflectance; $R_{\text{model}} = R_{\text{scattering matrix}} + R_{\text{BG}}$. The fitted parameters of the model are, E_0 = 6.51 meV, n_1 = 3.182 eV^{-1}, n_2 = 16.8 eV^{-2}, and ΔT_{offset} = 0.1 K, which are in the range of previous measurements[85,97]. For instance, the value of E_0 from Ref. [85] is ~7.5 meV, and a parabolic fit (similar to Eq. 2.10) to the refractive index data in Ref. [97] leads n_0 = 3.664, n_1 = 2.603 eV^{-1}, and n_2 = 22.117 eV^{-2}. The agreement of the fitted model parameters with the previously reported values as well as the good agreement of modelled resonator reflectance and experimental measurements indicate the validity of the physical model employed here.

3.7.8. Estimation of sensor footprint area

In order to estimate the sensor footprint area, we identified the portion of the sensor which has to thermalize (i.e. reach local thermal equilibrium) with the system of interest whose temperature needs to be measured. This portion of the device, which represents the active region of the device was used to consistently compare the sensor footprint for all the devices listed in Figure 3.4b. For the band-edge thermometer, the area of the incident probe beam, which is the region of the resonator where the temperature measurement is performed and therefore represents the area which need to thermalize with system of interest limits the smallest lateral dimensions of the sensor. Although the beam diameter on the resonator surface can be potentially reduced to a diffraction-limited area, for practical applications the convergence angle of the beam is limited due to the minimum distance between the collimator and the resonator (~40 mm in our case). Further, the arrangement of other optical components limits the beam waist diameter. Therefore, in our experimental setup, the beam spot diameter of 125 μm was directly measured (as explained in Section S2) and used for estimation of sensor footprint area. For the resonant cavity mode thermometer[15], the dimensions of main cavity (length 100 mm and diameter of ~25 mm), which has to thermalize with the environment, was used ignoring the reference cavity footprint since it can be placed outside the desired sensing region. To estimate the sensor footprint area of whispering-gallery mode (WGM) resonators[16,18], the resonator needs to thermalize with the environment for temperature sensing. Therefore, the resonator diameter, which ultimately limits the lateral dimensions of the sensor, was used. We note that we ignored the required coupling components such as prism, fiber, or waveguide couplers which need to be positioned adjacent to the WGM resonator[106] as they do not need to thermalize with the system of interest.

For the fiber loop mirror[19], the region that needs to thermalize is the photonic crystal fiber with a length of 61 mm and a diameter of ~120 μm. For the liquid-in-glass thermometer[20], the

length (23 mm) and the inner diameter (0.75 mm) of the capillary tube, which needs to thermalize with the environment for temperature sensing, were used to calculate the footprint area. For the bimaterial cantilever thermometer[23], the suspended cantilever needs to thermalize for temperature sensing which has an area of 200×50 μm^2. For the PM fiber resonator thermometer[17], the entire fiber ring needs to thermally equilibrate with the environment to sense the temperature, which has a length of 2000 mm and a fiber cladding diameter of 125 μm.

For thermistors[7,21], their footprint while placed on a surface (i.e. sensor length × width) was used ignoring the electrical connection leads. For the platinum resistance thermometer[24], a footprint area where a Pt line with a serpentine pattern with a resistance of ~10 kOhm can be fitted was considered which is ~50×50 μm^2. Finally, for quartz crystal thermometers[22], the dimensions of an ultra-low profile surface mount sensors such as Statek Ultra Miniature surface mount crystals (6.7×2.6 mm^2) was used.

Chapter 4 Quantitative Mapping of Unmodulated Temperature Fields with Nanometer Resolution

Reproduced with permission from the *American Chemical Society*.

Amin Reihani, Yuxuan Luan, Shen Yan, Ju Won Lim, Edgar Meyhofer, Pramod Reddy

Quantitative mapping of temperature fields with nanometric resolution is critical in various areas of scientific research and emerging technology, such as nanoelectronics, surface chemistry, plasmonic devices and quantum systems. A key challenge in achieving quantitative thermal imaging with scanning thermal microscopy (SThM) is the lack of knowledge of the tip-sample thermal resistance (R_{TS}), which varies with local topography and is critical for quantifying the sample temperature. Recent advances in SThM have enabled simultaneous quantification of R_{TS} and topography in situations where the temperature field is modulated enabling quantitative thermometry even when topographical features cause significant variations in R_{TS}. However, such an approach is not applicable to situations where the temperature modulation of the device is not readily possible. Here we show, using custom-fabricated scanning thermal probes (STPs) with a sharp tip (radius ~25 nm) and an integrated heater/thermometer, that one can quantitatively map unmodulated temperature fields, in a single scan, with ~7 nm spatial resolution and ~50 mK temperature resolution. This is accomplished by introducing a modulated heat input to the STP and measuring the AC and DC responses of the probe temperature which allows for simultaneous

mapping of tip-sample thermal resistance and sample surface temperature. The approach presented here—Contact-Resistance Resolved Scanning Thermal Microscopy (CR-SThM)—can greatly facilitate temperature mapping of a variety of microdevices under practical operating conditions.

4.1. Introduction

In recent years probing energy transport and dissipation in nanoscale devices has become critically important. In order to study these phenomena it is required to probe temperature fields with nanometer resolution. Nanoscale thermometry and thermal microscopy enable such studies and play an important role in various fields, including nanoscale transport[48,107-109], biomedical research[27,110,111], material synthesis and fabrication[38,112,113], electronics[8,34,114-116] and quantum devices[9,117,118]. Specifically, scanning thermal microscopy (SThM), which employs scanning thermal probes (STPs), has enabled temperature mapping with nanometer spatial resolution[31,32,119]. In performing quantitative studies in a vacuum environment, STPs are typically used in contact mode where the heat transfer between the sample and the STP is dominated by conduction via the contact between the STP tip and the sample[31,119].

A key challenge for quantitative temperature mapping of a sample using STPs is that the temperature measured by the probe depends on both the sample temperature and the tip-sample thermal contact resistance (R_{TS}). The value of R_{TS} depends on the exact geometry of the sample at the point of contact as well as the local thermal conductivity of the sample. Therefore, it is critical to know the value of R_{TS} when measuring temperature fields from surfaces with variations in topology and thermal conductivity, or time-dependent variations in tip geometry arising from abrasion, plastic deformation, or contamination of the tip while scanning, all of which can lead to spurious signals[31,119]. Due to these challenges, temperature maps obtained by scanning a sample

surface using STPs often includes artifacts[32-34,36,120]. Therefore, to obtain a quantitative map of the sample temperature, one needs to also simultaneously measure the spatial variation of R_{TS}.

Past studies have employed several techniques for quantitative temperature sensing using SThM such as the null-point (NP) measurement[121,122] that operates by identifying the probe temperature at which the probe-sample heat flow is nullified ensuring that the probe temperature equals the local sample temperature. Another method for quantitative temperature sensing is the double-scan measurement[123, 124], which first determines R_{TS} by comparing the temperature of the probe when it is out-of-contact to that of the probe when it is in-contact with the sample at ambient temperature. Subsequently, this map of R_{TS} values is used to determine the sample temperature under operation (i.e., when a temperature gradient is established on the sample). These techniques represent an important step forward as they quantify the tip-sample contact resistance by combining information obtained from multiple scans or multiple approach-retract cycles. However, they cannot completely capture the variation of R_{TS} with time for reasons described above.

A recent technique[34,125] has aimed to overcome these challenges by quantifying R_{TS} via measuring the amplitude of sample temperature modulation when the sample temperature is periodically modulated. However, this interesting approach cannot be directly applied to temperature mapping of samples or devices which operate under steady state conditions, or where modulation of sample temperature at reasonable frequencies is practically not possible. Examples include temperature fields generated in biological systems and by surface reactions where the heat source cannot be turned on and off on demand. Other important examples, relevant to this work, include microdevices where temperature modulation leads to periodic thermal expansion that both mechanically stresses the device as well as generates additional artifacts during scanning, or

devices where the amplitude of the modulated temperature field is large and invalidates the assumption of temperature-independence of R_{TS}. Therefore, in many practical applications, it is essential to have the device operate under steady conditions and perform thermal microscopy without perturbing device operation.

In this work we present a new approach—Contact-Resistance Resolved Scanning Thermal Microscopy (CR-SThM)—that leverages novel scanning probes to quantitatively map unmodulated temperature fields even on samples with topography and material variations. Briefly, our approach is based on applying a modulated heat input to the probe and simultaneously measuring the amplitude of temperature oscillations as well as the mean temperature of the probe while the probe scans the sample of interest, in contact mode, in an ultra-high vacuum environment. Data from these simultaneous measurements contain information on both the sample temperature and R_{TS}, which are extracted using a dynamic, lumped capacitance thermal model. Our approach suppresses artifacts generated by topography variations, STP tip abrasion, and temperature drift, enabling measurements of sample temperature with a temperature resolution of ~50 mK, a long-term temperature stability of <10 mK, and a spatial resolution of ~7 nm.

4.2. Results

In order to quantitatively measure unmodulated temperature fields, we custom-fabricated novel STPs (see Appendix Section 4.5.1. Scanning thermal probe fabrication for fabrication details). Images of the fabricated probes, obtained using optical microscopy, are shown in Figure 4.1a. The probe consists of two suspended regions: The first region, identified by a blue box, shows the suspended thermal reservoir, while the second region, identified by a red box, shows the scanning thermal probe. The suspended thermal reservoir serves to thermally isolate the suspended scanning

probe from the ambient environment and acts as a thermal reservoir for the suspended probe. This thermal reservoir features a 17 kOhm Pt serpentine line which is used as a platinum resistance thermometer (PRT) to sense the reservoir temperature T_R using a Wheatstone bridge and a lock-in measurement technique (see methods). The suspended scanning probe is characterized by both high thermal isolation (quantified below) for the tip as well as a relatively high mechanical stiffness (~7.7 N/m). This large mechanical stiffness (see Appendix Section 4.5.2. Mechanical stiffness and thermal conductance of scanning thermal probe for an estimate of the stiffness) is accomplished by incorporating T-shaped beams that can be seen in the scanning electron microscope images shown in Figure 4.1b. Further, a gold-coated region (see Figure 4.1b) that is used as a reflector for an incident laser is also incorporated into the probe and is thermally isolated from the rest of the probe using thin beams to minimize detrimental effects arising from laser heating. Finally, it can be seen that the tip of the probe has a radius of curvature of ~25 nm enabling very high spatial resolution imaging as described later.

The suspended scanning probe also features a ~9 kΩ PRT that is located close to the tip and is used for heating the probe and for sensing temperatures. In our experiments, this PRT is integrated into a full Wheatstone bridge that is driven by a time (t) dependent current ($I_{probe}(t)$) consisting of two superimposed sinusoidal waves, $I_{probe} = I_1 \sin(2\pi f_1 t) + I_2 \sin(2\pi f_2 t)$. The first current component (I_1 = 56 μA, f_1 = 4 Hz) leads to a modulated heat input resulting in sinusoidal oscillations of the temperature of the probe at a frequency of $2f_1$ and an amplitude T_{AC} that is recorded during scanning (see methods). The second AC current component (I_2 = 14 μA, f_2 = 212 Hz), which has a smaller amplitude and a higher frequency (the frequency was chosen to be much higher than the thermal cutoff frequency of the suspended scanning probe (~8.9 Hz, see Figure 4.2c), is used for sensing the unmodulated DC temperature of the STP (labeled T_{DC}) via a lock-in

technique (see methods). Our approach for quantitatively mapping unmodulated temperature fields via the STP is schematically shown in Figure 4.1c and d. The figures depict a STP near a Pt line sample that is heated by passing a DC current (I_{sample}) through it. The resulting steady-state surface temperature field $T_S(x, y)$ is quantified using CR-SThM.

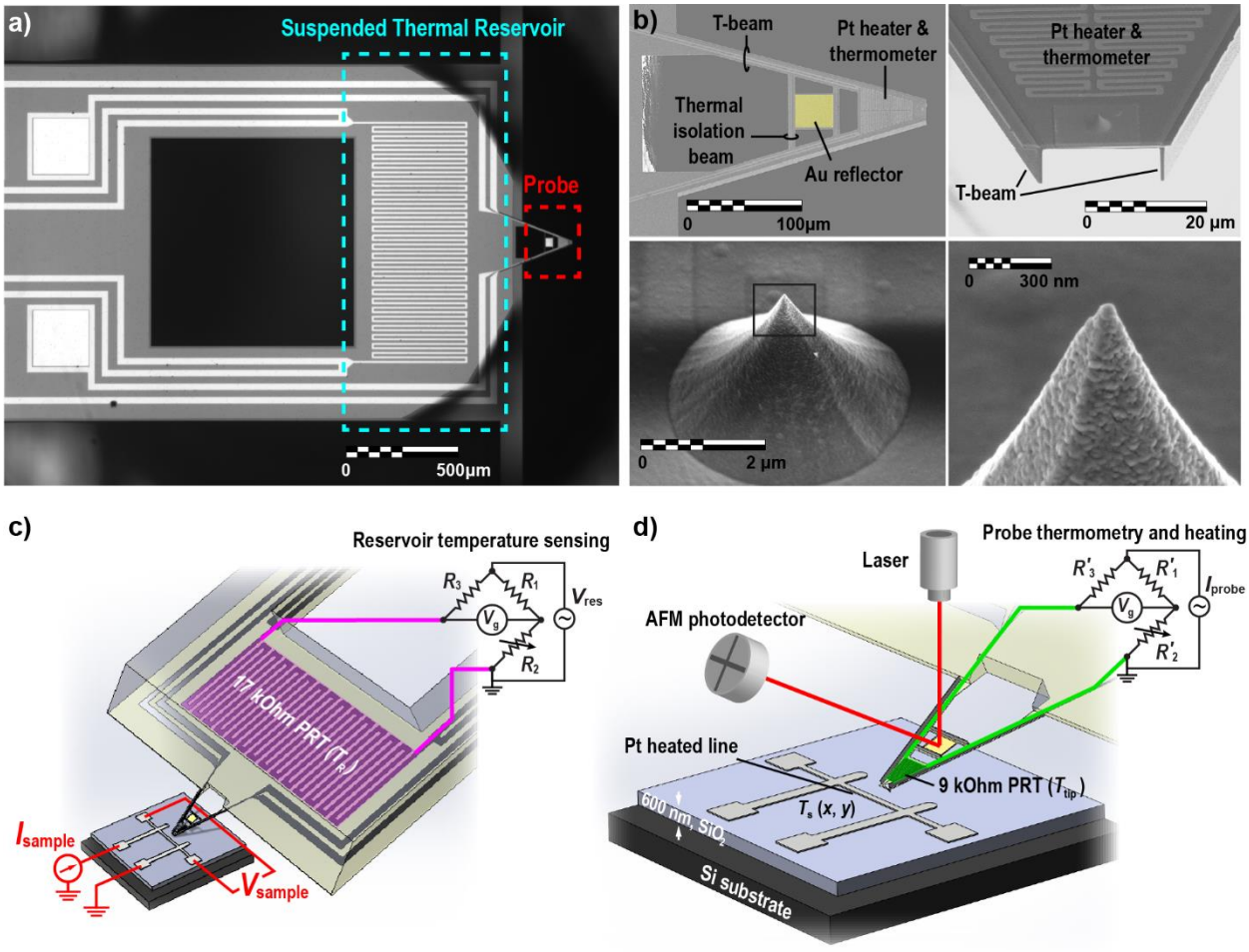


Figure 4.1 (a) Optical microscopy image of the scanning thermal probe showing a suspended region (red dashed box) which acts as a thermal reservoir and the scanning thermal probe (blue dashed box). (b) Tilted false color SEM micrographs (top left panel) of the scanning thermal probe (STP), along with zoomed in image (top right panel) showing the Pt serpentine and T-beams. Bottom panels show zoomed in images of the probe tip. (c) Schematic of the probe during measurement. A DC current (I_{sample}) is sourced through the Pt line which generates a steady state temperature field on the sample. A wheatstone bridge driven by an AC voltage is used to read the resistance of the first PRT for sensing the reservoir temperature (T_R). (d) Schematic of the scanning thermal microscope in contact with a heated Pt line. The second PRT integrated into the STP is connected to a Wheatstone bridge, driven by a specific current waveform (I_{probe}) which is used for temperature sensing and modulated heating of the STP (see main text and methods).

4.2.1. Thermal analysis for quantification of sample temperature

The thermal behavior of the STP when placed in contact with the sample can be modelled using a lumped capacitance thermal network[6,61,126] shown in Figure 4.2a. In the network, R_P and R_{TS} represent the thermal resistances to heat flow within the probe (i.e., the thermal resistance from the STP tip to the suspended thermal reservoir) and tip-sample thermal contact resistance, respectively, and C_P is the lumped thermal capacitance of the STP. The temperature sensed by the probe PRT (labeled T_P) has the components T_{DC} and T_{AC}, as discussed in the previous section, while T_R and T_S are the temperature of the probe thermal reservoir and sample, respectively. In addition, $\dot{q}_P$ is the heat deposited on the probe by the integrated probe heater as well as the atomic force microscopy (AFM) laser, which has both DC ($\dot{q}_{DC}$) and AC ($\dot{q}_{AC}$) components. By analyzing this network the surface temperature of the sample (T_S) can be related to other parameters (see Appendix Section 4.5.5. Lumped-capacitance thermal model of scanning thermal probe for derivation) via:

$$T_S = \frac{R_{TS}}{R_P}\left(T_{DC} - T_R - R_P\,\dot{q}_{DC}\right) + T_{DC} \tag{3.1}$$

As illustrated in Figure 4.2b, different contact geometries are established when a sample with topographical variations (such as a heated line) is studied leading to local points of weak or strong thermal contact. It is clear from Eq. 3.1 that knowledge of R_{TS}, R_P, T_{DC}, T_R and $\dot{q}_{DC}$ is necessary for evaluating T_s. As explained earlier, T_{DC} and T_R can be directly measured using the integrated PRTs (see methods for details). We determine R_P and C_P by placing the STP ~2 μm above the sample surface and measuring its thermal frequency response to modulated heat inputs at various frequencies and a peak amplitude of $\dot{q}_{AC}$= 8.5 μW. These measurements were repeated at various STP temperatures (T_{DC}) and the results from these measurements are shown in Figure

4.2c. It can be seen that the measured frequency response is consistent with that of a simple first order system with a frequency-independent behavior at low frequencies and a characteristic roll-off frequency (f_c, the –3 dB point), which is indicated by red circles in Figure 4.2c. Using the thermal network described earlier, one can show that the cantilever thermal resistance is given by $R_P = T_{AC}\,(f = 1\text{ Hz})/\dot{q}_{AC}$, while the thermal capacitance of the probe is given by $C_P = (2\pi\, R_P\, f_c)^{-1}$. The inset of Figure 4.2c shows the measured values of R_P and C_P along with their weak dependence on T_{DC}. As can be seen, R_p and C_p decrease and increase as a function of temperature, respectively. This can be attributed to the temperature dependence of thermal conductivity and the heat capacity of SiN_x films on the probe[46]. We note that in this study the maximum variation in the temperature of the sample is <10 K, which corresponds to <1 K variation of STP temperature. Therefore, the effect of temperature variation on R_P and C_P is small and thus neglected in our subsequent analysis. However, if the presented technique is employed for measurements where the sample is heated or cooled significantly[126], the temperature dependence of R_P and C_P must be considered.

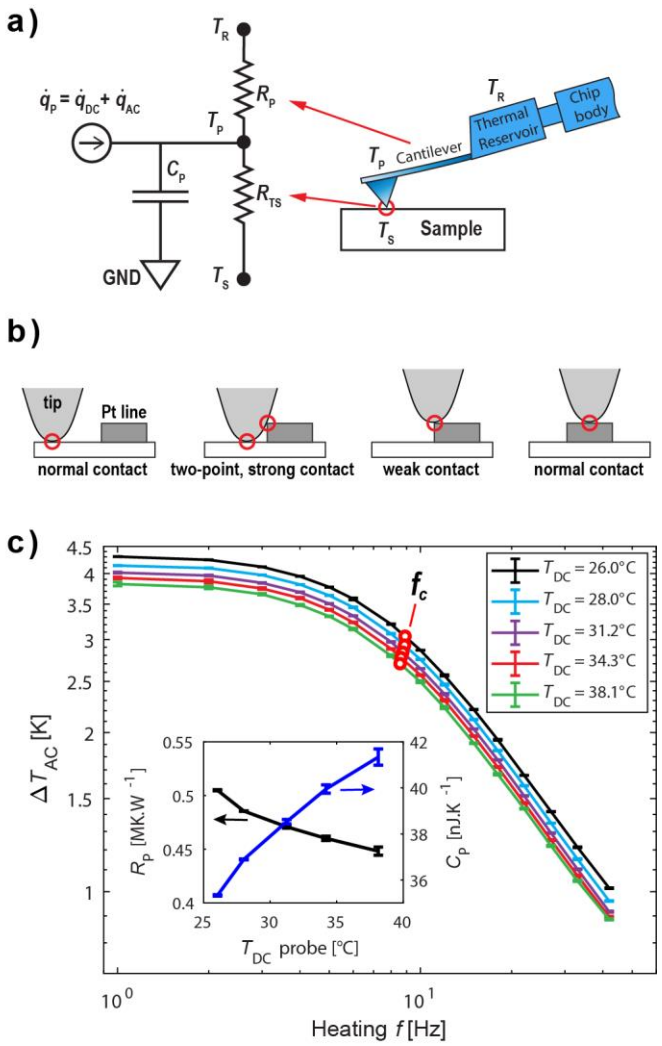


Figure 4.2 (a) Lumped-capacitance thermal network of the STP in contact with the sample. T_R, T_P, and T_S are the thermal reservoir temperature, probe temperature, and sample surface temperature respectively. R_P and C_P are the thermal resistance and thermal capacitance of the probe, and the R_{TS} is the probe tip-sample thermal contact resistance. Further, $\dot{q}_P$ is the heat deposited on the probe by the probe heater and the AFM laser. (b) Schematic demonstration of different contact geometries established during thermal scanning in perpendicular direction to a heated Pt line sample. (c) Thermal frequency response of the STP to an AC heat input with a peak amplitude of 8.5 µW that is deposited on the STP heater at various STP temperatures (T_{DC}). Inset shows the variation of thermal resistance and lumped capacitance of STP as a function of STP temperature (T_{DC}). The measurements were performed under out-of-contact conditions at a gap-size of ~2 µm from the sample surface.

Determination of T_S using Eq. 3.1 also requires knowledge of the spatiotemporally varying R_{TS}, which can be obtained by monitoring T_{AC} and using it to calculate R_{TS} via the following equations (see Appendix Section 4.5.5. Lumped-capacitance thermal model of scanning thermal probe for a derivation of Eq. 3.2 and 3.3):

$$R_{TS} = \frac{R_P}{\sqrt{r^2 + (r^2 - 1)(R_P C_P \omega)^2} - 1} \tag{3.2}$$

$$r = \frac{T_{AC\text{-}o}}{T_{AC}} \tag{3.3}$$

Here, $T_{AC\text{-}o}$ is the AC response of the probe to $\dot{q}_{AC}$ when the STP is positioned away (~2 μm) from the sample surface. Given that the STP is sufficiently far away from the sample, the effects of near-field heat transfer are negligible[48,127] and $T_{AC\text{-}o}$ is determined primarily by R_p. Finally, we note that $\dot{q}_{DC}$, which has contributions from both Joule heating and optical power input from the AFM laser, can be quantified by measuring the DC temperature rise when the probe is located far away from the sample. Further, small variations in the contributions of the laser power to $\dot{q}_{DC}$ arising from drift in the laser power output are systematically accounted for by monitoring the power output of the laser (see Appendix Section 4.5.5. Lumped-capacitance thermal model of scanning thermal probe).

4.2.2. Characterization of temperature sensing resolution and stability of CR-SThM

In order to illustrate our SThM approach we employed a microfabricated sample with a Pt line (Figure 4.3a). The 250 nm wide, 50 nm thick, and 18 μm long Pt line was deposited on a 600 nm thick SiO_2 layer, which was grown on a Si substrate[33]. We first placed the STP on the 250 nm-wide Pt line at a position marked as *location A* in Figure 4.3a. Next, we heated this Pt line by supplying a DC current (I_{sample}) whose magnitude was increased as a function of time in a stepwise fashion (with each step lasting Δt = 10 s), resulting in a corresponding stepwise increase in the heat input (see inset of Figure 4.3b). This process was repeated for two other durations (Δt = 20s and 80s). The resulting temperature rise of the STP, ΔT_{DC}, which represents the time-averaged

increase of T_{DC} at each sample heating power compared to the baseline T_{DC} value at zero sample heating power, is shown in Figure 4.3b as a function of I^2_{sample} which is proportional to supplied heating power. Subsequently, the temperature of the STP was converted to T_S using Eq. 3.1 and the R_{TS} values extracted from Eq. 3.2, which allowed for quantification of sample temperature rise as a function of I^2_{sample} (see Figure 4.3c). In addition, the average value of R_{TS} corresponding to each T_S data point is plotted on the right vertical axis of Figure 4.3c. As can be seen, the value of R_{TS} has small fluctuations (~10%) during this particular experiment since the probe is stationary. The dashed line in Figure 4.3c shows the sample temperature rise as measured independently by using the Pt line as a thermometer (see Appendix Section 4.5.4. Self-heated Pt line sample temperature rise measurement), which is in good agreement with the STP measurements. The noise floor for sensing T_S in Figure 4.3c is 41 mK, 55 mK, 37 mK, 26 mK for the 10s, 20s, 40s, and 80s heating durations, respectively.

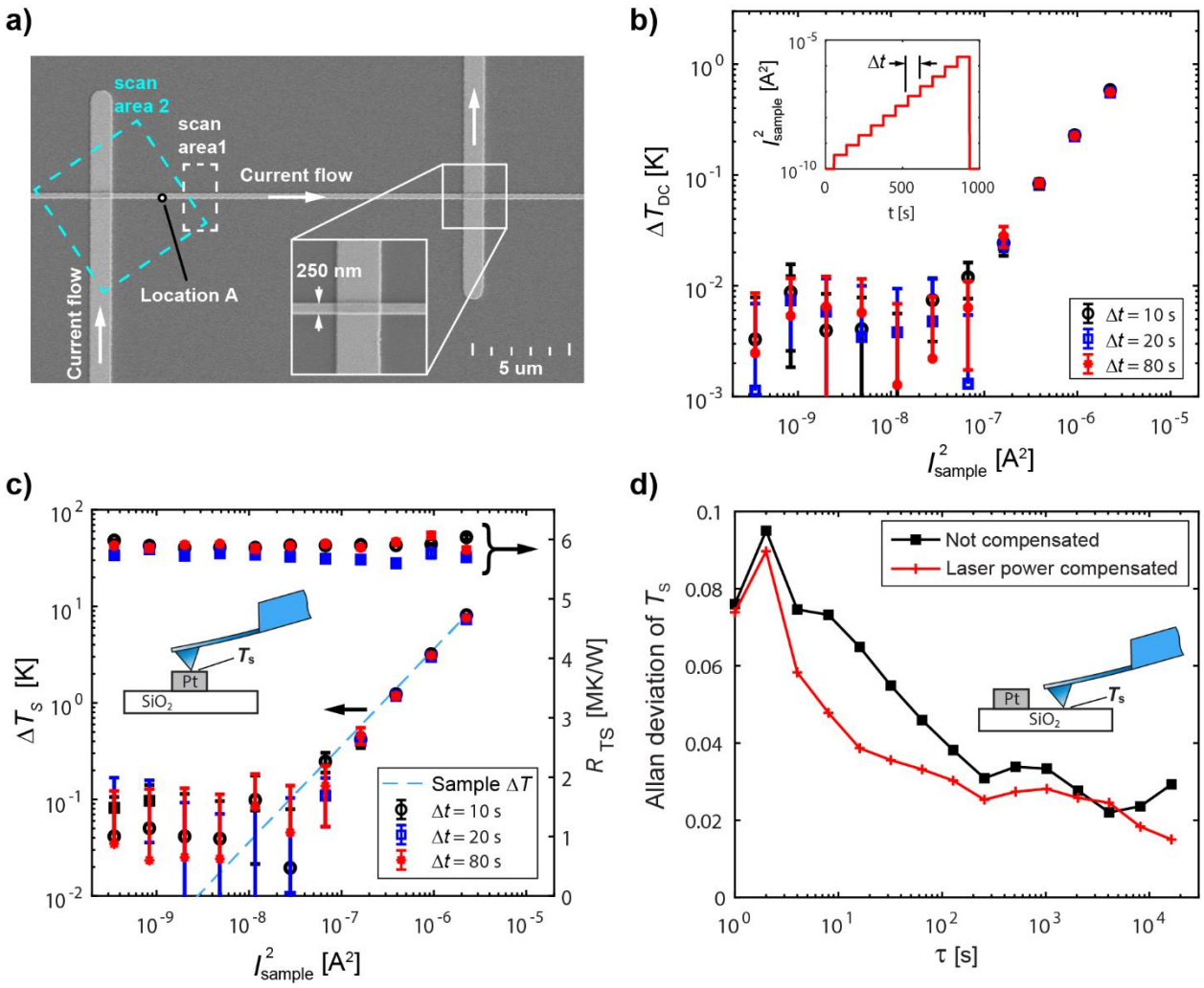


Figure 4.3 (a) SEM micrograph of the Pt line sample employed in this work. The Pt line is 250 nm wide and 50 nm thick. The white arrows show the path of the unmodulated electrical current (I_{sample}) employed to heat the Pt line via Joule heating, and the dashed square marks the region where thermal scanning was performed for the data shown in Figure 7. (b) Measured DC temperature rise of the probe when the probe is placed in contact with the Pt line at location A shown in panel (a) as a function of square of heating current sourced to the Pt line sample. Inset shows stepwise increase of square of heating current sourced to the sample during this experiment. (c) The data points on left vertical axis represent the rise in sample (Pt-line) temperature estimated using Eq. 3.1. To obtain the sample temperature, the value of R_{TS} was extracted using Eq. 3.2 and plotted in this panel on the right vertical axis. The dashed line represents the Pt temperature rise as estimated from independent measurements of temperature rise vs heating current described in Appendix Section 4.5.4. Self-heated Pt line sample temperature rise measurement. (d) Allan deviation plot illustrating the stability of the sensed sample temperature (T_S) with and without compensation for laser power fluctuations. It is clear from this data that accounting for fluctuations in laser power output improves the measurement stability at all time scales.

To characterize the intrinsic noise and drift in temperature sensing via CR-SThM, we stabilized the temperature of the sample shown in Figure 4.3 to 26 ± 0.0001 °C (as shown in Appendix Section 4.5.3. Sample temperature stabilization) and placed the STP on the SiO_2 region

of the sample. The experiment was performed over a duration of 12 hours. Since the sample temperature is stabilized, any fluctuation and drift in T_S (sample temperature measured using STP) that is greater than 0.1 mK is due to drift/noise in the temperature measured by the CR-SThM scheme presented here. Figure 4.3d shows the Allan deviation of the T_S measured by the STP. A plot of the Allan deviation quantifies the fluctuations of a time-series T_S over a range of time scales and contains information about short-term noise and long-term drift in the measurement[16]. The red and black curves demonstrate the measurement stability of T_S with and without the effect of fluctuations in deposited laser power (i.e. variations in $\dot{q}_{DC}$), respectively. To obtain the red curve, the variations of $\dot{q}_{DC}$ due to laser power fluctuations were measured and included in Eq. 3.1 for calculation of T_S (see Appendix Section 4.5.5. Lumped-capacitance thermal model of scanning thermal probe for details of this calculation). As can be seen, compensation for laser power fluctuations improves the measurement stability at all timescales, specifically in the 5-100s range. In addition, as shown in Appendix Section 4.5.6. Temperature measurement stability and noise, compensation for T_R drift improves the stability at timescales >500 s and results in a stability better than 10 mK for timescales >2 h. The amplitude spectrum of the measured T_S signal (see Appendix Section 4.5.6. Temperature measurement stability and noise) shows similar trends and confirms the above conclusion regarding the thermal noise and stability of the STP.

4.2.3. Thermal imaging of steady temperature fields

In order to illustrate the ability of mapping unmodulated temperature fields of a sample with topographical features we scanned across a heated line sample to measure the topology as well as T_{DC}, T_{AC} using the PRT integrated into the STP. Subsequently, we applied Eq. 3.1-3.3 to obtain the sample temperature at each pixel. Specifically, we scanned our samples using contact mode AFM at a constant contact normal force of 125 ± 25 nN, stopped at each pixel location for ~500

ms and collected data for T_{DC}, T_{AC}, T_R, as well as the instantaneous laser intensity (I), before moving to the next pixel. In these measurements we stabilized the bulk sample temperature to 26 °C by employing feedback control (see Appendix Section 4.5.3. Sample temperature stabilization). Next, we passed a DC current of a chosen magnitude through the Pt line, which resulted in a spatially varying temperature field $T(x, y)$ around the Pt line.

We began our thermal scans by first studying an area of the sample with unheated Pt line (i.e., a line to which no electrical current is supplied). Specifically, we scanned a 3 μm × 1.5 μm section (scan area 1 shown in Figure 4.3a, 90 degrees rotated) and measured the topography, T_{AC}, T_{DC} and T_R, which are shown in Figure 4.4a, b, c, and e, respectively. The raster scans were done in the horizontal direction (i.e. perpendicular to the Pt line) and the image size for Figure 4.4 and Figure 4.5 was 512 (horizontal) × 64 (vertical) pixels, and the scanning rate was ~12 nm/s. Although the entire sample is in thermal equilibrium and nominally at a constant, spatially-independent temperature, the temperature map (T_{DC}, Figure 4.4b) as recorded by the STP probe shows systematic artifacts from the expected uniform distribution that are as large as 0.5 K to 1 K and are aligned with the scan direction and the location of the heater line. Given the average thermal contact and the probe thermal resistances, one would expect that T_{DC} maps as shown in Figure 4.4b can only arise from local variations in sample temperature as large as 10 K, which is clearly not possible. Further, the T_{AC} data shown in Figure 4.4c also show features that are very similar to those seen in T_{DC} maps. Next, by using Eq. 3.2 along with the measured data, we obtain a spatial map of R_{TS} which is shown in Figure 4.4d. The data feature local minima at the edges of the Pt line where a two-point contact is presumably made, i.e. a contact that occurs both between the apex of the tip and the sample as well as a second contact between the edge of the Pt line and the side of the tip (see Figure 4.2b). Further, one can observe horizontal line-by-line variations in

R_{TS}, which are likely due to tip abrasion or tip modification by particle attachment (Figure 4.4d). In addition, we shown in Figure 4.4e the probe reservoir temperature (T_R) which drifts by ~20 mK over the ~9.1 hour duration of the thermal scan. Finally, using the measured R_{TS} and T_R maps, we construct the sample temperature T_S using Eq. 3.1 in a pixel-by-pixel fashion (see Figure 4.4f). As can be seen, the measured T_S is largely featureless. Measurements artifacts as revealed in the T_{DC} maps, including scan lines and the heater topology, are basically eliminated. Consequently, the recorded deviations in the T_S map (Figure 4.4f) from the nominal sample temperature of 26 $^{\circ}$C arise mainly from pixel-to-pixel variations and exhibit comparatively small temperature noise with a standard deviation of 174 mK. In Appendix Section 4.5.9. Histogram analysis of scanning thermal scans we present the corresponding histogram of the distribution of temperature from all pixels which confirms that the remaining variation in the T_S image (Figure 4.4f) is normally distributed measurement noise and generally devoid of the above discussed artifacts.

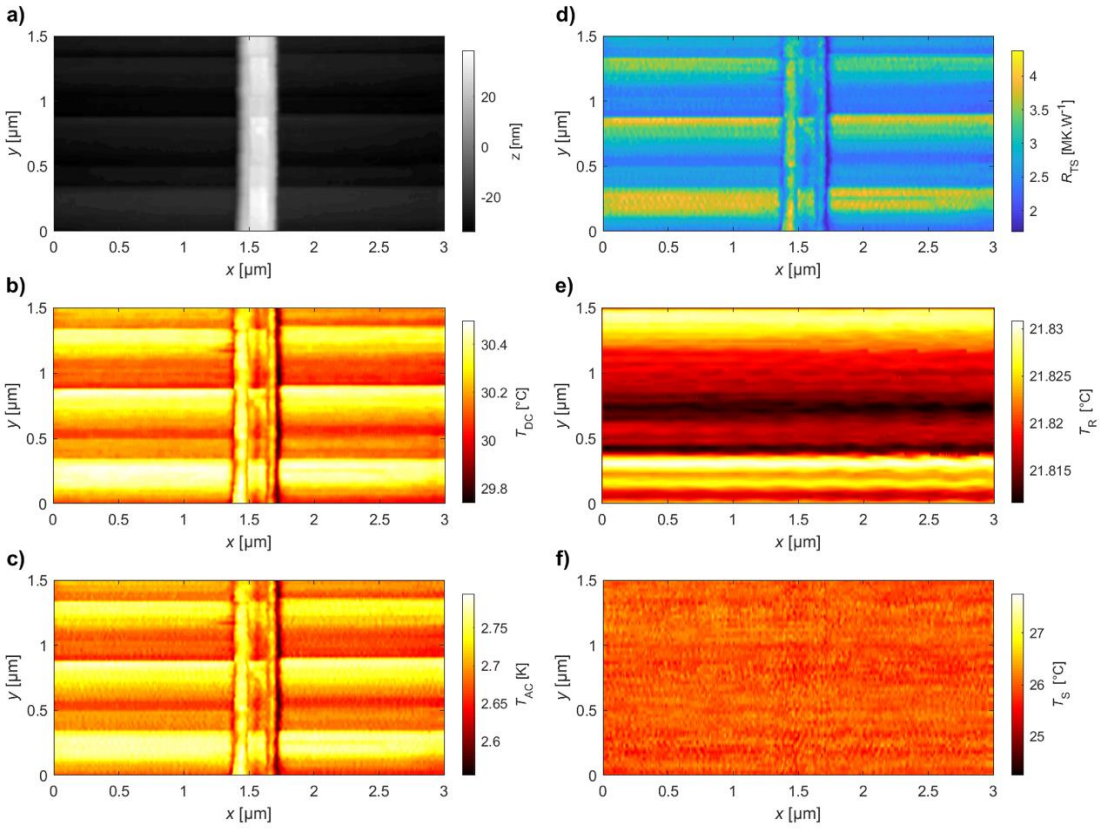


Figure 4.4 Data obtained from thermal scan of a Pt line sample at zero heating current. Data shown in all panels was obtained simultaneously in a single scan. (a) Topography map showing the 250 nm-wide Pt line on a SiO_2 substrate, (b) DC temperature (T_{DC}) measured by the probe's platinum resistance thermometer (PRT), (c) amplitude of AC temperature oscillations (T_{AC}) of the probe measured by probe's PRT. (d) Estimated tip-sample thermal resistance R_{TS} obtained from Eq. 3.2, (e) thermal reservoir temperature (T_R) measured using an integrated PRT on the probe thermal reservoir, (f) extracted surface temperature map (T_S) using Eq. 3.1, with a pixel-to-pixel standard deviation of 174 mK. Refer to Appendix Section 4.5.9. Histogram analysis of scanning thermal scans for the histogram distribution of the pixel values.

Next, we repeated the same measurements with a heated wire by supplying an electrical current of 0.5 mA to the Pt line (see Figure 4.5). As can be seen in Figure 4.5b, which presents the measured T_{DC}, the Pt line is at an elevated temperature; however, there are significant artifacts in the image that represent unphysical features (as explained earlier). In order to reduce these artifacts that are caused by variation of R_{TS} during scanning, we followed the same procedure outlined for the unheated Pt line (Figure 4.4) and obtained the data necessary to compensate for variation of R_{TS} during scanning. Using these data we generated a map of R_{TS} (Figure 4.5d) and used it in conjunction with the measured T_R (Figure 4.5e) to obtain the surface temperature shown in Figure

4.5e. The constructed surface temperature map (Figure 4.5f) demonstrates significantly enhanced image quality with dramatically reduced artifacts. For a statistical analysis of the pixel-by-pixel temperature data, we used the pixels inside the dashed box (see Figure 4.5f) that is located in a region where the gradient in the ample temperature caused by heating is small. The standard deviation of pixel values in this region is 221 mK, which is slightly higher than the value for the image shown in Figure 4.4f due to the small background temperature gradient. See Appendix Section 4.5.9. Histogram analysis of scanning thermal scans for the histogram of the distribution of pixel values in the dashed box of Figure 4.5f.

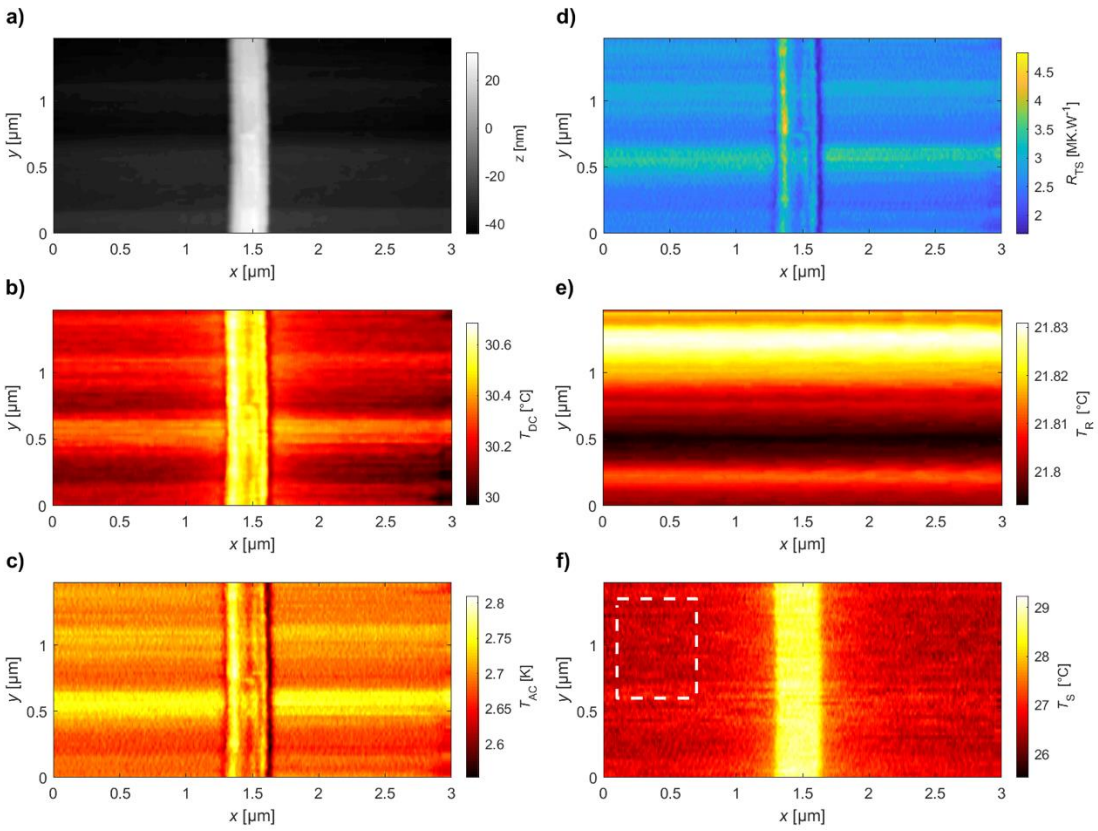


Figure 4.5 Data obtained from thermal scan of a Pt line sample at a heating current of I_{sample} = 0.5 mA. Data shown in all panels was obtained simultaneously in a single scan. (a) Topography map showing the 250 nm-wide Pt line on SiO_2 substrate, (b) DC temperature (T_{DC}) measured by the probe platinum resistance thermometer (PRT), (c) amplitude of AC temperature oscillations (T_{AC}) of the probe measured by probe's PRT (d) estimated tip-sample thermal resistance R_{TS} obtained from Eq. 3.2, (e) thermal reservoir temperature (T_R) measured using an integrated PRT on the probe thermal reservoir, (f) extracted surface temperature map (T_S) using Eq. 3.1. The pixels in the dashed box have a standard deviation of 221 mK. Refer to Appendix Section 4.5.9. Histogram analysis of scanning thermal scans, for the histogram distribution of the pixel values.

In order to confirm that the measured temperature fields are in quantitative agreement with modeling results, we averaged the measured temperature maps in Figure 4.5 along the *y* direction and plot them in Figure 4.6a - d. As can be seen in Figure 4.6b, the T_{AC} profile captures key features of the T_{DC} profile that are related to local change in R_{TS} (shown in Figure 4.6c). By accounting for these features through the thermal model (Eq. 3.1) an almost artifact-free profile of surface temperature can be obtained as shown in Figure 4.6d. We have plotted the surface temperature profiles for three sample currents of 0, 0.5 mA, and 0.707 mA, which are shown in Figure 4.6e. The shaded error bars represent the standard deviation of the measured temperature. The dashed profiles represent the modeled temperature from a continuum heat transfer model, which includes the interface thermal resistance between the Pt line and the SiO_2 substrate (see Appendix Section 4.5.8. Heat transfer model for estimation of temperature profile), thus generating a discontinuous temperature profile at the edge of the Pt line. The measured T_S profiles are in good agreement with the model. The root mean square error of the model with respect to the experimental profiles are 32 mK, 118 mK, and 224 mK for the 0 mA, 0.5 mA, and 0.707 mA cases, respectively. Further, the coefficient of determination (R^2) value of the model is 0.962 and 0.963 for the 0.5 mA and the 0.707 mA cases, respectively. We note that, the experimental profile of 0.707 mA case demonstrates a maximum slope of $(\partial T/\partial x)$ of ~31 mK/nm near the edges of the Pt line.

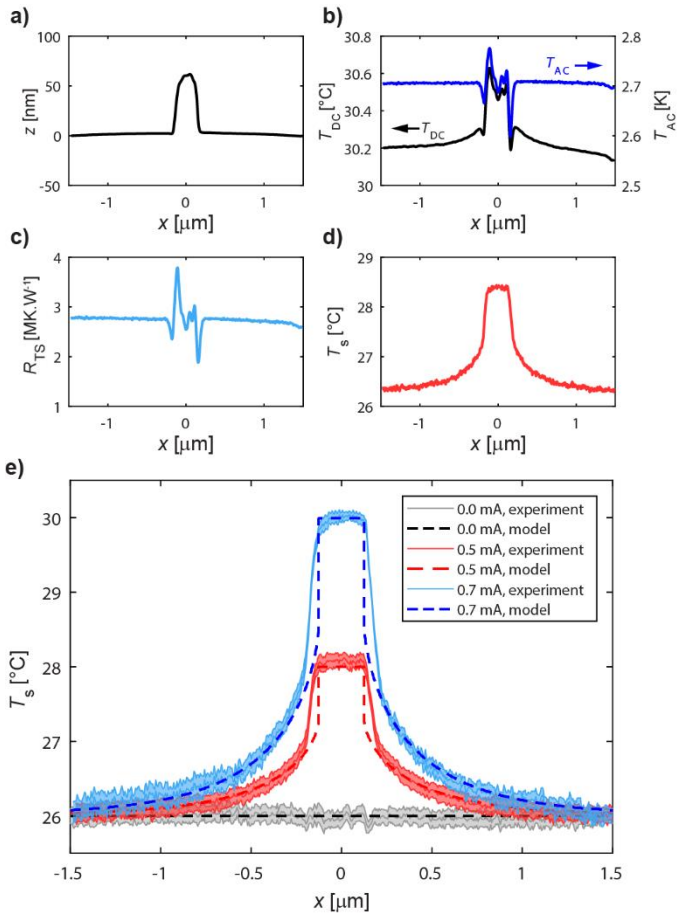


Figure 4.6 Averaged profiles obtained during thermal scanning of a Pt line such as the scans shown in Figure 4.4-5. To obtain the averaged profiles the image was averaged in y-direction (i.e. the line scans were averaged). (a) Topography profile showing the 250 nm-wide Pt line. (b) DC and AC temperatures measured by the probe's PRT. (c) Estimated tip-sample thermal resistance R_{TS} obtained from Eq. 3.2. (d) Extracted sample surface temperature profile when a DC electrical current of 0.5 mA was supplied to the Pt line sample. (e) Averaged sample surface temperature profiles for three sample heating currents of 0 mA, 0.5 mA, and 0.707 mA. Shaded error bars represent the standard deviation of the measured data.

We estimated the spatial resolution of our probes and the measurement technique as explained below. First, by combining the maximum experimentally observed temperature gradient ($\partial T/\partial x$) and the temperature sensing resolution (ΔT) we estimate the spatial resolution (Δx) using $\Delta x = \Delta T / (\partial T/\partial x)$, which results in a resolution of Δx = 50 [mK] / 31 [mK/nm] = 1.6 nm (see Appendix Section 4.5.7. Estimation of spatial resolution of scanning thermal microscopy for details). We note that, a temperature resolution of ~50 mK was obtained in stationary probe condition (from Figure 4.3c) and is valid for slow scanning rate condition (such as 1 nm/s scan

rate shown in Appendix Section 4.5.7. Estimation of spatial resolution of scanning thermal microscopy). However, for faster scan rates (12 nm/s in Figure 4.4 and Figure 4.5) the pixel-to-pixel variation is larger with a standard deviation of ~200 mK. Thus, for typical imaging conditions under faster scan rates we obtain a spatial resolution of 6.5 nm. Finally, we estimate the contact diameter of the tip and sample to be ~6 nm (see Appendix Section 4.5.7. Estimation of spatial resolution of scanning thermal microscopy). Considering all these factors, a conservative estimate of the spatial resolution of our technique is 7 nm.

To evaluate the capabilities of our thermal mapping approach in a thermally and topographically complex environment we imaged the steady-state temperature field at the junction of a 250 nm-wide and 1 μm-wide Pt lines (scan area shown dashed box in Figure 4.3a). The scan (see Figure 4.7) was performed with a sample heating current of I_{sample} = 0.707 mA, the scan direction was horizontal at a rate of ~22 nm/s and the image size was 512 (horizontal) × 128 (vertical) pixels. The electrical current direction is indicated in the topography scan of Figure 4.7a, highlighting that only the portion of the 250 nm-wide line carrying electrical current is expected to demonstrate significant heating due to a large current density. The T_{DC} map (Figure 4.7b) shows a temperature increase of this portion of the Pt line, but also includes significant topography-related (at the edges of the line) and line-by-line tip abrasion/modification artifacts. Similar to previous examples, by applying the thermal model, these artifacts are mostly removed from both heated and unheated parts of the scan, generating the surface temperature map of Figure 4.7f. This map reveals how portions of the Pt lines are heated in response to current flow and how the deposited heat spreads from the lines to the substrate. For example, the temperature of the narrow Pt line on SiO_2 substrate decays with a different characteristic length scale (~ 120 nm, corresponding to the length over which the temperature rise decays by 63%, see Appendix Section 4.5.11. Temperature profile

and characteristic length scales) as compared to the larger length (~560 nm) along the 1 μm-wide Pt line. The exact profiles of these decays (marked as *profile 1* and *profile 2* in Figure 4.7f for the Pt and SiO_2 substrates, respectively) are shown in Appendix Section 4.5.11. Temperature profile and characteristic length scales and relate to the thermal conductivities of the two substrates. It is also apparent that the upper portion of the 1 μm-wide Pt line is only slightly heated due to the lower current density and larger thermal conductance when compared to the 250 nm line. Lastly, the background noise (dashed box in Figure 4.7f, standard deviation equals 238 mK) is about equally low as compared to the surface temperature maps in Figure 4.4f and Figure 4.5f. The slight increase in noise is due to the higher scan rate and the presence of a small gradient in the background temperature. Moreover, we remark that the surface temperature noise is largely determined by the uncertainty in the measured R_{TS} values and can be minimize by decreasing the magnitude of the term $(T_{DC} - T_R - R_P \dot{q}_{DC})$ in eqn. 1 by adjusting T_R or $\dot{q}_{DC}$ prior to scanning.

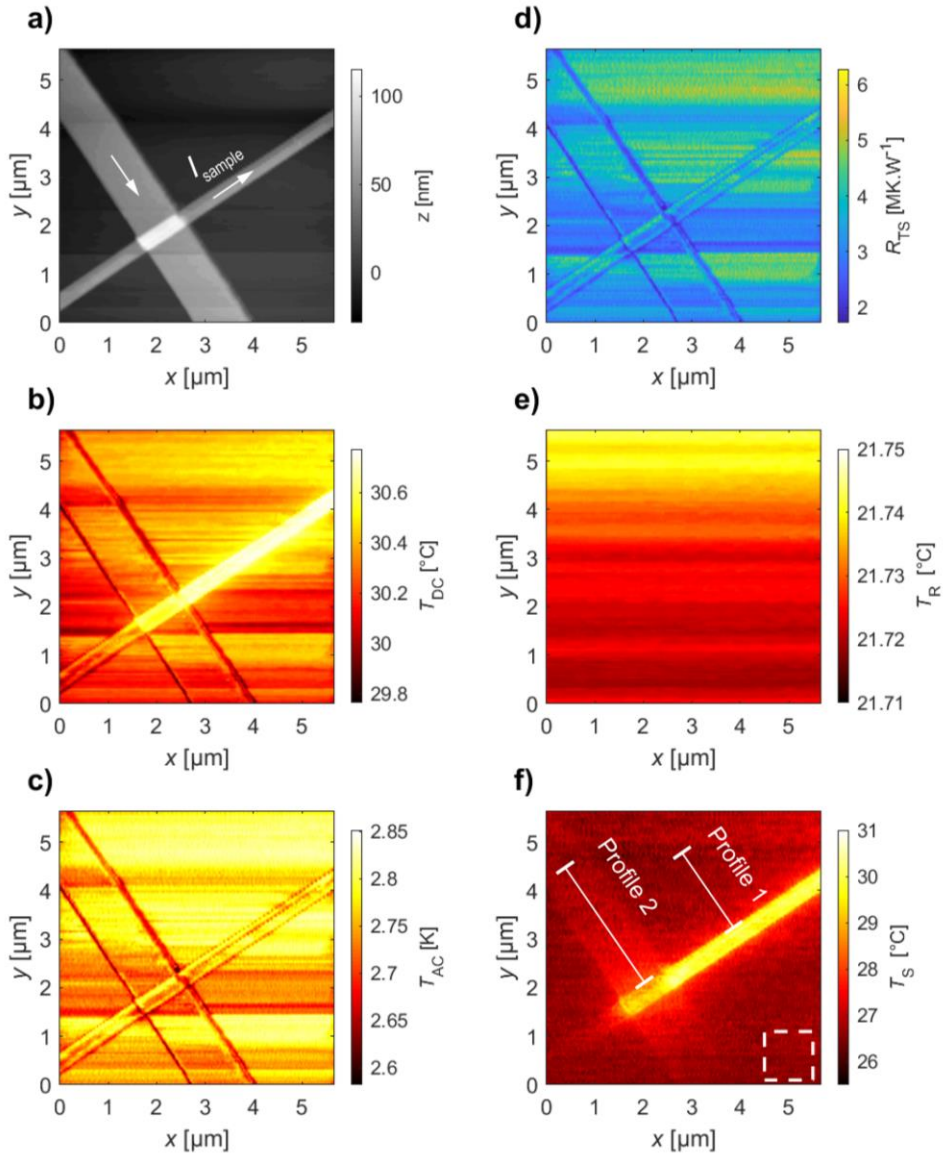


Figure 4.7 Quantitative mapping of temperature fields from a sample consisting of two overlapping 1 µm-wide and 250 nm-wide Pt lines that are heated by a DC current of 0.707 mA. Data shown in all panels were obtained simultaneously in a single scan. (a) Topography map showing the electrical current path by arrows, (b) DC temperature (T_{DC}) measured by the probe's PRT, (c) amplitude of AC temperature oscillations (T_{AC}) of the probe measured by probe's PRT (d) estimated tip-sample thermal resistance R_{TS} obtained from Eq. 3.2, (e) thermal reservoir temperature (T_R) measured using an integrated PRT on the probe thermal reservoir, (f) extracted surface temperature map T_S. The temperature profiles averaged along two lines indicated in the image are shown in Appendix Section 4.5.11. Temperature profile and characteristic length scales. All images were corrected for distortion arising from piezo scanner saturation (see Appendix Section 4.5.10. Scanning image distortion correction). The pixel values in the dashed box have a standard deviation of 238 mK.

4.3. Conclusion

To summarize, we have presented a new technique—Contact-Resistance Resolved Scanning Thermal Microscopy (CR-SThM)—which enables quantitative mapping of unmodulated temperature fields by carefully estimating the effects of variations in the tip-sample thermal resistance. This is accomplished by employing custom-fabricated STPs featuring an integrated platinum heater/thermometer and a sharp tip (radius ~25 nm). We simultaneously measured tip-sample thermal resistance during thermal scans by depositing a modulated heat input into the probe and measuring the DC and AC temperature responses of the probe. Further, the probe features a suspended thermal reservoir with temperature sensing capability, which enables compensation for ambient temperature drift and improves long-term measurement stability. We established the spatial and temperature resolution of this technique by measuring the steady-state temperature field around a 250 nm-wide Joule-heated Pt line. This technique demonstrated a temperature sensing resolution of ~50 mK and a spatial resolution of ~7 nm. We expect that the advances presented here will enable studies that aim to directly probe several nanoscale thermal phenomena that arise in active electronic, photonic and energy conversion devices that are of great current interest.

4.4. Methods

4.4.1. Experimental setup

The experiments were conducted in an ultra-high vacuum atomic force microscope (UHV 750, Beetle STM/AFM, RHK Technology) placed in an ultra-low noise chamber. The chamber temperature was controlled so that the drift over a 24 hour period was <0.1 K. All the measurement electronics and instruments were located in this chamber during the measurement to prevent thermal drift. A laser (895 nm wavelength) was used for AFM readout. This relatively long wavelength was used to minimize the absorption of laser light by the gold reflector of the probe

(hence minimizing the temperature rise of the probe) while maximizing the responsivity of the AFM photodetector.

4.4.2. Temperature readout circuits

Overall, the temperature signals from three different resistive temperatures sensors were recorded during the measurements. All these sensors were read out using balanced Wheatstone bridges driven by either AC-voltage or AC-current and subsequent measurement of amplitude of bridge output voltage oscillations at driving frequency using a lock-in amplified as described in Ref. [6,128]. The frequency of bridge excitation was chosen to be different for all three measurements to avoid cross talk during measurements. The bulk sample temperature was measured using a 10 kOhm glass encapsulated thermistor, and readout using a Wheatstone bridge driven by a voltage sine wave with peak amplitude of 200 mV at frequency 320 Hz. The probe thermal reservoir temperature was measured using a 17 kOhm platinum resistance thermometer (PRT), and read out using a Wheatstone bridge (R_1 = R_3 = 40 kOhm shown in Figure 4.1c) driven by a voltage sine wave with peak amplitude of 200 mV at frequency 388 Hz. The probe tip temperature is measured as explained below.

4.4.3. Scanning thermal probe heating and temperature sensing

A 9 kOhm platinum resistance thermometer (PRT) was integrated close to the probe tip which acts as a heater and thermometer. This PRT was connected to a Wheatstone bridge (R'_1 = R'_3 = 20 kOhm shown in Figure 4.1d) driven by a current waveform which was a superposition of two sinusoidal waves: $I_{probe} = I_1 \sin(2\pi f_1 t) + I_2 \sin(2\pi f_2 t)$. The first sine wave had a low frequency (f_1 = 4 Hz) and high amplitude (I_1 = 56 μA) which was used for modulated joule heating of the probe at frequency $2f_1$ = 8 Hz and amplitude T_{AC}. The amplitude of probe temperature modulation (T_{AC}) was measured by lock-in technique using the $3f_1$ = 12 Hz component of the Wheatstone bridge

output voltage[24]. To read the unmodulated temperature of the probe (T_{DC}) the second AC component was used which had high frequency (f_2 = 212 Hz) and low amplitude (I_2 = 14 μA) by locking-in on the f_2 component of bridge output. Please refer to Appendix for probe fabrication steps and thermal/mechanical properties of the probe.

4.5. Appendix

4.5.1. Scanning thermal probe fabrication

The fabrication steps of the scanning thermal probes (STPs) employed in this study are illustrated in Figure 4.8. Briefly, a T-beam was first defined on a bare Si wafer by deep reactive ion etching (DRIE) of Si. This was followed by wet oxidation of Si and low-pressure chemical vapor deposition (LPCVD) of 600 nm silicon nitride on the etched Si substrate which formed the T-beam. The purpose of the T-beams was to improve the stiffness of the probe cantilever which enabled a stable thermal contact with the sample during thermal scanning[33], while simultaneously minimizing the thermal conductance of the probe. Next, the back side of the wafer was patterned by reactive ion etching (RIE). Subsequently, we deposited a 3 μm thick low temperature oxide (LTO) with Cr caps defined on the front side to prepare for formation of conical tips in the next step. Then, the LTO was etched by buffered HF (BHF), leaving a probe tip with a height of ~3 μm under the region where the Cr cap was previously located. Afterwards, the tip was coated by a 150 nm Cr layer. Next, we deposited and patterned a 50 nm thick serpentine Pt line to form a Pt heater-thermometer for resistive heating and thermometry on the probe. Later, we deposited and patterned the Au reflector and electrodes. Next, the front side of the wafer was covered by a 50 nm thick plasma-enhanced chemical vapor deposition (PECVD) nitride layer to protect it by reducing the etching rate during the final etch step. Finally, the probe was released and a suspended thermal reservoir was formed on the probe body by KOH etching of Si (step 9 of Figure 4.8).

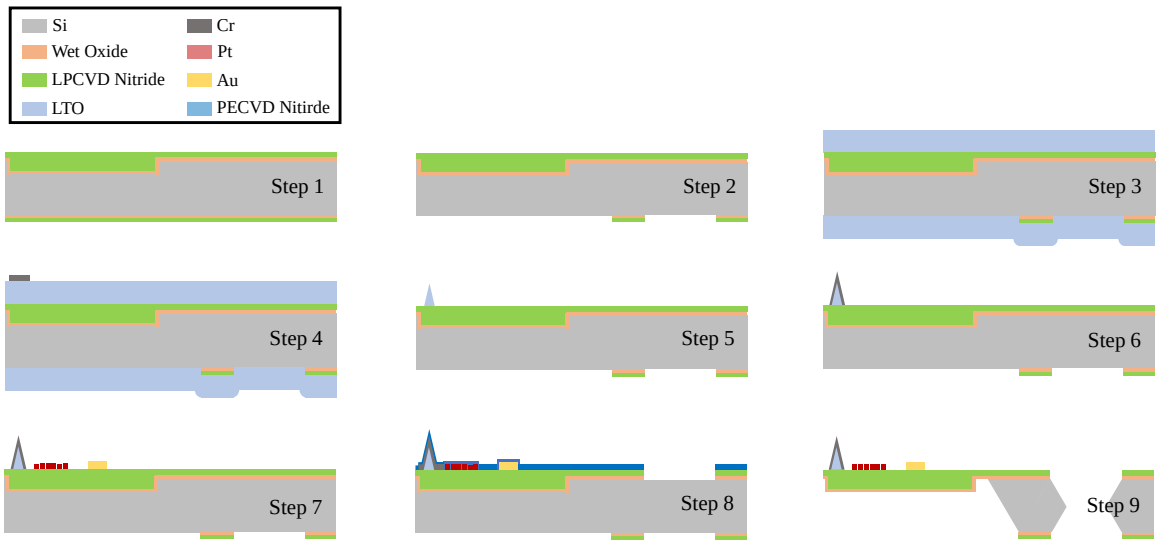


Figure 4.8 Process steps for fabrication STPs with integrated platinum resistive heater/thermometer and thermal reservoir temperature sensing capability

4.5.2. Mechanical stiffness and thermal conductance of scanning thermal probe

The mechanical stiffness of the scanning thermal probe was estimated by performing finite element simulations in COMSOL™. The probe geometry including various layers of Au, Pt and Cr were incorporated into the model. The probe is 215 µm long and is formed from 600 nm thick SiN_x films with thin films of Pt (50 nm), Au (100 nm) and Cr (150 nm) patterned on it. In order to estimate the mechanical stiffness we imposed a fixed boundary condition at the base of the probe and a force of F = 1 µN was applied to the probe tip resulting in a deflection of δ = 0.13 µm. From these data (see Figure 4.9a) we estimate the probe stiffness to be ~7.69 N/m.

The thermal resistance of the probe was also studied using the aforementioned model by considering a thermal conductivity of 5.0 W/m·K for SiN_x thin films[46]. A constant temperature (20 °C) boundary condition was chosen for the probe base, while a heat flux was applied to the probe tip which generated a temperature gradient along the probe body. The temperature rise of the tip

was monitored under various input heat fluxes and the thermal resistance of the probe was extracted as the slope of linear fit to the data shown in Figure 4.9b to be $R_P = 0.46\times10^6$ K/W around 20 °C which is in good agreement with the experimental measurements shown in Figure 4.2b.

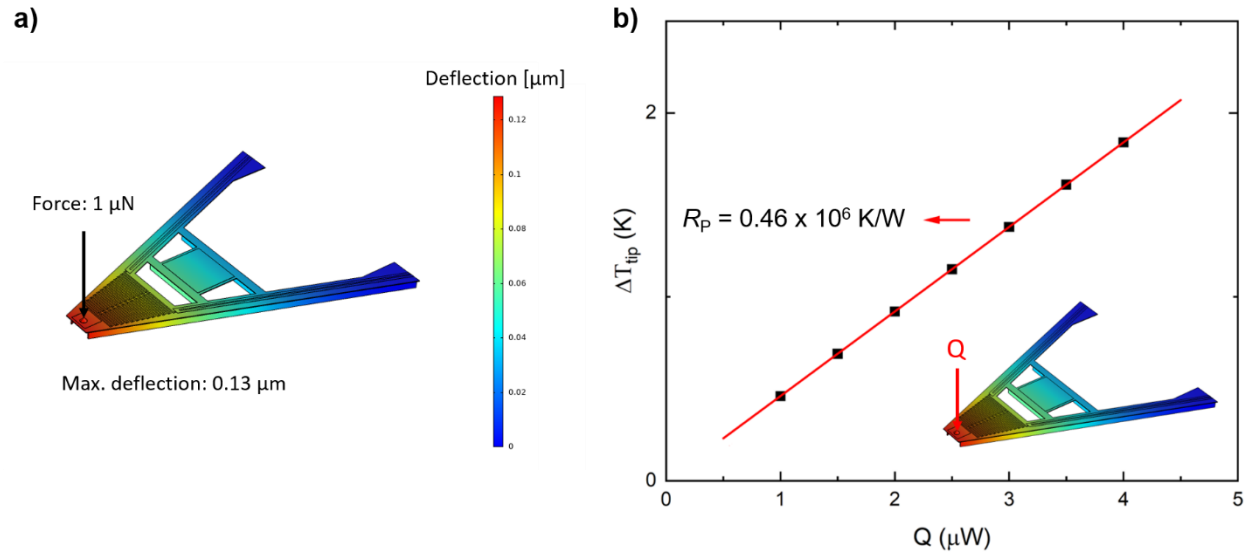


Figure 4.9 (a) Finite element simulation of STP deflection under an applied load. (b) Temperature rise of the probe as a function of heat input to the tip. The slope of the linear fit shows the probe thermal resistance R_P.

4.5.3. Sample temperature stabilization

The sample temperature was measured by mounting a glass encapsulated thermistor (TDK Electronics B57550G1103F000) on the surface of the sample chip, ~3 mm away from the center of the sample (where the Pt line was located), using silver paste to make a strong thermal contact. The temperature of the sample was measured using a Wheatstone bridge driven by a sine wave with a peak amplitude of 200 mV at a frequency of 320 Hz and a lock-in technique. The temperature was controlled using a PID controller, with gains tuned using the Ziegler-Nichols method[79], at a bandwidth of 4 Hz to a stability level of ~100 µK as shown in the time-series measurement of Figure 4.10. To heat the sample to 26 °C, a filament heater integrated into the sample holder of the atomic force microscope (UHV 750, Beetle STM/AFM, RHK Technology) was employed which radiatively heated the sample from back side.

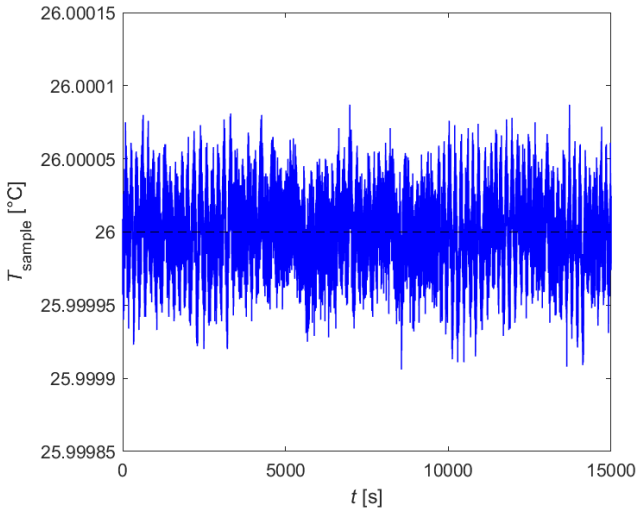


Figure 4.10 The measured bulk temperature of the feedback-stabilized sample as a function of time.

4.5.4. Self-heated Pt line sample temperature rise measurement

In order to verify that our SThM measurements accurately quantify the sample temperature, we need an independent measure of temperature rise of the heated Pt line sample when an electrical current is supplied to the Pt line. To this end, we used the temperature dependent resistance of the Pt line to independently measure its average temperature rise. In this measurement, the sample was placed in a half Wheatstone bridge circuit (see Ref.[24] for details) and an AC current at a frequency of f = 2 Hz at various amplitudes was sourced through the Pt line. Subsequently, the corresponding temperature modulations of the sample were measured using a 3ω method via the relation[33] $\Delta T(2f) = 2\,(\mathrm{d}T/\mathrm{d}R)\,V_{3f}/I_0 = 2\,V_{3f}/(\alpha\,R\,I_0)$. In this relation V_{3f} is the voltage output of the aforementioned circuit at a frequency $3f$, I_0 is the amplitude of sinusoidal heating current, α and R are the temperature coefficient of resistance and the resistance of the Pt line (measured using the 4-probe method) respectively. Figure 4.11 shows the results of this measurement which is the average temperature modulation amplitude of the heated Pt line as a function of the square of heating current amplitude (I_0^2) sourced to the Pt line.

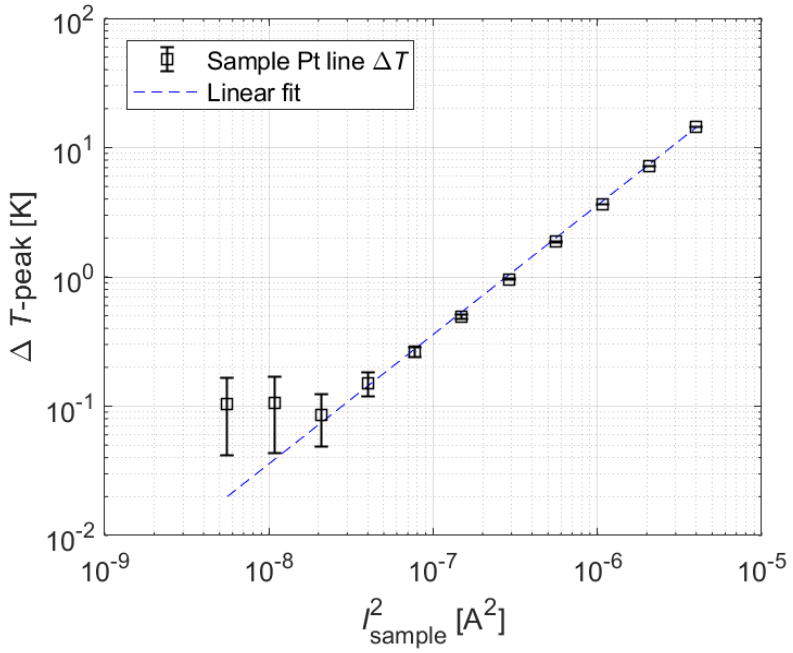


Figure 4.11 Temperature rise of the heated Pt line (250 nm wide, 50 nm thick, 18 µm long) as a function of square of heating current amplitude.

4.5.5. Lumped-capacitance thermal model of scanning thermal probe

Based on the equivalent thermal circuit of Figure 4.2a one can relate the probe temperature as sensed by the platinum resistance thermometer (PRT) close to the tip (T_P) to the input heat flux ($\dot{q}_P(t)$) and the surface temperature (T_S) via:[61].

$$\dot{q}_P(t) = \frac{T_P(t) - T_R}{R_P} + \frac{T_P(t) - T_S}{R_{TS}} + C_P \frac{dT_P(t)}{dt} \tag{3.4}$$

Here, R_P and R_{TS} are the probe-to-reservoir and probe tip-to-sample thermal resistances respectively, C_P is the lumped probe thermal capacitance, and $\dot{q}_P$ is the heat flow deposited on the probe either by the integrated probe heater or the AFM laser. Note that, given the proximity of the PRT to the probe tip, here we approximate the probe tip temperature by the temperature sensed by PRT (T_P). However, this approximation does not limit our analysis as one can sum the constant

value of PRT-tip thermal resistance with tip-sample thermal resistance (which varies during the scan) to form a lumped value of R_{TS}. In general, the value of PRT-sample thermal resistance can be ignored in this analysis, as it does not have any variations.

For convenience, we define R_{tot} as the total thermal resistance of the probe to the environment (i.e. thermal reservoir and sample):

$$\frac{1}{R_{tot}} = \frac{1}{R_P} + \frac{1}{R_{TS}} \tag{3.5}$$

In our experiments, we source an AC current at frequency f_1 to the integrated probe heater which generates an AC heat flux via Joule heating at angular frequency $\omega = 4\pi f_1$. Therefore, the total probe heat flux ($\dot{q}_P(t)$) has a DC and AC component as shown below:

$$\dot{q}_P(t) = \dot{q}_{DC} + \dot{q}_{AC}\cos(\omega t) \tag{3.6}$$

Based on Eq. 3.4, this heat input generates a DC and AC temperature change at the probe tip as shown in Eq. 3.7, where φ is the phase shift of temperature response with respect to the heat input.

$$T_P(t) = T_{DC} + T_{AC}\cos(\omega t + \varphi) \tag{3.7}$$

Now consider a calibration experiment, where the probe is retracted from the surface so that there is no thermal contact and $R_{TS} \rightarrow \infty$ (i.e. $R_{TS} >> R_C$). We label the DC and AC probe temperatures in out-of-contact (or open) condition as $T_{DC\text{-}o}$ and $T_{AC\text{-}o}$. Assuming small variation of probe temperature in out of contact condition compared to in contact condition, $|T_{DC\text{-}o} - T_{DC}| < 5K$, the variation in probe heater resistance would be <1% and can safely be ignored. In addition, under the assumption of small probe temperature variations one can assume temperature independent

probe thermal properties (R_P and C_P). Substituting Eq. 3.6 and Eq. 3.7 in Eq. 3.4, we obtain for the in contact case the following:

$$T_{DC} = R_{tot}\left(\dot{q}_{DC} + \frac{T_R}{R_P} + \frac{T_S}{R_{TS}}\right) \tag{3.8}$$

$$T_{AC} = \frac{R_{tot}\,\dot{q}_{AC}}{\sqrt{1+(R_{tot}\,C_P\,\omega)^2}} \tag{3.9}$$

$$\varphi = -\tan^{-1}(R_{tot}\,C_P\,\omega) \tag{3.10}$$

Similarly, for the out of contact case we obtain:

$$T_{DC\text{-}o} = T_R + R_P\,\dot{q}_{DC} \tag{3.11}$$

$$T_{AC\text{-}o} = \frac{R_P\,\dot{q}_{AC\text{-}o}}{\sqrt{1+(R_P\,C_P\,\omega)^2}} \tag{3.12}$$

$$\varphi_o = -tan^{-1}(R_P\,C_P\,\omega) \tag{3.13}$$

Using Eq. 3.8 and Eq. 3.11 the surface temperature can be obtained as:

$$T_S = \frac{R_{TS}}{R_P}(T_{DC} - T_{DC\text{-}o}) + T_{DC} \tag{3.14}$$

To use Eq. 14, one can make a single measurement of $T_{DC\text{-}o}$ before the experiment and assume that it remains constant during scanning. However, in general, $T_{DC\text{-}o}$ varies with time as the environment temperature drifts (which is sensed as T_R drift), or as the laser power fluctuates (which is sensed as fluctuations in $\dot{q}_{DC}$). The extent of the aforementioned variations is dependent on the temperature stability of the measurement setup and the intensity stability of the laser source. These

variations can be accounted for using Eq. 3.11, which combined with Eq. 3.14 leads the following relation.

$$T_S = \frac{R_{TS}}{R_P}\left(T_{DC} - T_R - R_P\,\dot{q}_{DC}\right) + T_{DC} \tag{3.15}$$

To obtain T_S using the above equation, the value of R_{TS} is required. To find R_{TS}, we start by calculating the ratio of probe AC temperature in out-of-contact to in-contact (during scanning) condition ($r = T_{AC\text{-}o}/T_{AC}$) as shown below. In addition, for generality we include the temperature dependence of probe thermal resistance (R_P) and lumped thermal capacitance (C_P).

$$r = \frac{T_{AC\text{-}o}}{T_{AC}} = \frac{R_P}{R_{tot}}\sqrt{\frac{1 + R_{tot}^{\,2} C_P^{\,2} \omega^2}{1 + R_P^{\,2} C_P^{\,2} \omega^2}} \tag{3.16}$$

It can be seen that at the limit of fast excitation, $\omega >> \tau_P^{-1} = (R_P\,C_P)^{-1}$, the AC temperature signal becomes invariant of thermal contact resistance; therefore, this technique is only useful at low and intermediate heating frequencies (i.e. when ω is comparable to τ_P^{-1}) as shown below:

For slow excitation: $\tau_P\omega \ll 1$: $\frac{T_{AC\text{-}o}}{T_{AC}} \approx \frac{R_P}{R_{tot}}$,

For fast excitation: $\tau_P\omega \gg 1$: $\frac{T_{AC\text{-}o}}{T_{AC}} \approx 1$.

For intermediate excitation frequencies, the following quadratic equation must be solved to obtain R_{TS}.

$$R_{TS} = \frac{R_P}{\sqrt{r^2 + (r^2 - 1)(R_P C_P \omega)^2} - 1} \tag{3.17}$$

After calculation of R_{TS}, the value of T_S can be obtained using Eq. 3.14 or 3.15, depending on whether the measured values of T_R and $\dot{q}_{DC}$ are available or not, these quantities are required to use Eq. 3.15. The quantity ($\dot{q}_{DC}$) has contributions from heat deposited by the integrated probe heater ($\dot{q}_{DC\text{-}heater}$) and that deposited by the AFM laser on the probe ($\dot{q}_{DC\text{-}laser}$) as shown below:

$$\dot{q}_{DC} = \dot{q}_{DC\text{-}heater} + \dot{q}_{DC\text{-}laser} \tag{3.18}$$

In order to account for variations of $\dot{q}_{DC}$ as a result of fluctuations in laser power, one needs to quantify $\dot{q}_{DC\text{-}laser}$. However, direct measurement of this quantity is nontrivial; therefore, in our measurements, we estimated $\dot{q}_{DC\text{-}laser}$ by measuring the change in temperature of the probe when the laser was turned on compared to when it was turned off using the relation: $\dot{q}_{DC\text{-}laser} = (T_{DC\text{-}laser\ on} - T_{DC\text{-}laser\ off})/R_P$. Subsequently, fluctuations in $\dot{q}_{DC\text{-}laser}$ were estimated by measuring the fluctuations in the total AFM photodetector signal which are proportional to the fluctuations in $\dot{q}_{DC\text{-}laser}$.

4.5.6. Temperature measurement stability and noise

Figure 4.12a shows the Allan deviation of the measured sample surface temperature (T_S) when the probe was parked on a SiO_2 substrate (as explained in Figure 4.3d). The black curves demonstrate the measurement stability of T_S without including the effect of fluctuations of deposited laser power (i.e. variations in $\dot{q}_{DC}$) and reservoir temperature (T_R) drift. The red curve represents the stability after compensating for the effects of fluctuations in laser power, while the blue curve includes the effects of compensating for both laser power fluctuations and T_R drift. As can be seen, the compensation for laser power fluctuations improves the measurement stability at all timescales (specifically at 5-100 s time scales), whereas compensation for T_R drift improves the stability at

timescales >500 s, achieving a stability of <10 mK for timescales of >2 h. Figure 4.12b shows the amplitude spectrum of temperature corresponding to the same measurement. It can be seen that compensation for laser power also improves the measurement noise at all frequencies specifically around 0.01 Hz. Further, inclusion of T_R compensation very slightly improves the low frequency noise.

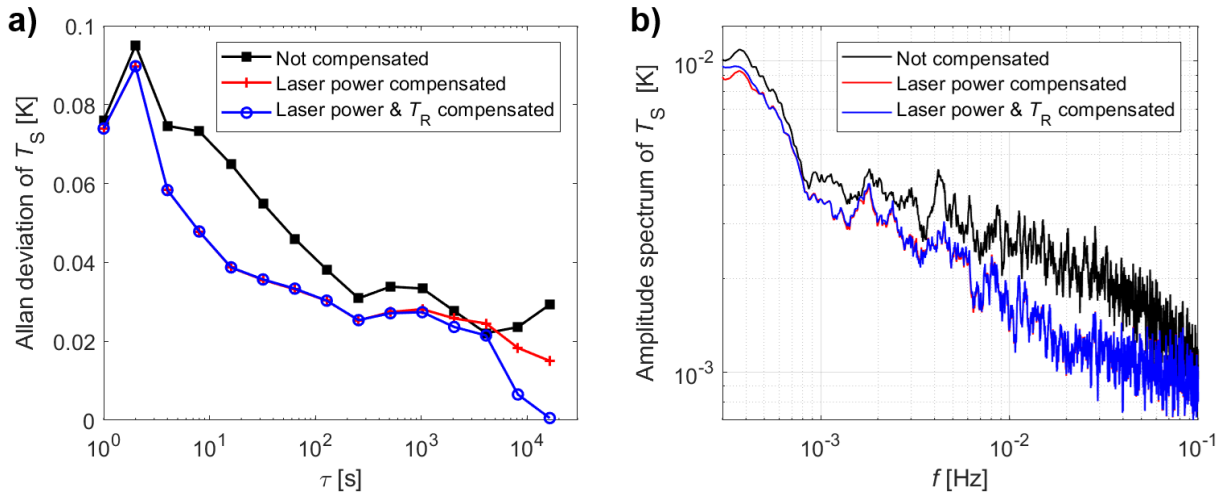


Figure 4.12 (a) Allan deviation plot illustrating the stability of the measured sample temperature (T_S) with and without compensation for laser power fluctuations and reservoir temperature (T_R) drift. (b) Amplitude spectrum of measured sample temperature (T_S) for the three cases mentioned above. It is clear from this data that accounting for drift in laser power output and reservoir temperature increases mid to long-term stability and noise.

The observed modest improvement in the long-term drift is due to the low drift of T_R in our vacuum chamber as the experimental room temperature was stabilized to about 0.1 K (see methods). In a less ideal setup, where there is more drift in the ambient temperature, we expect that the compensation for T_R would have a more beneficial effect at smaller time-scales.

4.5.7. Estimation of spatial resolution of scanning thermal microscopy

We estimated the spatial resolution of our SThM scheme using the maximum measurable gradient as observed in Figure 4.6e, and the temperature sensing resolution via the relation: $\Delta x = \Delta T /$

($\partial T/\partial x$) which yields a resolution of $\Delta x \approx 50$ [mK] / 31 [mK/nm] = 1.6 nm. In order to check if this estimated resolution can be experimentally realized, we performed a fine line scan perpendicular to the 250 nm-wide Pt heated line sample with pixel spacing of 0.488 nm when a DC current of 0.707 mA was supplied to the Pt line sample, with a scanning time was ~500 ms/pixel. To extract the spatial resolution, the scanning rate was chosen to be ~1 nm/s which was slower than the data in Figure 4.4 and Figure 4.5 (with a scan rate of 12 nm/s). The obtained surface temperature profile close to the line edge (a location of large temperature gradient) is shown in Figure 4.13a with a data point spacing of 0.488 nm. Next, we subsampled the data at a rate of 1/3 using an antialiasing low pass filter to obtain data spacing of 1.46 nm which is shown in Figure 4.13b. As can be seen, the data in Figure 4.13b clearly resolves the temperature gradient at the edge of the line with data point spacing of 1.46 nm, which is consistent with the claimed ~2 nm resolution of this technique. However, for faster scan rates, the estimated spatial resolution would be 6.5 nm as previously indicated. In addition, the spatial resolution is ultimately limited by the tip-sample contact diameter. We estimated the contact diameter using classical Hertzian theory via Eqs. S16 and S17:

$$d_{Hertz} = \left(\frac{6rP}{E^*}\right)^{1/3} \tag{3.19}$$

$$E^* = \left[\frac{1-{\nu_1}^2}{E_1} + \frac{1-{\nu_2}^2}{E_2}\right]^{-1} \tag{3.20}$$

where r is the probe tip radius (~25 nm), P is the normal contact force (~125 nN), and E^* is the effective elastic modulus obtained from Eq. 3.20, where E_1 = 277 GPa[129] and E_2 = 165 GPa[130] are Young's moduli and ν_1 = 0.21[131] and ν_2 = 0.21[132] are the Poisson's ratios of Chromium tip and Al_2O_3 coated sample, respectively. For a chromium-coated tip and Al_2O_3 surface, the calculated

contact diameter is 5.58 nm, which is smaller than the estimated spatial resolution of ~7 nm. Therefore, we estimate the spatial resolution of our technique to be at least 7 nm.

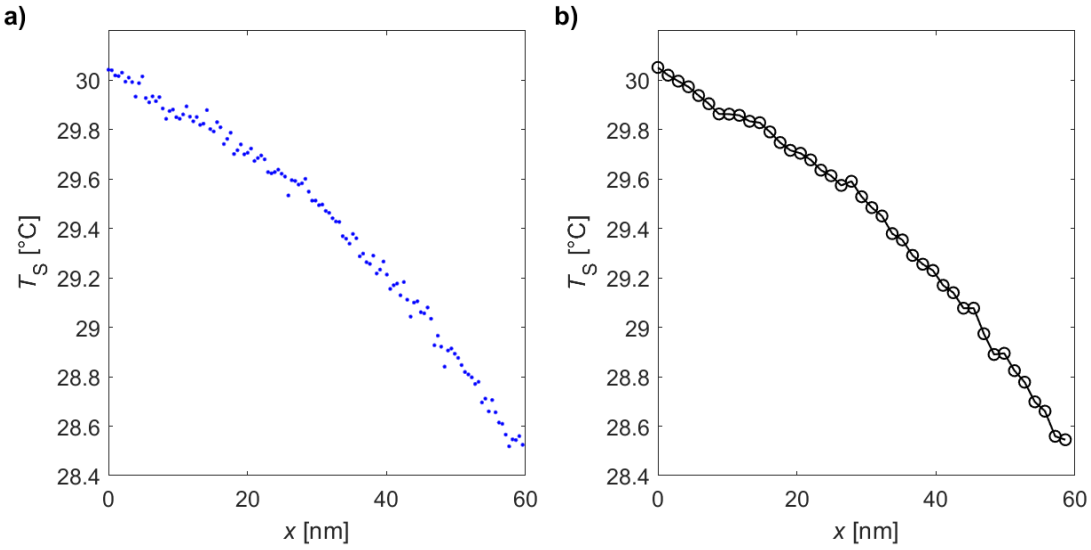


Figure 4.13 Surface temperature obtained using a line scan perpendicular to a 200 nm-wide Pt line close to the edge of the Pt line (where a significant thermal gradient is present). The surface current corresponds to a situation where an electrical DC current of 0.7 mA is supplied. (a) Original line scan data with data point spacing of 0.488 nm, (b) Subsampled data at a rate of 1/3, with data point spacing of 1.46 nm.

4.5.8. Heat transfer model for estimation of temperature profile

We used a continuum finite element heat transfer model (COMSOL^{TM}) to calculate the temperature profile around the 250 nm-wide self-heated Pt line. A steady-state 2D heat transfer model was used where only half the sample was modeled by taking advantage of symmetric geometry. The computational domain is illustrated in Figure 4.14a, which consists of a structured quadrilateral grid with refinement close to the Pt line where a large thermal gradient is expected. The total length and thickness of the computational domain were 3.5 mm and 0.5 mm, respectively, which represent the bulk device dimensions. The following thermal conductivity values were used in this model: 148.0 W/m·K for Si substrate[61], 1.4 W/m·K for SiO_2 layer[61], and 29.5 W/m·K for the thin film Pt layer which is significantly lower than the bulk value[133]. The boundary conditions set in this model are: (i) a fixed temperature boundary condition (26 °C) at the bottom edge, (ii)

symmetric boundary condition (i.e. insulating boundary condition) on the left edges, (iii) insulating boundary condition for all other edges, (iv) volumetric heat source applied to the top Pt layer, and (v) an interfacial thermal resistance of 3.41×10^{-8} m^2K/W was considered between the deposited metal (Ti/Pt) layer on top and the SiO_2 layer based on the experimental results of Ref. [134]. As an example, the obtained temperature field for a heat source of 6×10^{14} W/m^3 is shown in Figure 4.14b which demonstrates a discontinuity in the temperature field between the top Pt line and the SiO_2 layer as a result of interface thermal resistance. Finally, the amplitude of volumetric heat source was adjusted to match the experimentally measured temperature rise of the Pt line in order to obtain the profiles in Figure 4.6.

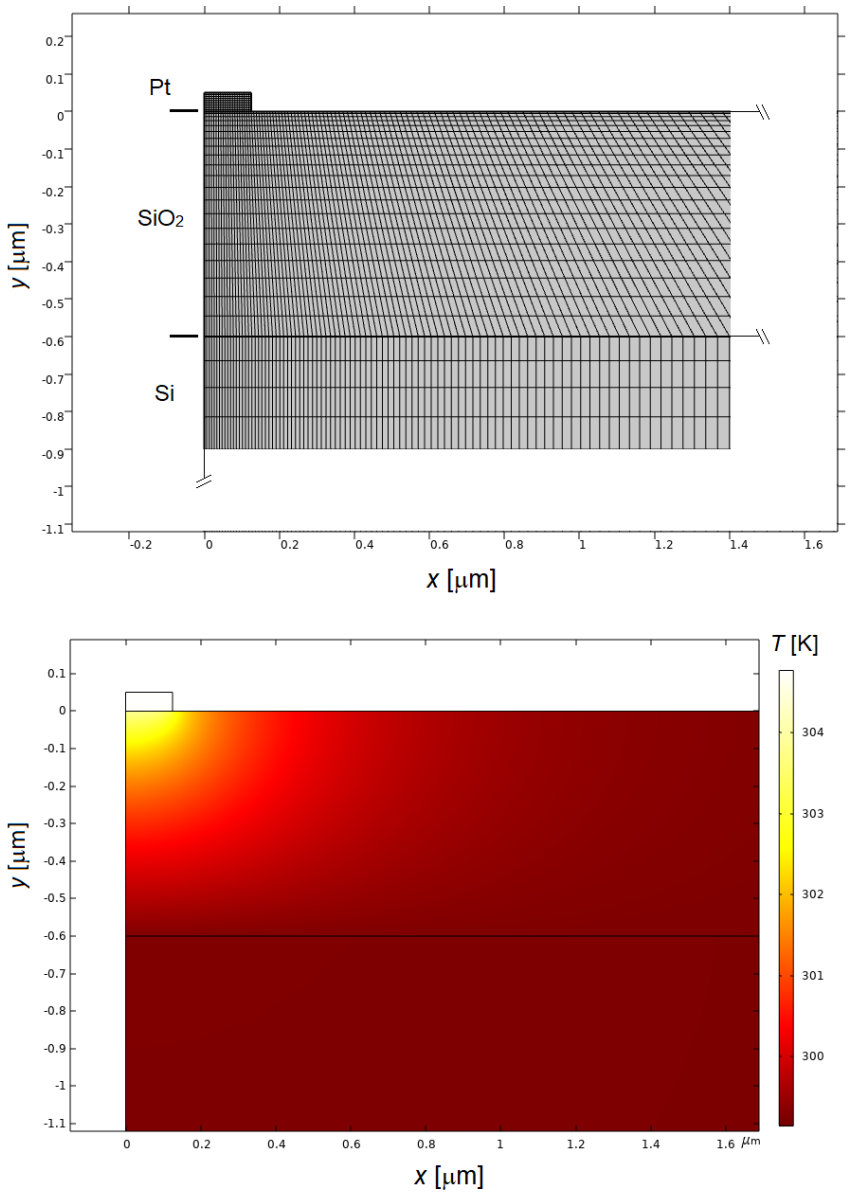


Figure 4.14 (a) Computational domain for the finite-element heat transfer model. (b) Example of obtained steady-state temperature contour for a volumetric heat source of 6×10^{14} W/m^3 applied on the Pt line.

4.5.9. Histogram analysis of scanning thermal scans

To analyze the distribution of scanned surface temperature we show in Figure 4.15a the pixel value histogram obtained from the entire Figure 4.4f which shows a standard deviation of 174 mK. This variation arises partly from measurement noise and partly due to residual effects from spatial variation of R_{TS} which although drastically reduced, cannot be completely removed. Similarly,

Figure 4.15b shows the histogram distribution of pixel values obtained from the dashed box in Figure 4.5f which has a standard deviation of 221 mK, which is slightly larger than the previous case due to the small temperature gradient generated by heating the Pt line.

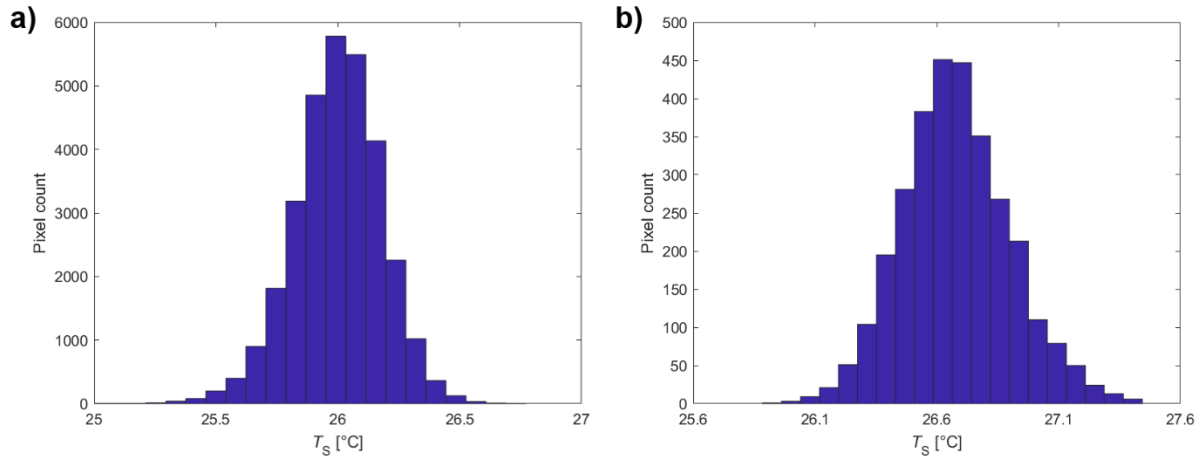


Figure 4.15 (a) Scanned surface temperature (T_S) pixel histogram obtained from: (a) the entire image of Figure 4.4f, which shows a standard deviation of 174 mK, and (b) from the pixels inside the dashed box in Figure 4.5f which shows and standard deviation of 221 mK.

4.5.10. Scanning image distortion correction

As the piezo scanner in our SPM (UHV 750, Beetle STM/AFM, RHK Technology) had a limited lateral (*x* and *y*) range of 6 µm, during scanning a large area (comparable to the full range) a distortion in the scanned image was observed as shown in the raw topography scan of Figure 4.16a. This distortion was corrected by applying a sublinear transformation defined as $x_{new} = \tanh(a\, x_{old})/a$ where *a* is the parameter defining the strength of transformation. A similar transformation was applied to the *y* direction. Finally, both the *x* and *y* coordinates were scaled independently to obtain perpendicular Pt lines (as indicated by SEM images of the device). The distortion-corrected topography image is shown in Figure 4.16b. A similar distortion correction procedure was employed to obtain the images of Figure 4.7.

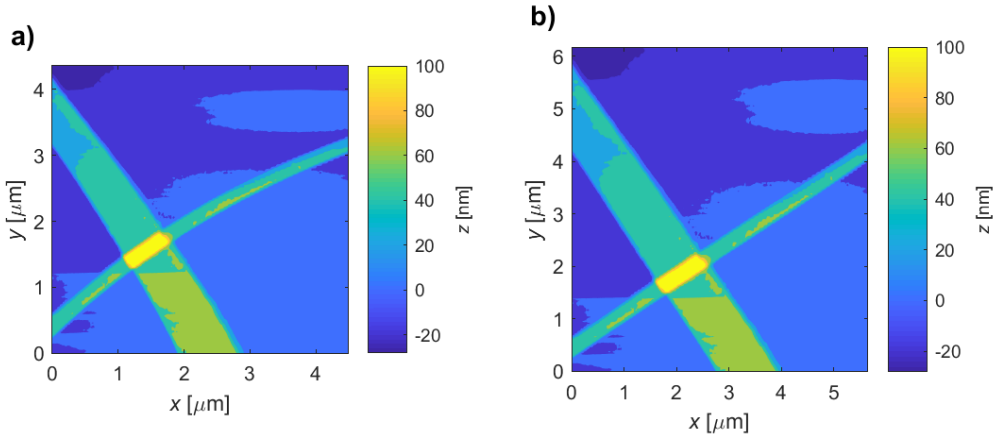


Figure 4.16 (a) Raw AFM topography image, (b) distortion-corrected topography image.

4.5.11. Temperature profile and characteristic length scales

The temperature profiles obtained from Figure 4.7f along the plotted lines are shown in Figure 4.17, where the shaded region indicates the standard deviation of averaged pixel values. The characteristic length scale defined by 63% decay of temperature rise is indicated by red points are 120 nm and 560 nm for profile 1 and 2 respectively.

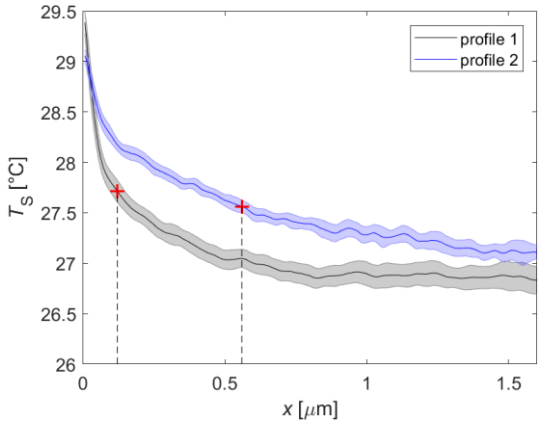


Figure 4.17 Averaged temperature profiles obtained along the lines plotted in Figure 4.7. Profile 1 corresponds to temperature distribution on SiO_2 substrate, and profile 2 corresponds to the temperature profile on 50 nm thick Pt line.

Chapter 5 Quantifying the Temperature of Heated Microdevices Using Scanning Thermal Probes

Reproduced with permission from *Applied Physics Letters*. See Ref. [126]

Amin Reihani, Shen Yan, Yuxuan Luan, Rohith Mittapally, Edgar Meyhofer, Pramod Reddy

Quantifying the temperature of microdevices is critical for probing nanoscale energy transport. Such quantification is often accomplished by integrating resistance thermometers into microdevices. However, such thermometers frequently become structurally unstable and fail due to thermal stresses at elevated temperatures. Here, we show that custom-fabricated scanning thermal probes (STPs) with a sharp tip and an integrated heater/thermometer can accurately measure the temperature of microdevices held at elevated temperatures by contacting the microdevice surface. This measurement is accomplished by introducing a modulated heat input to the STP, and characterizing the DC and AC components of the STP's temperature. From these measured temperature components, the tip-to-sample thermal resistance and the microdevice surface temperature are deduced simultaneously via a simple lumped-capacitance model. The advances presented here can greatly facilitate temperature measurements of a variety of heated microdevices.

5.1. Introduction

Quantifying the temperature of heated microscale devices is critical for successfully employing them in probing nanoscale transport via conduction and radiation. Such quantification becomes challenging for small devices at high temperatures due to the difficulties in integrating reliable temperature sensors. Past work for quantifying high temperatures at the micro/nanoscale has relied on employing approaches such as phase change of nanoparticles[51], Raman spectroscopy[52], complicated approaches involving integration of fine thermocouples[49] that lead to destruction of the microdevice and other optical approaches[53]. Typical examples requiring the characterization of the temperature of microdevices are related to the exploration of near-field thermal transport[135,136] and near-field based thermophotovoltaic energy conversion[49,137] where heated microdevices are routinely employed. In this work we show that scanning thermal probes (STPs), which have been recently employed for probing a number of interesting thermal phenomena[34,48,107-109,124,138-142], can be used to quantitatively measure the temperature of heated microdevices (referred as also a device under test (DUT)) in a non-destructive fashion.

The main challenge for quantitative temperature sensing using STPs is the determination of tip-sample thermal contact resistance (R_{TS}), which dominates heat transfer between the sample and the probe in the contact mode. Past studies have employed techniques such as the null-point measurement[121,122], which nullifies the probe-sample heat flow, and a two-step approach[124], which employs two independent measurements at each point/pixel corresponding to the sample to account for R_{TS}. While these techniques represent an important step forward, they may not fully capture changes in R_{TS} during scanning associated with the complex sample topology or probe and sample abrasion. Therefore, accurate measurements of surface temperature require simultaneous determination of R_{TS}. One such technique has been previously developed[34] for sensing modulated

sample temperatures. However, that approach cannot be directly applied for measuring temperatures of heated DUTs, such as those considered in this work, because modulation of the temperature may lead to thermal stresses which damage the sample or may cause measurement artifacts due to thermal expansion and contraction of the sample.

5.2. Results

Our approach to quantify the temperature of heated DUTs relies on custom-fabricated STPs (see Figure 5.1a) with "T-shaped" beams that enable both a relatively large mechanical stiffness and a low thermal conductance (see Appendix). These probes feature an integrated Pt resistance thermometer, which allows both temperature sensing and heating of the STP (see Appendix). In our method, we measure the thermal response of the STP to heat inputs in two *scenarios*: i) when the STP is in contact with the DUT (see Figure 5.1c) and ii) when it is far away from the DUT. As explained below, the measured thermal responses in these two conditions enable us to quantify the temperature of the heated DUT. All the measurements reported here were performed under ultra-high vacuum conditions (~10^{-9} mbar), and in contact mode with a constant contact force of 50 nN.

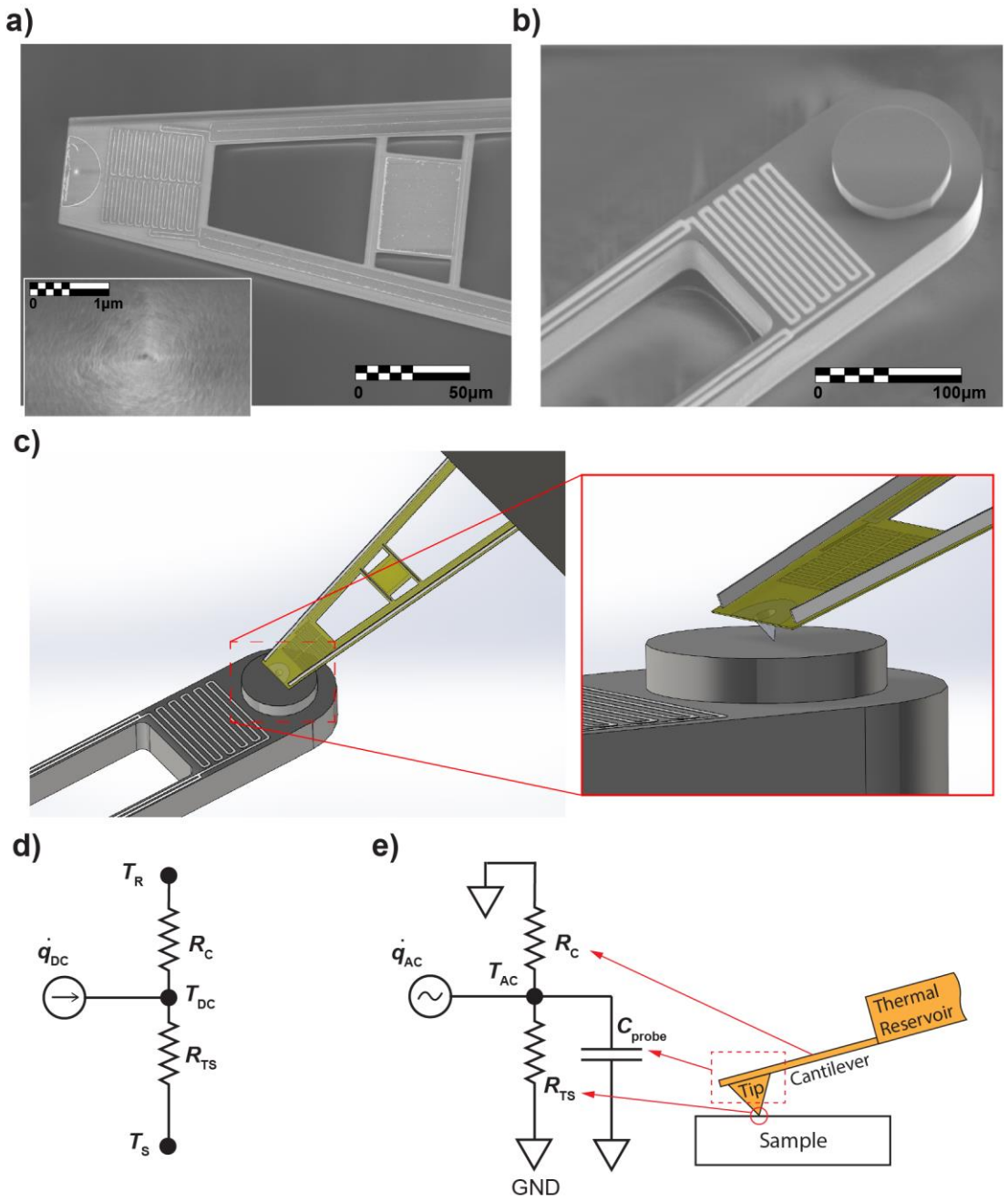


Figure 5.1 Scanning electron micrograph (SEM) of the STP probe with an integrated Pt heater thermometer and T-shaped beams. The inset shows the STP tip. (b) SEM of the suspended microdevice (DUT) with embedded Pt heater/thermometer. (c) Schematic illustrating the geometry of the STP in contact with heated DUT. Note, to obtain a clear view, the tip height is exaggerated. (d) DC- and (e) AC-equivalent thermal resistance network corresponding to the geometry shown in (the temperatures T_R and T_S are set to zero for AC network) (c). T_{DC} and T_{AC} represent the STP tip DC temperature and AC temperature amplitude respectively. T_S, R_C and R_{TS} represent the DUT temperature, thermal resistance corresponding to the beams of the STP and tip-sample thermal contact resistance, respectively. While $C_{probe,}$, $\dot{q}_{DC}$ and $\dot{q}_{AC}$ represent the lumped thermal capacitance of the STP, and the DC and AC components of the heat input to the STP, respectively.

The thermal behavior of the STP under unmodulated (DC) and modulated (AC) heat inputs can be described by a dynamic lumped-capacitance thermal model[6], as represented by the thermal networks illustrated in Figs. 1(d) and (e), respectively. In these figures, T_S represents the surface temperature of the DUT that needs to be quantified, and T_R and T_{DC} represent the thermal reservoir and probe tip DC temperatures. The thermal capacitance of the probe, C_{probe}, is lumped in the probe tip node. In addition, R_C and R_{TS} represent the thermal resistances of the probe cantilever and tip-sample contact. The parameters C_{probe}, and R_C depend on temperature-dependent material properties and are obtained from a set of calibrations. Key to quantitative measurement of T_S is a direct measurement of R_{TS}, which depends on the detailed geometry, tip-sample force, and the local thermal and mechanical properties of the tip at the point of contact and can vary spatially and temporally as the tip-sample geometry and mechanics change. Below, we explain how R_{TS} is characterized via a modulated heat input to the probe.

We first note that the STP can be heated by supplying an AC current at frequency f_1 to the probe heater, which results in an AC heat input at frequency $2f_1$ as well as a DC heat input via Joule heating. Further, the laser employed to detect the deflections of the STP introduces additional DC heating. Hence, the total heat input to the STP has DC and AC components, $\dot{q}_{probe}(t) = \dot{q}_{DC} + \dot{q}_{AC}\cos(\omega t)$, resulting in DC and AC temperature of the probe tip, $T_{tip}(t) = T_{DC} + T_{AC}\cos(\omega t+\varphi)$, where φ is the phase lag (see Appendix for details).

To quantify the values of R_C and C_{probe} we characterized the thermal frequency response of our STP. These experiments were performed at various DC temperatures (T_{DC}) achieved by varying the incident laser power on a STP not in contact with the DUT. At each T_{DC} a modulated heat input $\dot{q}_{AC}$ = 6.1 μW at various frequencies was applied to the STP heater. The resulting temperature oscillation amplitudes of the STP (T_{AC}) are shown in Figure 5.2a as distinct curves at

each DC temperature. Using the low frequency (0.5 Hz) data, the thermal conductance of the probe ($G_C = 1/R_C$) was estimated for various values of T_{DC} as shown in Figure 5.2b. It can be seen that the probe conductance increases as a function of temperature, which can be attributed partly to an increase in thermal conductivity[46] of SiN_x, from which our STPs are made, and partly to the radiative conductance of the membranes (which feature large absorption cross-sections[143-145]) of the STP that increases with temperature. Finally, Figure 5.2c shows the thermal cutoff frequency (-3 dB point) that is weakly dependent on temperature, from which one can estimate the thermal capacitance of the probe ($C_{probe} = G_C/2\pi f_C$).

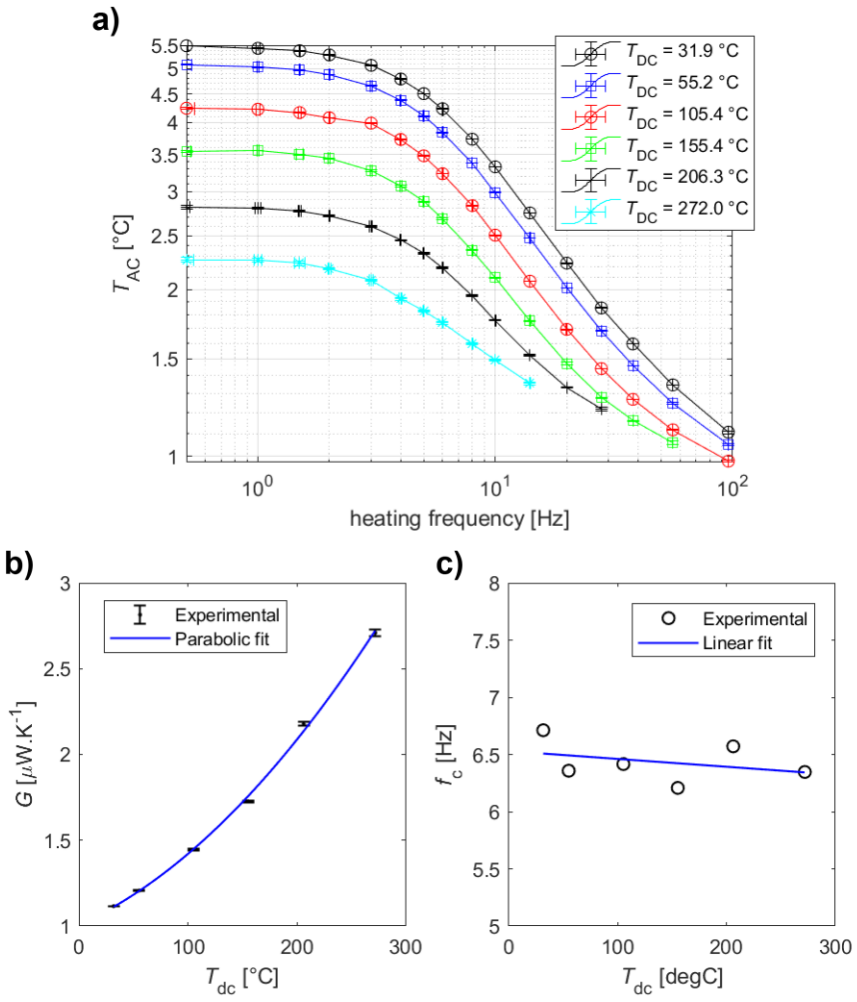


Figure 5.2 Frequency response of a STP probe that is located away (10 μm) from the sample surface measured at various STP tip DC temperatures established by varying the laser power incident on the STP. All data points obtained at constant heating amplitude of $\dot{q}_{AC}$ = 6.1 μW. (b) Thermal conductance of the probe at the low-frequency limit (0.5

Hz) as a function of probe temperature. (c) Thermal cut-off frequency of the STP probe based on the -3dB point as a function of probe temperature.

In order to quantify R_{TS}, we performed an experiment where the STP cyclically contacts the surface of the DUT and moves up to a height of ~2 μm above the surface. At these gap-sizes, contributions from radiative heat transfer (especially near-field radiative heat transfer) are expected to be negligibly small[48,127] (i.e. $R_{TS} >> R_C$)). As the STP contacts the sample and separates from it, T_{DC} and T_{AC} values were continuously recorded. In order to distinguish the two cases, we label the DC and AC temperatures of the STP as $T_{DC\text{-}o}$ and $T_{AC\text{-}o}$ (when the STP tip is separated from the sample), and $T_{DC\text{-}c}$ and $T_{AC\text{-}c}$ (when the STP is in contact with the sample). We note that contact of the STP with the DUT results in a change in the AC and DC components of the STP temperature. We quantify the change in AC temperature by defining the ratio $r = (T_{AC\text{-}o}/\dot{q}_{AC\text{-}o})/(T_{AC\text{-}c}/\dot{q}_{AC\text{-}c})$, where ($\dot{q}_{AC\text{-}o}$) and ($\dot{q}_{AC\text{-}c}$), are the AC heat inputs before and after contact, respectively. These two heat inputs are slightly different due to a change in the electrical resistance of the heater upon contact. One can calculate R_{tot} (defined as $R_{tot}^{-1} = R_C^{-1} + R_{TS}^{-1}$) using the measured r and the relation below where $\omega = 4\pi f_1$ is the angular frequency of AC heat input to the STP (see Appendix for full derivation).

$$R_{tot} = \sqrt{\frac{R_C(T_{DC\text{-}o})^2}{r^2\left(1+R_C(T_{DC\text{-}o})^2 C_{probe}(T_{DC\text{-}o})^2\omega^2\right) - R_C(T_{DC\text{-}o})^2 C_{probe}(T_{DC\text{-}c})^2\omega^2}} \qquad (4.1)$$

Subsequently, the tip sample contact resistance can be obtained from $R_{TS}^{-1} = R_{tot}^{-1} - R_C(T_{DC\text{-}c})^{-1}$. Note that R_c is temperature-dependent, whose value at any given probe temperature ($T_{DC\text{-}c}$) can be obtained from the data in Figure 5.2b, and is utilized in evaluating R_{TS}. Once R_{TS} is determined, the sample temperature can be obtained from (see Appendix):

$$T_S = \frac{R_{TS}}{R_C}(T_{DC\text{-}c} - T_{DC\text{-}o}) + T_{DC\text{-}c} + R_{TS}(\dot{q}_{DC\text{-}o} - \dot{q}_{DC\text{-}c}) \quad (4.2)$$

In order to confirm the validity and accuracy of the proposed measurement technique, we employed a suspended microdevice as DUT whose temperature (T_S) can be increased and simultaneously measured via an integrated Pt resistance thermometer/heater (PRT) (Figure 5.1b, see Appendix for measurement details). In these studies, the STP was placed close to the center of the microdevice mesa as shown in Figure 5.1c. At each value of heating power applied to the microdevice, a sequence of approach and retract cycles were performed and T_{DC}, T_{AC} values were recorded. Figs. 3(a) and (b) show the time series of this measurement (bandwidth of ~1 Hz) at two heating powers of the microdevice (0 and 56 mW) corresponding to surface temperatures of T_s = 25.1 and 330.6 °C respectively, each showing two repeats of approach and retract cycle.

As can be seen in Figure 5.3a, $T_{DC\text{-}o} \approx 45$ °C, this is due to $\dot{q}_{DC}$ provided by the AFM and the DC component of heat input by probe heater. When the probe is placed in contact with an unheated microdevice $T_{DC\text{-}c}$ drops to ~35 °C as a result of contact to a colder surface. In the subsequent retract and contact phases the probe establishes a significantly different contact and reaches ~40 °C, which indicates the stochastic behavior of R_{TS}. This variation in R_{TS} is also reflected in the independently measured T_{AC}, which is correspondingly lower. In Figure 5.3b, we present data from an experiment where the DUT is heated. It can be seen that $T_{DC\text{-}o} \approx 50$ °C when the probe is retracted, this is higher than the previous case of Figure 5.3a due to additional far-field radiative heating of the probe by the DUT surface. During the first approach, the $T_{DC\text{-}c}$ reaches ~149 °C while during second approach it reaches ~147 °C which indicates that in this experiment the two approaches lead to similar contacts. This is also reflected in the T_{AC} signal, which shows a very small difference between the two contacts.

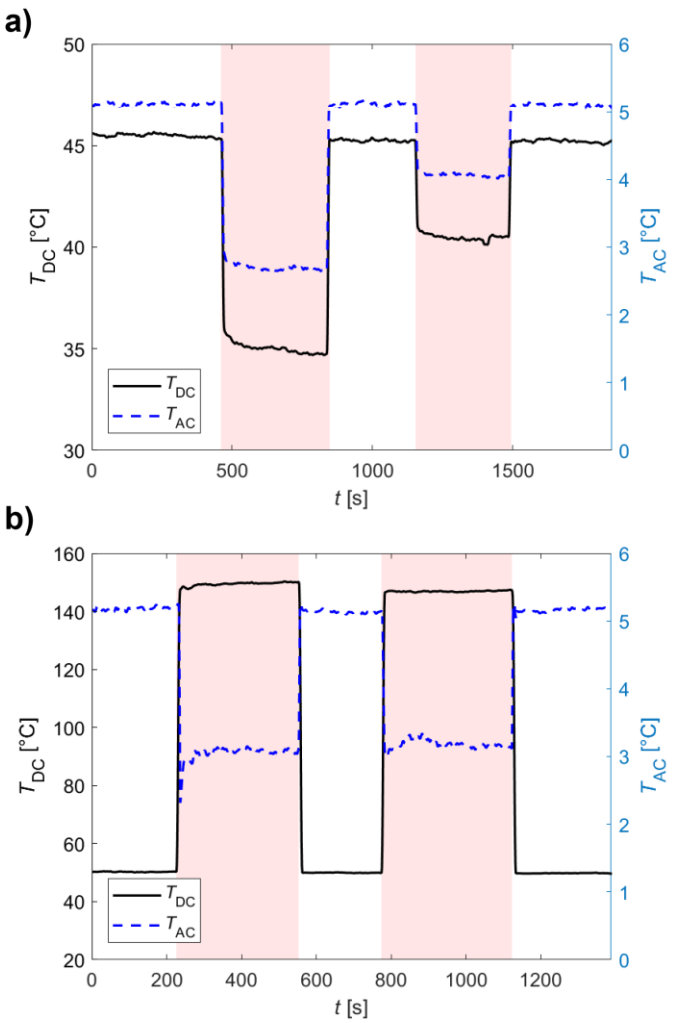


Figure 5.3 Time series of DC and AC temperatures of STP tip (T_{tip}) during two successive contact (pink shaded regions) and retraction cycles (unshaded) on the silicon mesa of the heated microdevice. The surface temperatures are chosen to be T_S = 25.1 °C for the experiment shown in (a) and T_S = 330.6 °C for the experiment show in (b).

In order to quantify the surface temperature, we use Eqs. 1, and 2, where each data point corresponding to probe contact (shaded regions in Figure 5.3) is used separately to obtain various estimates of $T_{DC\text{-}c}$, and an average of data points when probe is retracted (unshaded regions in Figure 5.3) is used to estimate $T_{DC\text{-}o}$. This procedure leads to evaluation of R_{TS} and T_S for each data point during contact. The results from this analysis are shown in Figure 5.4a and c, from which it can be seen that the R_{TS} values for the first and second approach demonstrate different mean values of 0.87×10^6 K·W^{-1} and 3.00×10^6 K·W^{-1}, indicating that different contacts were established during these two approaches. On the other hand, the mean values of R_{TS} for the second experiment, shown

in Figure 5.4b, are similar i.e. 1.08×10^{6} $K\cdot W^{-1}$ and 1.21×10^{6} $K\cdot W^{-1}$ for the first and second approach, respectively. Overall these measured values of R_{TS} were found to be in good agreement with expectations (see Appendix) based on models from past work[146].

Histograms corresponding to the measured temperature T_s from the data in Figs. 4(a), (c) are shown in Figs. 4(b), (d), respectively. From Gaussian fits to each histogram the mean values of T_S in each of the experiments are estimated to be 24.5°C and 327.0°C with standard deviations of 0.7°C and 9.0°C (standard deviations corresponding to raw data are 1.2°C and 13.3°C), respectively. These estimates are to be compared with independent temperature measurements using the thermometer embedded into the DUT, which indicates 25.1°C and 330.6°C. As can be seen, the agreement between the two measurements is good, however, at higher temperatures the uncertainty is found to increase possibly due to fluctuations in R_{TS} at high temperatures.

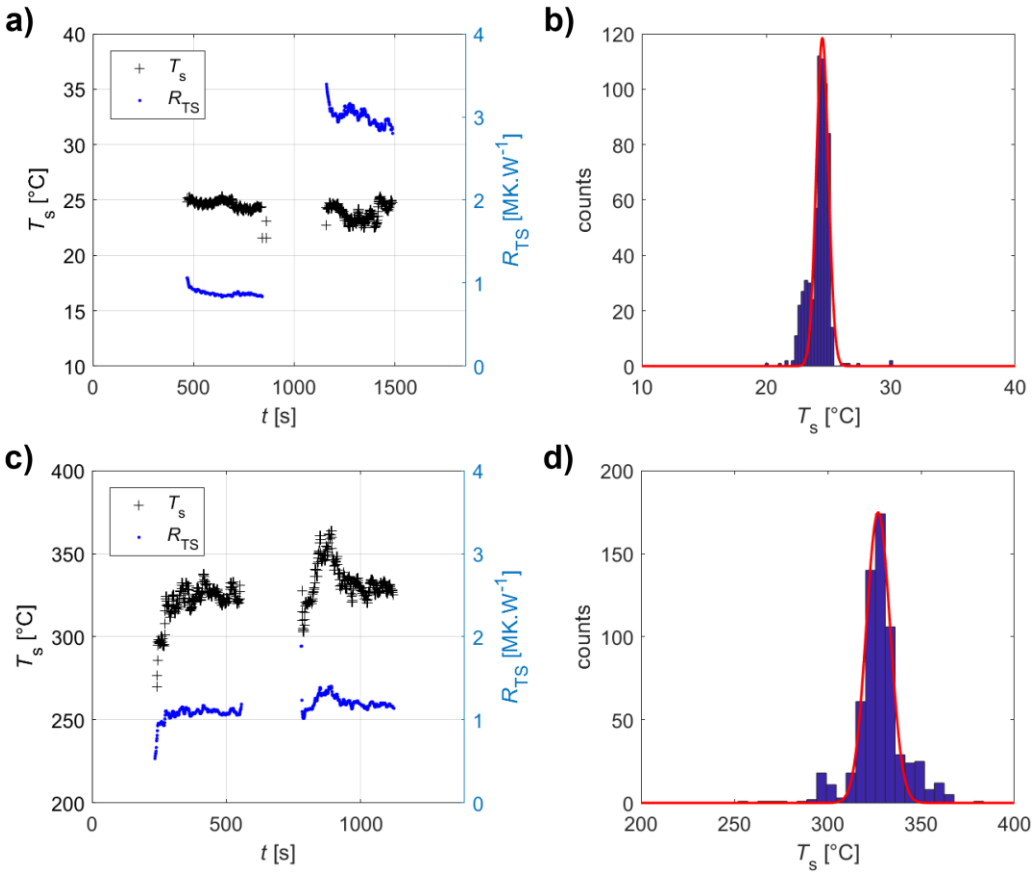


Figure 5.4 Values of surface temperature (T_S) and tip-sample thermal contact resistance (R_{TS}) estimated from the data shown in Figure 5.3. For the data shown in (a), the surface temperature of the microdevice (T_S) was set to be 25.1 °C, whereas for the data shown in (c), it was chosen to be 330.6 °C. (b) Histogram constructed from the T_S data shown in (a). (d) Same as (b), but for data shown in (c). Gaussian fits to the data in (c) and (d) shown in red.

Finally, in Figure 5.5, we present experimental data from validation measurements at various surface temperatures that were achieved by varying the power dissipated in the instrumented DUT. As can be seen, the measured data from the STP are in very good agreement with DUT PRT measurements up to 330°C. Above ~370°C, the PRT resistance of the heated DUT starts to drift making the measurements unreliable. However, the measurements performed using the STP continue to correlate well with the increasing power up to 417 °C (as estimated from the STP measurements) at which point the Pt heater on the DUT failed, making it impossible to evaluate the response at even higher temperatures. It is not entirely surprising that the STP is capable of measurements at high surface temperatures as the net temperature rise of the STP is

much smaller than that of the DUT due to the large tip-sample thermal resistance (R_{TS}). In general, a higher R_{TS} value is expected to result in an increased operating temperature range of the STP at the expense of reduced temperature sensitivity. In future studies, the R_{TS} value can in principle be tuned for each experiment, for instance, one can increase the R_{TS} by depositing a thin layer of low conductivity material on the sample or the probe (such as Al_2O_3). However, a detailed analysis of the temperature distribution across the deposited thin film may be required for achieving quantitative measurements of the true sample temperature.

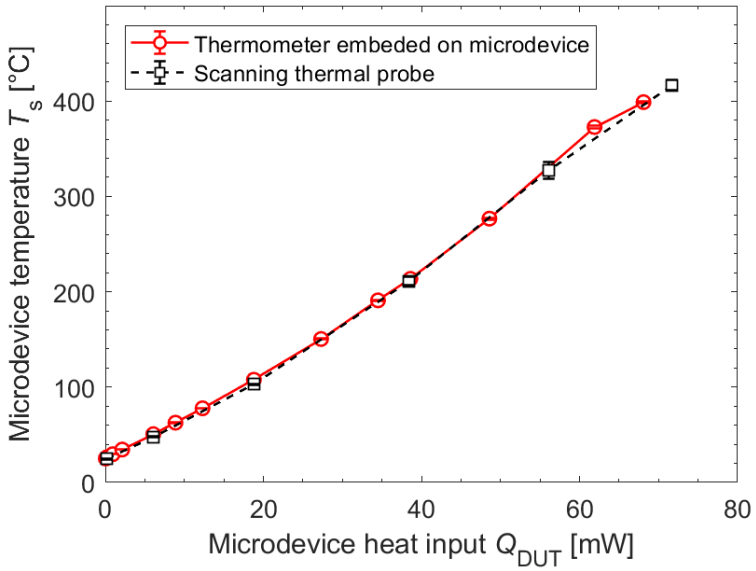


Figure 5.5 Measured temperature (T_S) of heated microdevice (DUT) using the STP (blue) and a Pt resistance thermometer (red) integrated into the heated microdevice as a function of power dissipated in the microdevice (Q_{DUT}). Note, T_S is not a linear function of Q_{DUT} because the thermal conductance of the heated microdevice decreases from 238 $\mu W \cdot K^{-1}$ to 178 $\mu W \cdot K^{-1}$ as the temperature is increased from 25°C to 372 °C. The error bars correspond to ±1 standard deviation as estimated from the Gaussian fits to the histograms shown in Figure 5.4.

5.3. Conclusions

In summary, the temperature measurement approach described here represents a direct method for measuring the temperature of microdevices that is particularly well-suited for small devices operated at high temperatures. This approach leverages the large thermal resistance of a nanoscale contact, which serves to both minimize the perturbation of the microdevice temperature

and limits the temperature rise of the probe enhancing the range of temperatures that can be measured. The agreement between the temperatures measured with the STP and those with the Pt thermometer integrated into the microdevice supports the robustness of the approach reported in this paper. We expect that the developed method can greatly help in characterizing microscale devices employed in a range of nanoscale energy transport experiments.

5.4. Appendix

5.4.1. Scanning thermal probe fabrication

The steps involved in the fabrication of the STPs employed in this work are shown in Figure 5.6. In brief, a T-beam was first defined on a bare Si wafer through deep reactive ion etching (DRIE), followed by wet oxidation and low pressure chemical vapor deposition (LPCVD) of 600 nm silicon nitride. The T-beams improve the stiffness of the probe cantilever which enable stablishing stable thermal contacts to the sample during measurements[33]. After that, the back side of the wafer was patterned by reactive ion etching (RIE). Subsequently, a 3 μm thick low temperature oxide (LTO) was deposited with Cr caps defined on the front side to form conical tips. Then, LTO was etched by buffered HF (BHF), leaving a tip of 3 μm height under the region where the Cr cap was located. Afterwards, the tip was coated by a 150 nm Cr layer. Next, a 50 nm thick serpentine Pt line was deposited for creating a heater-thermometer for resistive heating and thermometry. Later, an Au reflector and electrode were patterned. Then the front side of the wafer was covered by a 50 nm thick plasma enhanced chemical vapor deposition (PECVD) nitride layer to hinder the etching rate at the front side. Finally, the probe was released by KOH etching of Si.

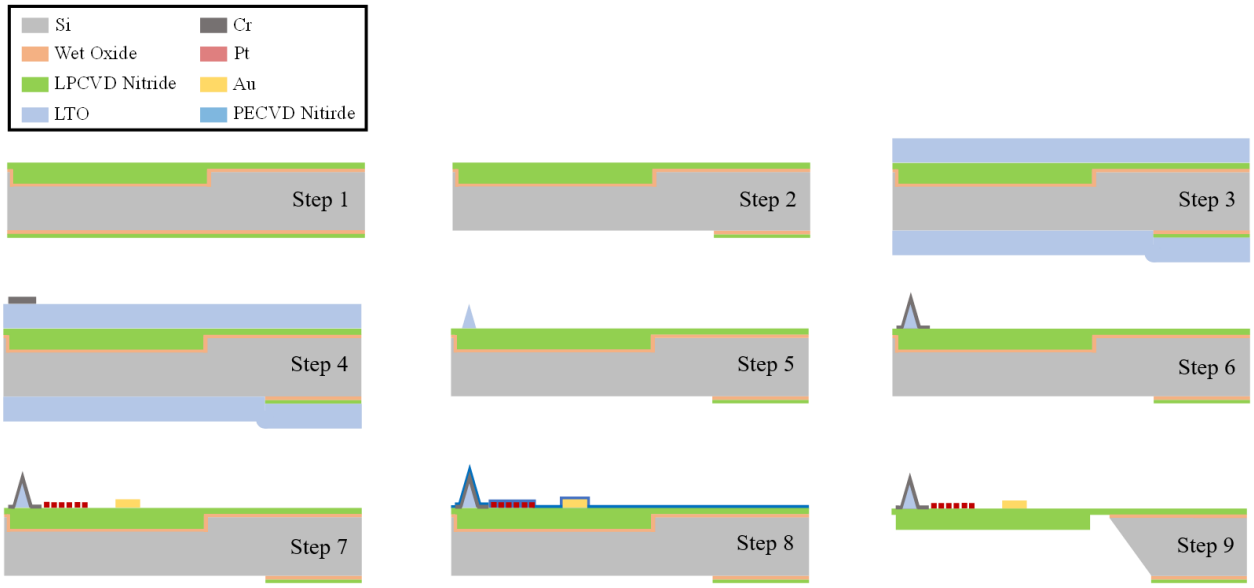


Figure 5.6 Process steps for fabrication STPs with integrated platinum resistive heater/thermometer.

5.4.2. Finite element modeling of scanning thermal probe

We estimated the mechanical stiffness of the probe by performing finite element simulations in COMSOL™. Both the geometry of the probe and various layers of Au, Pt and Cr were included in the model. The probe consisted of 280 µm long, 600 nm thick SiN_x cantilever with thin films of Pt (50 nm), Au (100 nm) and Cr (150 nm) on it. A force (F) of 1 µN was applied to the tip end of probe body while the other end of probe was fixed. Tip deflection (δ**)** was calculated under the applied force and the stiffness of the probe ($k = F/\delta$) was estimated to be 1.79 N/m as shown in Figure 5.7a.

The thermal conductance of the probe was also studied using the same model. For the SiN_x thin films, a thermal conductivity of 5.0 W/m-K was assumed[46]. A known heat flux was applied to the tip end of the probe while the temperature of the other end was fixed at room temperature (293.15 K), generating a temperature gradient along the probe body. Tip temperature rise was monitored under various input heat fluxes and the thermal conductance of the probe was extracted by linearly fitting the data to be 0.69 µW/K close to room temperature as shown in Figure 5.7b.

Note that the discrepancy observed between the model and the experimentally obtained value (1.11 µW/K at 31.9 °C from Figure 5.2c) can be attributed to the variation in SiN_x thin film thermal conductivity from the assumed value, differences in the location of heat input (tip end in the model, distributed along the Pt serpentine in experiments), and contributions from thermal radiation.

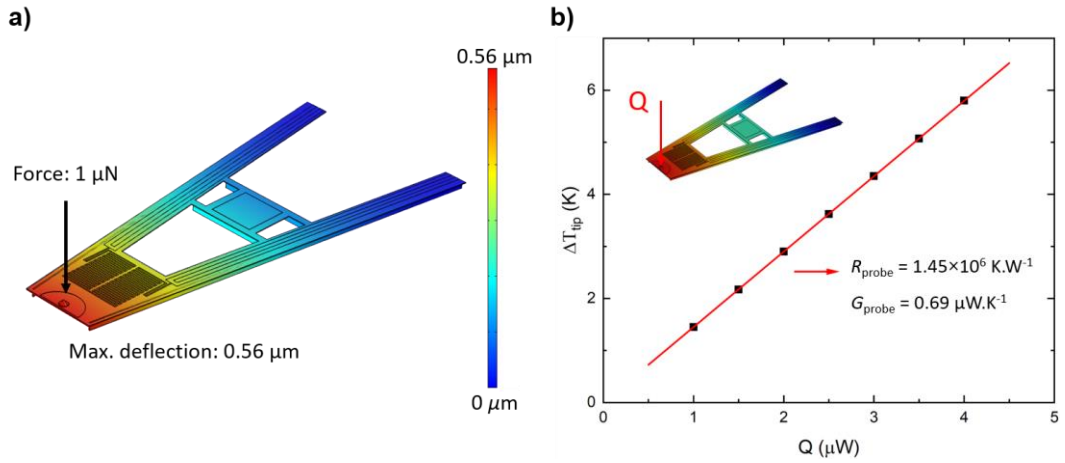


Figure 5.7 Finite element simulation of STP deflection under an applied load. **(b)** Temperature rise of the probe as a function of heat input to the tip, the slope of the linear fit shows the probe thermal resistance ($R_{probe} = 1/G_{probe}$).

5.4.3. Scheme employed for heating and measuring temperatures of STPs

A platinum resistive thermometer (PRT) with 8 kΩ nominal resistance was integrated into the end of the STP. Temperature sensing was performed by reading the resistance of the PRT using a full Wheatstone bridge[6] via a multi-frequency lock-in approach as described below. The bridge was driven by a current source with a waveform which was a superposition of two sine waves as $I(t) = A_1 \sin(2\pi f_1 t) + A_2 \sin(2\pi f_2 t)$. The first sine wave had a low frequency (f_1 = 1 Hz) and high amplitude (A_1 = 56 µA) which was used for modulated heating of the probe. Since the joule heating frequency $2f_1$ = 2 Hz was smaller than the thermal cutoff frequency (~6.5 Hz) efficient heating of the probe was achieved. The modulated temperature amplitude of the probe, T_{AC}, was measured by lock-in technique using the $3f_1$ component of the Wheatstone bridge output voltage[24]. The

second sine wave had a high frequency (f_2 = 200 Hz) and lower amplitude (A_2 = 14 μA), which was used for readout of DC temperature of the probe by lock-in technique using the f_2 component of the Wheatstone bridge output voltage.

5.4.4. Heating and temperature sensing of the heated microdevice sample

A microdevice used as a heated sample for verification of STP temperature measurements (Figure 5.1b). This microdevice featured a very stiff suspended silicon region which included a circular mesa and has a nominal thermal conductance of 240 μW.K^{-1}. Details on the fabrication and design of this device can be found in Ref. [49]. This device includes a 4 kΩ Pt heater/thermometer on the suspended region. This Pt heater/thermometer was placed in a half Wheatstone bridge circuit driven by a current source (see Ref. [24] for more details). This circuit allowed passing a current through the heater for DC heating and simultaneously measuring the heater resistance which was then used for sensing the temperature of the microdevice.

5.4.5. Thermal analysis

Based on the equivalent thermal circuit of Figure 5.1d and e the following first order ordinary differential equation can be written to obtain T_{tip} as a function of time[61].

$$\dot{q}_{probe}(t) = \frac{T_{tip}(t) - T_R}{R_C} + \frac{T_{tip}(t) - T_S}{R_{TS}} + C_{probe}\frac{dT_{tip}(t)}{dt} \tag{4.3}$$

For convenience we define the total thermal resistance of the probe to the environment as:

$$\frac{1}{R_{tot}} = \frac{1}{R_C} + \frac{1}{R_{TS}} \tag{4.4}$$

Now consider the following scenario, the total heat deposited on the probe is the sum of constant heat flux delivered by AFM readout laser and heat flux from integrated Pt heater on the probe. By

sourcing an AC current at frequency f_1 to the probe heater an AC heat flux at angular frequency $\omega=4\Pi f_1$ can be generated via Joule heating. Therefore, the total probe heat flux would have a DC and AC component as shown below:

$$\dot{q}_{\text{probe}}(t) = \dot{q}_{\text{DC}} + \dot{q}_{\text{AC}}\, cos(\omega t) \tag{4.5}$$

When combined with Eq. 4.3, this heat input generates a DC and AC temperature change at the probe tip with a phase lag φ as shown below:

$$T_{\text{tip}}(t) = T_{\text{DC}} + T_{\text{AC}}\, cos(\omega t+\varphi) \tag{4.6}$$

Now consider an experiment, where the probe is initially retracted from the surface so that there is no contact and $R_{\text{TS}} \rightarrow \infty$ (i.e. $R_{\text{TS}} >> R_{\text{C}}$), and then the probe approaches the surface establishing contact. We label the DC and AC probe temperatures as $T_{\text{DC-o}}$ and $T_{\text{AC-o}}$ when the probe is out of contact (or open), and $T_{\text{DC-c}}$ and $T_{\text{AC-c}}$ when the probe is in contact with the sample. We note that, since the electrical resistance of the probe heater (R_{heater}) is temperature-dependent, the heat deposited on the probe by the heater ($R_{\text{heater}}I^2$) also changes when its temperature is varied. Therefore, we introduce the probe heat fluxes $\dot{q}_{\text{DC-o}}$ and $\dot{q}_{\text{AC-o}}$ when the probe is out of contact (open) and $\dot{q}_{\text{DC-c}}$ and $\dot{q}_{\text{AC-c}}$ when the probe is in contact with the sample. Substituting Eq. 4.5 and Eq. 4.6 in Eq. 4.3, the following equation can be obtained.

For contact condition;

$$T_{\text{DC-c}} = R_{\text{tot}}\left(\dot{q}_{\text{DC-c}} + \frac{T_{\text{R}}}{R_{\text{C}}} + \frac{T_{\text{S}}}{R_{\text{TS}}}\right) \tag{4.7}$$

$$T_{\text{AC-c}} = \frac{R_{\text{tot}}\, \dot{q}_{\text{AC-c}}}{\sqrt{1+\left(R_{\text{tot}}\, C_{\text{probe}}\, \omega\right)^2}} \tag{4.8}$$

$$\varphi_c = -tan^{-1}\left(R_{tot}\, C_{probe}\, \omega\right) \tag{4.9}$$

For out of contact condition;

$$T_{DC\text{-}o} = T_R + R_C\, \dot{q}_{DC\text{-}o} \tag{4.10}$$

$$T_{AC\text{-}o} = \frac{R_C\, \dot{q}_{AC\text{-}o}}{\sqrt{1+\left(R_C\, C_{probe}\, \omega\right)^2}} \tag{4.11}$$

$$\varphi_o = -tan^{-1}\left(R_C\, C_{probe}\, \omega\right) \tag{4.12}$$

Using Eq. 4.7 and Eq. 4.10 the surface temperature can be obtained as:

$$T_S = \frac{R_{TS}}{R_C}\left(T_{DC\text{-}c} - T_{DC\text{-}o}\right) + T_{DC\text{-}c} + R_{TS}\left(\dot{q}_{DC\text{-}o} - \dot{q}_{DC\text{-}c}\right) \tag{4.13}$$

To obtain R_{TS} we start by calculating the ratio of $T_{AC\text{-}o}$ /$T_{AC\text{-}c}$ as shown below. In addition, for generality we include the temperature dependence of probe thermal resistance (R_c) and lumped thermal capacitance (C_{probe}).

$$\frac{T_{AC\text{-}o}}{T_{AC\text{-}c}} = \frac{R_C(T_{DC\text{-}o})\, \dot{q}_{AC\text{-}o}}{R_{tot}(T_{DC\text{-}c})\, \dot{q}_{AC\text{-}c}} \sqrt{\frac{1+R_{tot}(T_{DC\text{-}c})^2 C_{probe}(T_{DC\text{-}c})^2 \omega^2}{1+R_C(T_{DC\text{-}o})^2 C_{probe}(T_{DC\text{-}o})^2 \omega^2}} \tag{4.14}$$

It can be seen that at the limit of fast excitation ($\omega >> 1/(R.C)$), the AC temperature signal becomes invariant of thermal contact resistance; therefore, this technique is only useful at low and intermediate frequencies.

Slow excitation: $\tau\omega \ll 1$, $\frac{T_{AC\text{-}o}}{T_{AC\text{-}c}} \cdot \frac{\dot{q}_{AC\text{-}c}}{\dot{q}_{AC\text{-}o}} \approx \frac{R_c(T_{DC\text{-}o})}{R_{tot}(T_{DC\text{-}c})}$,

Fast excitation: $\tau\omega \gg 1$, $\frac{T_{AC\text{-}o}}{T_{AC\text{-}c}} \cdot \frac{\dot{q}_{AC\text{-}c}}{\dot{q}_{AC\text{-}o}} \approx \frac{C_{probe}(T_{DC\text{-}c})}{C_{probe}(T_{DC\text{-}o})}$.

For intermediate excitation frequencies the following quadratic equation must be solved to obtain R_{tot} and then R_{TS}.

$$R_{tot} = \sqrt{\frac{R_C(T_{DC\text{-}o})^2}{r^2\left(1+R_C(T_{DC\text{-}o})^2 C_{probe}(T_{DC\text{-}o})^2\omega^2\right)-R_C(T_{DC\text{-}o})^2 C_{probe}(T_{DC\text{-}c})^2\omega^2}} \tag{4.15}$$

Where r is the ratio of AC temperature amplitudes (normalized by AC heat input) when the probe is out of contact, to contact condition, and is given by:

$$r = \frac{T_{AC\text{-}o}}{T_{AC\text{-}c}} \cdot \frac{\dot{q}_{AC\text{-}c}}{\dot{q}_{AC\text{-}o}} \tag{4.16}$$

After calculation of R_{tot}, the value of R_{TS} can be readily obtained from Eq. 4.4 and subsequently used for calculation of T_S via Eq. 4.13.

5.5.6. Analysis of thermal contact resistance

In order to compare the measured values of R_{TS} with theoretical expectations, we estimated R_{TS} from the following equation that was used in past work by us[146] and others[32].

$$R_{TS} = \frac{1}{\pi a} \cdot \frac{2k_s + k_{tip}\tan\theta}{k_s\, k_{tip}\tan\theta} \tag{4.17}$$

Here, k_{tip} (93 $Wm^{-1}K^{-1}$ for chromium[147]) and k_s (130 $Wm^{-1}K^{-1}$ for silicon[148]) are the thermal conductivities of the STP tip and sample, respectively. The contact diameter, a = 5.5 nm, was obtained from Hertzian theory[33] for a tip radius of 50 nm, tip angle of θ = 45° and contact force of 50 nN. The estimated value of R_{TS} is 1.68×10^6 $K\cdot W^{-1}$, which is indeed in the range of experimentally observed values.

Chapter 6 Measurement of Heat Exchange on Operating Tunnel Diodes via Quantitative Scanning Thermal Microscopy

This study was done in collaboration with Shen Yan, Yuxuan Luan, Prof. Edgar Meyhofer, and Prof. Pramod Reddy from University of Michigan, and Zheng Li, Jin Xue, and Prof. Rajeev Ram from Massachusetts Institute of Technology

Heterojunctions are the building blocks of electronics, optoelectronics, and quantum devices. Specifically, semiconductor p-n junctions, are essential elements of devices such as light-emitting diodes (LEDs), transistors, and solar cells[149]. Thermal management is a critical issue in electronics and device packaging and one of the primary limitations of further miniaturization and improvement in computational speed[150]. Theoretical studies have predicted internal cooling via the Peltier effect at the p-n junction[151], which can reduce the need for external cooling systems. Further, internal cooling can improve the energy conversion efficiency of LEDs by effectively operating on a thermodynamic cycle of a heat pump, where the heat removed from the lattice (phonons) is converted and radiated as photons[152,153]. Similarly, internal cooling is theoretically predicted at the junction of tunnel diodes[154], which operate based on quantum tunneling of charge carriers, and are important for several applications including tunneling field-effect transistors, tandem solar cells, and multi-junction laser diodes.

Despite several theoretical studies and great practical potential of internal cooling at p-n junctions, to date, there has been no direct experimental demonstration of this phenomenon. In this study, in collaboration with the Physical Optics and Electronics Group at MIT, we conducted scanning thermal microscopy (SThM) to probe the time-dependent temperature field in the cross section of a tunnel diode. By employing our recently developed quantitative SThM approach (as explained in Chapter 3), we can readily suppress the artifacts related to topography and material variations on the cross section of the diode. Further by employing an averaging scheme, we can resolve temperature variations as small as ~1 mK on the sample. The experimental results clearly indicate cooling at the cross section of the diode, with a temperature profile showing a local minimum close to the p-n junction, when biased with voltages in the range of (-100 mV, 0 V). At larger reverse bias values (V < -100 mV) and forward bias conditions heating was detected in the cross section of the device. These observations are consistent with previous theoretical predictions of Zheng et al.[154], and can be explained based on the energy change of carriers as they transition from the bulk transport states to the tunneling state. We note that while these studies present interesting new finding future work is necessary to further strengthen these findings.

6.1. Introduction

Tunneling is a quantum mechanical phenomenon that allows particles to cross a potential barrier although the energy of the particle is less than the potential barrier. The probability of tunneling is significantly dependent on the width of the potential barrier and the energy of the particles. In this context, we are interested in tunneling of charge carriers, which occurs if the barrier is thin enough and empty sites are available in the right range of energies so that carriers from one side of the barrier can tunnel to these empty sites[155].

The tunnel diode was discovered by Esaki in 1958 and is often called the Esaki diode[156]. A tunnel diode consists of a p-n junction formed by very heavily doped p- and n-sides and a sharp transition in doping profile at the junction and operates based on interband tunneling of carriers across the p-n junction. Tunneling is possible as a result of the small width of the depletion region, on the order of 10 nm (significantly smaller than conventional p-n junctions). Further, tunnel diodes exhibit a negative differential resistance in forward bias, which has enabled a number of applications in high-frequency oscillators, amplifiers, and switches. A similar tunneling effect is used in tandem solar cells, which employ tunnel junctions to integrate different subcells[157], tunneling field-effect transistors (TFETs) which are one of the promising technologies for low-voltage operation and reduced energy consumption in electronics[25], as well as multi-junction laser diodes[158] used as high efficiency and high power illumination sources in LIDAR and 3D sensing applications[159].

In this study, we experimentally investigated heat transfer processes involved in a tunnel diode at a range of bias values. The study of energy conversion and heat transfer in tunnel junctions will assist the analysis and design of a variety of electronic and optoelectronic devices. Below, we briefly introduce various operating regimes of a tunnel diode.

6.1.1. Current-voltage characteristic of tunnel diodes

Figure 6.1 shows the static current-voltage characteristic of a typical tunnel diode. As can be seen, in the reverse bias condition the current increases monotonically. However, in the forward bias, the current first increases to a peak value of I_P (at voltage V_P), then decreases to a local minimum with a valley current of I_V (at voltage V_V), and then it increases monotonically with further increase in forward bias. The total current is the sum of three different components which are shown by

dashed lines in Figure 6.1: (i) interband tunneling current, (ii) excess current, and (iii) diffusion current[155,160].

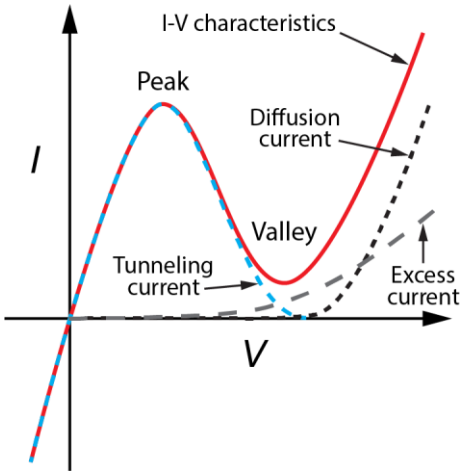


Figure 6.1 Static current-voltage characteristics of a typical tunnel diode (solid line). The total current comprises three components: tunneling current, excess current, and diffusion current as shown by dashed lines[155].

Figure 6.2 shows the simplified energy-band diagram of a tunnel diode at absolute zero temperature (where all the energy states below the Fermi level are fully occupied) and at various bias conditions[155]. Because of high doping, the Fermi level is located within the conduction band in n-side and the valence band in p-side. At zero bias (thermal equilibrium), the Fermi level is constant across the junction (Figure 6.2b). Since there are no empty states (holes) below the Fermi level, and no filled states (electrons) above the Fermi level there is no tunneling current at zero bias. When a reverse or forward bias is applied, the electrons may tunnel from the conduction band to the valence band or vice versa (Figure 6.2a and c). In forward bias, there exists a point where the common bands of energies of occupied states in n-side and unoccupied states in p-side are maximally aligned, at this point the tunneling current reaches its peak value (Figure 6.2c). If the forward bias is further increased, the common energy bands decrease causing a decrease in the tunneling current (generating a region of negative differential resistance on the I-V curve) as shown in Figure 6.2d. If the forward bias is further increased so that the edge of the n-side conduction

band is aligned with the top of the p-side valence band, there are no available common energy bands and the tunneling current will reduce to negligible levels. At this point (valley of the I-V curve), the excess current will dominate which is mainly caused by carrier tunneling via energy states within the forbidden gap. By further increase in the bias, a normal diffusion current starts to flow as shown in Figure 6.2e.

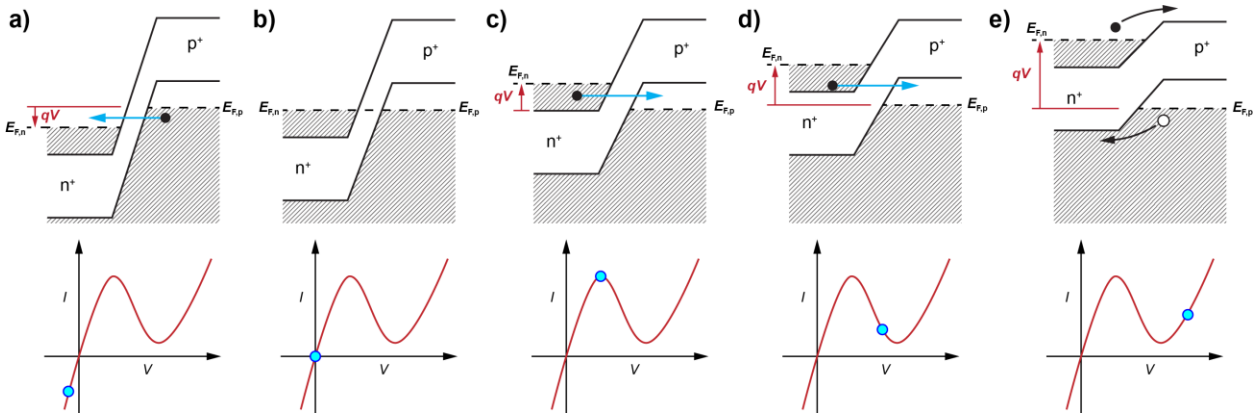


Figure 6.2 Simplified energy-band diagram of a tunnel diode for: (a) reverse bias with monotonically increasing tunneling current, (b) zero bias or thermal equilibrium, (c) forward bias at $V = V_P$ to obtain the peak tunneling current I_P, (d) forward bias approaching valley current in the negative differential resistance region, (e) forward bias with diffusion current.

6.1.2. Energy transfer in various operating regimes of tunnel diodes

To study heat generation and cooling in tunnel diodes, one should consider the average transport energy of carriers within each region of the device, and the energy levels of the tunneling state. Zheng et al.[154] have theoretically studied heating in tunnel diodes operating in forward and reverse tunneling regimes. Here we use Figure 6.3 to explain the mechanisms of heating and cooling within the tunnel diode at different bias conditions, where the effect of Joule heating in the electrodes, active region, and the substrate has been neglected. Figure 6.3a shows the schematic of the band diagram of a tunnel diode and metal contacts (electrodes) in an unbiased condition (thermal equilibrium) at a temperature above absolute zero. The density profiles of electrons $n(E)$ and holes $p(E)$ are also shown in Figure 6.3a. The average transport energies of carriers are shown by red

dashed lines, which are $q|\pi_{n/p}|$ with respect to bulk Fermi levels, where $\pi_{n/p}$ are the Peltier coefficients in the n- and p-bulk respectively.

As can be seen in Figure 6.3b, when a small reverse bias is applied a tunneling current flows at the average tunneling energy shown by the dashed blue line. As electrons that are above the quasi Fermi level tunnel through the barrier, they remove energy from the p-side lattice (by removing energy from the phonons). Similarly, the electrons acquire energy from the n-side lattice to jump from the tunneling energy level to the average transport energy in the n-bulk. Both of these transitions (shown by curved blue arrows in Figure 6.3b) contribute to the cooling of the lattice close to the p-n junction. The removed thermal energy from the lattice close to the p-n junction is later deposited on the metal contacts or in the bulk region close to the metal contacts as shown by red arrows in Figure 6.3b.

As the reverse bias is further increased (Figure 6.3c), heating occurs close to the p-n junction as the electrons deposit energy to the lattice in order to transition to and from the tunneling state. Further, the electrons also deposit heat to the metal contacts via Peltier heating. This heating effect is expected to grow at higher reverse biases as the total energy drop of the carriers increases.

When a forward bias is applied and the device operates in the tunneling current regime ($V \leq V_P$ as shown in Figure 6.3d) the carriers will deposit heat to the lattice close to the p-n junction, in order to transition to and from the tunneling state. Further, as the Fermi levels of electrodes in the n-/p-sides are aligned with their corresponding n-/p- bulk regions, the electrons need to gain energy from the electrodes in order to transfer to the average transport energy in the bulk, which leads to the Peltier cooling effect close to the metal electrodes on both sides of the device[151].

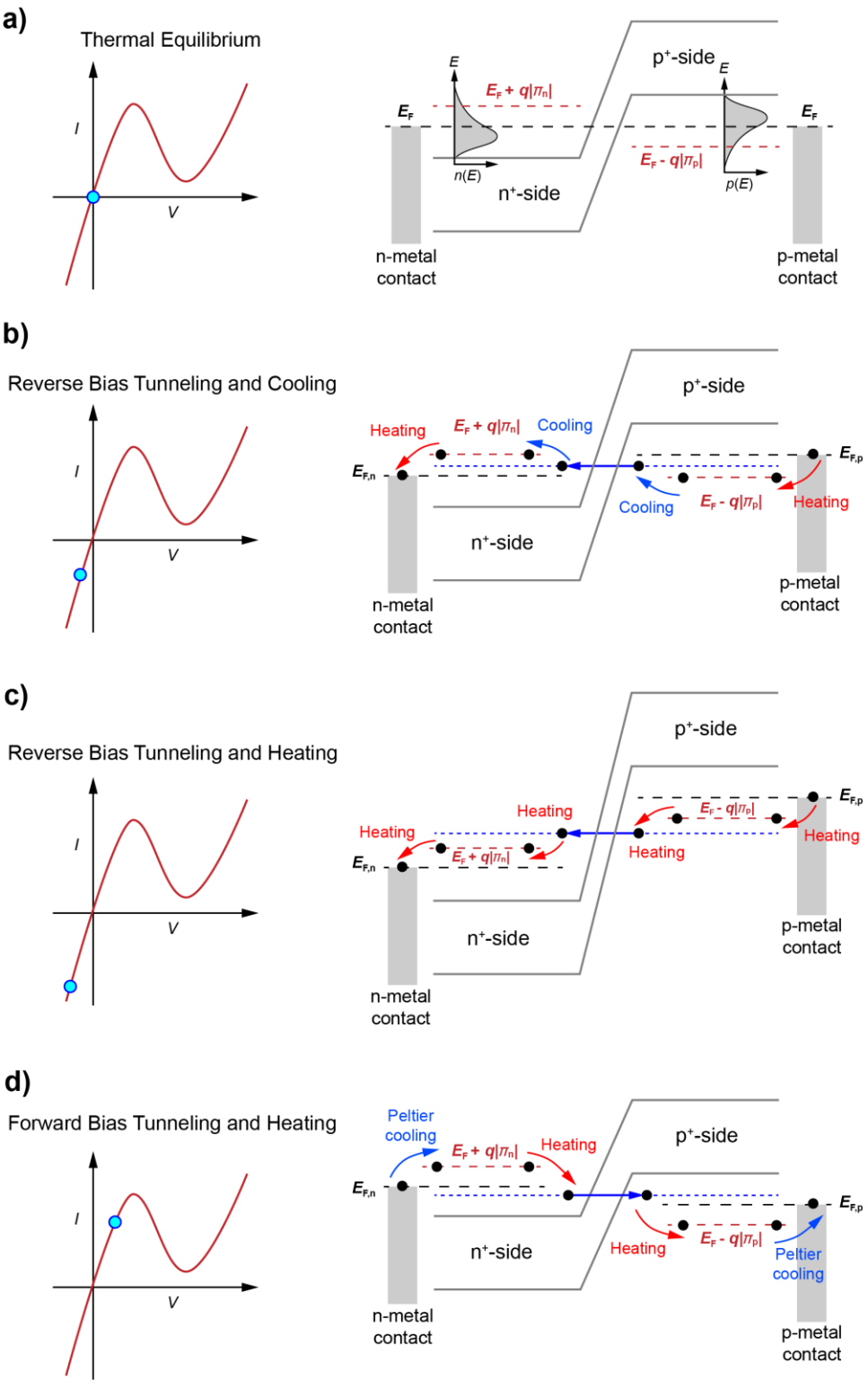


Figure 6.3 The electrical and thermal transport processes in a tunnel diode at various operating regimes, neglecting the effects of Joule heating and excess current. Left panels show the operating point of the tunnel diode on the I-V characteristic. Right panels show the energy-band diagram.

6.2. Measurement setup

Figure 6.4 illustrates the measurement setup of the cross-sectional scanning thermal microscopy on operating diodes. Figure 6.4a shows the scanning probe microscopy stage, which has a Beetle design in which the scanner head is standing directly on three piezo legs on the ramps on the sample holder stage[161]. A custom-fabricated Aluminum sample holder is mounted on the SPM stage which allows for tip/tilt/z alignment via three set screws which have a ceramic ball attached to them, each making a point contact with the SPM stage. A glass-encapsulated thermistor with 10 kOhm nominal resistance (TDK Electronics B57550G1103F000) was mounted on the Aluminum sample holder close to the sample location to measure a temperature labeled as T_{bulk}. As shown in the inset of Figure 6.4a, the cleaved diode sample is mounted on a leadless ceramic chip carrier (Spectrum Semiconductor Materials LCC00305) via a 25 μm thick Indium film to provide an electrical connection to the backside of the diode. The front electrode of the diode is a gold film with ~400 nm thickness which protrudes above the cleaved surface to ensure a 1D through-plane electrical current direction on the cleaved surface of the diode. The scanning thermal probe (STP) is shown schematically in the inset of Figure 6.4a, which scans a rectangular area in a direction perpendicular to the device edge.

Figure 6.4b shows the cross section of the SPM stage, which is simultaneously cooled via a liquid nitrogen cryostat cold finger and heated radiatively via a filament. The temperature of the Al sample holder (T_{bulk}) is controlled and stabilized at a desired setpoint by using a PID feedback controller, which adjusts the filament current. As the power dissipated in the diode sample varies at different bias voltages, the filament current is adjusted automatically to compensate for the change in the total heating power dissipated on the SPM stage.

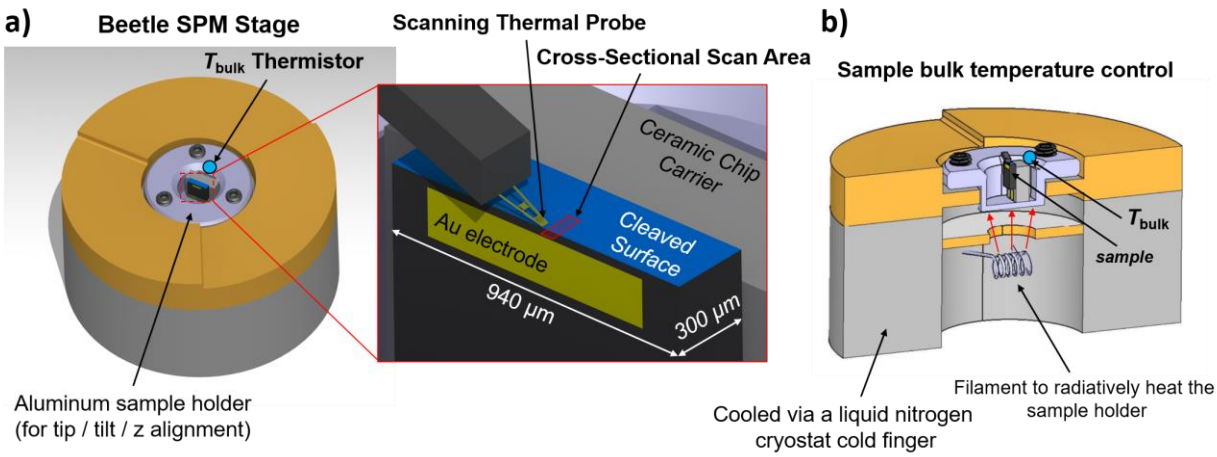


Figure 6.4 Schematic of the measurement setup for cross-sectional scanning thermal microscopy of tunnel diodes. (a) A Beetle type scanning probe microscopy (SPM) stage containing a custom-made aluminum sample holder with tip/tilt/z alignment. Inset shows a cleaved diode sample mounted on a ceramic chip carrier which is mounted on the aluminum sample holder. The scanning thermal probe is shown, which scans on the cross section of the device. (b) Cross section of the SPM stage. The blue ball indicates a glass-encapsulated thermistor used for measurement and stabilization of sample holder temperature (T_{bulk}). A filament heater is used to heat the Aluminum sample holder radiatively from backside.

6.3. Tunnel diode sample

Figure 6.5 shows an SEM micrograph of the cleaved cross section of a tunnel diode sample close to the device edge showing various device layers and doping levels. The device has the following layers and nominal dimensions: n-InP substrate, 1 µm layer of n^+-InGaAs, 1 µm layer of p^+-InGaAs, 0.1 µm layer of p^{++}-InGaAs, plus a ~0.4 µm Au film as the top electrode. The current-voltage characteristic of this tunnel diode device is shown in Figure 6.6, which was measured when the device was mounted in the SPM for subsequent thermal scanning. As can be seen, the peak current occurs at V_P = 382 mV and the valley current occurs at V_V = 433 mV.

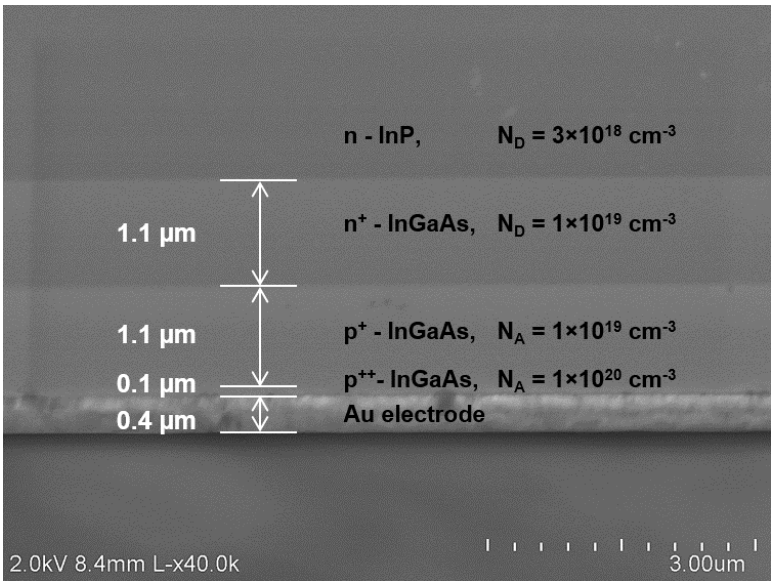


Figure 6.5 SEM micrographs of the cleaved diode surface showing multiple device layers and the doping levels.

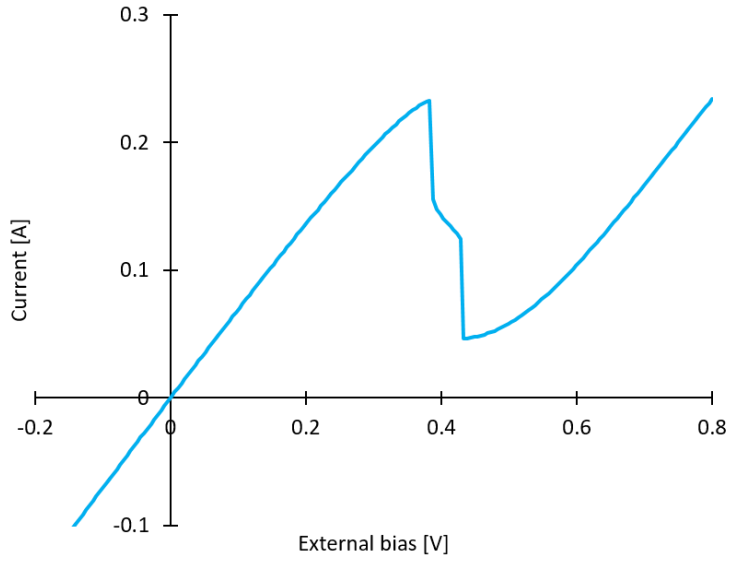


Figure 6.6 Current-voltage characteristics of the tunnel diode sample used in this study.

To check the quality of epitaxial growth of various layers of the tunnel diode sample, we took cross-sectional Scanning Transmission Electron Microscopy (STEM) images of this device by preparing a thin (50 – 100 nm thickness) cross section sample using focused ion beam (FIB). Figure 6.7a shows cross-sectional STEM images obtained at the interface of the n-InP substrate and n^+-InGaAs layer. Clear contrast is observed between the top region (n-InP) and bottom region

(n^+-InGaAs). By traversing along the interface and taking multiple images, we observed no dislocations or defects in the interface. Figure 6.7b shows the averaged intensity profile indicating an intensity contrast across the interface, where the width of the interface for a complete transition from one material to the other occurs within five atomic layers. Figure 6.7c shows a large area (115 nm × 115 nm) STEM image taken from the expected location of the p-n junction. As can be seen, no intensity gradient, dislocations, or defects can be observed. In fact, it was impossible to find the p-n junction using STEM images. Therefore, it is expected that there is no interface thermal resistance across the p-n junction as the crystal lattice is completely uniform.

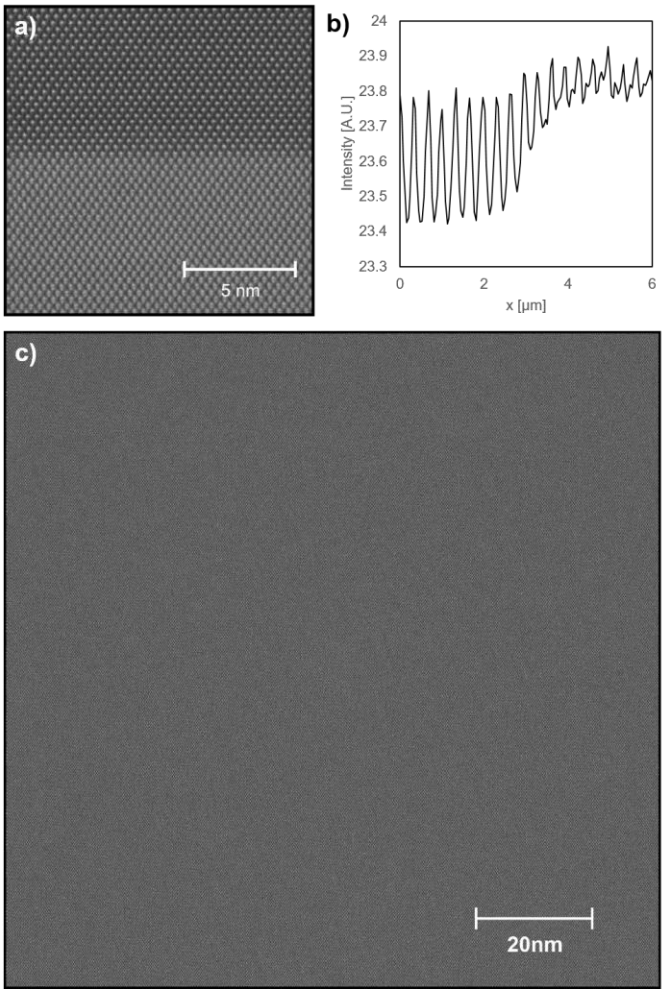


Figure 6.7 Cross sectional STEM images of a tunnel diode sample. (a) image taken at the interface of n-InP (top material) and n^+-InGaAs (bottom material). (b) Averaged intensity profile which shows the intensity contrast across

the InP/InGaAs interface. (c) Large area STEM image at the expected location of the p-n junction, which shows a uniform crystal structure with no defects or discontinuity across the junction.

In order to identify the location of the p-n junction and the width of the depletion region, we imaged the built-in electric field at the p-n junction using Differential Phase Contrast (DPC)-STEM (TFS Talos F200X G2 STEM microscope) with an imaging technique described in Ref. [162]. Figure 6.8a shows the DPC image obtained at low magnification from the entire active region of the diode. The arrangement of the DPC segmented detector is shown in the top right corner of the image. The image shows the differential (A-C) signal of the segmented detector which shows a dark vertical line at the center of the image which is generated by the built-in potential of the p-n junction and indicates the location of the junction. Further, the image shows a bright vertical line on the left side of the image, which shows the built-in potential at the n-n^+ interface. Figure 6.8b shows a zoomed-in DPC (A-C) image of the p-n junction. The averaged (A-C) signal along the red arrow in Figure 6.8b is shown in Figure 6.8c. The width of the dip in the A-C signal, i.e. the full width at half max (FWHM), is 18.67 nm and can be used as an estimate of the width of the depletion region within the resolution limits of the image.

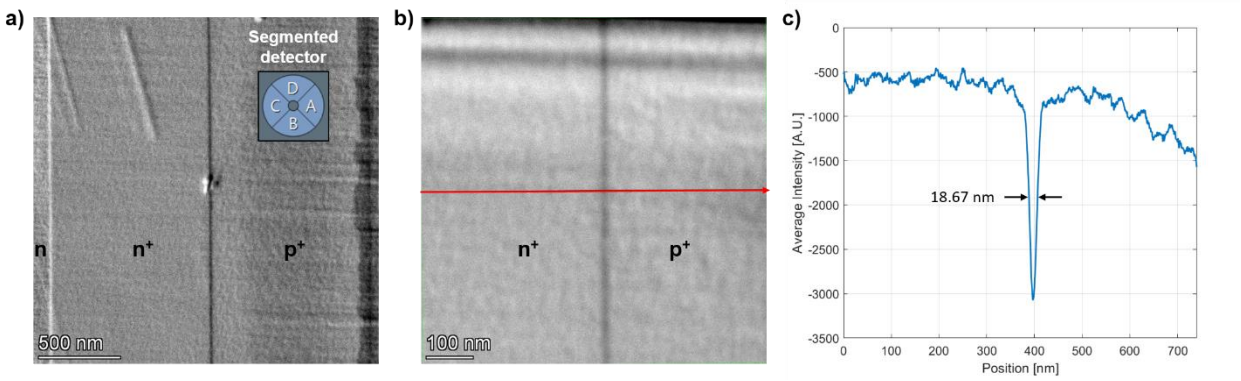


Figure 6.8 (a) DPC-STEM image of the cross section of a tunnel diode. The top right corner shows the arrangement of segmented DPC detector. The image shows the differential (A-C) signal of the segmented detector. (b) Zoomed in DPC-STEM image (A-C) of the p-n junction. (c) Averaged intensity of the image in panel b along the profile direction shown by red arrow.

6.4. Scanning thermal microscopy results

To scan the temperature field on the cross section of the active region of the diode, first, we needed to identify the edge of the device. This was particularly a challenging task as it required approaching the probe on the cross section in a location 50-100 μm away from the cross section to make sure the probe does indeed form contact via its tip to the sample surface. Then marching the probe in a stepwise manner towards the edge with increments of < 5 μm and taking a topography scan at each step. The edge of the device is identified as a location where a portion of the topography scan shows a sharp declining step where the probe cannot detect any contact with the sample (i.e. the AFM normal force setpoint cannot be maintained). However, such a topographical feature may also exist in places other than the edge of the device, for instance, large steps were observed in the Scanning Electron Microscopy (SEM) images, which were generated during the cleaving process. Therefore, in addition to the sharp declining step, we search for a location where there is a bump in the topography as a result of the cleaved gold electrode, and where a similar topography is observed as we move laterally along the edge of the device. An example topography scan at the edge of the diode is shown in Figure 6.9, where the gold electrode protrudes ~100 nm above the device cross section. As can be seen in the inset of Figure 6.9b, the cleaved cross section is very flat and features a topography standard deviation of ~1.75 nm.

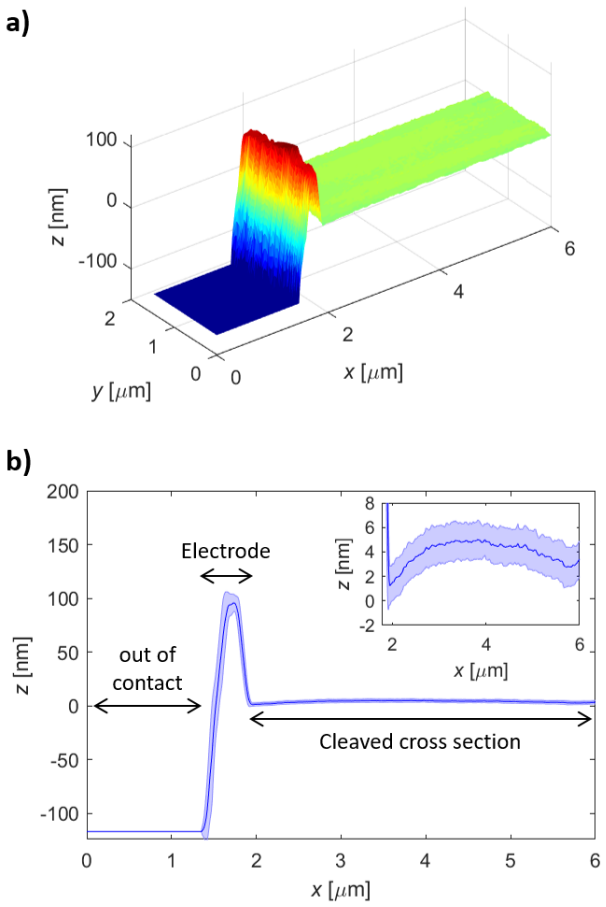


Figure 6.9 (a) Topography scan at the edge of the cleaved diode, (b) Averaged topography profile along the y-axis of panel a showing different regions of the topography. The inset shows the surface topography on the cleaved cross section of the device having a standard deviation of 1.75 nm.

6.4.1. Steady state temperature field measurements under unmodulated bias conditions

To map the temperature field of the sample under steady (unmodulated) bias conditions, we first retracted the probe to ~300 nm above the surface to avoid any damage due to thermal expansion or mechanical drift of the device when the bias was changed. Next, we incrementally changed the bias, starting from a zero bias voltage to the target bias. After each bias increment, the temperature of the stage was perturbed as a result of a change in the dissipated power on the device which required waiting for the stage temperature controller to settle back to the desired setpoint.

The thermal scan condition was as follows. The scan area dimensions are ~6 μm × 1.5 μm and the scanned image size is 512 × 64 pixels. The scan was performed in a pixel mode where the probe was stopped at a pixel location and acquired data for 500 ms before moving to the next pixel at a rate of 300 nm/s. The line scan direction was horizontal (in the following scan images) and the normal force setpoint for the scan was ~20 nN.

Figure 6.10 shows the results of a thermal scan on the cross section of the diode at zero bias. At this condition there is no power dissipated in the device; therefore, it is expected that the entire device is in thermal equilibrium with the Aluminum sample holder at 300 K. Figure 6.10a shows the topography scan where the regions corresponding to the electrode, active region, and the substrate are indicated. The T_{DC} image is shown in Figure 6.10b. Although it is expected that the entire sample is at a uniform temperature (since no bias is applied to the diode), the T_{DC} image still shows a clear contrast between the substrate (InP with thermal conductivity of 68 W/m-k[163]) and the active region (InGaAs with thermal conductivity of 5 W/m-K[163]), where a sharp transition in T_{DC} is observed as a result of different thermal conductivities of these two materials, which affect the probe tip-sample thermal resistance as discussed in section 5.5.6. Analysis of thermal contact resistance). In addition, the Au electrode is also observed to be at a higher average temperature in the T_{DC} image because of abrupt topography variation and convex surface making poor thermal contact with the STP tip. The aforementioned material and topography variations are independently captured in the T_{AC} image of Figure 6.10c allowing for estimation of tip-sample thermal contact resistance R_{TS} in Figure 6.10d. Finally, the surface temperature was obtained using the CR-SThM technique in Figure 6.10e, which has mostly removed the effect of material variation on the surface temperature. However, the effect of topography of electrode on the surface

temperature is not completely removed due to abrupt topography variation with many small topographical features.

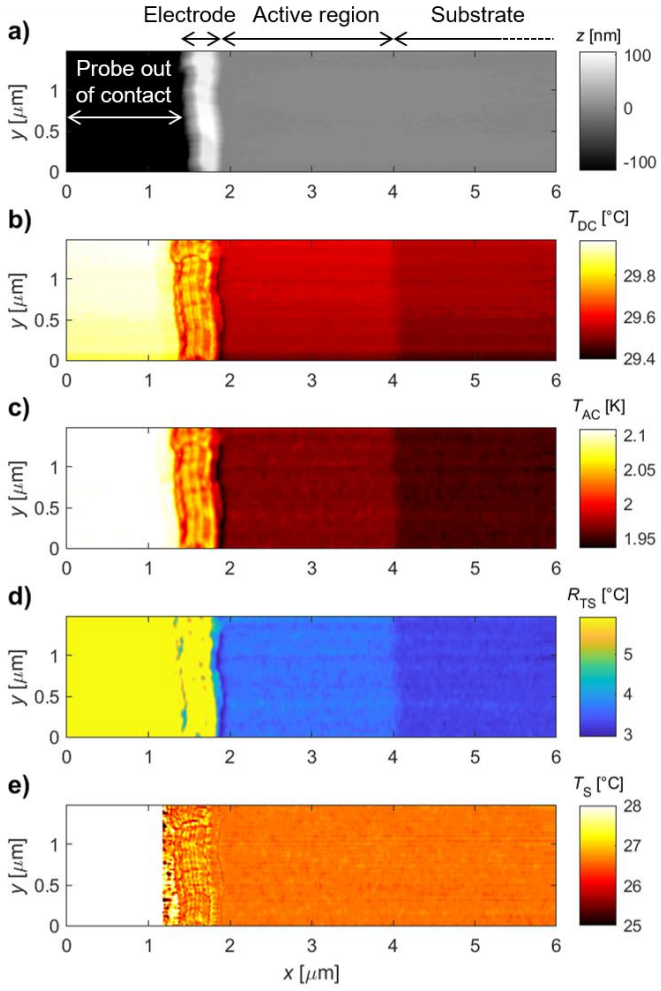


Figure 6.10 Data obtained from thermal scan using the CR-SThM method at the cross section of a tunnel diode at zero bias. Data shown in all panels were obtained simultaneously in a single scan. (a) Topography scan showing different regions of the device, (b) DC temperature (T_{DC}) measured by the probe, (c) Amplitude of AC temperature oscillations (T_{AC}) of the probe measured by probe. (d) Estimated tip-sample thermal resistance R_{TS} obtained using Eq. 3.2, (e) extracted surface temperature map (T_S) using Eq. 3.1. The pixel-to-pixel standard deviation of T_S on the active region plus the substrate is 65 mK.

Due to the translational symmetry of the device along the *y*-axis of the thermal scan in Figure 6.10, we averaged the scans along the *y*-axis and plotted them in Figure 6.11 along with a shaded error bar showing ±1 standard deviations of the averaged profiles. The dashed vertical lines in all the panels of Figure 6.11 indicate various regions of the device as labeled in Figure 6.11a. The probe

T_{DC} and T_{AC} profiles are shown in Figure 6.11b, which both indicate a sharp contrast between the active region and the substrate with an averaged transition full width of 174 nm. The averaged probe tip-sample thermal resistance (R_{TS}) profile is shown in Figure 6.11c which indicates a large value on the electrode region. As discussed above, this is due to the high roughness and convex surface of the electrode generating a poor thermal contact with the probe tip. In addition, the R_{TS} value is 3.657 ± 0.077 MK/W on the active region of the device (InGaAs) and is 3.296 ± 0.061 MK/W for the substrate region (InP). As discussed previously, this contrast in R_{TS} is due to the difference in the thermal conductivities of the two materials.

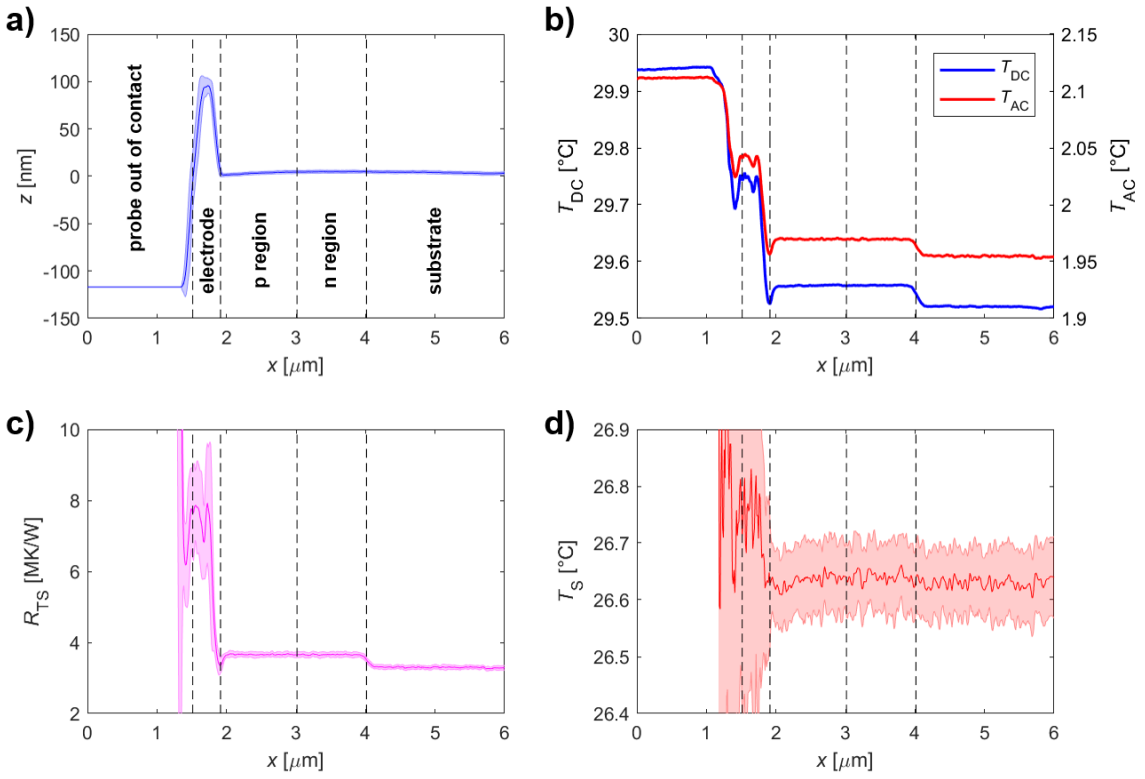


Figure 6.11 Averaged profiles obtained during thermal scanning of a tunnel diode at zero bias. To obtain the averaged profiles the image was averaged in *y*-direction (i.e. the line scans were averaged). The shaded region indicates ±1 standard deviations of the averaged profiles. (a) Topography profile, (b) DC and AC temperatures measured by the probe, (c) Estimated tip-sample thermal resistance R_{TS} obtained from Eq. 2. (d) Extracted sample surface temperature.

We repeated the thermal scan at different unmodulated (DC) sample bias values. The temperature resolution of the DC bias scans was not sufficient to resolve a temperature gradient on the surface. However, we note that spatial variations of temperature with smaller magnitudes exist which are measured in modulated bias condition as explained in the following sections.

6.4.2. Time-dependent local temperature measurements under modulated bias conditions

Now that we established the CR-SThM technique correctly maps the surface temperature on the tunnel diode by removing artifacts caused by variation of material thermal conductivity, we implement the same technique to measure smaller temperature changes on the surface under modulated bias conditions. The reason for measurements under modulated bias condition is twofold: (i) to improve the signal-to-noise ratio of the sample surface temperature measurement, (ii) to make a time-dependent measurement of sample surface temperature field which allows us to account for effects from slow heating of various components such as the ceramic chip carrier and Aluminum sample holder (shown in Figure 6.4a).

We started by making a time-dependent measurement of sample surface temperature at a fixed spatial location. To do so, we parked the scanning thermal probe close to the p-n junction and applied a three-level bias pulse to the device. The bias waveform had a total period of 20s which consisted of 0 mV with a duration of 9s, followed by -25 mV for 1s, 0 mV for 9s, and +25 mV for 1s. This bias waveform is plotted as the dashed line in all panels of Figure 6.12. As a result of applied bias waveform the sample surface temperature changes over time which were measured via the CR-SThM technique. A total of 9900 pulse periods were recorded, and the resulted $T_S(t)$ time series were averaged to improve the signal-to-noise ratio. Figure 6.12 shows the averaged surface temperature as a function of time for different numbers of averaged periods starting from

200 periods (Figure 6.12a) to 9900 periods (Figure 6.12f). The shaded error bars in Figure 6.12 indicate 95% confidence interval of the averaged signal. As can be seen in Figure 6.12f, by averaging 9900 periods, the confidence interval of the time series signal has decreased to an average of ±0.71 mK, significantly improving the signal-to-noise ratio of the measurement.

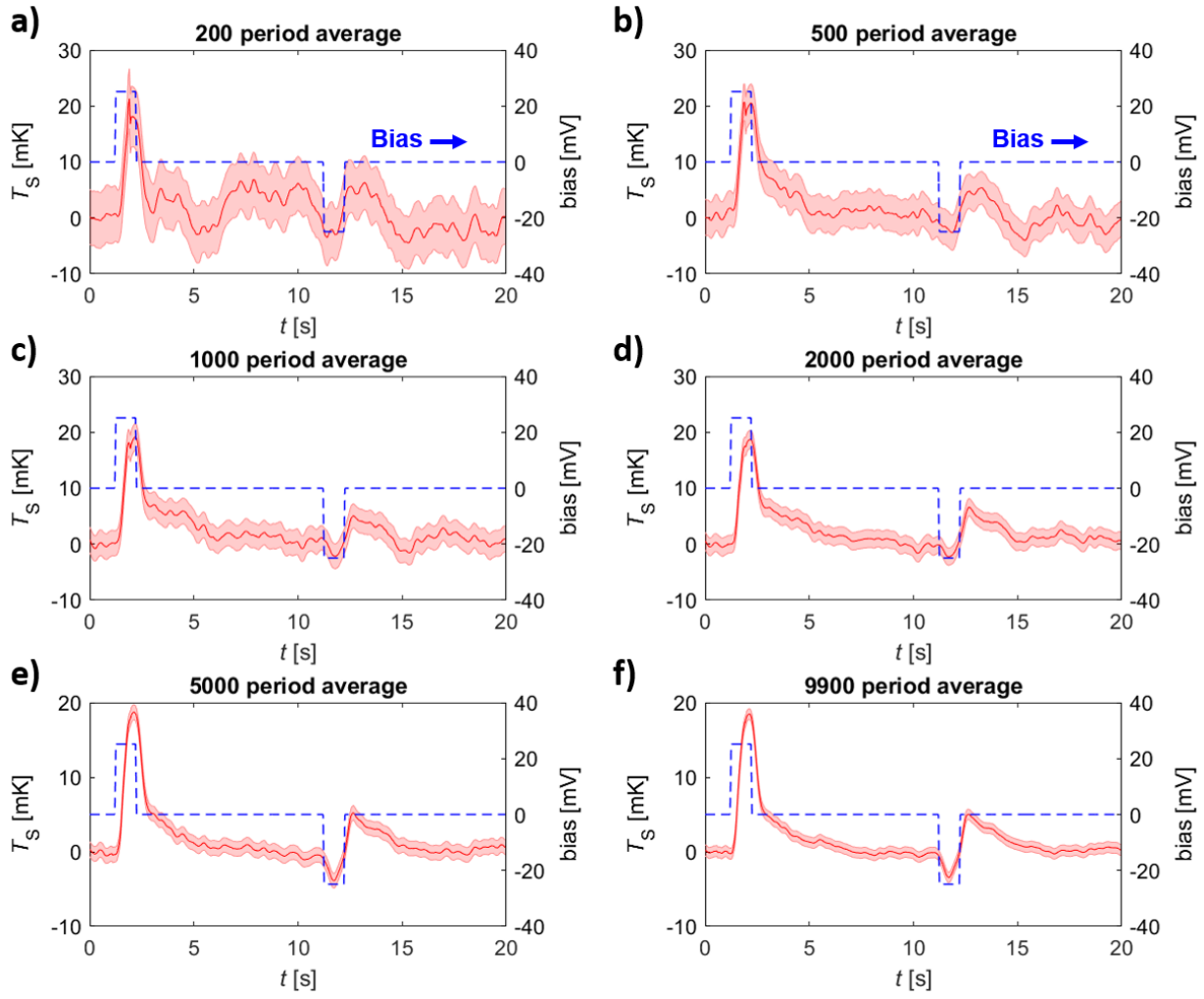


Figure 6.12 Averaging scheme used in time-domain measurement of sample surface temperature (T_S) when a three-level pulse (-25 mV/ 0 mV/ +25 mV) was applied to the diode. The dashed lines indicate the applied bias waveform. The scanning thermal probe was stationary and parked close to the p-n junction on the cross section of the diode. The red curves indicate the averaged time-series, and the shaded regions indicate the 95% confidence interval of the averaged signal. (a) 200 pulse periods averaged, (b) 500 pulse periods averaged, (c) 1000 pulse periods averaged, (d) 2000 pulse periods averaged, (e) 4000 pulse periods averaged, (f) 9900 pulse periods averaged.

The results of Figure 6.12f is replotted in the larger plot of Figure 6.13. As can be seen, the surface temperature signal indicates heating during the positive bias (+25 mV) pulse, and cooling during the negative bias (-25 mV) pulse. The heating profile during the positive pulse resembles the response of a first-order thermal system with a saturating temperature increase when the pulse is turned on, and an exponential decay when the pulse is turned off. However, the cooling profile during the negative bias shows a different behavior with four different steps (labeled in Figure 6.13) as we briefly explain below:

Step 1: When the -25 mV bias pulse begins, a rapid drop in the temperature of the diode chip is observed because of a negative heat source located on the diode and the short thermal response time of the diode chip.

Step 2: As the -25 mV pulse continuous, slow heating of the diode was observed as a result of heating primarily in the ceramic chip carrier, due to the positive heat source (Joule and Peltier heating) deposited on the chip carrier and its long thermal response time.

Step 3: When the -25 mV pulse is turned off, a sudden increase in the diode temperature was observed because of the removal of the negative heat source on the diode and rapid thermal equilibrium of the diode chip with the heated ceramic chip carrier, which has a long response time and still has a high temperature at this time.

Step 4: The previously heated chip carrier slowly cools as a result of the long thermal response time, resulting in a slow reduction in diode temperature until thermal equilibrium is reached.

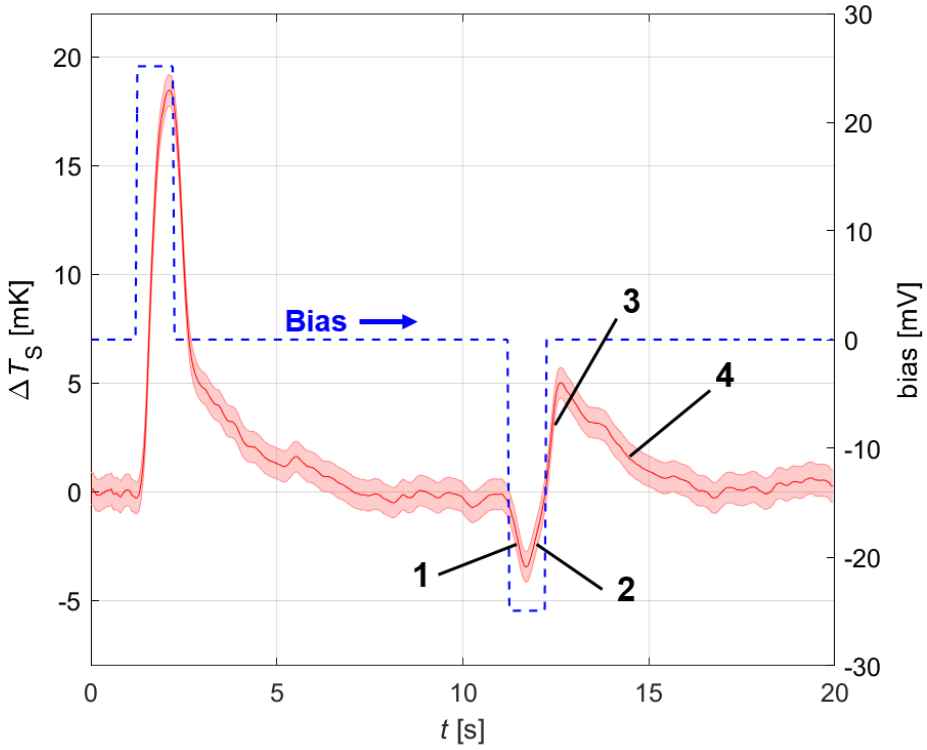


Figure 6.13 Time-domain response of the diode temperature to an applied 3-level bias pulse (-25 mV/ 0 mV/ +25 mV) shown by the dashed blue line. For this measurement, the scanning thermal probe was stationary and parked close to the p-n junction on the cross section of the diode. The red curve shows average of 9900 measurements and the shaded region shows the 95% confidence interval. Four steps of the temperature change during and after the -25 mV bias pulse are labeled.

6.4.3. Time-dependent temperature field measurements under modulated bias conditions

Now that we have established the capability of the CR-SThM with a long averaging scheme to measure the time-dependent temperature of the diode, we apply the same measurement procedure to perform a line scan on the cross section of the device. First, we applied a 2-level pulse bias between zero bias and the target bias value with a period of 2s, and a duty cycle of 50 %. Next, the line scan was done by stopping the probe at each pixel for a duration of 10,000 s to collect a total of 5000 full cycles of bias, which were averaged to obtain a time-domain signal for each pixel, As an example, Figure 6.14 shows the averaged time-domain signal for a 2-level bias pulse of (0 mV/-25 mV). Next, we calculated the temperature change by applying the bias at location x_i

with respect to the zero-bias condition as defined in Eq. 5.2. Where, $T_{s\text{-}zero}$ is the average of all data points in the averaged time-domain signal where the bias is zero (shown by the blue region in Figure 6.14), and $T_{s\text{-}high}$ is the average of data points when a non-zero bias is applied starting with a lag time of t_{lag} after the start of the pulse (green region in Figure 6.14). The lag time in averaging was incorporated to obtain the time dependence of temperature change during the pulse. When t_{lag} = 0, all the data points during the bias pulse are incorporated in calculating the average temperature change.

$$\Delta T_s\,(x_i,\, t_{lag}) = T_{s\text{-}high}\,(x_i,\, t_{lag}) - T_{s\text{-}zero}\,(x_i) \tag{5.2}$$

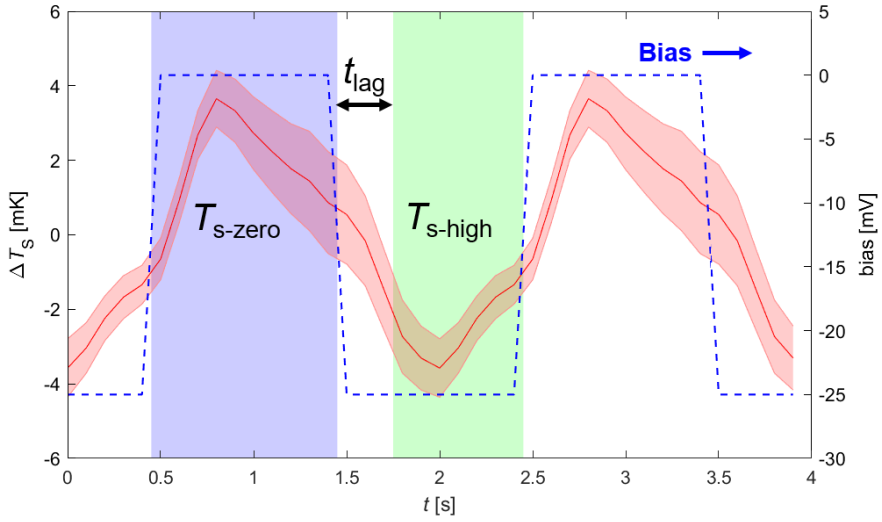


Figure 6.14 Time-domain response of the diode surface temperature to an applied 2-level bias pulse at 0 mV / -25 mV. To calculate the temperature change when a bias pulse is applied, we defined two regions of the time series, shown by blue (for zero bias), and green (for non-zero bias).

We conducted line scans with 8 pixels per line at several bias pulse values and calculated the temperature change (ΔT_s) for various t_{lag}. Figure 6.15 shows the results of a line scan on the active region of the device at a modulated bias of 0 mV/ -50 mV. Figure 6.15a shows the coarse topography scan obtained during the thermal scan (circle markers), as well as a fine topography scan (dashed line) which was obtained exactly before starting the thermal scan which helps to

identify the location of each pixel on the coarse scan. Figure 6.15b shows the mean ΔT_s for each pixel and a number of t_{lag} values, and the error bars indicate 95% confidence interval of the mean which is on average ±1.5 mK. As can be seen, the surface temperature of the diode shows a local minimum close to the p-n junction with a value of -5.4 mK for t_{lag} = 0, which may be a result of local negative heat sources close to the junction on both the p- and n-doped regions as theoretically shown by Zheng et al.[154]. Further, as the t_{lag} increases, the ΔT_S increases at all locations as a result of heating of the ceramic chip carrier as demonstrated and explained in step 2 of Figure 6.13.

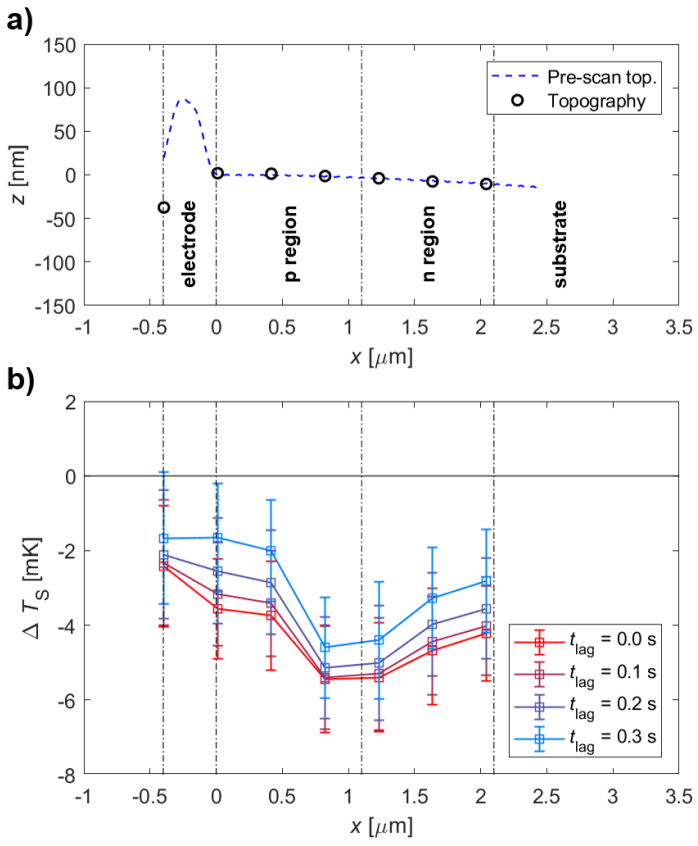


Figure 6.15 Thermal line scan under modulated bias pulse of 0 mV / -50 mV with a period of 2 s and duty cycle of 50%. (a) Topography scan obtained during the coarse thermal scan (circle markers), and a fine topography scan obtained exactly before the thermal scan (dashed line). (b) Mean surface temperature change ΔT_s obtained by averaging 5000 bias pulses as a function of location and lag time. Error bars represent 95% confidence interval of the mean.

We repeated the thermal scans under modulated bias conditions (similar to Figure 6.15) at various bias values. Figure 6.16 shows the average temperature change (ΔT_S), considering a lag time of t_{lag} = 0.1s, for the entire active region of the device (excluding the electrode). The error bars represent the 95% confidence interval in the averaged value of ΔT_S. The largest average temperature drop is 4.9 mK at a bias voltage of -50 mV. The blue curve shows quadratic fit to the data points, and the green shaded area shows the region of the curve where cooling is observed.

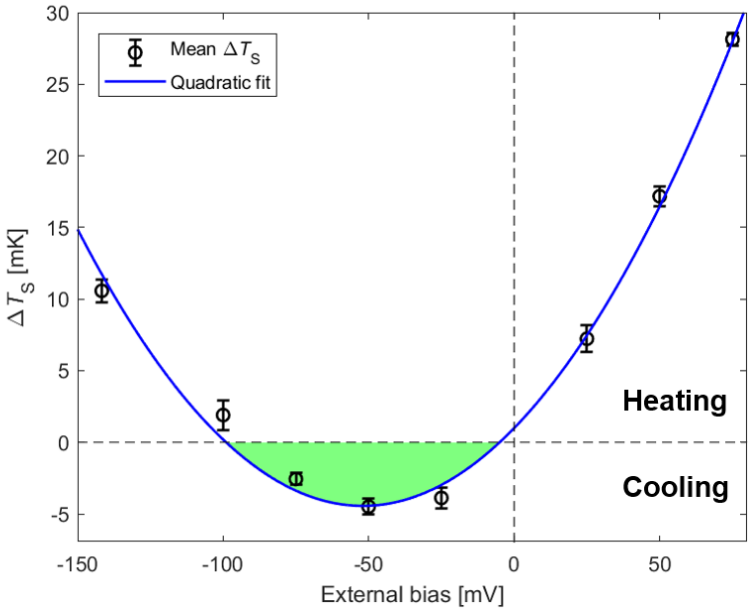


Figure 6.16 Measured average temperature change (ΔT_S) on the cross section of the tunnel diode under modulated bias condition, with a lag time of t_{lag} = 0.1s, for the entire active region of the device. Error bars represent 95% confidence interval of the mean. Blue curve shows a quadratic fit to the data, and the green shaded region indicates cooling.

6.6. Conclusions

In summary, we experimentally studied the heat exchange in a tunnel diode via cross-sectional thermal scans using the CR-SThM technique (presented in Chapter 3). Using a pulsed bias technique with long averaging times, we observed cooling in the reverse bias tunneling current regime at small bias values (-100 mV < bias < 0), and heating in larger reverse bias and forward

bias conditions. Using coarse thermal scans with a long averaging time per pixel, we identified a local minimum in the temperature field close to the p-n junction at small reverse bias values. These observations are consistent with the previous theoretical study of Zheng et al.[154], and can be explained based on the energy change of carriers as they transition from bulk n- and p- regions to the tunneling state leading to energy extraction from the lattice, which causes a cooling effect close to the p-n junction.

References

1 Kardar, M. *Statistical physics of particles*. (Cambridge University Press, 2007).

2 Carlos, L. D. & Palacio, F. *Thermometry at the nanoscale: Techniques and selected applications*. (Royal Society of Chemistry, 2015).

3 Bailyn, M. A survey of thermodynamics(Book). *New York: AIP Press, 1994.* (1994).

4 Feynman, R. P., Leighton, R. B. & Sands, M. *The Feynman lectures on physics, Vol. I: The new millennium edition: mainly mechanics, radiation, and heat*. Vol. 1 (Basic books, 2011).

5 Tan, S. *Sub nano kelvin thermometry and temperature stabilization using resonant cavity thermometry*, Stanford University, (2016).

6 Reihani, A., Lim, J. W., Fork, D. K., Meyhofer, E. & Reddy, P. Microwatt-Resolution Calorimeter for Studying the Reaction Thermodynamics of Nanomaterials at High Temperature and Pressure. *ACS Sensors* **6**, 387-398 (2020).

7 Hur, S., Mittapally, R., Yadlapalli, S., Reddy, P. & Meyhofer, E. Sub-nanowatt resolution direct calorimetry for probing real-time metabolic activity of individual C. elegans worms. *Nature Communications* **11**, 1-9 (2020).

8 Luo, K., Herrick, R., Majumdar, A. & Petroff, P. Scanning thermal microscopy of a vertical-cavity surface-emitting laser. *Applied Physics Letters* **71**, 1604-1606 (1997).

9 Halbertal, D. *et al.* Nanoscale thermal imaging of dissipation in quantum systems. *Nature* **539**, 407-410 (2016).

10 Richards, P. Bolometers for infrared and millimeter waves. *Journal of Applied Physics* **76**, 1-24 (1994).

11 Pirro, S. & Mauskopf, P. Advances in bolometer technology for fundamental physics. *Annual Review of Nuclear and Particle Science* **67**, 161-181 (2017).

12 Sengupta, K., Nagatsuma, T. & Mittleman, D. M. Terahertz integrated electronic and hybrid electronic–photonic systems. *Nature Electronics* **1**, 622-635 (2018).

13 Calizo, I., Balandin, A., Bao, W., Miao, F. & Lau, C. Temperature dependence of the Raman spectra of graphene and graphene multilayers. *Nano Letters* **7**, 2645-2649 (2007).

14 Schirhagl, R., Chang, K., Loretz, M. & Degen, C. L. Nitrogen-vacancy centers in diamond: nanoscale sensors for physics and biology. *Annual Review of Physical Chemistry* **65**, 83-105 (2014).

15 Tan, S., Wang, S., Saraf, S. & Lipa, J. A. Pico-Kelvin thermometry and temperature stabilization using a resonant optical cavity. *Optics Express* **25**, 3578-3593 (2017).

16 Weng, W. *et al.* Nano-Kelvin thermometry and temperature control: beyond the thermal noise limit. *Physical Review Letters* **112**, 160801 (2014).

17 Loh, W., Yegnanarayanan, S., O'Donnell, F. & Juodawlkis, P. W. Ultra-narrow linewidth Brillouin laser with nanokelvin temperature self-referencing. *Optica* **6**, 152-159 (2019).

18 Strekalov, D., Thompson, R., Baumgartel, L., Grudinin, I. & Yu, N. Temperature measurement and stabilization in a birefringent whispering gallery mode resonator. *Optics Express* **19**, 14495-14501 (2011).

19 Qian, W. *et al.* High-sensitivity temperature sensor based on an alcohol-filled photonic crystal fiber loop mirror. *Optics Letters* **36**, 1548-1550 (2011).
20 David, R. & Hunter, I. W. A liquid-in-glass thermometer read by an interferometer. *Sensors and Actuators A: Physical* **121**, 31-34 (2005).
21 Festa, C. Thermostat with±0.5 μ K monitoring sensitivity. *Journal of Physics E: Scientific Instruments* **16**, 683 (1983).
22 Benson, B. B. & Krause Jr, D. Use of the quartz crystal thermometer for absolute temperature measurements. *Review of Scientific Instruments* **45**, 1499-1501 (1974).
23 Sadat, S. *et al.* Room temperature picowatt-resolution calorimetry. *Applied Physics Letters* **99**, 043106 (2011).
24 Sadat, S., Meyhofer, E. & Reddy, P. High resolution resistive thermometry for micro/nanoscale measurements. *Review of Scientific Instruments* **83**, 084902 (2012).
25 Markov, I. L. Limits on fundamental limits to computation. *Nature* **512**, 147-154 (2014).
26 Yang, J.-M., Yang, H. & Lin, L. Quantum dot nano thermometers reveal heterogeneous local thermogenesis in living cells. *ACS Nano* **5**, 5067-5071 (2011).
27 Kucsko, G. *et al.* Nanometre-scale thermometry in a living cell. *Nature* **500**, 54-58 (2013).
28 Weaver, J. B. Hot nanoparticles light up cancer. *Nature Nanotechnology* **5**, 630-631 (2010).
29 Brites, C. D. *et al.* Thermometry at the nanoscale. *Nanoscale* **4**, 4799-4829 (2012).
30 Christofferson, J. *et al.* Microscale and nanoscale thermal characterization techniques. (2008).
31 Zhang, Y. *et al.* A review on principles and applications of scanning thermal microscopy (SThM). *Advanced Functional Materials* **30**, 1900892 (2020).
32 Majumdar, A. Scanning thermal microscopy. *Annual Review of Materials Science* **29**, 505-585 (1999).
33 Kim, K., Jeong, W., Lee, W. & Reddy, P. Ultra-high vacuum scanning thermal microscopy for nanometer resolution quantitative thermometry. *Acs Nano* **6**, 4248-4257 (2012).
34 Menges, F. *et al.* Temperature mapping of operating nanoscale devices by scanning probe thermometry. *Nature Communications* **7**, 1-6 (2016).
35 Gomes, S. *et al.* Application of scanning thermal microscopy for thermal conductivity measurements on meso-porous silicon thin films. *Journal of Physics D: Applied Physics* **40**, 6677 (2007).
36 Juszczyk, J., Kaźmierczak-Bałata, A., Firek, P. & Bodzenta, J. Measuring thermal conductivity of thin films by Scanning Thermal Microscopy combined with thermal spreading resistance analysis. *Ultramicroscopy* **175**, 81-86 (2017).
37 Bozec, L. & Odlyha, M. Thermal denaturation studies of collagen by microthermal analysis and atomic force microscopy. *Biophysical Journal* **101**, 228-236 (2011).
38 Ryu Cho, Y. K. *et al.* Sub-10 nanometer feature size in silicon using thermal scanning probe lithography. *ACS Nano* **11**, 11890-11897 (2017).
39 Lytken, O., Lew, W. & Campbell, C. T. Catalytic reaction energetics by single crystal adsorption calorimetry: hydrocarbons on Pt (111). *Chemical Society Reviews* **37**, 2172-2179 (2008).
40 Fischer-Wolfarth, J.-H. *et al.* An improved single crystal adsorption calorimeter for determining gas adsorption and reaction energies on complex model catalysts. *Review of Scientific Instruments* **82**, 024102 (2011).

41 Giel, H., Henriques, D., Bourne, G. & Markus, T. Investigation of the heat generation of a commercial 2032 (LiCoO2) coin cell with a novel differential scanning battery calorimeter. *Journal of Power Sources* **390**, 116-126 (2018).
42 Zhong, G. *et al.* Thermal runaway and fire behavior investigation of lithium ion batteries using modified cone calorimeter. *Journal of Thermal Analysis and Calorimetry* **135**, 2879-2889 (2019).
43 Akiba, H. *et al.* Development of adiabatic calorimetry system for enthalpy of gas absorption/adsorption and its application to H2/D2 absorption into palladium nanoparticles. *Thermochimica Acta* **670**, 87-91 (2018).
44 Huang, S.-Y., Huang, C.-D., Chang, B.-T. & Yeh, C.-T. Chemical activity of palladium clusters: sorption of hydrogen. *The Journal of Physical Chemistry B* **110**, 21783-21787 (2006).
45 Robinson, D. B., Luo, W., Cai, T. Y. & Stewart, K. D. Metal hydride differential scanning calorimetry as an approach to compositional determination of mixtures of hydrogen isotopologues and helium. *International Journal of Hydrogen Energy* **40**, 14257-14270 (2015).
46 Jain, A. & Goodson, K. E. Measurement of the thermal conductivity and heat capacity of freestanding shape memory thin films using the 3 ω method. *Journal of Heat Transfer* **130**, 102402 (2008).
47 Cappella, A. *et al.* High Temperature Thermal Conductivity of Amorphous Al2 O 3 Thin Films Grown by Low Temperature ALD. *Advanced Engineering Materials* **15**, 1046-1050 (2013).
48 Kim, K. *et al.* Radiative heat transfer in the extreme near field. *Nature* **528**, 387-391 (2015).
49 Fiorino, A. *et al.* Nanogap near-field thermophotovoltaics. *Nature Nanotechnology* **13**, 806-811 (2018).
50 Mittapally, R. *et al.* Near-field thermophotovoltaics for efficient heat to electricity conversion at high power density. *Nature Communications* **12**, 1-8 (2021).
51 Brintlinger, T., Qi, Y., Baloch, K. H., Goldhaber-Gordon, D. & Cumings, J. Electron thermal microscopy. *Nano Letters* **8**, 582-585 (2008).
52 Abel, M. R., Wright, T. L., King, W. P. & Graham, S. Thermal metrology of silicon microstructures using Raman spectroscopy. *IEEE T Compon Pack T* **30**, 200-208 (2007).
53 O'Callahan, B. T. & Raschke, M. B. Laser heating of scanning probe tips for thermal near-field spectroscopy and imaging. *Apl Photonics* **2** (2017).
54 Mohtadi, R. & Orimo, S.-i. The renaissance of hydrides as energy materials. *Nature Reviews Materials* **2**, 1-15 (2016).
55 Xu, Z. *et al.* Size-dependent catalytic activity of supported metal clusters. *Nature* **372**, 346-348 (1994).
56 Mauron, P., Bielmann, M., Bissig, V., Remhof, A. & Züttel, A. High-pressure and high-temperature differential scanning calorimeter for combined pressure-concentration-temperature measurements of hydrides. *Review of Scientific Instruments* **80**, 095113 (2009).
57 MacLeod, B. *et al.* High-temperature high-pressure calorimeter for studying gram-scale heterogeneous chemical reactions. *Review of Scientific Instruments* **88**, 084101 (2017).
58 Smith, A. L. & Shirazi, H. M. Principles of quartz crystal microbalance/heat conduction calorimetry: Measurement of the sorption enthalpy of hydrogen in palladium. *Thermochimica Acta* **432**, 202-211 (2005).

59 Fiorino, A. *et al.* Parallelized, real-time, metabolic-rate measurements from individual Drosophila. *Scientific Reports* **8**, 1-10 (2018).
60 Lide, D. R. *CRC handbook of chemistry and physics*. Vol. 85 (CRC press, 2004).
61 Bergman, T. L., Incropera, F. P., DeWitt, D. P. & Lavine, A. S. *Fundamentals of heat and mass transfer*. (John Wiley & Sons, 2011).
62 Assael, M., Botsios, S., Gialou, K. & Metaxa, I. Thermal conductivity of polymethyl methacrylate (PMMA) and borosilicate crown glass BK7. *International Journal of Thermophysics* **26**, 1595-1605 (2005).
63 Powell, R., Ho, C. Y. & Liley, P. E. *Thermal conductivity of selected materials*. Vol. 8 (US Department of Commerce, National Bureau of Standards Washington, DC, 1966).
64 Roder, H. Thermal conductivity of hydrogen for temperatures between 78 and 310 K with pressures to 70 MPa. *International Journal of Thermophysics* **5**, 323-350 (1984).
65 McMahon, H. O. Thermal radiation characteristics of some glasses. *Journal of the American Ceramic Society* **34**, 91-96 (1951).
66 Tava´ rez, A. & Gonza´ lez, J. Modeling the thermal behavior of solder paste inside reflow ovens. *Journal of Electron Packaging* **125**, 335-346 (2003).
67 Vries, T. D. Specific Heat of Pyrex Glass from 25 to 175 C. *Industrial & Engineering Chemistry* **22**, 617-618 (1930).
68 Sharp, D. & Ginther, L. Effect of composition and temperature on the specific heat of glass. *Journal of the American Ceramic Society* **34**, 260-271 (1951).
69 Griessen, R., Strohfeldt, N. & Giessen, H. Thermodynamics of the hybrid interaction of hydrogen with palladium nanoparticles. *Nature Materials* **15**, 311-317 (2016).
70 Syrenova, S. *et al.* Hydride formation thermodynamics and hysteresis in individual Pd nanocrystals with different size and shape. *Nature Materials* **14**, 1236-1244 (2015).
71 Yamauchi, M., Ikeda, R., Kitagawa, H. & Takata, M. Nanosize effects on hydrogen storage in palladium. *The Journal of Physical Chemistry C* **112**, 3294-3299 (2008).
72 Behm, R., Penka, V., Cattania, M. G., Christmann, K. & Ertl, G. Evidence for ‘‘subsurface’’hydrogen on Pd (110): An intermediate between chemisorbed and dissolved species. *The Journal of Chemical Physics* **78**, 7486-7490 (1983).
73 Langhammer, C., Zhdanov, V. P., Zorić, I. & Kasemo, B. Size-dependent kinetics of hydriding and dehydriding of Pd nanoparticles. *Physical Review Letters* **104**, 135502 (2010).
74 Johnson, N. J. *et al.* Facets and vertices regulate hydrogen uptake and release in palladium nanocrystals. *Nature Materials* **18**, 454-458 (2019).
75 Jewell, L. L. & Davis, B. H. Review of absorption and adsorption in the hydrogen–palladium system. *Applied Catalysis A: General* **310**, 1-15 (2006).
76 Dantzer, P. & Millet, P. Advances in hydride phase growth: Automatic high precision calorimeter-volumetric devices, for thermodynamic and kinetics analyses. *Review of Scientific Instruments* **71**, 142-153 (2000).
77 Wadell, C. *et al.* Thermodynamics of hydride formation and decomposition in supported sub-10 nm Pd nanoparticles of different sizes. *Chemical Physics Letters* **603**, 75-81 (2014).
78 Bardhan, R. *et al.* Uncovering the intrinsic size dependence of hydriding phase transformations in nanocrystals. *Nature Materials* **12**, 905-912 (2013).
79 Ziegler, J. G. & Nichols, N. B. Optimum settings for automatic controllers. *Transactions of the ASME* **64** (1942).
80 Åström, K. J. & Wittenmark, B. *Computer-controlled systems: theory and design*. (Courier Corporation, 2013).

81 Ioannou, P. A. & Sun, J. *Robust adaptive control*. (Courier Corporation, 2012).
82 Hong, S. *et al.* Sub-nanowatt microfluidic single-cell calorimetry. *Nature Communications* **11**, 1-9 (2020).
83 Lee, G.-H. *et al.* Graphene-based Josephson junction microwave bolometer. *Nature* **586**, 42-46 (2020).
84 Wei, J., Murray, J. M., Barnes, J., Gonzalez, L. P. & Guha, S. Determination of the temperature dependence of the band gap energy of semiconductors from transmission spectra. *Journal of Electronic Materials* **41**, 2857-2866 (2012).
85 Johnson, S. & Tiedje, T. Temperature dependence of the Urbach edge in GaAs. *Journal of Applied Physics* **78**, 5609-5613 (1995).
86 Marple, D. Refractive index of GaAs. *Journal of Applied Physics* **35**, 1241-1242 (1964).
87 Vendelbo, S. *et al.* Visualization of oscillatory behaviour of Pt nanoparticles catalysing CO oxidation. *Nature Materials* **13**, 884-890 (2014).
88 Li, D. *et al.* Thermal conductivity of individual silicon nanowires. *Applied Physics Letters* **83**, 2934-2936 (2003).
89 Seol, J. H. *et al.* Two-dimensional phonon transport in supported graphene. *Science* **328**, 213-216 (2010).
90 Neumann, P. *et al.* High-precision nanoscale temperature sensing using single defects in diamond. *Nano letters* **13**, 2738-2742 (2013).
91 Jarzyna, M. & Zwierz, M. Quantum interferometric measurements of temperature. *Physical Review A* **92**, 032112 (2015).
92 Luerssen, D., Hudgings, J. A., Mayer, P. M. & Ram, R. J. in *Semiconductor Thermal Measurement and Management IEEE Twenty First Annual IEEE Symposium, 2005.* 253-258 (IEEE).
93 Cahill, D. G., Goodson, K. & Majumdar, A. Thermometry and thermal transport in micro/nanoscale solid-state devices and structures. *Journal of Heat Transfer* **124**, 223-241 (2002).
94 Whittaker, D. & Culshaw, I. Scattering-matrix treatment of patterned multilayer photonic structures. *Physical Review B* **60**, 2610 (1999).
95 Johnson, P. B. & Christy, R.-W. Optical constants of the noble metals. *Physical Review B* **6**, 4370 (1972).
96 Lautenschlager, P., Garriga, M., Logothetidis, S. & Cardona, M. Interband critical points of GaAs and their temperature dependence. *Physical Review B* **35**, 9174 (1987).
97 Schaefer, S., Gao, S., Webster, P., Kosireddy, R. & Johnson, S. Absorption edge characteristics of GaAs, GaSb, InAs, and InSb. *Journal of Applied Physics* **127**, 165705 (2020).
98 Åström, K. J. & Murray, R. M. *Feedback systems*. (Princeton university press, 2010).
99 Lee, Y.-H. *et al.* Room-temperature optical nonlinearities in GaAs. *Physical Review Letters* **57**, 2446 (1986).
100 Ganeev, R. Nonlinear refraction and nonlinear absorption of various media. *Journal of Optics A: Pure and Applied Optics* **7**, 717 (2005).
101 Masalov, A., Kuzhamuratov, A. & Lvovsky, A. Noise spectra in balanced optical detectors based on transimpedance amplifiers. *Review of Scientific Instruments* **88**, 113109 (2017).
102 McCammon, D. *et al.* Thermal calorimeters for high resolution X-ray spectroscopy. *Nuclear Instruments and Methods in Physics Research Section A: Accelerators, Spectrometers, Detectors and Associated Equipment* **326**, 157-165 (1993).

103 Gehrsitz, S. *et al.* The refractive index of Al x Ga 1− x As below the band gap: accurate determination and empirical modeling. *Journal of Applied Physics* **87**, 7825-7837 (2000).
104 Byrd, R. H., Hribar, M. E. & Nocedal, J. An interior point algorithm for large-scale nonlinear programming. *SIAM Journal on Optimization* **9**, 877-900 (1999).
105 Ozaki, S. & Adachi, S. Spectroscopic ellipsometry and thermoreflectance of GaAs. *Journal of Applied Physics* **78**, 3380-3386 (1995).
106 Cai, L., Pan, J. & Hu, S. Overview of the coupling methods used in whispering gallery mode resonator systems for sensing. *Optics and Lasers in Engineering* **127**, 105968 (2020).
107 Cui, L. *et al.* Quantized thermal transport in single-atom junctions. *Science* **355**, 1192-1195 (2017).
108 Shi, L., Plyasunov, S., Bachtold, A., McEuen, P. L. & Majumdar, A. Scanning thermal microscopy of carbon nanotubes using batch-fabricated probes. *Applied Physics Letters* **77**, 4295-4297 (2000).
109 Lee, W. *et al.* Heat dissipation in atomic-scale junctions. *Nature* **498**, 209-212 (2013).
110 Bai, T. & Gu, N. Micro/nanoscale thermometry for cellular thermal sensing. *Small* **12**, 4590-4610 (2016).
111 Wang, C. *et al.* Tunable carbon-dot-based dual-emission fluorescent nanohybrids for ratiometric optical thermometry in living cells. *ACS Applied Materials & Interfaces* **8**, 6621-6628 (2016).
112 Howell, S. T., Grushina, A., Holzner, F. & Brugger, J. Thermal scanning probe lithography—A review. *Microsystems & Nanoengineering* **6**, 1-24 (2020).
113 Chen, S. *et al.* Monolayer MoS2 nanoribbon transistors fabricated by scanning probe lithography. *Nano Letters* **19**, 2092-2098 (2019).
114 Mecklenburg, M. *et al.* Nanoscale temperature mapping in operating microelectronic devices. *Science* **347**, 629-632 (2015).
115 Menges, F., Riel, H., Stemmer, A., Dimitrakopoulos, C. & Gotsmann, B. Thermal transport into graphene through nanoscopic contacts. *Physical Review Letters* **111**, 205901 (2013).
116 Datye, I. M. *et al.* Localized heating and switching in MoTe2-based resistive memory devices. *Nano Letters* **20**, 1461-1467 (2020).
117 Halbertal, D. *et al.* Imaging resonant dissipation from individual atomic defects in graphene. *Science* **358**, 1303-1306 (2017).
118 Marguerite, A. *et al.* Imaging work and dissipation in the quantum Hall state in graphene. *Nature* **575**, 628-633 (2019).
119 Gomès, S., Assy, A. & Chapuis, P. O. Scanning thermal microscopy: A review. *Physica Status Solidi (A)* **212**, 477-494 (2015).
120 Martinek, J., Klapetek, P. & Campbell, A. C. Methods for topography artifacts compensation in scanning thermal microscopy. *Ultramicroscopy* **155**, 55-61 (2015).
121 Chung, J. *et al.* Quantitative temperature measurement of an electrically heated carbon nanotube using the null-point method. *Review of Scientific Instruments* **81**, 114901 (2010).
122 Chung, J. *et al.* Quantitative temperature profiling through null-point scanning thermal microscopy. *International Journal of Thermal Sciences* **62**, 109-113 (2012).
123 Kim, K. *et al.* in *International Conference on Micro/Nanoscale Heat Transfer*. 899-904.
124 Menges, F., Riel, H., Stemmer, A. & Gotsmann, B. Quantitative thermometry of nanoscale hot spots. *Nano Letters* **12**, 596-601 (2012).
125 Menges, F., Riel, H., Stemmer, A. & Gotsmann, B. Nanoscale thermometry by scanning thermal microscopy. *Review of Scientific Instruments* **87**, 074902 (2016).

126 Reihani, A. *et al.* Quantifying the temperature of heated microdevices using scanning thermal probes. *Applied Physics Letters* **118**, 163102 (2021).
127 Cui, L. *et al.* Study of radiative heat transfer in Ångström-and nanometre-sized gaps. *Nature Communications* **8**, 1-9 (2017).
128 Madhavan Unni, P., Gunasekaran, M. & Kumar, A. ±30 μK temperature controller from 25 to 103° C: Study and analysis. *Review of scientific instruments* **74**, 231-242 (2003).
129 Whiting, R. & Angadi, M. Young's modulus of thin films using a simplified vibrating reed method. *Measurement Science and Technology* **1**, 662 (1990).
130 Purkl, F. *et al.* Measurement of Young's modulus and residual stress of atomic layer deposited Al2O3 and Pt thin films. *Journal of Micromechanics and Microengineering* **27**, 085008 (2017).
131 Brandes, E. A. & Brook, G. *Smithells metals reference book.* (Elsevier, 2013).
132 Shackelford, J. F. & Alexander, W. *CRC materials science and engineering handbook.* (CRC press, 2000).
133 Zhang, X. *et al.* Thermal and electrical conductivity of a suspended platinum nanofilm. *Applied Physics Letters* **86**, 171912 (2005).
134 Chien, H.-C., Yao, D.-J. & Hsu, C.-T., Study for the Interface Thermal Resistance of Metal-Dielectric Layers, in *International Conference on Integration and Commercialization of Micro and Nanosystems.* 423-427 (2008).
135 Fiorino, A. *et al.* Giant Enhancement in Radiative Heat Transfer in Sub-30 nm Gaps of Plane Parallel Surfaces. *Nano Letters* **18**, 3711-3715 (2018).
136 Song, B. *et al.* Enhancement of near-field radiative heat transfer using polar dielectric thin films. *Nature Nanotechnology* **10**, 253-258 (2015).
137 Inoue, T. *et al.* One-Chip Near-Field Thermophotovoltaic Device Integrating a Thin-Film Thermal Emitter and Photovoltaic Cell. *Nano Letters* **19**, 3948-3952 (2019).
138 Thompson-Pettes, M. & Shi, L. A reexamination of phonon transport through a nanoscale point contact in vacuum. *Journal of Heat Transfer* **136** (2014).
139 Grosse, K. L., Bae, M. H., Lian, F., Pop, E. & King, W. P. Nanoscale Joule heating, Peltier cooling and current crowding at graphene–metal contacts. *Nature Nanotechnology* **6**, 287-290 (2011).
140 Shi, L. *et al.* Thermal probing of energy dissipation in current-carrying carbon nanotubes. *Journal of Applied Physics* **105**, 104306 (2009).
141 Boroumand, F. A., Voigt, M., Lidzey, D. G., Hammiche, A. & Hill, G. Imaging Joule heating in a conjugated-polymer light-emitting diode using a scanning thermal microscope. *Applied Physics Letters* **84**, 4890-4892 (2004).
142 Cui, L. *et al.* Thermal conductance of single-molecule junctions. *Nature* **572**, 628-633 (2019).
143 Thompson, D. *et al.* Hundred-fold enhancement in far-field radiative heat transfer over the blackbody limit. *Nature* **561**, 216-221 (2018).
144 Fernández-Hurtado, V., Fernández-Domínguez, A. I., Feist, J., García-Vidal, F. J. & Cuevas, J. C. Super-Planckian far-field radiative heat transfer. *Physical Review B* **97**, 045408 (2018).
145 Shin, S., Elzouka, M., Prasher, R. & Chen, R. Far-field coherent thermal emission from polaritonic resonance in individual anisotropic nanoribbons. *Nature Communications* **10**, 1-11 (2019).
146 Kim, K. *et al.* Quantification of thermal and contact resistances of scanning thermal probes. *Applied Physics Letters* **105**, 203107 (2014).

147 Moore, J. P., Williams, R. K. & Graves, R. S. Thermal conductivity, electrical resistivity, and Seebeck coefficient of high-purity chromium from 280 to 1000 K. *Journal of Applied Physics* **48**, 610-617 (1977).
148 Glassbrenner, C. J. & Slack, G. A. Thermal conductivity of silicon and germanium from 3 K to the melting point. *Physical Review* **134**, A1058 (1964).
149 Pierret, R. F. *Semiconductor device fundamentals*. (Pearson Education, 1996).
150 He, Z., Yan, Y. & Zhang, Z. Thermal management and temperature uniformity enhancement of electronic devices by micro heat sinks: A review. *Energy*, 119223 (2020).
151 Pipe, K., Ram, R. J. & Shakouri, A. Bias-dependent Peltier coefficient and internal cooling in bipolar devices. *Physical Review B* **66**, 125316 (2002).
152 Sadi, T., Radevici, I. & Oksanen, J. Thermophotonic cooling with light-emitting diodes. *Nature Photonics* **14**, 205-214 (2020).
153 Santhanam, P., Gray Jr, D. J. & Ram, R. J. Thermoelectrically pumped light-emitting diodes operating above unity efficiency. *Physical Review Letters* **108**, 097403 (2012).
154 Li, Z., Xue, J. & J. Ram, R. Heat exchange with interband tunneling. *Journal of Applied Physics* **126**, 165107 (2019).
155 Sze, S. M., Li, Y. & Ng, K. K. *Physics of semiconductor devices*. (John wiley & sons, 2021).
156 Esaki, L. New phenomenon in narrow germanium p− n junctions. *Physical Review* **109**, 603 (1958).
157 Colter, P., Hagar, B. & Bedair, S. Tunnel junctions for III-V multijunction solar cells review. *Crystals* **8**, 445 (2018).
158 Knodl, T. *et al.* Multistage bipolar cascade vertical-cavity surface-emitting lasers: Theory and experiment. *IEEE Journal of Selected Topics in Quantum Electronics* **9**, 1406-1414 (2003).
159 Dummer, M., Johnson, K., Rothwell, S., Tatah, K. & Hibbs-Brenner, M., The role of VCSELs in 3D sensing and LiDAR, in *Optical Interconnects XXI*. 116920C, International Society for Optics and Photonics (2021).
160 Moulin, N., Amara, M., Mandorlo, F. & Lemiti, M. Tunnel junction I (V) characteristics: Review and a new model for pn homojunctions. *Journal of Applied Physics* **126**, 033105 (2019).
161 *UHV 750 Variable Temperature Ultra-High Vacuum Atomic Force Microscope User's Guide*. (RHK Technology, Inc., 2007).
162 Shibata, N. *et al.* Imaging of built-in electric field at a pn junction by scanning transmission electron microscopy. *Scientific Reports* **5**, 1-8 (2015).
163 Adachi, S. Lattice thermal resistivity of III–V compound alloys. *Journal of Applied Physics* **54**, 1844-1848 (1983).